SCUOLA DI DOTTORATO

UNIVERSITÀ DEGLI STUDI DI MILANO-BICOCCA

Department of Materials Science

PhD Course in Materials Science and Nanotechnology, XXXIV Cycle

Hybrid and Nanostructured materials for low power photon upconversion based on triplet-triplet annihilation

Alessandra Ronchi

Matr. n. 748053

Tutor:
Prof. Francesco Meinardi
Supervisor:
Prof. Angelo Maria Monguzzi

Coordinator:
Prof. Marco Bernasconi

ACADEMIC YEAR 2020/2021

Contents

Introduction

The continuously increasing energy demand for human activities is making the necessity of new energy sources more and more imperative and essential. At the same time the environmental preservation requires an urgent shift towards greener energy sources, possibly abandoning fossil fuels, that are the main responsible for the greenhouse gas emissions. Among the technologies developed in the last decades to overcome our dependency on fossil fuels there is the direct exploitation of solar light by means of photovoltaic (PV) devices, that allow to convert the solar radiation in electricity. The sun in just one and a half hours provides indeed enough energy to cover our energy need of an entire year, therefore it is an inestimable energy source that can be extensively exploited in a sustainable way. The most common PV devices that can be now easily found worldwide in many houses due to their commercial availability are the first generation silicon-based PV devices. According to the Shockley-Quisser limit, the maximum conversion efficiency in single-junction PV devices based on silicon is $\sim 31\%$ (34% for a band-gap of 1.3 eV).[1,2] The research is still massively thriving in this field with the development of the third generation PV devices towards alternative architectures (e.g. organic and dye-sensitized solar cells) as well as towards higher conversion efficiencies.[3] A promising means to increase the conversion efficiency beyond the Shockley-Quisser limit is to employ multijunction devices. De Vos calculated that by employing three junctions with energy bandgap of 2.3 eV, 1.4 eV, and 0.8 eV respectively, the theoretical conversion limit increases to 49%.[4] A different approach in this regard is to use low-energy photons as well, i.e. those photons with energy lower than the active material's energy bandgap, that otherwise would be lost. Photon upconversion, a photophysical process that allows to covert low energy photons into high energy ones, has caught great attention as a possible approach to increase the storage ability of PV devices. It can take place thanks to non-linear properties of peculiar non-linear crystals (second-harmonic generation),[5] two-photon absorption,[6] or a multistep excitation of lanthanides ions embedded in proper hosts.[7] These techniques usually

require coherent light sources and high excitation intensities, much greater than solar irradiance. Conversely, the so-called photon upconversion assisted by triplet-triplet annihilation (*s*TTA-UC) is particularly suited for solar applications as its intrinsic features allow to work efficiently also under solar light. Here, the high energy radiation, that can be absorbed by the PV device, is emitted from the fluorescent recombination of the excited singlet state of an emitter molecule, previously populated via annihilation of the metastable triplet states of two emitters. This is a sensitized process since a sensitizer is necessary to harvest the low energy incident light and to transfer the stored energy to the emitters via energy transfer. Because its functioning relies on long-lived metastable triplets, this process can be highly efficient also under low power, noncoherent light. As such, *s*TTA-UC is considered one of the most promising *photon management* techniques, as it potentially allows to adapt the solar spectrum to match the absorption profile of a PV device's active material.[8] As rough indication, Trupke et al. demonstrated that by coupling a 2 eV bandgap solar cell with an upconverter with 0.94 eV energy gap, the maximum conversion efficiency achievable can be as high as 47.6% under non concentrated sunlight.[9]

Despite this process was firstly unveiled by Parker and Hatchard in the 1960s,[10–15] the research in this field rapidly developed only starting from the last two decades, mainly owing to the independent studies of Castellano and Baluschev,[16,17] because the advancement in the synthesis of heavy metal–organic complexes with long-lived triplet states working as efficient sensitizers and energy donors allowed to drastically increase the upconversion performances. Since then, outstanding improvements were achieved on many different levels, from the optimization of sensitizers and annihilators/emitters,[18,19] to the development of proof-of-concept devices for solar applications, such as solar cells, devices for hydrogen production, photocatalytic cells, whose functioning is based on *s*TTA-UC.[20–25]

Nevertheless, the actual application of *s*TTA-UC in real-world devices is still hindered by two main limitations. The first is related to the sensitizer moiety. The availability of molecular sensitizers able to absorb near-infrared photons and work efficiently as energy donors is extremely limited and the complications to be faced in the design and synthesis of this kind of molecules are typically hard to handle and circumvent. Moreover, organic sensitizers show narrow absorption features, meaning that their storage ability is highly restricted. In this regard, in 2015 the new class of hybrid sensitizers composed of semiconductor nanostructures functionalized with conjugated organic ligands has been introduced. The advantages afforded,

such as broadband absorption spectrum and size-tunable optical properties, make hybrid sensitizers a promising alternative to organic sensitizers in solar technologies based on *s*TTA-UC. On the other hand, while the *s*TTA-UC performances in liquid environments are well-assessed, the research is still ongoing to translate the same performances in the solid-state, where the diffusion-limited nature of the photophysical processes involved often hinders the exploitation of *s*TTA-UC at low excitation intensities. This is a crucial limitation because solid-state upconverters are better suited for technological applications with respect to liquid systems, thereby many different approaches are being investigated to address this issue, but the best results achieved so far in the solid-state are still too poor for actual implementation.

In this Thesis I report the results that I collected throughout my PhD studies aimed at the investigation of the two aforementioned limitations still affecting *s*TTA upconverters.

After a brief overview of the *s*TTA-UC process and state of the art, in Chapter 4 I introduce a novel design of hybrid sensitizers, composed of CdSe nanocrystals doped with gold cations and functionalized with 9-anthracene carboxylic acid. I show that the exciton manipulation offered by the nanocrystal electronic doping allows to improve the triplet sensitization efficiency with respect to the undoped counterpart, because the photogenerated hole is provided with an alternative, more favored pathway compared to hole transfer from the nanocrystal valence band to the ligand HOMO level affecting undoped nanocrystals. Owing to this hole re-routing strategy I achieved an upconversion efficiency of 12%, which is the record efficiency for hybrid upconverting systems and comparable to the efficiencies commonly obtained in organic upconverting systems.

In Chapter 5, I consider a different example of hybrid sensitizers, where the doped CdSe nanocrystals are substituted with CdSe nanoplatelets, because their surface and photophysical properties make nanoplatelets potential desirable sensitizers. I show that the ligand exchange process necessary to functionalize the nanoplatelets surfaces with the conjugated organic ligands employed proceeds in an island-like way rather than homogeneously and this leads to the formation of molecular aggregates bound to the nanoplatelets surfaces. This has the paramount effect of changing the ligand triplet energy, with potential crucial repercussions on the emitter choice, since the thermodynamic driving force for the ligand-to-emitter

energy transfer can be negatively altered.

I then move to the study of two solid-state upconverters characterized by a nanostructured morphology, where liquid nanodomains with size < 50 nm containing the upconverting dyes are embedded in a rigid polymer matrix, discussed in Chapter 6 and 7 respectively. Importantly, to relieve the *s*TTA-UC efficiency dependence on the triplet excitons diffusivity, I demonstrate how an approach based on the controlled confinement of upconverting dyes in volumes smaller than those explored by the triplets during their diffusion is a successful method towards technological applications. This technique allows to handle upconverters with macroscopic performances comparable to those observed in the best upconverting solutions, but in the solid-state, with the further advantage to lower the threshold excitation intensity required to reach the maximum upconversion yield. These results directly arise from the locally enhanced triplet exciton density accomplished through the artificial dyes confinement that allows to maximize the TTA probability regardless of the molecular/exciton diffusion.

In Chapter 8, I introduce a new annihilator composed of two perylene units linked by a proper spacer and spatial orientation, specifically designed to prevent the limitations in the upconversion efficiency related to the fluorescence quantum yield losses often observed when employing annihilators that show the tendency to aggregate and form excimers under high dye concentrations. Thanks to the optimization of the fluorescence efficiency that directly results from the designed molecular structure, I obtained the excellent upconversion quantum yield of 42%, which is the record efficiency achieved so far in organic systems.

In the last Chapter, I draw a perspective of the upconversion performances that can be achieved by developing proper solid-state upconverters. I compare the *s*TTA-UC performances of three different ideal systems, i.e. a homogeneous bulk UC system, a confined single-sized UC system and a confined UC system with log-normal size distribution, to point out how the performances are affected by structural parameters (e.g. the nanostructures mean radius or the size distribution), and composition parameters (such as the system absorption bandwidth or the emitter triplet lifetime). I show that by reaching the best trade-off between nanostructure size and energy distribution, the threshold excitation intensity can be lowered orders of magnitude below the solar irradiance. Therefore, the important information gained through the

theoretical calculations presented can be used as guidelines to design solid-state upconverters towards future implementation in solar technologies.

State of the art

1.1 Brief overview of optical transitions

When a molecule interacts with light, the absorption of a photon of proper energy can promote a molecular transition from the initial state *i* to a final state *f*. The incident photon can be absorbed if the electromagnetic field can interact with the molecular charge through the transition dipole moment $M_{i,f}$ given by[26]

$$M_{i,f} = \langle \Psi_f | \, \boldsymbol{\mu} \, | \Psi_i \rangle \tag{1.1}$$

where in the first approximation $\boldsymbol{\mu}$ is the electric dipole moment operator, depending on the charge and positions of both electrons ($\boldsymbol{\mu_e}$) and nuclei ($\boldsymbol{\mu_N}$) as

$$\boldsymbol{\mu} = \boldsymbol{\mu}_e + \boldsymbol{\mu}_N = -e \sum_i \boldsymbol{r}_i + e \sum_j Z_j \boldsymbol{R}_j$$

and Ψ_i and Ψ_f are the wavefunctions describing the molecular initial and final state, respectively. From Fermi's golden rule, the transition probability from an initial to a final state is given by the square of the absolute value of the corresponding transition dipole moment, thereby a transition will be much more intense the more probable it is.

A simplistic but effective treatment of molecular wavefunctions is afforded by the Born- Oppenheimer approximation.[27] In this framework, the molecular wavefunction Ψ can be written as the product of an electronic, a vibrational and a rotational wavefunction $\Psi = \psi_e \psi_v \psi_r$ and the energy of the corresponding state can be written as the sum of an electronic, vibrational and rotational energy:[26]

$$E = E_e + E_v + E_r$$

Given the energies involved, the rotational terms can be generally neglected, therefore the wavefunction of a given molecular state can be approximated to $\Psi = \psi_e\psi_v$. However, the spin configuration χ must also be taken into account, therefore the complete approximated molecular wavefunction can be expressed as $\Psi = \psi_e\psi_v\chi$. A transition that simultaneously involves electronic and vibrational levels is called a vibronic transition and the probability, and thus the intensity, of vibronic transitions can be expressed in the framework of the *Franck-Condon principle*, that allows to get important information about the selection rules governing optical transitions.[26] In this picture, one can consider a transition dipole moment M from an initial vibrational state of the electronic ground state Ψ to a final vibronic state Ψ'. The transition probability is proportional to $|M|^2 = |\langle\Psi'|\,\boldsymbol{\mu}\,|\Psi\rangle|^2$ with

$$M = \langle\Psi'|\,\boldsymbol{\mu}\,|\Psi\rangle = \int \Psi'^{*}\boldsymbol{\mu}\Psi d\tau$$

where the wavefunctions are the product of the vibrational, electronic and spin wavefunctions $\Psi = \psi_e\psi_v\chi$:

$$M = \int \psi_e'^{*}\psi_v'^{*}\chi'^{*}\boldsymbol{\mu}_e\psi_e\psi_v\chi d\tau + \int \psi_e'^{*}\psi_v'^{*}\chi'^{*}\boldsymbol{\mu}_N\psi_e\psi_v\chi d\tau$$

resulting, in the first approximation, in:

$$M = \int \psi_v'^{*}\psi_v d\tau_n \int \psi_e'^{*}\boldsymbol{\mu_e}\psi_e d\tau_e \int \chi'^{*}\chi d\tau_s + \int \psi_e'^{*}\psi_e d\tau_e \int \psi_v'^{*}\boldsymbol{\mu_N}\psi_v d\tau_v \int \chi'^{*}\chi d\tau_s \quad (1.2)$$

The first term is the vibrational overlap integral also referred to as *Franck-Condon factor*, the second accounts for the orbital selection rule and the third for the spin selection rule. The second addend is null because of the orthogonality of electronic wavefunctions relative to different electronic states. As a whole, the resulting selection rules lead to the vibronic replicas, with an intensity distribution mirroring the probability of each transition. Here, the electronic transition dipole moment $\int \psi_e'\boldsymbol{\mu_e}\psi_e d\tau_e$ determines the overall intensity of the transition, and it is strictly related to the oscillator strength, while the Franck-Condon factors set the intensity of each vibrational component. Only transitions with non-vanishing transition dipole moments are allowed, so in principle the intensity of a forbidden transition is zero. For example, a transition with $\int \psi_e'\boldsymbol{\mu_e}\psi_e d\tau_e = 0$ is said to be *dipole forbidden*. Analogously, from the spin selection rule it is clear that only transitions between states with the same spin multiplicity are allowed.

The processes that can take place once a molecule is promoted to an excited state after photon absorption are depicted in the so-called Jablonski diagram.[28] Referring to Figure 1.1, almost

all molecules in their ground state are in singlet configuration, denoted as S_0, therefore upon photon absorption the spin selection rule allows only transitions to an excited singlet state, and given the energies typically employed the molecule is promoted to the first (S_1) or second (S_2) excited singlet state. Each electronic state is characterized by its own set of vibrational levels (depicted by the light blue solid lines in the figure). After excitation, the molecule relaxes via internal conversion (IC) and/or vibrational relaxation (VR) to the lowest excited state S_1 (Kasha's rule) on a picosecond timescale. The relaxation from S_1 to the ground state can then

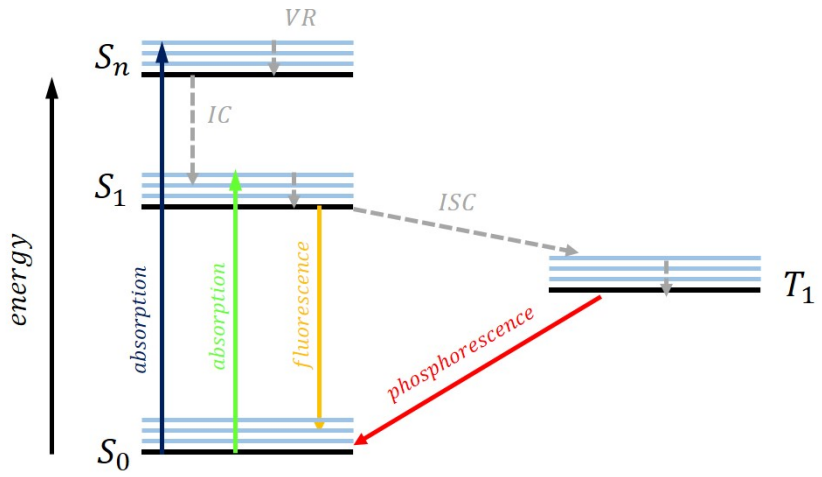

Figure 1.1: Jablonski diagram representing the possible photophysical processes occurring in a molecule after photon absorption: fluorescence, phosphorescence, intersystem crossing (ISC), internal conversion (IC), and vibrational relaxation (VR). The horizontal black and light blue lines mark the electronic and vibrational energy levels of the singlet (S) and triplet (T) states, respectively. The radiative transitions are represented by solid arrows, while the nonradiative transitions are represented by dashed arrows.

take place radiatively or nonradiatively. In the first case, the absorption of the incident photon is followed by the emission of a redshifted photon owing to energy losses due to vibrational relaxation and, if it occurs, to internal conversion. This process is called *fluorescence* and is fully allowed in the quantum mechanical picture. In the second case, the molecular relaxation is mediated by internal conversion and vibrational relaxation without photon emission. Along with fluorescence, a second radiative process can take place if specific conditions are met. The molecule from its S_1 excited state can undergo *intersystem crossing* (ISC) to an excited triplet state T_n. Intersystem crossing is a nonradiative transition, in principle forbidden as it involves initial and final states with different spin multiplicity. But if the *spin-orbit coupling* is sufficiently strong to mix the spin angular momentum and the orbital angular momentum,

the transition can take place.[26] If the subsequent $T_1 \rightarrow S_0$ transition is radiative, the process is called *phosphorescence*, which is only partially allowed in the quantum mechanical picture. Since the intensity of the spin-orbit coupling increases in the presence of heavy atoms (as it scales as Z^4, with Z the atomic number), phosphorescent molecules can be easily found among metalated complexes such as metalated porphyrins containing heavy metal atoms, as Pt or Pd.[29–31] The allowed nature of fluorescence results in recombination lifetimes on the nanosecond timescale, whereas phosphorescent molecules show typical lifetimes on the millisecond timescale and beyond. The emissive recombination is always in competition with all the possible nonradiative recombination pathways, therefore the fluorescence (phosphorescence) quantum yield Φ_{fl} (Φ_{ph}) of a fluorophore (phosphore) is set by the ratio between the radiative rate and the sum of the rates over all the possible recombination pathways, according to:[26,28]

$$\Phi_{fl,ph} = \frac{k_{rad}}{k_{rad} + k_{nonrad}} \tag{1.3}$$

and it can be highly influenced by external factors such as dye concentration and environment.

1.2 Photophysical processes in *s*TTA-UC

A generic *s*TTA-UC system is composed of two components: a sensitizer/light harvester and an annihilator/emitter, also called energy *donor* (D) and energy *acceptor* (A).[32,33,35–39] In this process the upconverted light comes from the encounter and annihilation of two emitter molecules in their triplet states. It is a "sensitized" process because, given that the $S_0 \rightarrow T_1$ transition is optically forbidden,[40] it is not possible to directly populate the acceptor triplet states, but the sensitizer absorbs the incident photons and then transfers the excitation to the emitter triplet states.

The photophysical steps involved in *s*TTA-UC are sketched in Figure 1.2. In this first general treatment I assume that both sensitizer and emitter are organic molecules, which constitute the most thoroughly investigated upconverting system so far.[41,42]

Dexter energy transfer. With the absorption of an incident photon, the sensitizer is promoted from its ground state S_0 to the first excited singlet state S_1, rapidly relaxing to the triplet state T_1 via fast intersystem crossing. The sensitizer triplet exciton can then recombine radiatively with rate k_D^T, emitting red-shifted photons (via phosphorescence), or the sensitizer triplet exciton is transferred to the emitter through a Dexter-type triplet-triplet energy trans-

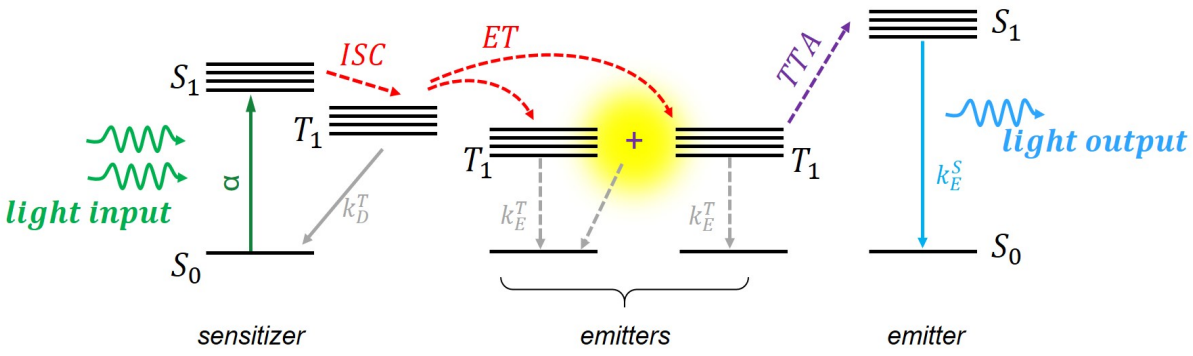

Figure 1.2: Jablonski diagram describing the photophysics of photon upconversion sensitized by triplet-triplet annihilation (*s*TTA-UC). Upon photon absorption, a sensitizer with absorption coefficient α is excited into its singlet state (S_1) that efficiently undergoes intersystem crossing (*ISC*) to its triplet state (T_1). The triplet exciton is then transferred via Dexter energy transfer (ET) towards the triplet state T_1 of an emitter molecule. The as-populated emitter triplets can either spontaneously decay (with rate constant k_E^T) or undergo triplet-triplet annihilation (*TTA*). As a result one emitter molecule is promoted to its excited singlet state S_1, that recombines emitting the high energy photon, while the other returns to its ground state S_0. The dashed arrows mark nonradiative transitions.

fer (ET), if during the triplet lifetime it encounters an unexcited emitter, populating the emitter triplet state. Dexter ET is a short range interaction that requires collision between donor and acceptor with an interaction distance on a nanometer scale, as it occurs owing to the exchange interaction. Dexter ET can intrinsically populate energy levels that are not optically accessible, such as the triplets themselves. In fact, the probability that the excitation is transferred from the donor to the acceptor is:[43]

$$P_{et} = \frac{2\pi}{\hbar}\left|\int \Psi_i^* H \Psi_f d\tau\right|^2 \rho_E \tag{1.4}$$

where Ψ_i (Ψ_f) is the initial (final) state with the acceptor (donor) in the ground state and the donor (acceptor) is excited, H is the perturbation Hamiltonian $H \simeq \frac{e^2}{\boldsymbol{r_{12}}}$, where $\boldsymbol{r_{12}}$ is related to the distance between the electrons of the two molecules, and ρ_E is the density of states. Expressing the donor/acceptor wavefunction as $\psi(\boldsymbol{r}, \boldsymbol{\sigma}) = \phi(\boldsymbol{r})\chi(\boldsymbol{\sigma})$, with $\phi(\boldsymbol{r})$ and $\chi(\boldsymbol{\sigma})$ the spatial and spin wavefunction respectively, the matrix element $< H >$ between the initial and final states is:

$$\begin{aligned} < H > = & \int \phi_d^{'*}(\boldsymbol{r_1})\phi_a^*(\boldsymbol{r_2})H\phi_d(\boldsymbol{r_1})\phi_a^{'}(\boldsymbol{r_2}) \;\; \chi_d^{'*}(\boldsymbol{\sigma_1})\chi_a^*(\boldsymbol{\sigma_2})\chi_d(\boldsymbol{\sigma_1})\chi_a^{'}(\boldsymbol{\sigma_2}) \\ & - \int \phi_d^{'*}(\boldsymbol{r_1})\phi_a^*(\boldsymbol{r_2})H\phi_a^{'}(\boldsymbol{r_1})\phi_d(\boldsymbol{r_2}) \;\; \chi_d^{'*}(\boldsymbol{\sigma_1})\chi_a^*(\boldsymbol{\sigma_2})\chi_a^{'}(\boldsymbol{\sigma_1})\chi_d(\boldsymbol{\sigma_2}) \end{aligned} \tag{1.5}$$

where the terms $\phi^{'}$ and $\chi^{'}$ indicate the excited states wavefunctions, while the terms ϕ and χ are relative to the ground state configurations. The first term in Eq. 1.5 is the Coulomb term and, as the hamiltonian does not operate on the spin wavefunction, it is null unless $\chi_d^{'} = \chi_d$ and $\chi_a^{'} = \chi_a$ (spin selection rule). The second integral is the exchange term, that goes to zero unless $\chi_d^{'} = \chi_a^{'}$ and $\chi_d = \chi_a$, but importantly $\chi^{'}$ can differ from χ. The selection rules over the spatial variables forbid only specific transitions so, even if the Coulomb term goes to zero, the exchange interaction can lead to the excitation of the acceptor triplets.

The probability of energy transfer between a donor and an acceptor at distance *R* by means of the exchange interaction, can be also written as:[43–45]

$$P_{ET} \sim k_{ET} = \frac{2\pi\zeta^2}{\hbar} \int f_d(E) F_a(E) dE \tag{1.6}$$

with $\zeta^2 \sim e^{-2r/L}$, where *L* is the effective Bohr radius, that measures the ϕ_d and ϕ_a spatial extension, and f_d (F_a) is the donor (acceptor) normalized emission (absorption) spectrum. Therefore, the ET rate k_{ET} depends exponentially on the intermolecular distance *R* and the overlap between donor and acceptor wavefunctions is crucial: because it does not depend on the product of the transitions oscillator strengths, Dexter ET can involve forbidden transitions too. From Eq. 1.6 it is also clear that to maximize the transfer efficiency, it is essential for $f_d(E)$ and $F_a(E)$ to be resonant.

Triplet-triplet annihilation. Once populated, the emitter triplets can either recombine non-radiatively with rate k_E^T or they can annihilate if two triplet excitons interact before their spontaneous decay. The TTA rate k_{TTA} is defined as[41]

$$k_{TTA} = \gamma_{TT} T_E \tag{1.7}$$

where γ_{TT} is the second order rate constant characterizing the TTA process[46] and T_E is the emitter triplet density. Importantly, TTA is another Dexter ET which requires the direct interaction of two emitter triplets (homo-molecular energy transfer) and is mediated by the formation of a *collisional complex*, following the dimerization of two identical species in their triplet state.[47–50] It is worth discussing about the collisional complex as it gives information about the probability to obtain an emitter in its excited singlet state from a single TTA event. The discussion about the spin statistics in *s*TTA-UC has been usually carried out assuming the intertriplet exchange interaction to be negligible (strongly exchange-coupled triplet-pair states limit).[51] In this limit, when two molecules in their triplet state $^3M^*$ interact, they can form a collisional complex with pure spin character that can be of singlet, triplet and quintet

multiplicity, according to:[47]

$$
{}^3M^* + {}^3M^* \begin{cases} \rightleftharpoons {}^1|M \cdots M|^* \rightleftharpoons {}^1M + {}^1M \\ \rightleftharpoons {}^3|M \cdots M|^* \rightleftharpoons {}^1M + {}^3M^{**} \\ \rightleftharpoons {}^5|M \cdots M|^* \rightleftharpoons {}^1M + {}^5M^* \end{cases} \tag{1.8}
$$

From the degeneracy of the spin states the probability ratio to form one of these complexes is 1:3:5.[42,52] From the fission of a complex one molecule returns to the ground state (${}^1M$), while the other can be promoted to its excited singlet (${}^1M^*$), triplet (${}^3M^{**}$) or quintet state (${}^5M^*$). The only excited state able to emit photons is the singlet state, as the triplets and quintets cannot decay radiatively because of spin selection rules, thereby the nonradiative recombination from these states translates into undesired energy losses, while if the fission results in an excited singlet state, this can relax to the ground state by emitting the upconverted photon via fluorescence. Thus in principle since the first channel is the only bimolecular pathway that allows to populate the molecule's excited singlet state, the probability to populate an excited singlet state from a TTA event - hereafter referred to as f factor - should be as low as 0.11 (i.e. $\frac{1}{9}$). Nevertheless, the quintet complex usually dissociates into the initial ${}^3M^* + {}^3M^*$ states because the promotion of a molecule into its quintet state would require too much energy, much higher than the energy typically available. Therefore the quintet complex channel is usually inaccessible, and this contributes in increasing the f factor to 0.25.[33,53] Moreover, the triplet complex can dissociate into a molecule in its ground state ${}^1M$ and the other in an excited triplet state ${}^3M^{**}$, if the energy of the *n-th* excited triplet state is less than twice the energy of the initially interacting triplet state ${}^3M^*$. In common annihilators only the first and second excited triplets states (T_1 and T_2) can be populated via TTA. If the energetic condition $E(T_2) < 2 \times E(T_1) + k_B T$ is fulfilled, then T_2 usually relaxes to T_1 through internal conversion and becomes available again for TTA. In this case the effective fraction of singlet states created is ~ 0.4. But if $E(T_2) > 2 \times E(T_1) + k_B T$, the T_2 cannot be populated, and only the T_1 is accessible and remains available for the next TTA event.[54] This is the ideal condition, because there are no energy losses and the f factor can be 1. This is the case of annihilators such as perylene and rubrene, widely employed because since $E(T_2) > 2 \times E(T_1)$ they feature a f factor greater than 0.5, up to ~ 0.6 for rubrene[33,51,55] and ~ 1 for perylene.[33,34]

Conventionally, for the sake of simplicity, it has been usually assumed that all the encounter complexes created through TTA are strongly exchanged-coupled. Nevertheless, it has been recently and thoroughly shown how not only intertriplet coupling but also molecular orien-

tation play a crucial role in setting the f factor.[51] It has been shown that in the limit of weak coupling the nine possible triplet-pair states have no longer pure spin, but have a mixed character which is determined by the intertriplet exchange energy. The kind of mixing (singlet-triplet, triplet-quintet, singlet-quintet) also depends on the intermolecular orientation. Thus, it has been shown that the f factor goes from $^2/_5$ for orthogonal molecules to $^2/_3$ for parallel molecules, as a consequence of the variations of the spin mixing of the triplet-pairs wavefunctions. Moreover, the f factor can be affected by internal conversion from the triplet pair to single triplet states and by *high-level reverse intersystem crossing* (RISC).[51] As a matter of fact, internal conversion is a loss channel for one triplet in the pair. If its rate is slower than triplet-pair fusion and separation, its effects on f can be neglected, and if the level position is such to funnel the triplet-pair states to S_1 through T_2, RISC can occur efficiently resulting in $f \sim 1$. The combination of proper alignment among triplet-pair states, T_1, T_2 and S_1 with RISC explains the $f \sim 0.6$ observed in rubrene in solution.[51] These observations also highlight that the spin statistics of a TTA event does not depend only on the molecular intrinsic excited states properties, but it can also be manipulated by the local environment and molecular arrangement.

Interestingly, the fact that in the *s*TTA-UC process the emitters promotion to the high-energy excited singlets relies on the encounter of long-lived triplet states has as major consequence that this process does not require coherent light and if the system's composition is optimized good performances can be achieved under excitation intensities on the order of hundreds of mW cm^{-2},[19,32,56,57] comparable with the solar irradiance, i.e. 100 mW cm^{-2} under AM1.5 when integrated over the entire solar spectrum.[58] On the contrary, upconverting processes such as two-photon absorption observed with lanthanide ions typically require coherent light and excitation intensities on the order of MW cm^{-2}.[6,7,24,32,59–64] As such, *s*TTA-UC is the best candidate technique for photon management, as it allows to adapt the solar spectrum to better match the absorption spectrum of the solar device's active material. Other photon management techniques are photon down-conversion and singlet fission.[65–68] While these latter focus on the reduction of thermalization losses, *s*TTA-UC aims at improving the performances of photovoltaic or photocatalytic devices, also for water-splitting, by exploiting the sub-bandgap portion of solar spectrum.[20–24,32,61,69–78] Moreover, some proof-of-concept solar devices functioning on *s*TTA-UC have already been developed, where charges are extracted from the upconverted states populated via TTA.[59,73,74,79–83] It is worth emphasizing that photon

upconversion is extremely versatile as it finds applicability in a variety of technological fields, deeply different from each other, that exploit the intrinsic properties of this process, such as bio-imaging,[84–90] photodynamic therapy,[91,92] optogenetics,[93,94] anti-counterfeit,[95–99] oxygen detection,[100–103] sensoristic applications,[104–108] or optoelectronics.[109–113]

1.3 Sensitizers and annihilators/emitters requisites

The two bimolecular interactions underpinning the *s*TTA-UC process are the Dexter energy transfer from the sensitizer's triplet state to the annihilator's triplet state and the triplet-triplet annihilation between two annihilators in their triplet state. From this starting point it is possible to highlight what are the key requisites that sensitizers and annihilators must feature to optimize the *s*TTA-UC performances.

The sensitizer should have high absorption coefficient at the excitation wavelength to absorb the incident photons at the maximum extent,[42] and because high sensitizer concentrations can be necessary to increase the incident light absorption, the sensitizer should show a limited tendency to form aggregates, that usually introduce efficient nonradiative excitonic recombination channels.[35,114] To avoid the reabsorption of the emitted upconverted light, the sensitizer should also feature a limited spectral overlap between its absorption spectrum and the emitter photoluminescence spectrum.[76,77] Since the annihilator triplets are populated by means of a triplet-triplet energy transfer, the sensitizer should exhibit a unit intersystem crossing efficiency, meaning that all the energy absorbed can in principle be transferred to the annihilators and then upconverted,[76] and to minimize the energy losses between the absorbed and upconverted emitted light towards a maximized anti-Stokes shift the splitting between sensitizer's singlet and triplet states should be as small as possible.[115,116] For a high probability that a sensitizer in its triplet state encounters within its lifetime an annihilator available to receive energy, it should feature a long-lived triplet state (lifetime on the timescale of μs-ms), with a $T_1 \rightarrow S_0$ transition highly unfavorable.[36] In the framework of solar applications, an optimal sensitizer should also exhibit a broadband absorption spectrum to increase the ability to harvest the incident solar light.

Large conjugated compounds have been extensively studied over the past decades as suitable triplet sensitizers as they show many beneficial features for efficient sensitization of the emitters triplet states. The most common organic sensitizers are found among aromatic conjugated

compounds: organometallic compounds, compounds showing metal-to-ligand charge transitions (MLCT)[117–122] such as Ru(II) complexes, phtalocyanines,[123–126] but the most common are metalated porphyrins, such as platinum (II) octaethylporphyrin or palladium (II) octaethylporphyrin.[31,41,115,127–130] The conjugated nature of these compounds affords high optical densities, also approaching the near-infrared spectral range,[88,131,132] while the heavy atoms in the molecular structure increase the spin-orbit coupling, yielding ultrafast intersystem crossing that outcompetes the $S_1 \rightarrow S_0$ fluorescent transition, and thereby almost all the energy harvested on the sensitizers can be efficiently transferred to the annihilators. These compounds also typically feature triplet states with characteristic lifetimes $> \mu$s, which guarantee efficient energy transfer. Metalated porphyrins show a peculiar absorption profile, with the Soret band and Q-band, which is usually exploited to excite the system, well separated by a wide transparency window with low absorption with the great benefit of limiting the reabsorption of upconverted light.[31] To push the absorption further towards the near-infrared, new sensitizers with direct singlet-to-triplet (S_0 - T_1) absorption have been recently designed.[133–135] This spin-forbidden transition becomes partially allowed because of strong spin-orbit coupling and allows to avoid the energy loss of typically hundreds of meV observed in the intersystem crossing step, affording large anti-Stokes shift from the near-infrared to the visible range, which is an optimal result for solar applications. The performances of upconverters based on this class of sensitizers are still limited by the short phosphorescence lifetime and by the relatively low extinction coefficient ϵ of the S_0 - T_1 transition ($\epsilon \sim 1000\ M^{-1}\ cm^{-1}$), but since these factors can be tuned via molecular design, metal and ligand selection, and ligand functionalization, these materials are promising candidates for efficient upconversion of the near-infrared.[136]

As far as the annihilators/emitters are concerned, it is worth noting that two possible systems can be developed, one where the annihilators and emitters are the same molecule, the other where they are two different molecules. The second option is typically employed when the fluorescence properties of the annihilator are deficient, therefore the excitation resulting from the TTA event is transferred via Förster energy transfer to the emitter excited singlet state.[137] Nevertheless, in this discussion, I will consider only the scenario where annihilator and emitter are the same species for simplicity without loss of generality.

For efficient TTA, the annihilator triplet lifetime should be as long as possible to increase the probability that two annihilators in their triplet state encounter, similarly to the sensitizer-to-annihilator ET.[36] This is usually achieved with highly symmetrical molecules, since molecular

symmetry contributes to reduce the intersystem crossing efficiency. It should also have a unit fluorescence efficiency QY_{fl} to maximize the ability to emit upconverted photons.[36] The QY_{fl} generally depends on the emitter concentration, as the molecules can aggregate at high concentrations, as observed for perylene,[116] and on external factors such as the local environment experienced by the emitter as it influences the nonradiative recombination channels.[28] The energy of the excited singlet state S_1 should be lower than twice the energy of the triplet state T_1, in order to reach S_1 via TTA, but also with the energy of T_1 such that higher-energy triplet states or quintet states cannot be populated to avoid populating deleterious states that ultimately would lower the conversion efficiency.[34,42,88] The electronic properties of the sensitizer-annihilator ensemble should also favor exothermic energy transfer, and maximize the *anti-Stokes shift*. The ET should be exothermic, with the energy difference between the sensitizer and annihilator triplet states bigger than the thermal energy at temperature T ($\Delta E > k_B T$, where k_B is the Boltzmann constant), otherwise *back-energy transfer*, i.e. re-population of the sensitizer from the annihilator by means of thermal energy, can occur reducing the overall ET efficiency and ultimately reducing the population of emitter triplets that can undergo TTA.[138,139] The most common annihilators/emitters are found among polycyclic aromatic hydrocarbons, such as conjugated molecules derivative of acenes, that are fluorophores usually showing almost unit fluorescence efficiencies and high *f* factors. Examples of efficient annihilators/emitters can be found in 9,10-diphenylanthracene, 9,10-bis(phenylethynyl)anthracene (BPEA) and perylene, or in other classes of fluorophores such as boron dipyrromethene (BODIPY).[33,34,41,107,135,140–142]

1.4 *s*TTA-UC in organic bulk systems

To understand the dynamics of *s*TTA-UC and to predict the behavior of an upconverting system it is essential to introduce a kinetic model, a useful tool that allows to follow the dynamics of the excitons created in the system and the transitions they can undergo by means of coupled rate equations:[41]

$$\partial T_D/\partial t = \alpha(\lambda_{exc}) I_{exc} - k_D^T T_D - k_{ET} T_D \tag{1.9a}$$

$$\partial T_E/\partial t = k_{ET} T_D - k_E^T T_E - k_{TTA} T_E = k_{ET} T_D - k_E^T T_E + \gamma_{TT} T_E^2 \tag{1.9b}$$

$$\partial S_E/\partial t = \frac{1}{2} f \gamma_{TT} T_E^2 - k_E^S S_E \tag{1.9c}$$

The equations describe the rate of variation of the sensitizer excited triplets (donors) T_D, annihilator/emitter triplets T_E and annihilator/emitter singlets S_E population by means of the pumping and deactivation terms previously sketched in Figure 1.2. The sensitizer triplets in Eq. 1.9a are populated by the photons absorbed $\alpha(\lambda_{exc})I_{exc}$ (where $\alpha(\lambda_{exc})$ is the absorption coefficient at the excitation wavelength and I_{exc} is the incident excitation intensity setting the photon flux). Since in the typical organic upconversion systems the sensitizers are chosen to have an ISC efficiency $\sim$100%, in Eq. 1.9a I am assuming that all the sensitizer excited singlets, i.e. $\alpha(\lambda_{exc})I_{exc}$, populate the sensitizer triplets T_D. These can either decay spontaneously or undergo ET towards the emitter triplets with the corresponding rates k_D^T and k_{ET}. The emitter triplets T_E can then decay spontaneously with rate k_E^T or alternatively TTA can occur, as expressed in Eq. 1.9b. The last equation highlights that the emitter singlets are populated through TTA, which results in molecules in their singlet state with a probability *f*, and then deactivate via radiative recombination ($k_E^T S_E$). The upconverted emission intensity I_{uc} is therefore proportional to $k_E^T S_E$. Because the differential equations introduced cannot be solved analytically, proper approximations must be employed to obtain useful information. In the first approximation, a simple assumption is to treat the system under a continuous excitation in steady-state conditions, so the excited populations do not change during time:

$$\alpha(\lambda_{exc})I_{exc} - k_D^T T_D - k_{ET} T_D = 0 \tag{1.10a}$$

$$k_{ET} T_D - k_E^T T_E + \gamma_{TT} T_E^2 = 0 \tag{1.10b}$$

$$\frac{1}{2} f \gamma_{TT} T_E^2 - k_E^S S_E = 0 \tag{1.10c}$$

It is crucial to stress that the terms $k_E^T T_E$ and $\gamma_{TTA} T_E^2$ in Eq. 1.10b represent the possible deactivation channels for the emitter triplets and that the *s*TTA-UC is effective only when the TTA becomes the dominant channel, making the emitter spontaneous recombination negligible ($k_{TTA} = \gamma_{TT} T_E \gg k_E^T$).[41] This observation infers that the *s*TTA-UC is a power-dependent process, since the I_{exc} sets the emitter triplet density T_E, and that the TTA rate k_{TTA} increases under higher excitation intensities. To gain insight into the dependency of the upconverted emission intensity I_{uc} on I_{exc} I consider two limit situations, i.e. the low-power regime and the high-power regime. In the low-power regime the T_E density is so low that $k_{TTA} \ll k_E^T$, thereby the majority of T_E decays spontaneously as collisions between two T_E are unlikely. The term $\gamma_{TT} T_E^2$ in Eq. 1.10b can be neglected and with few simple substitutions it results that $I_{uc} \propto I_{exc}^2$. At this point it is essential to introduce the *s*TTA-UC quantum yield Φ_{uc}, which is

an important figure of merit of the *s*TTA-UC process and gives helpful indications about the upconversion performance of the system considered. The Φ_{uc}, defined as the ratio between the number of upconverted photons and the number of the absorbed ones, is given by the product of the efficiencies of all the processes leading to the emission of the high-energy photons:[143]

$$\Phi_{uc} = \Phi_{ISC}\Phi_{ET}\Phi_{TTA}\Phi_{fl}. \tag{1.11}$$

Here, Φ_{ISC} and Φ_{ET} are the efficiencies of ISC (assumed equal to 100 $\%$ from here onward) and ET respectively, Φ_{fl} is the emitter fluorescence quantum yield and Φ_{TTA} is the TTA efficiency, which is the only power-dependent term in Eq. 1.11. In fact, the TTA efficiency can be defined as:

$$\Phi_{TTA}(I_{exc}) = \frac{1}{2} f \frac{k_{TTA}(I_{exc})}{k_{TTA}(I_{exc}) + k_E^T} \tag{1.12}$$

where the $\frac{1}{2}$ factor accounts for energy conservation, as one high-energy photon results from two low-energy photons, therefore the maximum Φ_{uc} achievable is 50$\%$.[143,144] Thereby in the low-power regime Φ_{TTA} - and consequently Φ_{uc} - depends linearly on I_{exc} as expected for bimolecular processes, and even small changes in the excitation power determine substantial variations in the process efficiency. On the contrary, in the high-power regime $k_{TTA} \gg k_E^T$, the spontaneous recombination term in Eq. 1.10b becomes negligible and $I_{uc} \propto I_{exc}$. The TTA reaches a 100$\%$ efficiency and the Φ_{uc} becomes independent of the excitation intensity, reaching its maximum value determined by the parameters in Eq. 1.11, which are characteristic of the system considered. This behavior leads to the introduction of a second figure of merit for the *s*TTA-UC, the so-called threshold excitation intensity I_{th}. It is defined as the excitation intensity where Φ_{uc} is half of its maximum value and it is reached when $k_{TTA} = k_E^T$, meaning that an upconverting system enters the regime of high TTA efficiency only when $I_{exc} > I_{th}$. A straightforward expression for I_{th} can be derived by equating the expressions for I_{uc} in the two regimes:[41]

$$I_{th} = \frac{(k_E^T)^2}{\alpha(\lambda_{exc})\Phi_{ET}\gamma_{TT}}. \tag{1.13}$$

An optimal upconverter should exhibit high Φ_{uc} and low I_{th}, because it means that lower excitation intensities are necessary to enter the regime of high efficiency and this is especially true for solar applications as the upconverter is meant to work under the solar irradiance. In oxygen-free solutions with optimized organic emitter/sensitizer dye pairs upconversion quantum efficiencies of about 30$\%$, not far from the energy-conservation limit, have been achieved under excitation intensities that are comparable to solar irradiance.[32,34]

The behavior of the *s*TTA-UC intensity that shows a quadratic-to-linear dependency on the excitation power, or analogously linear-to-constant dependency for the upconversion efficiency, is usually referred to as *classical sTTA-UC regime*. It is observed in all those bulk systems where the volume accessible to the triplet excitons is much greater that the volume actually explored by the triplet excitons themselves via diffusion, such as common upconverting solutions, but also nanomaterials characterized by slow triplet diffusion and short lifetimes.[41,145]

The *s*TTA-UC emission is an example of *delayed fluorescence*[14,15] as it occurs on a μs-ms timescale instead of the typical nanosecond timescale of prompt fluorescence, because it stems from bimolecular interactions between metastable triplet states and it is characterized by a peculiar dynamics, that can be probed through time-resolved photoluminescence spectroscopy techniques. Because the upconverted emission only originates from the emitter excited singlet states, the I_{uc} intensity is proportional to the square of the emitter triplets density as:[42,50,116]

$$\frac{\mathrm{d}\sqrt{I_{uc}(t)}}{\mathrm{d}t} \propto \frac{\mathrm{d}T_E}{\mathrm{d}t} = -k_1 T_E - k_2 T_E^2 \tag{1.14}$$

where k_1 is the first order decay rate constant ($k_1 \sim k_E^T$), mainly due to the spontaneous T_E decay, but also to pseudo first order processes such as triplet quenching from oxygen, while k_2 is the second-order decay rate constant ($k_2 = \gamma_{TT}$), associated to the triplet quenching through TTA.[47] The solution to this equation is:

$$\frac{T_E(t)}{T_{E,0}} = \frac{1 - \Phi_{TTA}}{e^{k_E^T t} - \Phi_{TTA}} \tag{1.15}$$

where $T_{E,0}$ is the initial emitter triplet population.[50] Therefore, after an excitation pulse, the emitter triplets immediately start to annihilate generating the upconverted light, whose intensity progressively decreases until the residual triplet density T_E is such that the average intermolecular distance between two triplets is so large that collisional events become improbable, preventing the annihilation. Therefore, the time evolution of the upconverted intensity I_{uc} is described by

$$I_{uc} \propto \left(\frac{1 - \Phi_{TTA}}{e^{k_E^T t} - \Phi_{TTA}}\right)^2 \tag{1.16}$$

It is worth noting that in the low-power regime the initial triplet density $T_{E,0}$ is so small that k_{TTA} is negligible with respect to k_E^T, meaning that Φ_{TTA} is close to zero and the UC emission intensity results

$$I_{uc} \propto e^{-2k_E^T t} \tag{1.17}$$

with a decay rate $k_{uc} = 2 \times k_E^T$ since the emitter triplets tend to decay spontaneously. On the other hand, under higher I_{exc} the initial availability of triplets is greater, and consequently

k_{TTA} and Φ_{TTA} increase as well.

The initial triplet population and the TTA rate also influence how fast the system can reach the maximum Φ_{TTA} according to a trend $\sim 1 - e^{-k_{rise}t}$, where $\tau_{rise} = k_{rise}^{-1}$ is the rise time of the upconverted emission signal, which depends on the excitation pump, because by increasing the I_{exc}, $T_{E,0}$ increases too, and if the triplets can move fast in the system, the TTA occurs rapidly and efficiently.

The investigation of the *s*TTA-UC dynamics by means of time-resolved photoluminescence experiments is therefore central to thoroughly model the *s*TTA-UC process and to obtain key parameters such as k_E^T which are specific of the system analyzed and that are necessary to estimate the *s*TTA-UC figures of merit.

1.5 Broadband hybrid sensitizers

In the perspective of solar technologies, despite the positive features afforded by organic sensitizers previously discussed, their application in *s*TTA-UC is still hindered given the lack of efficient sensitizers able to absorb the NIR photons. Absorbing the NIR requires a red-shift of the absorption spectrum, achievable developing larger conjugated systems, which is not straightforward from a synthetic point of view.[146–148] Moreover, when the S_0 - S_1 and therefore the S_0 - T_1 energy difference decreases, the nonradiative recombination rate increases, potentially outcompeting the energy transfer step.[149–151] It should also be noted that the good performances of molecular sensitizers generally stem from the heavy metal atoms, which are typically rare, costly and toxic, thus this is a crucial aspect to take into account in the perspective of large-scale production.[118] Moreover, sensitizers like porphyrins usually show the tendency to aggregate and low solubility in solution,[152] meaning that low sensitizer concentrations must be typically employed ($10^{-4} - 10^{-5}$ M), reducing the system's optical density. Also, they show narrow absorption bandwidths, that if on one hand it allows to reduce reabsorption of upconverted light, on the other it results in a too limited ability to store the solar light. This issue has been partially overcome by employing multicomponent sensitizers or multilayer systems with complementary absorption profiles,[34,60,73,74,153–157] but it is desirable to deal with a single broadband harvester/sensitizer to avoid possible deleterious interactions between different moieties and to simplify the system's architecture.

Colloidal semiconductor nanostructures decorated with conjugated organic molecules have

been recently proposed as alternative sensitizers,[141,158–165] because they exhibit unique properties appealing for solar applications and potentially able to outcompete molecular sensitizers. In bulk semiconductors the energy bandgap $E_g(bulk)$ is set by the crystal structure and by the material atomic composition and this is a fixed, well-defined quantity characteristic of the semiconductor itself. They can absorb photons with energy equal or larger than their energy bandgap. In this case, an electron is promoted to the semiconductor conduction band and it binds through Coulomb interaction to a hole in the valence band, forming an *exciton*. When the exciton recombines, it can emit a photon of fixed energy determined by the material $E_g(bulk)$. However, when the size of semiconductor particles becomes comparable to the bulk exciton Bohr radius, which typically ranges from 2.1 nm in II-VI to 60 nm in III-V group semiconductors,[166] the energy bandgap and therefore the photophysical properties of these systems become dependent on the particle size itself. Because of the strong spatial confinement and localization of the charge carries, they not only experience the Coulomb interactions as in the bulk counterpart, but they also sense the particle boundaries.[161,167] This condition is referred to as *quantum confinement effect* and it results in discrete atomic-like energy levels because of the bulk energy bands quantization in 1, 2 or 3 dimensions. Semiconductor nanostructures are the nanosized entities that exhibit quantum confinement properties, and they are called nanoplatelets, nanowires, and nanocrystals when the carriers motion is confined in 1, 2 or 3 directions, respectively. To highlight the main quantum confinement effects on the nanostructure photophysics I now consider the case of nanocrystals, but similar conclusions can be drawn also for nanoplatelets and nanowires, with proper modifications due to the different number of confined dimensions.

In the first approximation, a semiconductor nanocrystal, assumed spherical for simplicity, can be treated through the spherical quantum box model in which the charge carriers's wavefunctions are isotropically confined by an infinite potential barrier.[167] In this framework, the continuous bulk energy bands are replaced with the discrete electronic state structure characteristic of 3D nanostructures and the corresponding energies are:[168,169]

$$E_{eh}(n_e L_e n_h L_h) = E_g(bulk) + \frac{\hbar^2}{2R^2}\left(\frac{\alpha^2_{n_e,L_e}}{m_e} + \frac{\alpha^2_{n_h,L_h}}{m_h}\right) - E_c \tag{1.18}$$

labelled by the electron (*e*) and hole (*h*) principal quantum number *n* (1, 2, 3,...) and the orbital angular momentum quantum number *L* (S, P, D,... for *L* = 1, 2, 3 etc); m_e and m_h are the electron and hole effective mass in conduction and valence band, respectively, and α are the zeros of the Bessel functions. E_c is the Coulomb interaction, that in the first approximation can

be neglected with respect to the confinement energy, because under the strong confinement condition, the *e-h* pair is mainly bound because the carriers are forced in the same spatial region. Thereby, the energy bandgap in nanocrystals is:

$$E_g(NC) = E_g(bulk) + \frac{\hbar^2\pi^2}{2R^2}(\frac{1}{m_e + m_h}) \tag{1.19}$$

This is an approximated approach, but nevertheless it allows to highlight the main features and energetic dependencies, and it also generally affords quite reliable theoretical predictions not far from the experimental results. The key information to stress is that the excitonic energies depend on the semiconductor material through the bulk energy gap, the electron and hole effective mass in the material and they quadratically depend on the nanocrystal size *R*.
Colloidal semiconductor nanocrystals, and nanostructures in general, gained increasing attention in the last decades because they are highly tunable and their photophysical properties can be manipulated on diverse conceptual levels.[161] For instance, as Eq. 1.19 suggests, the nanocrystals optical and electronic properties can be tailored through size, shape and composition control. But the exciton photophysics can be manipulated also through the so-called wavefunction engineering, achieved heterostructuring the nanocrystals with proper core-shell structures.[170–172] The idea underpinning heterostructuring is to control the localization of one or both charge carries in the core and shell regions, made of semiconductors with energy gap, composition and thickness specifically selected to achieve the desired goal. Heterostructuring allows for example to increase the nanocrystals photoluminescence quantum yield, to engineer the emission Stokes shift or to change the exciton recombination dynamics.[173–176]
Colloidal nanocrystals are also characterized by a surface-to-volume ratio much greater than the bulk counterpart, and this property has two important implications.[177–180] The first is that the excitons must be properly protected from the surface dangling bonds that are easily created and that represent deleterious trapping centers for the photoexcited carriers, reducing the nanocrystal photoluminescence efficiency. For colloidal nanocrystals the exciton protection can be achieved by capping the surfaces with proper ligands that passivate the dangling bonds, where common passivating ligands are carboxylic acids and amines,[36,141,181] or by growing a thin shell of proper semiconductors.[182,183] The second important implication is that new properties can be assigned to the nanocrystals by decorating their surfaces with specific ligands that allow, for instance, to extract the energy harvested, or conversely to inject an external excitation into the nanocrystals.[184–187] In this regard, it was recently demonstrated that it is possible to manage spin-flip processes,[184,188–190] allowing semiconductor nanocrystals to inject into

and accept triplet excitons from organic molecules, typically derivatives of conjugated organic dyes.[141,185,191,192] Therefore we can employ semiconductor nanocrystals as light harvesters in hybrid sensitizers, conceptually composed of a nanostructure decorated with molecular ligands anchored on the nanostructure surface.[158,159] As a whole, colloidal semiconductor nanostructures offer a variety of advantages as light harvesters with respect to the organic compounds investigated so far. Along with the aforementioned benefits, they afford high photostability and large molar extinction coefficients; also, since their photophysical properties can be tailored through size and composition control, it is possible to have sensitizers able to absorb in the ultra-violet, visible, and importantly, near-infrared spectral range just by acting on these two parameters.[20,158,178,180,191,193–196] Important developments of hybrid systems allowed to achieve broad anti-Stokes shift from near-infrared excitation to visible emission.[197–199] They also offer the advantage of being easily synthesized according to well-established, scalable colloidal procedures.[160,178,179,200,201] Importantly, they feature a broadband optical absorption spectrum, meaning that the energy storage ability can be extensively increased with respect to organic sensitizers. All these advantages make semiconductor nanostructures an optimal platform towards the development of efficient hybrid sensitizers.[202,203] Still, the typical nanocrystals absorption has a critical drawback. Since they absorb over a wide spectral range, an open challenge is to circumvent the reabsorption of the upconverted light by the sensitizers, which intrinsically lowers the overall upconversion performances. It should also be noted that the semiconductor nanocrystals that have been extensively studied so far as light-harvesters are based on group VI elements, such as CdSe, CdS, PbS, or PbSe, because their underlying photophysics is well-known and this affords a useful benchmark when studying complex hybrid systems for *s*TTA-UC. Unfortunately, elements such as cadmium and lead are extremely toxic, therefore for sustainable technologies it is mandatory to find alternative compositions.[204] In this regard, good candidates are $CuInS_2$ (CIS) nanocrystals, based on non-toxic components, which have been recently proposed as light-harvesters in efficient hybrid sensitizers, that also offer the advantage to push the absorption towards the red, near-infrared spectral range.[163,205]

Transmitter surface ligands. It is worth stressing that to have efficient hybrid sensitizers able to transfer the harvested energy to the emitters, the presence of proper surface ligands is mandatory.[206] The exciton lifetime in nanostructures is usually on the nanosecond timescale,[161] making the spontaneous exciton recombination competitive with energy transfer, when it is not the dominant decay channel. Therefore, transmitter surface ligands acting

as bridges to transfer the triplet excitons from the nanostructures to the emitters play a crucial role. This moiety should exhibit a mixture of the sensitizer and emitter properties discussed in Sec. 1.3, as two Dexter-type energy transfer processes are now involved. The first, $ET^{'}$, is from the nanostructure to the transmitter ligand, that acts as energy acceptor, whereas the second, $ET^{''}$, is from the transmitter ligand, acting as energy donor, to the emitter. Therefore the overall ET process in hybrid systems is more delicate and requires more efforts to be controlled than in organic systems as it is composed of two successive processes, and thus the probability to introduce competitive recombination pathways increases. This picture implies that the surface ligand should have a triplet state resonant with the nanostructure exciton to maximize the $ET^{'}$ efficiency, and resonant with the emitter triplet state to optimize the $ET^{''}$ efficiency.[207] Importantly, its HOMO and LUMO levels should be such to avoid charge transfer from the light harvester to the ligand, which would disrupt the exciton and hinder the emitter triplets sensitization. Also, to increase the probability of interaction with the emitters, the ligands should show long-lived triplet states. The most employed ligands belong to the same molecular class of the emitter species, typically acenes, that provide long-lived triplet states, with prohibited $T_1 \rightarrow S_0$ transition. These organic molecules are properly functionalized with an anchoring group, such as the carboxylic acid, to decorate the light harvester surface.[162, 177] The transmitter ligands are attached to the nanocrystals surfaces through a ligand exchange procedure aimed at replacing the native capping ligands that afford colloidal stability. This is usually a delicate and critical process because it is extremely easy to introduce deleterious surface defects, which hinder the triplet sensitization ability, because the transmitter ligands are typically bulkier than the capping ligands, so the surfaces hardly are perfectly passivated. Another important consideration about the ligand selection is because $ET^{'}$ is a Dexter process, as discussed in Sec. 1.2, the rate k_{ET} strongly depends on the spatial overlap between the donor (nanostructure) and acceptor (ligand) wavefunctions, with a $\sim e^{-R/L}$ dependence on the donor-acceptor distance *R*. It straightforwardly follows that the ligand choice is crucial in optimizing the distance *R*, also considering the typical ligands bulkiness. In the work in Ref.,[208] Li et al. thoroughly demonstrated that by increasing the distance *R* between the nanocrystal and the anthracene ligand through variable-length rigid oligo-*p*-phenylene bridges, the $ET^{'}$ rate rapidly decreases as the ligand length increases, with a $\sim e^{-d}$ dependence, where *d* is the overall ligand length.

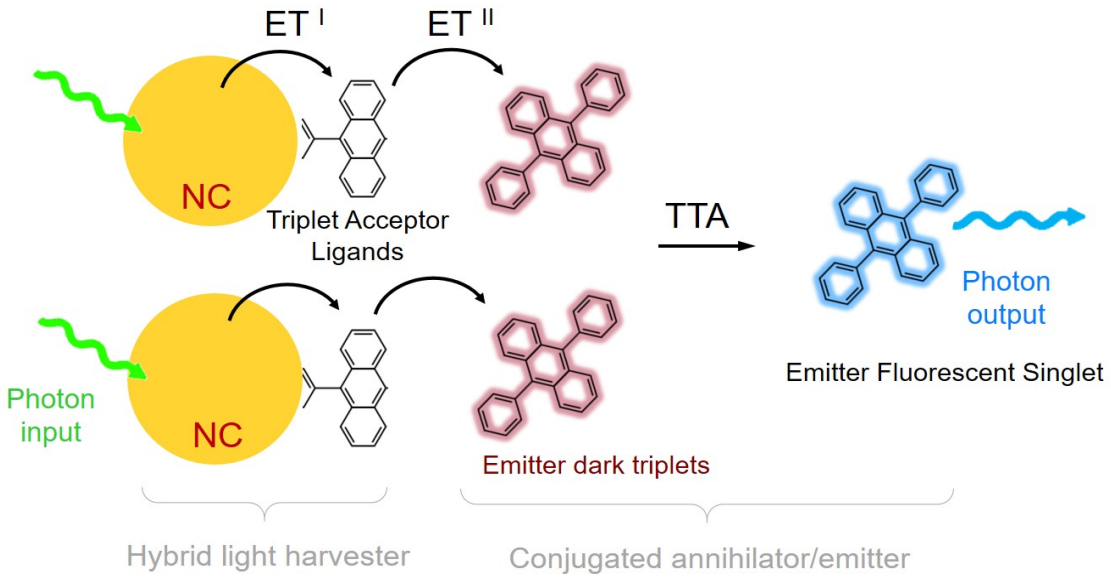

Figure 1.3: Energy flux in *s*TTA-UC in a green-to-blue hybrid upconverting system. Upon absorption of a green photon by the nanocrystal (NC), the exciton energy is transferred through energy transfer (ET$'$) to the triplet acceptor ligand that then populates the triplet state of the emitter via ET$''$. The annihilation of two emitter triplets (TTA) results in the formation of a high-energy fluorescent singlet state responsible for the upconverted blue luminescence.

1.5.1 Hybrid *s*TTA-UC system

In Sec. 1.4 I discussed the main features and figures of merit of *s*TTA-UC in bulk organic systems. It is possible to derive how these results change when considering hybrid upconverting systems, where the organic sensitizer is replaced with an inorganic semiconductor nanostructure decorated with conjugated organic ligands. The main concepts and considerations previously described are still valid, but some additional processes must be accounted for. In this discussion, I consider as guideline a hybrid sensitizer where the harvester is a nanocrystal.[209] Here, upon absorption of an incident photon, an exciton labelled as *Nc* is created in the nanocrystal, and it can recombine with rate k_{Nc} or it can be transferred via Dexter energy transfer with rate $k_{ET'}$ to the ligands, resulting in the population of the ligand triplet states T_L. These triplets can decay spontaneously with rate k_L^T or a second Dexter energy transfer can occur during the T_L lifetime with rate $k_{ET''}$, populating the emitter triplets T_E.

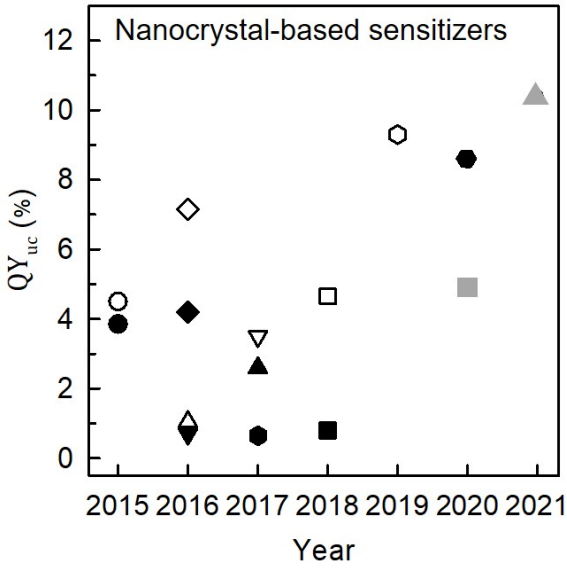

Figure 1.4: Chronological evolution of the *s*TTA-UC quantum yield QY_{uc} in hybrid systems since their appearance in 2015. White circle, Ref.;[191] black circle, Ref.;[211] white diamond, Ref.;[208] black diamond, Ref.;[212] white triangle, Ref.;[196] black reversed triangle, Ref.;[213] white reversed triangle, Ref.;[187] black triangle, Ref.;[182] black hexagon, Ref.;[214] white square, Ref.;[215] black square, Ref.;[137] white hexagon, Ref.;[163] horizontal black hexagon, Ref.[210]); gray square, Ref.,[204] gray triangle Ref.[216] The QY_{uc} values are reported according to the standard convention, i.e. out of 50%.

The differential equations system thus becomes:

$$\partial Nc/\partial t = \alpha(\lambda_{exc})I_{exc} - k_{ET'}Nc - k_{Nc}Nc \tag{1.20a}$$

$$\partial T_L/\partial t = k_{ET'}Nc - k_{ET''}T_L - k_L^T T_L \tag{1.20b}$$

$$\partial T_E/\partial t = k_{ET''}T_L - k_E^T T_E - \gamma_{TT}T_E^2 \tag{1.20c}$$

$$\partial S_E/\partial t = 0.5f\gamma_{TT}T_E^2 - k_E^S S_E \tag{1.20d}$$

Therefore, the crucial difference lies in the presence of two successive energy transfer processes. The system of rate equations can be treated in steady-state conditions, following the same approach adopted previously, allowing to assess the theoretical behavior in the two power regimes.

In the high-power limit, $k_E^T \ll \gamma_{TT}T_E$, so:

$$S_E = \frac{0.5f}{k_E^S}\phi_{ET'}\phi_{ET''}\alpha(\lambda_{exc})I_{exc} \propto I_{exc} \tag{1.21}$$

while in the low-power limit $k_E^T \gg \gamma_{TT}T_E$:

$$S_E = \frac{0.5f\gamma_{TT}}{k_E^S}(\frac{\phi_{ET'}\phi_{ET''}\alpha(\lambda_{exc})I_{exc}}{k_E^T})^2 \propto I_{exc}^2 \tag{1.22}$$

finding the very same quadratic-to-linear trend of the organic counterpart.
The threshold intensity becomes:

$$I_{th} = \frac{(k_E^T)^2}{\alpha(\lambda_{exc})\phi_{ET'}\phi_{ET''}\gamma_{TT}} \tag{1.23}$$

where

$$\Phi_{ET'} = \frac{k_{ET'}}{k_{ET'} + k_{Nc}} \tag{1.24a}$$

$$\Phi_{ET''} = \frac{k_{ET''}}{k_{ET''} + k_L^T} \tag{1.24b}$$

are the efficiencies of the NC-to-ligand and ligand-to-emitter energy transfer, respectively, and the UC efficiency can be expressed as:

$$\Phi_{uc} = \Phi_{ET'}\Phi_{ET''}\Phi_{TTA}\Phi_{fl} \tag{1.25}$$

Since their first appearance in 2015, many efforts have been devoted to the optimization of hybrid sensitizers, based on semiconductor nanocrystals decorated with organic molecules. In this regard, Fig. 1.4 reports the time evolution of the main improvements achieved in maximizing the upconversion efficiency in hybrid systems over the years. Importantly, the continuous understanding of the energy transfer process at the inorganic/organic interface led to notable enhancement of the upconversion performances in hybrid systems in just few years.[165]
Consistently with the great versatility of hybrid sensitizers, the first solar cell based on *s*TTA-UC sensitized by functionalized CdSe nanocrystals has been recently proposed,[217] where the charge is extracted from the excited singlet state populated via TTA. Specifically, Hansson et al. developed a device where 4,4′- (anthracene-9,10-diyl)bis(4,1-phenylene)diphosphonic acid is the annihilator molecule (A) bound to a nanocrystalline TiO_2 substrate, and CdSe nanocrystals are the sensitizers bound to the annihilator in a layered architecture TiO_2-A-NC. Even though there is still plenty of room for improvements and optimization, this is a crucial first proof-of-concept design towards the development of real-world devices based on broadband absorbing sensitizers highlighting the great potential and flexibility of hybrid sensitizers.

1.6 Dependence of bimolecular processes on diffusivity

The equations for the *s*TTA-UC figures of merit derived in the previous Sections are highly instructive, as they stress that the environment and structural properties of the upconverting

systems play a significant role in determining the process efficiency. For instance, the triplets recombination rate can be written as[26,27]

$$k_T = k_T^{rad} + k_T^{\text{non rad}} \tag{1.26}$$

which accounts for both radiative and nonradiative recombination pathways. Considering that the triplet state is optically dark due to the spin selection rule,[40] $k_T^{rad} \sim 0$, thereby the triplet decay rate is heavily affected by nonradiative recombination mechanisms that include collisions with inert moieties, such as solvent molecules, and the coupling with the environment vibrational bath.[105] The local interactions with the surrounding environment can therefore introduce additional decay pathways competing with the spontaneous decay of the long-living triplets, and also small local variations in the environment and/or material structure can result in substantial variations of the triplets lifetime and since I_{th} has a quadratic dependency on k_E^T the ultimate effects can be extensive. Also, importantly, the sensitizer-to-emitter ET and the TTA steps commonly depend on external factors, such as molecular mobility, or intermolecular distance, which is typically a function of the chromophore concentration.[218] These processes are highly sensitive to the environment and structural properties of the upconverting system, and this dependency stems from their diffusion-limited nature.[219,220] They are short-range bimolecular interactions between an energy donor D and an energy acceptor A that require spatial overlap between the D and A wavefunctions, according to the decay in space of the orbital wavefunctions.[43] The typical interaction distances are of the order of 1-2 nm, meaning that these interactions can be effective only if the molecules/excitons collide.[221,222] Consequently, since the local properties of the medium where the *s*TTA-UC takes place may favor or hinder the molecular/exciton mobility, it is crucial to understand how the upconverter structural features influence the short-range interactions in order to maximize their - and ultimately the *s*TTA-UC - efficiency.[223]

To get insight into the dependency of the *s*TTA-UC performances on the environment and on the upconverting material structure I first discuss the general properties of bimolecular interactions. The analytical treatment of these processes is not trivial, so it is typically simplified by means of approximations, one of the most employed is the Perrin model.[224] In this picture, given an energy donor D and an energy acceptor A with intermolecular distance *s*,

the interaction rate constant $k_{D,A}$ between D and A is such that[225]

$$k_{D,A}(s) = \begin{cases} \infty & s < r_0 \\ 0 & s > s_0 \end{cases} \tag{1.27}$$

where r_0 is the effective interaction distance, where the interaction efficiency is 50%. For instance, in Dexter-type ET, r_0 is the Dexter radius where the ET rate k_{ET} equals the donor triplet spontaneous decay rate k_D^T. The condition expressed in Eq. 1.27 can also be interpreted as follows: it is possible to define an effective sphere of radius r_0 centred on a donor so that the D-A collisional probability is negligible when the acceptors are outside the sphere.[225] This means that the interaction probability is set by the D-A distance *s* and by the number of acceptors inside the effective sphere. As a consequence, any energy diffusion process via molecular translation, for instance in liquid environments, or exciton diffusion, as in solid-state systems, can play an important role in determining the ET and TTA efficiencies. Both molecular and exciton diffusion can be described as the motion of a particle by random Brownian walk, so in this description a key parameter is the particle diffusion length L_{diff}

$$L_{diff} = \sqrt{2ZD\tau} \tag{1.28}$$

calculated as the particle mean square displacement in any isotropic direction, where D [cm^2 s^{-1}] and τ are the diffusivity coefficient of the system and the lifetime of the excited stated of interest, respectively.[27] The parameter Z is 1, 2 or 3 for 1D, 2D or 3D isotropic diffusion environments.[226] Notably, in the 3D case, Eq. 1.28 enables to calculate the diameter of the sphere explored by the excited donor molecule/exciton within its spontaneous recombination. An excited donor can reach the fraction of acceptors included in the volume of the diffusion sphere, and for all the acceptors outside the spheres the collisional rate $k_{D,A}$ is negligible. Therefore, the D-A collisional rate $k_{D,A}$ depends on the acceptor concentration C_A in the effective volume explored by the donor in its lifetime, and $k_{D,A}$ increases with increasing C_A. Fig. 1.5 illustrates these two possible scenarios. The relationship between $k_{D,A}$ and C_A is not trivial to establish, especially at low C_A, but a simple approach can be used when the so called *rapid-diffusion limit* is reached.[227,228] This regime is valid when the donor diffusion length L_{diff} is much greater than the average D-A intermolecular distance *s*, so for the isotropic 3D framework

$$L_{diff} \gg s \quad \text{or} \quad \frac{6D\tau}{s^2} \gg 1. \tag{1.29}$$

This major condition implies that each D–A pair within the diffusion volume has the same collisional probability and that the donor molecule/exciton encounters all the acceptors available

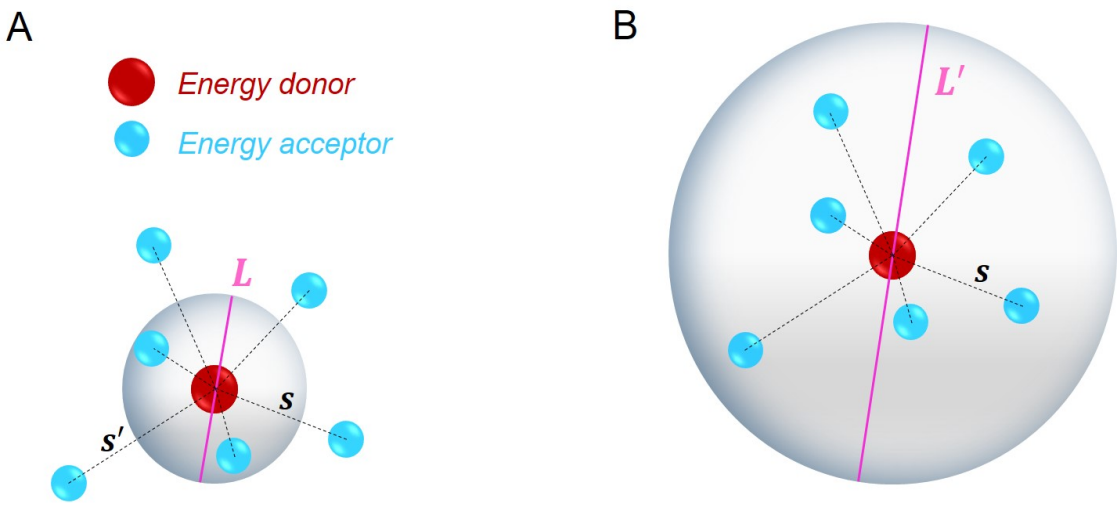

Figure 1.5: Illustration of the diffusion spheres drawn by the energy donors (D) through random walk, according to different diffusion lengths L. (a) For all the acceptors (A) within the spheres of diameter L, i.e., for D–A distances $s < L$, the collisional probability between excited D and A molecules is 100%. Conversely, for those acceptors outside the spheres $s^{'} > L$ and the D–A interaction rate is zero. (b) If $s < L^{'}$ for any acceptor molecule in the unit volume, all acceptors are accessible to the excited donor during its lifetime.

before recombination, i.e. $k_E^T \ll k_{D,A}$. When the rapid-diffusion condition is fulfilled, $k_{D,A}$ becomes proportional to C_A according to[225,229]

$$k_{D,A} = 4\pi D_{tot} r_0 C_A, \tag{1.30}$$

where D_{tot} is the total diffusivity of the system, calculated as $D_{tot} = D_D + D_A$. Therefore the Dexter ET and TTA rates can be expressed as

$$k_{ET} = 4\pi D_{tot} r_{ET} C_{em}, \tag{1.31}$$

$$k_{TTA} = 8\pi D_T r_{TT} T_E = \gamma_{TT} T_E. \tag{1.32}$$

In Eq. 1.31 D_{tot} is the sum of the sensitizer and emitter diffusivities, $r_{ET} \sim 1$ nm is the Dexter radius between sensitizer and emitter and C_{em} is the emitter concentration. Similarly, in Eq. 1.32 D_T is the emitter triplet diffusivity, $r_{TT} \sim 1$ nm is the effective TTA interaction distance between two emitter triplets, and T_E is the emitter triplet density. The second order rate constants $\gamma_{ET} = 4\pi D_{tot} r_{ET}$ and $\gamma_{TT} = 8\pi D_T r_{TT}$ [cm^3 s^{-1}] characterize the ET and TTA processes.

1.7 Landscape of solid-state upconverters design

It is straightforward from Eqs. 1.31 and 1.32 that for diffusion-limited bimolecular processes a sufficiently high *D* can balance very low values of C_{em} and S_E, and this is a key consideration when designing a system for applications where the energy density available is intrinsically limited. For instance, in bio-imaging, the number of excitons generated in the system is severely limited by the maximum excitation intensity exploitable before damaging the tissues. The situation is even more critical in solar applications, where the maximum triplet density is set by the solar irradiance. Therefore, when the exciton densities are intrinsically limited, k_{TTA} can be maximized by choosing an environment that favors short-range interactions.
The environments where the short-range interactions are most favorite are low viscosity organic solvents, where energy diffusion is boosted by molecular translational diffusion.[41,220,227] Here, the diffusivity of a given species, treated as a sphere of radius *r*, is usually estimated by the Stokes-Einstein equation[230]

$$D = \frac{k_B T}{6\pi\eta r} \tag{1.33}$$

where η is the solvent viscosity at temperature T. This dependence on η emphasizes the dependency of bimolecular processes on the environment, as it influences the molecular diffusion, besides setting the molecular excited state lifetime.[231] In low viscosity solutions molecular diffusivities greater than 10^{-6} cm^2 s^{-1} are typically obtained,[19,230,232] and the emitter triplet lifetimes are generally on the hundreds of microseconds - milliseconds timescale, therefore the rapid-diffusion condition is easily reached,[233] contributing to excellent *s*TTA -UC performances, also at excitation intensities comparable to the solar irradiance.[19,234,235]
Despite the excellent upconversion performances recorded in liquid environments, these systems are not suited for practical applications. Therefore, several approaches have been proposed to develop solid systems that are more suitable for real-world devices. A key condition to preserve optimal *s*TTA-UC performances is to design the upconverter to guarantee the rapid-diffusion condition. As already pointed out, to maximize the efficiency of the bimolecular interactions involved two main requisites need to be fulfilled: large energy diffusivity, typical of low viscosity solvents, and/or low decay rate of the involved excited states, which is typically ensured by hosts with large local rigidity to suppress vibrational-assisted quenching of the triplet excitons. In this regard, Fig. 1.6 reports the theoretical I_{th}, calculated with Eq. 1.13, for ideal systems in three different environments, to highlight the influence of the triplet dif-

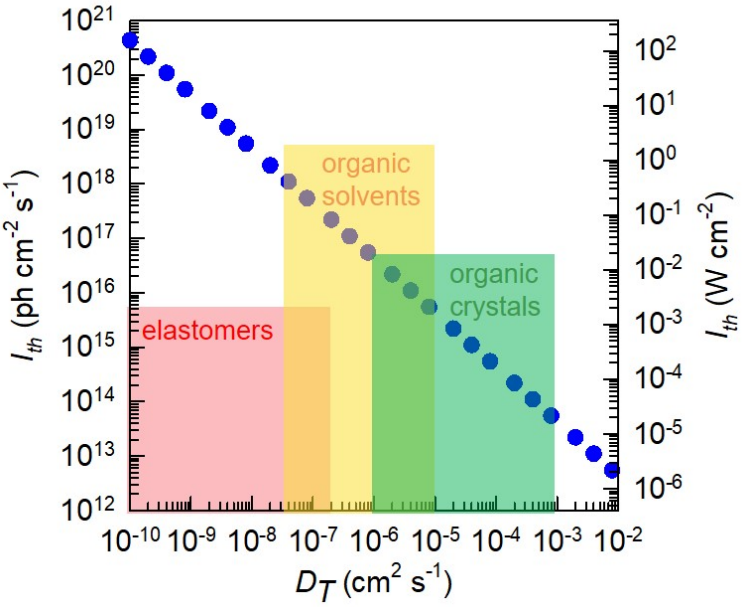

Figure 1.6: Excitation intensity threshold I_{th} calculated with Eq. 1.13 as a function of the triplet diffusivity D_T considering $\alpha = 10$ cm^{-1} at the excitation wavelength of 532 nm, $k_T^E = 1$ kHz, and intersystem crossing and energy transfer yield $\Phi_{ISC}, \Phi_{ET} = 1$. I considered three model systems with deeply different D_T values, elastomers (red), organic solvents (yellow) and organic crystals (green).

fusivity in determining the *s*TTA-UC performances. I adopted $\alpha = 10$ cm^{-1} at 532 nm, emitter $k_T = 1$ kHz, and intersystem crossing and energy transfer yield $\Phi_{ISC}, \Phi_{ET} = 1$. I considered three model systems with deeply different D_T values, i.e. elastomers (red), which are an example of low-viscosity rubber polymers, organic solvents (yellow) and molecular crystals (green). A first strategy to fabricate solid *s*TTA-UC systems is to embed the upconverting chromophores into materials that provide residual translational molecular mobility to favor short-range interactions.[236] Ideal matrices are low-viscosity rubber polymers like polyacrylates and polyurethanes,[237,238] which afford viscoelastic properties.[239] Even though molecular diffusion is lower than in common low viscosity organic solvents ($D_T \sim 10^{-10} - 10^{-9}$ cm^2 s^{-1}, Figure 1.6),[240] the advantage offered by these polymers is the reduction of the triplets decay rate, as they are less perturbed by the rubbery matrix, being a more rigid environment. Therefore, in rubber polymers the optimized trade-off between residual molecular diffusivity and triplet recombination rate allows to easily achieve the rapid-diffusion limit. Nevertheless, the use of solid matrices still suffers from difficulties in managing high dye concentrations that can easily result in aggregation and phase segregation, with deleterious effects on the *s*TTA-UC

performances.

The *s*TTA-UC can also take place among close-packed chromophores, exploiting exciton diffusion instead of molecular motions.[111,145,241–243] Solid-state upconverters have been developed by embedding large dyes amounts in amorphous polymers[79,244] or by exploiting ordered self-assembled structures in liquids,[245,246] gels,[247,248] and films.[249] Among assembled systems, molecular crystals with ordered chromophore arrangements show the most interesting properties for *s*TTA-UC. Here, the molecular excitons are strongly localized of Frenckel type, meaning that they can only diffuse by hopping among nearest-neighbour resonant energy centers along any allowed crystalline direction *n* = x, y, z with diffusivity[27,250]

$$D_n = (k_{hop} R^2)_n \tag{1.34}$$

where k_{hop} is the hopping rate between two molecules separated by a centre-to-centre distance *R* along the *n* direction. The exciton hopping rate between an initial *i* and final *f* molecule, according to the Fermi's golden rule, is[251]

$$k_{hop} = k_{if} \propto |J_{if}|^2 \tag{1.35}$$

where J_{if} is the excitonic coupling term related to the interaction considered (ET or TTA). The major advantage afforded by molecular crystals is that thanks to the inherent close molecular packing ($R < 1$ nm) the triplet diffusion is fast, with D_T values that can exceed those typically available in low-viscosity organic solvents ($D_T \sim 10^{-6} - 10^{-3}$ cm^2 s^{-1}, Figure 1.6).[27,252–254] A possible approach to fabricate solid upconverters consists in using organic crystals made of emitter molecules, which receive energy from sensitizer molecules incorporated in the crystals as dopants, or from the sensitizer portion in sensitizer/emitter co-crystals. This arrangement enables fast ET, due to the close proximity between sensitizers and emitters, and the emitter triplets can rapidly diffuse within the crystal and undergo TTA.[89,255,256] However, emitting crystals often feature larger triplet decay rates and lower fluorescence quantum yield with respect to the constituent chromophores, because the exciton recombination - and this is true especially for triplet excitons, being extremely sensitive to the environment - can be significantly affected by the presence of defect states, typical of crystalline environments, which act as nonradiative recombination centers.[257] It is thus mandatory to fabricate defect free, high purity organic crystals, but this is still an arduous task to handle. Also, generally solid-state systems suffer from critical drawbacks mainly related to the management of high dyes concentrations often required to maximize the light harvesting. In fact, the commonly employed

sensitizers tend to aggregate and segregate from the emitters, introducing additional energy loss channels and limiting the interaction with emitters, partially hindering the ET.[33,258]
As proposed by Oldenburg and co-authors, feasible candidates as emitters are metal-organic frameworks (MOFs),[57,256] that are ordered networks of molecules linked by metal ions and this is proved to be a good strategy to avoid phase segregation issues. Since the constituent molecules of a MOF do not interact with each other, they retain the photophysical properties of the emitter molecules, as well as the high exciton diffusivity typical of molecular assemblies.[89] MOF nanocrystals can be fabricated with excellent dimensional control, resulting in monodispersed nanocrystal populations, with dimensions as low as tens of nanometers. Moreover, MOF nanocrystals are versatile, easy-to-handle and can be extensively tailored. Specifically, they are suited to host a secondary functionality, e.g. the sensitizer, which can be included into the MOF structure, or alternatively linked to the MOFs surfaces. In these systems, the *s*TTA-UC is successfully achieved thanks to high triplet excitons diffusivity and MOFs high purity.[255] It is worth pointing out that since the diffusion length of triplet excitons in crystalline systems ranges from few nanometers to several micrometers and because MOF nanocrystals of tens of nanometers can be fabricated, the rapid-diffusion condition can be easily verified and the triplet excitons can explore all the nanocrystal before recombination.[259] The authors of the aforementioned work successfully fabricated an upconverting heterostructure by coupling a sensitizer-based MOF with an emitter-based MOF, in order to fully exploit the fast triplet diffusion in crystals. Indeed, despite the low emission efficiency, a threshold value as low as 1 mW cm^{-2} was achieved. Yet, MOF nanocrystals still have some drawbacks, like poor stability and low fluorescence yield that ultimately limit the UC outcome.[136]
Another striking strategy to maximize the use of *s*TTA-UC is the one developed by Hanson and co-workers, which consists in the realization of self-assembled upconverting molecular multilayers on inorganic scaffolds to facilitate *s*TTA-UC and obtain also direct charge separation from the upconverted state.[82] They further developed this architecture realizing an integrated *s*TTA-UC solar cell[83] and, notably, this strategy has been recently demonstrated to work also by harvesting near-infrared light.[243] Direct charge separation of the upconverted singlets can be therefore a straightforward strategy to avoid parasitic quenching of the upconverted emission in solids, but it does not allow to overcome the issues related to low triplet diffusivity in disordered systems, sensitizers aggregation that induces nonradiative recombination before ET, and annihilator-to-sensitizer triplet back transfer that can compete with the upconverted

excitons radiative recombination.[138, 242]

1.8 *s*TTA-UC in nanostructured systems

A captivating category of solid-state upconverters is that of nanosized/nanostructured materials.[75, 260, 261] Among these, nanostructured glassy polymers are recently proposed appealing materials composed of a polymer matrix and a dispersed liquid phase in the form of nanosized droplets which contain the upconverting dyes.[262] As the solid and liquid phases are well separated this peculiar structure enables to combine in a single material the optimal *s*TTA-UC performances typical of solutions with the benefits offered by the polymeric matrix. The liquid droplets have mean diameter of tens of nanometers, with considerable implications. Because the molecules are forced in small volumes, the intermolecular distances are on the nanometer scale. Moreover, the volume of the domains in which the dyes accumulate is a small fraction of the host volume (5-10$\%$), implying that the triplet excitons generated in different domains do not interact with each other, and each droplet represents a self-standing independent upconverting unity, referred to as *UC-center* in the following discussion.
I will examine thoroughly the main features and the structural implications of this class of materials discussing two nanostructured polymeric systems in Chapter 6 and 7, where I highlight the innovations introduced by this peculiar structure not only for upconversion purposes, but also for more general technological optical applications. In this section I discuss how the *s*TTA-UC dynamics behave in nanosized and nanostructured upconverting systems in comparison with the common homogeneous bulk *s*TTA-UC systems presented in the earlier text. Specifically, I expand the already existing theoretical model describing UC-centers all exhibiting the same size,[259] and develop the analogous model that describes the *s*TTA-UC behavior of an ensemble of UC-centers characterized by a size distribution.

1.8.1 Single-sized nanostructures

The design of nanostructured solid-state upconverters relies on the forced confinement of the excitation energy, i.e. the annihilating triplets T_E, in UC-centers smaller than the exciton diffusion sphere drawn by the triplets random walk. Assuming for simplicity the UC-centers to be spheres of radius *r*, whenever the condition $L_T \gg r$ is fulfilled the so called *confined sTTA-UC regime* can be observed. This regime was observed for the first time in the work at

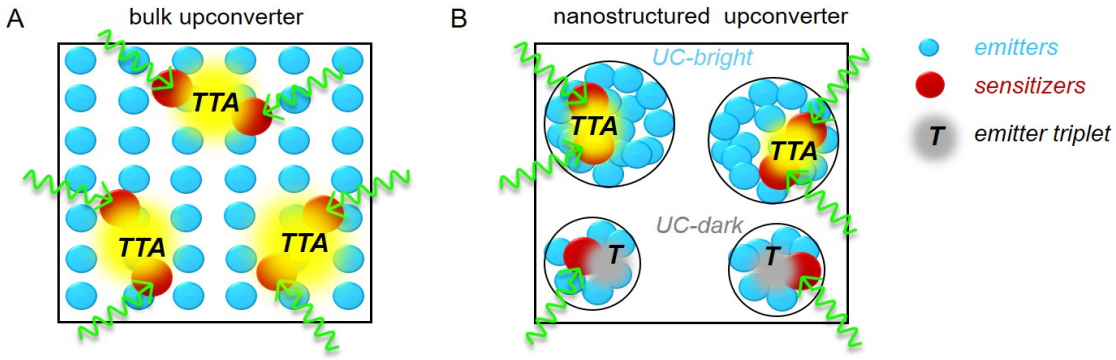

Figure 1.7: (a,b) Sketches of the different *s*TTA-UC kinetics in a classical bulk upconverter (a) and in a nanostructured upconverter (b) considering the same excitation volume and chromophore density. In the classical upconverter, the dyes are distributed homogeneously and the volume accessible to the triplet excitons is much larger than their diffusion sphere. Conversely, if the dyes are artificially confined in UC-centers, those that contain simultaneously two emitter triplets are UC-bright, while those containing unpaired triplets are UC-dark, i.e., inactive for the upconversion process.

Ref.[259] in MOFs based on Zn^{2+} ions and 4,4′-(anthracene-9,10-diyl)dibenzoate as organic ligand, with average size of ∼26 nm. In this picture, the maximum distance between two triplet excitons that coexist in a UC-center is 2*r*, intrinsically shorter than L_T, and thereby the collisional probability for the triplet pair by diffusion is 100%. This implies that in a UC-center only two outcomes are possible. If at least a triplet pair is generated in the same UC-center, each pair annihilates making the UC-center a *bright* upconverting unit, whereas those centers that contain one triplet are *dark* and the unpaired triplet decays spontaneously (Fig. 1.7). Therefore, the global intensity of the upconverted light emitted from a collection of UC-centers is the sum of the upconverted photons emitted by the fraction of bright centers. The UC-centers can be considered as a sort of threshold-less upconverters because if they contain at least two triplets no other condition influences the *s*TTA-UC outcome. Importantly, the population of bright centers is determined by the statistical distribution of the triplet excitons among the UC-centers which is set by the I_{exc}.

Since the triplets diffusion lengths L_T are typically of the order of hundreds of nanometers up to micrometers, nanosized or nanostructured materials are the ideal platform to observe the confined *s*TTA-UC regime.[259,263,264] Systems where the UC-centers are entities such as MOF nanocrystals or upconverting nanoparticles, with dimensions ranging from tens to hundreds of nanometers, are excellent examples of the condition where all the UC-centers have the same size because they can be synthesized with good dimensional control.[89,256,259,265] Con-

sidering identical upconverting nanoparticles embedded homogeneously in a transparent and rigid host that does not take part in the upconversion process, the dye loading level in the nanoparticles that determines the system optical density allows to estimate the average chromophore density in the system. Under cw homogeneous excitation, the emitter triplet exciton density T_E created in the UC-centers ensemble is

$$T_E = \frac{\alpha I_{exc} \Phi_{ET}}{\rho k_E^T} \tag{1.36}$$

where ρ, defined as the ratio between the total volume of the excited nanoparticles containing the absorbing dyes and the total excitation volume, marks the effective energy localization achieved in comparison to the corresponding bulk system containing the same chromophore amount. The mean number of triplet excitons $\overline{T_E}$ created in each UC-center of volume V is

$$\overline{T_E} = T_E \times V \tag{1.37}$$

and since the upconverted luminescence is generated only from those UC-centers where $\overline{T_E} \geq 2$, the upconversion quantum yield in a monodispersed confined system is

$$QY_{uc}(I_{exc}) \approx \frac{1}{2} f \Phi_{ET} \Phi_{fl} P_{n\geq 2}(I_{exc}) \tag{1.38}$$

where $P_{n\geq 2}$ (I_{exc}) is the cumulative probability to have $n \geq 2$ triplet excitons per UC-center for a given $\overline{T_E}$ (i.e. the fraction of UC-centers containing $n \geq 2$ triplet excitons) and it is calculated by means of the Poisson binomial distribution.[259] Importantly, Eq. 1.38 points out the independence of the upconversion process of the triplets diffusivity. The excitation threshold intensity for confined systems is defined as the minimum excitation intensity to get $P_{n\geq 2} = 0.5$, i.e. when 50% of the UC-centers ensemble contain at least two excitons, becoming active for the conversion process. This condition is satisfied for $\overline{T_E} = 1.7$, so the threshold intensity for the confined *s*TTA-UC can be written as

$$I_{th} = 1.7 \frac{\rho k_E^T}{\alpha \Phi_{ET} V} \tag{1.39}$$

As for the classical case, this figure of merit highlights the role of the intrinsic characteristics of the system's components and affords straightforwardly the guidelines to design efficient nanostructured upconverters. The *s*TTA-UC behavior results in a linear dependency of the upconverted emission intensity I_{uc} on I_{exc} when the UC-centers are bright, while at low powers, when most nanostructures are still dark, this dependency is superlinear, as the I_{uc} depends

only on the excitation energy distribution and not on the triplet excitons collisional probability.

At this point, an observation is mandatory. Eq. 1.38 gives an overestimation of the global efficiency, because the annihilation probability P_{TTA} is not exactly 100% in UC-centers where an odd number of triplets is generated. Therefore, at a given excitation intensity the exact QY_{uc} should be calculated considering also the presence of the unpaired exciton that does not contribute to the upconverted emission. Considering an excitation intensity equal to I_{th}, which sets an average number of triplet excitons $\overline{T_E} = 1.7$ in each UC-center, I calculated the fraction of UC-centers P_n that contain *n* triplet excitons and the contribution to the QY_{uc} of each P_n through the corresponding $P_{TTA,n}$ and the results are reported in Tab. 1.1. For instance,

	$n < 2$	$n \geq 2$, even	$n = 3$	$n = 5$	$n = 7$	$n = 9$	...
P_n	0.5	0.33	0.15	0.02	0.002	< 0.0001	...
$P_{TTA,n}$	0	1	0.66	0.80	0.85	0.9	...

Table 1.1: Distribution of the excitation energy in the UC-centers ensemble calculated considering that for $I_{exc} = I_{th}$ the average exciton number per UC-center is 1.7. The UC-centers fraction P_n containing *n* excitons was calculated using the Poisson binomial distribution.

when each UC-center contains $n = 3$ excitons, only two of them can interact, thus the P_{TTA} is $\frac{2}{3} = 0.66$. Referring to Tab. 1.1, the fraction of UC-centers that contain $n \geq 2$, with *n* even, is $(0.5 - 0.15 - 0.02 - 0.002 - ... \approx 0.33)$ and for these centers the probability to have annihilation is $P_{TTA} = 1$.

Therefore, the QY_{uc} at $I_{exc} = I_{th}$ calculated as the limit of the series

$$QY_{uc}(I_{th}) = \lim_{n\to\infty} \frac{1}{2} f \Phi_{ET} \Phi_{fl} \sum_n P_n \times P_{TTA,n} = \frac{1}{2} f \Phi_{ET} \Phi_{fl} \times 0.45 \tag{1.40}$$

overestimates of less than 10% the approximated efficiency calculated considering all the UC-centers containing $n \geq 2$ UC-bright with $P_{TTA} = 1$.

Importantly, from Eq. 1.38 it is also clear that the TTA rate and efficiency lose their dependency on the excitation intensity in confined systems, because if the excitation energy distribution is such to allow the TTA, it always takes place. Moreover, Eq. 1.16 cannot be employed to describe confined systems, because, by changing the excitation power, the same upconverted emission dynamics is expected, given the achieved TTA rate independence of the excitation power.

1.8.2 Nanostructures featuring a size distribution

Considering single-sized nanostructures is instructive, but this modelling applies to a restricted number of systems that grant high dimensional control. For a more general perspective UC-centers showing a size distribution should be considered. The aforementioned nanostructured glassy polymers constitute a possible system where the UC-centers, considered as spheres of radius *r*, are the liquid nanodomains, containing the upconverting dyes, embedded in the rigid polymeric matrix. Given the nature of the polymer synthesis and nanostructuring, it is not reasonable to expect and assume that all the liquid nanodomains show the same size. In this regard, it has been demonstrated that homogeneous growth or structuring processes usually result in an ensemble of structures with size *r* well described by a log-normal distribution *L(r)*[266, 267]

$$L(r) = \frac{1}{\sqrt{2\pi}\sigma r} \quad e^{-\frac{(ln(r)-\mu)^2}{2\sigma^2}} \tag{1.41}$$

where μ and σ are the mean value and the standard deviation of $ln(r)$, respectively.
The upconversion activity of such a system is still determined by the excitation intensity that sets the average exciton density in the ensemble but, importantly, the difference with the single-size case is that now the UC-centers in the ensemble become active for the upconversion process at different powers according to their size. To model the UC performances of this system, I approximate the ensemble to a discrete set of UC-centers with different *r* to which apply Eq. 1.37, and I calculate the cumulative probability $P_{n\geq 2}$ as a function of I_{exc} by means of a size-specific binomial distribution, multiplied by $L(r)$. Larger structures host indeed a larger amount of sensitizers that increase their absorption ability if compared to smaller structures, and this effect must be taken into account to evaluate correctly the $P_{n\geq 2}$ (I_{exc}) value, because the weight of larger centers is greater in determining the system's UC performances. Considering that the sensitizers concentration is proportional to the UC-center volume, I assume a linear relationship between absorption and UC-center radius *r*. The overall *s*TTA-UC performances are thus determined by an "effective" log-normal distribution $L^{'}(r)$ that accounts for the greater absorbing ability of the bigger UC-centers

$$L(r)^{'} = \frac{1}{\sqrt{2\pi}\sigma r} \quad e^{-\frac{(ln(r)-\mu)^2}{2\sigma^2}} \times r \tag{1.42}$$

Thereby, Eq. 1.38 evolves to the more general expression

$$QY_{uc}^{\text{confined}}(I_{exc}) \approx \frac{1}{2} f \Phi_{ET} \Phi_{fl} \sum_{r} P_{n\geq 2}(I_{exc}) L^{'}(r) \tag{1.43}$$

This equation is a powerful tool to obtain information about the nanostructure size distribution in nanostructured polymers and allows to determine the mean size of the UC nanostructures by fitting the QY_{uc} vs I_{exc} experimental data. From the μ and σ parameters one can get the mean nanostructure radius $\overline{r}$ by:[268]

$$\overline{r} = e^{\mu + \frac{\sigma^2}{2}} \tag{1.44}$$

It is worth stressing that in this description, $L(r)$ describes the real UC-center size distribution, while $L(r)^{'}$ is the "effective" log-normal distribution that describes the UC performances of the ensemble, as if the UC-centers were distributed according to $L(r)^{'}$.

From Eq. 1.43 it is also clear that the only effect on the UC performances of varying the nanostructure size is to change the excitation energy distribution, i.e. the I_{exc} at which each nanostructure becomes UC-bright, and ultimately the excitation threshold intensity, without affecting the maximum yield achievable. It is worth pointing out also that the single-size results can be retrieved as a special case of the more general discussion, where the cumulative probability P_n is neglected, as all the UC-centers behave in the same exact way.

The proposed model allows to reproduce experimental results on nanostructured upconverters, as highlighted in Chapters 6 and 7, and, importantly, in Chapter 9 I show how it can be employed to investigate the effects of the exciton confinement on the QY_{uc} dependency on I_{exc} especially in relation to different size distributions, and most importantly to obtain useful guidelines for the future development of upconverting photonic devices operating at subsolar irradiances suitable for technological implementation.

Methods

In this Chapter, I describe the methods and experimental setups I employed to investigate the photophysical properties of the systems discussed in this Thesis, probed by means of continuous wave (cw) and time-resolved photoluminescence (PL) measurements.

2.1 Absorption spectra

The Lambert-Beer law gives information about the ability of a species to absorb light at a given energy, expressed by the molar extinction coefficient ϵ (measured in M^{-1} cm^{-1}), and it quantifies the reduction of the initial intensity I_0 of the incident light as it propagates into the sample after a certain path length *d*. The fraction of light at the excitation wavelength absorbed by the species is given by its absorbance (A), or optical density (OD). The absorbance at a specific wavelength depends on the absorbing species concentration *M* and on the optical path *d* covered by the light beam. Specifically, the transmitted intensity after a path length *d* is:

$$I = I_0 \times 10^{-\epsilon M d}. \tag{2.1}$$

The ratio between the transmitted and incident intensity is the transmittance T:

$$T = \frac{I}{I_0}$$

and the absorbance is given by:

$$A = -logT = -log\frac{I}{I_0}$$

therefore,

$$A = \epsilon M d. \tag{2.2}$$

I recorded the absorption spectra of the samples investigated with a dual beam Varian Cary 50 UV-Vis spectrophotometer in normal incidence conditions. It operates in *Czerny-Turner* configuration with a Xe pump lamp and bandpass 1.5 nm and it allows to measure the optical density for every wavelength in the spectral range of interest. To isolate only the sample's contribution to the optical density, I corrected the signals with a baseline, recorded with the cuvette and solvent for the samples in solutions, and recorded with a blank sample composed of the polymeric matrix without the upconverting dyes for the solid-state nanostructured glassy polymers.

2.2 Excitation sources

According to the kind of measurement performed, I adopted continuous wave (cw) or pulsed lasers as excitation sources, with the energy and pulse width (for time-resolved measurements) adequate to the sample and kind of measurement to perform. I carried out the steady-state upconversion photoluminescence (PL) investigations with a cw Coherent Verdi 532 nm laser, except for Chapter 8 where I employed a DPSS 635 nm laser (model MRL III635).
To perform the time-resolved PL measurements I employed different pulsed excitation sources, such as a 532 nm Nd:YAG pulsed laser (Laser-Export Co. LSC-DTL-374QT, pulse width 5 ns), with tunable repetition rate between 0 and 10 kHz, or pulsed lasers of the EPL series from Edinburgh Instruments, with emission wavelength of 405 nm and 510 nm and typical pulse width of 60 ps, with repetition rate tunable from 2.5 kHz to 20 MHz, and the 380 nm laser of the EPLED series, with repetition rate tunable from 20 kHz to 10 MHz. The short pulse width allows to correctly measure fast recombination lifetimes without artifacts from the instrumental response.

2.3 Power-dependent photoluminescence measurements

The excitation intensity plays a crucial role when studying an upconverting system, since it sets the density of excited states available and therefore it influences the efficiency of the annihilation process. As such, power-dependent measurements are a key tool to investigate the properties of upconverting systems, allowing to extract information like the excitation threshold intensity or to determine what trend the upconverted emission follows upon changing the population of triplet states in the system. I performed all the cw power-dependent measure-

ments reported in the next Chapters adopting the following procedure. I employed a Coherent Verdi cw laser at 532 nm as excitation source, provided with TTL modulation. To remove the fundamental harmonic of Nd:YAG and the 808 nm emission of the pumping diode, I added a line filter (FL532-10, Thorlabs) right after the laser output. I modulated the excitation intensity by means of neutral filters with varying optical density (Thorlabs and Edmund Optics), from 0.1 to 4 OD. I focused the excitation beam on the sample using a focusing lens, and the sample emission was collimated and focused on a optical fiber taking the signal to the detector. I also used a notch filter (NF533-17, Thorlabs) in emission to remove the laser stray light. I employed a nitrogen-cooled charge-coupled device (CCD Spex 2000) coupled to a polychromator (Triax 190 from J-Horiba) with a spectral resolution of 0.5 nm for signal detection. With this detector it is crucial to focus the signal from the optical fiber on the spectrometer entrance slit with a collimating lens and a focusing lens. It is possible to choose among three diffraction gratings with different groove density, according to the needed dispersion. For the aim of this work I did not need high resolutions, but I was interested in a wide spectral range, so I always worked with the 150 grooves/mm diffraction grating (Jobin-Yvon). The laser irradiance was measured with a Thorlabs S120VC photodiode power sensor. Moreover, when performing power-dependent measurements comparing different samples it is mandatory to compare the performances taking into account the power densities, calculated from the incident power and spot size. To measure the spot size I adopted the *knife-edge* method: I sequentially measured the incident power by gradually blocking the laser beam. Since the laser profile I used was gaussian, the intensity profile obtained followed a sigmoid curve. By fitting the first derivative of the sigmoid profile with a gaussian function, I extracted the full width at half-maximum of the gaussian beam. For convention, I assumed as laser spot the area accounting for 95% of the signal. Importantly, I corrected the spectra for the instrumental response, procedure especially critical when comparing the PL intensities and spectra in different spectral ranges.
For the power-dependent measurements reported in Chapter 8 I followed the same procedure but using the 635 nm laser as excitation source, provided with TTL modulation. In this case, I employed a 635 nm notch filter (FLH635-10, Thorlabs) to reduce the stray light.

2.4 Steady-state photoluminescence measurements

The second setup I employed to record photoluminescence spectra is a fluorescence spectrophotometer (Varian - Cary Eclipse) that allows to record the photoluminescence spectra by selecting with a monochromator the desired excitation wavelength over a wide wavelength range from the emission spectrum of a Xe lamp. The sample photoluminescence spectra can be acquired over a wavelength range between 190 nm and 1100 nm and the signal from each wavelength in the emission spectra is recorded by a photomultiplier tube. To reduce the stray light I carried out the measurements in anti-reflection configuration.
Regardless of the experimental setup employed, for quantitative comparisons, such as to calculate the energy transfer efficiency, I performed the comparative measurements in the same experimental conditions (excitation fluence, accumulation time, and geometry) and samples optical density at the excitation wavelength. When the samples optical density was not the same, I corrected the spectra for the fraction of photons absorbed to have comparable results.

2.5 Time-resolved measurements

Time-resolved experiments allow to determine the lifetime of the excited states generated after photoexcitation, but also to get meaningful information about the photophysical processes occurring in the systems such as energy transfer or annihilation rates. These measurements require a pulsed excitation source, in order to analyze the time decay of the emission under consideration after a laser pulse of given repetition rate. The repetition rate fixes the time between two successive pulses and it has to be chosen properly as it has to be slower than the rate of the photophysical processes governing the emission. I selected the emission wavelength by a 74 100 Cornerstone 2601/4 (ORIEL) monochromator (15 nm band pass) and I recorded the signal intensity using a nitrogen cooled Hamamatsu R5509-73 photomultiplier coupled with a high-speed amplifier (Hamamatsu C5594), and a PCI plug-in multichannel scaler ORTEC 9353 time digitizer/MCS in a photon counting acquisition mode, with a temporal resolution of 100 ps. This instrument allows to acquire a maximum time span of 6.7 ms.
To investigate the delayed upconverted emission on a μs-ms timescale, I modulated the cw 532 nm laser (or the cw 635 nm laser in Chapter 8) with a TTi TG5011 wavefunction generator producing square signals, affording a time resolution better than 0.1 μs. Also for these stud-

ies, the excitation intensity was adjusted and tuned using neutral filters with varying optical density.

I performed the fluorescence and phosphorescence time-resolved measurements as a function of temperature reported in Chapters 6 and 7 by using the II harmonic of Nd:YAG Continuum Minilite laser (10 ns pulse width), detecting the luminescence decay with an Edinburgh LP90 flash photolysis setup.

Finally, I performed the time-resolved measurements to determine the phosphorescence lifetime and decay behavior of the sensitizer reference samples in Chapters 6 and 7 employing the Varian - Cary Eclipse fluorescence spectrophotometer, as the pulsed Xe lamp allows to record the emission kinetics over several hundreds of milliseconds.

As for the steady-state measurements, for quantitative comparisons, I performed the comparative measurements in the same experimental conditions (excitation fluence, accumulation time, and geometry) and samples optical density at the excitation wavelength. When the samples optical density was different, I rescaled the intensities accordingly to have comparable results.

2.6 Ultrafast time-resolved measurements

For the ultrafast time-resolved measurements discussed in Chapter 5, I employed a mode-locked ultrafast Coherent Mira 900 source that uses a Ti:Al_2O_3 crystal as gain medium. This crystal is pumped with a cw Coherent Verdi V-10 diode-pumped laser, which provides a 10 W 532 nm emission. The Ti:Al_2O_3 crystal amplifies any wavelength from 710 and 1000 nm with peak width of 200 fs. The pulse repetition rate is fixed at 76 MHz and the emission energy can be doubled by a nonlinear optical crystal of beta barium boride (BBO). To detect the ultrafast decays on a ps timescale, I used a Hamamatsu C5680 streak tube coupled to a Hamamatsu digital CCD camera C4742-95. The temporal resolution of the whole system is less than 2 ps.

2.7 Fluorescence and upconversion quantum yield

An important parameter that characterizes a luminescent species is its emission quantum yield (Sec. 1.1), that gives the fraction of the absorbed photons that are emitted, i.e.

$$QY = \frac{number\ of\ photons\ emitted}{number\ of\ photons\ absorbed} \tag{2.3}$$

Analogously, one of the parameters used to quantify the performance of an upconverting system is the upconversion quantum yield, defined as the fraction of absorbed photons that are emitted at higher energy:

$$QY_{uc} = \frac{number\ of\ photons\ upconverted}{number\ of\ photons\ absorbed} \tag{2.4}$$

In this work, I performed the measurements of fluorescence QY and QY_{uc} following a relative method, i.e. using a fluorophore or an upconverting solution with known quantum yield QY_{ref} as reference, according to the following equation:[28]

$$QY_{sample} = QY_{ref} \times \frac{1 - 10^{-A}_{ref}}{1 - 10^{-A}_{sample}} \times \frac{I_{sample}}{I_{ref}} \times \frac{n^2_{sample}}{n^2_{ref}} \tag{2.5}$$

where *A* is the absorbance at the excitation wavelength, so $1 - 10^{-A}$ is the fraction of photons absorbed; *I* is the PL intensity and *n* is the refractive index of the sample's medium. I prepared the samples and reference solutions with optical densities at the excitation wavelength as similar as possible and, importantly, with $A < 0.1$, to limit concentration-related issues, such as inner filter effects or self-absorption, that lead to misleading results. Importantly, to draw meaningful information, I performed the measurements on the sample and the relative reference under the same experimental conditions. It is worth noting that the photoluminescence quantum yield is usually quantified by using an integrating sphere. However, in this context, this method can easily give wrong results because of the typical partial sensitizer reabsorption of the upconverted light and the power-dependent nature of the *s*TTA-UC. For a reliable evaluation of the *s*TTA-UC quantum yield using an integrating sphere, it is essential to carry out the experiment so that the excitation power density is above the threshold in the entire excited volume. This condition is barely achievable in an integrating sphere, where the upconverted emission is scattered and it is partially reabsorbed by the sample itself. This reabsorbed light, however, has not an irradiance comparable to the threshold level and therefore re-generates upconverted photons with an unpredictable efficiency, but typically rather low. In the last years, some researchers thoroughly investigated this issue,[269] and at least for scattering-free and high-absorption samples, relative measurements are more reliable than the absolute evaluation of the QY_{uc}, which usually overestimates the residual donor emission and underestimates the upconverted intensity. The relative experiment allows indeed to accurately measure the intensity of the upconverted emission in a limited and controlled volume where

the process shows its maximum efficiency. Moreover, the use of a front geometry for the emission detection allows to limit reabsorption effects. Therefore, I measured all the QY_{uc} values reported in this Thesis following the relative method.

Materials

Broadband hybrid sensitizers

3.1 CdSe and Au:CdSe Nanocrystals

3.1.1 Chemicals

Gold(III) chloride hydrate, (99.99%), L-glutathione (≥98%), tetrabutylammonium bromide (≥98%), 1-dodecanethiol (≥98%), ultrapure water (Chromasolv Plus, for HPLC), sodium myristate (≥99%), selenium powder-100 mesh (99.99%), oleic acid (≥90%), cadmium nitrate tetrahydrate (≥98%), 2-propanol (≥99.8%), ethanol (≥99.8%), methanol (≥99.8%), toluene (≥99.5%), 1-octadecene (≥90%), 9-anthracene carboxylic acid and 9,10-diphenylanthracene were purchased from Sigma-Aldrich.

3.1.2 Synthesis of CdSe nanocystals

CdSe nanocrystals (NCs) were synthesized following a well-established procedure[270] according to a heat-up method, starting from a Cd-myristate precursor following an *ex-situ* method, where 0.05 M of cadmium nitrate dispersed in 40 mL methanol were loaded in 0.025 M of sodium myristate dispersed in 240 mL of methanol. The white precipitate obtained was then washed twice with methanol and to remove the solvent it was dried under vacuum. A reaction mixture was then prepared by adding 0.1 mmol of Cd-myristate to 0.05 mmol of Se powder in a 25 mL flask containing 6.38 mL of 1-octadecene (ODE) and 1 mL of oleic acid (OA) and put under vacuum for 15 minutes. This mixture was then heated to 210 °C for 1 hour and

kept under nitrogen flux. To remove the OA in excess and unreacted precursors, the resulting NCs were purified via centrifugation (4500 rpm, 10 minutes) twice using hexane/ethanol as co-solvents.

3.1.3 Synthesis of gold clusters and doped CdSe nanocrystals

Doped NCs can be obtained according to different methods, such as growth doping[271,272] or cation exchange.[273–275] In this work, a nucleation doping route was followed, where metal quantum clusters, consisting of a core of metal atoms held together by stable metal-metal bonds were employed as seeds for the NCs nucleation.[276–278] Metal quantum clusters are monodispersed particles inherently composed of a precise number of atoms (the so-called "magic numbers"), depending on the nature of the atom itself. The advantage afforded by this method is that the resulting NCs have a "quantized" doping, as each NC contains the same amount of impurities and therefore has the same photophysical properties resulting from doping. This is a fundamental novelty with respect to conventional doping approaches that lead to the incorporation of the dopants in variable number, yielding a statistic distribution of the doping level across the ensemble. Monometallic clusters composed of seven gold atoms (Au_7) were employed as nucleation seeds for cadmium selenide (CdSe) NCs, with glutathione (GHS) as capping ligands.[278]

Au_7-GSH clusters were synthesized according to a published procedure,[279] where 2 mL of gold(III) chloride hydrate $HAuCl_4$ (0.02 M) were mixed with 0.6 mL of L-glutathione (0.1 M) together with 17.4 mL of ultrapure water. This mixture was vigorously stirred for 24 hours at 70 °C, and the resulting clusters were purified adding isopropanol to the solution with a 1:2 volume ratio and centrifuged at 6500 rpm for 20 minutes. This purification process was repeated three times and the final purified clusters were dispersed in ultrapure water. To transfer the clusters in an organic environment, a ligand exchange procedure was carried out. To this aim, $\sim$0.3 mL of NaOH 1 M were loaded in 5 mL of the Au_7-GSH solution (76 μM) until a pH $\sim$9.0 was reached, along with 5 mL of tetrabutylammonium bromide 0.02 M in ethanol. This mixture was vigorously stirred for 2 minutes and then 0.15 M of 1-dodecanethiol (DDT) dispersed in 5 mL of toluene were added. After heating the mixture to 70 °C under vigorously stirring for 1 hour, the organic phase was separated, washed three times with ultrapure water to eliminate the water-soluble impurities and the resulting Au_7-DDT clusters were dispersed in ODE.

The gold clusters were then employed as nucleation seeds for the doped NCs (Au:CdSe), following a procedure similar to the one adopted for undoped NCs. The only difference is that 2.5 mL of Au_7-DDT clusters 76 μM were added to the reaction mixture. This synthesis yielded NCs with diameter 2.5 nm.

For comparative analyses also NCs with different diameter, 2.3 nm and 2.85 nm, were synthesized. To obtain NCs with diameter 2.85 nm the reaction mixture was heated for 2 hours, while to obtain NCs with diameter 2.3 nm the synthesis was carried out with an excess of OA, with 2 mL of OA instead of 1 mL added to the reaction mixture.

3.1.4 Ligand exchange

The undoped and doped NCs so produced were covered with a shell of OA ligands to stabilize the NCs. A ligand exchange process was mandatory to decorate the NCs surfaces with 9-anthracene carboxylic acid (9-ACA), which was employed as bridge to transfer the excitons harvested on the NCs to the emitters via a Dexter energy transfer. To do so, 1 mL of 9-ACA dispersed in toluene (2.5 mg/mL) was added to 0.5 mL of NCs (both for the doped and undoped NCs) dispersed in toluene and the mixture was stirred overnight at 50 °C. According to literature, this procedure yields about three 9-ACA molecules per nanocrystal bound to the surfaces.[208]

Since oxygen is an effective quencher of the triplet states,[42,280] this procedure was carried out in a glovebox under nitrogen atmosphere (with oxygen concentration below 1 ppm and water concentration below 0.5 ppm). All the samples were prepared in the glove box, loaded in 1 mm quartz cuvettes, and sealed with hot glue and parafilm to prevent oxygen contamination.

3.1.5 Material characterization

The elemental analysis of clusters and doped NCs, thoroughly reported in Ref.,[278] performed by electrospray ionization mass spectrometry (ESI-MS), X-ray fluorescence and inductively coupled plasma atomic emission spectroscopy (ICP-AES), along with optical spectroscopy measurements, indicates that each Au:CdSe NC in the ensemble contains seven gold atoms and confirms that the growth of the doped NCs is triggered by single Au_7 clusters, which act as a "quantized" source of dopant impurities. ICP mass spectroscopy indicates that the doping level is $\sim$0.4 at%, corresponding to 7 ± 2 Au atoms per NC.[278]

Structural characterization of nanocrystals. High-Resolution Transmission Electron Mi-

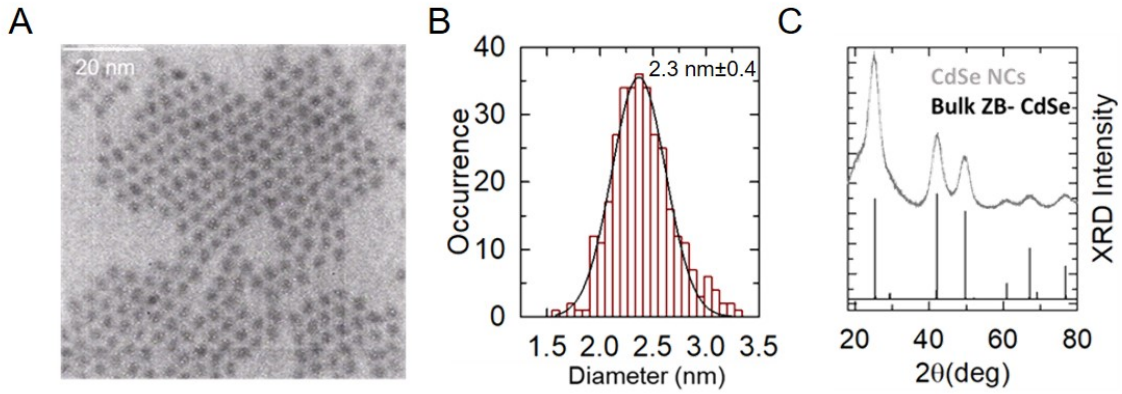

Figure 3.1: Au:CdSe nanocrystals (NCs) characterization. (a) TEM imaging and (b) size distribution of Au:CdSe NCs with a mean particle diameter of 2.3 $\pm$ 0.4 nm. The black line is the Gaussian fit to the experimental data. (c), XRD pattern of Au:CdSe NCs indicating a zincblende crystal structure.

croscopy (HR-TEM) imaging was performed on a JEOL JEM-2200FS microscope equipped with a field emission gun working at an accelerating voltage of 200 kV, a CEOS spherical aberration corrector of the objective lens, allowing to reach a spatial resolution of 0.9 Å, and an in-column Omega filter. Powder X-ray Diffraction (XRD) patterns were acquired in Bragg-Brentano geometry with CuKα radiation (Panalytical X'Pert Pro powder diffractometer).

In Figure 3.1 a representative characterization of Au:CdSe NCs with diameter 2.3 nm is reported.

I estimated the NCs size *R* from the 1S peak wavelength λ, according to an established empirical formula:[281]

$$R = (1.6122 \times 10^{-9})\lambda^4 - (2.6575 \times 10^{-6})\lambda^3 + (1.6242 \times 10^{-3})\lambda^2 - (0.4277)\lambda + 41.57 \quad (3.1)$$

From the size *R* I also estimated the nanocrystals' VB and CB energies in the effective mass approximation,[161] for a direct comparison with the 9-ACA highest occupied molecular orbital (HOMO) level and with the dopant energy level, according to:

$$VB_{NC} = VB_{bulk} - \frac{\hbar^2\pi^2}{2m_hR^2} \quad (3.2)$$

$$CB_{NC} = CB_{bulk} + \frac{\hbar^2\pi^2}{2m_eR^2} \quad (3.3)$$

where VB_{bulk} = -6 eV and CB_{bulk} = -4.3 eV are the corresponding VB and CB energies in bulk CdSe,[282] $m_h = 0.45m_0$ and $m_e = 0.13m_0$ are the hole and electron effective mass in CdSe, respectively. Considering NCs with *R*=2.3 nm, the resulting VB and CB are $\sim$-6.16 eV and $\sim$-3.75 eV.

3.2 CdSe Nanoplatelets

3.2.1 Chemicals

1-Octadecene (technical grade 90%, O806-1L), oleic acid (90%, 364525-1L), Cadmium acetate dihydrate (Cd(OAc)2(H_2O)$_2$, 98%, 317131000) were purchased from Acros Organics. Selenium powder -200 mesh (Se, 99.999%, 36208) was purchased from Alfa Aesar. Hexane (95% n-hexane, analytical reagent grade, H/0355/21), toluene (analytical reagent grade $\geq$ 99.8%, T/2300/17) and tetrahydrofuran (THF, analytical reagent grade 99.99%, T/0701/17) were purchased from Fisher Chemical. 9-anthracene carboxylic acid (99% A8,940-5) (9-ACA), perylene ($\geq$99%) and 9,10-diphenylanthracene (DPA) were purchased from Aldrich. Absolute ethanol (20821.330) was purchased from VWR chemicals. All molecules were used as received.

3.2.2 Synthesis of 5-monolayer thick CdSe nanoplatelets

Preparation of cadmium myristate [Cd(myristate)$_2$]. Cadmium myristate was synthesized following a modified protocol by Hendricks et al.,[283] where 5.75 g CdO and 20 ml acetonitrile were combined in a 100-ml round-bottom flask and the mixture was stirred and cooled in an ice bath. Then, 0.7 ml trifluoroacetic acid and 6.2 ml of trifluoroacetic anhydride were added. After 10 min, the ice bath was removed and the flask heated at 50 °C until the solution turned white. In a 500-ml Erlenmeyer flask, 20.6 g myristic acid, 180 ml 2-propanol, and 14.0 ml of triethylamine were mixed and stirred. The cadmium trifluoroacetate solution was then slowly added to the myristic acid solution while stirring. The resulting white precipitate was vacuum filtered through a fritted glass funnel and rinsed thoroughly with methanol. The final product was dried in a vacuum oven at 40 °C and stored under ambient conditions.

Synthesis of 5-monolayer-thick (5 ML) CdSe nanoplatelets The CdSe nanoplatelets (NPLs) synthesis adopted was slightly modified from a protocol by Tessier et al.,[284] where 170 mg Cd(myristate)$_2$, 12 mg Se powder, and 15 ml ODE were added to a 100-ml round-bottom flask and degassed under vacuum for 30 min. Then, the mixture was heated up to 240 °C under nitrogen. At 200 °C, 80 mg Cd(acetate)$_2$ dihydrate was added. The mixture was kept at 240 °C for 8 min. Afterwards, the reaction flask was cooled using an air gun to 150 °C. During this cooling step, 0.5 ml OA was added when the temperature reached 180 °C. Once at 150 °C, the flask was placed in a water bath and cooled to room temperature, and then 5 ml hexane was

added. The mixture was centrifuged at 7500 rpm (5849 g) at 25 °C for 10 min. The precipitate was re-dispersed in 5 ml hexane and centrifuged at 7000 rpm (5095 g) for 8 min. Unwanted 3-monolayer NPLs were removed through precipitation. The 5-monolayer NPLs in the supernatant were then stored in the dark under ambient conditions. Centrifugation was performed using a Sigma spin control 3-30k centrifuge, with the 19776 rotor (6 x 50 mL tubes, fixed angle).

3.2.3 Samples preparation for photophysical studies and ITC

To maximize the solubility of NPLs, a solvent mixture of hexane, THF and toluene (ratio 80:15:70) was employed to disperse the samples. Stock solutions of each component were prepared in a glove box (NPLs in hexane, 9-ACA, DPA and perylene in the solvent mixture). Specifically, two stock solutions of 9-ACA in the solvent mixture were prepared. The high concentration solution was prepared dissolving 1.2 mg of 9-ACA in 3.5 mL of the solvent mixture, while the second was prepared by diluting the high concentration solution by a factor of 10. Then, the NPLs, 9-ACA and perylene/DPA were mixed to the desired ratio right before each measurement. For instance, to obtain a surface ligand density of 0.45 nm^{-2}, the procedure is the following. 274 μL of nanoplatelets in hexane (with optical density 0.12 at the 1S transition in 1 mm cuvette) were evaporated and re-dispersed in 185 μL of solvent mixture. Then, 20 μL of the dilute stock solution were added. The maximum surface coverage of 24 ligands per nm^{-2} was achieved by adding 80 μL of the dilute stock solution and 100 μL of the concentrated stock solution. For the titration experiments, each component was dispersed in the mixed solvent to avoid changing the ratio of the solvent mixture during the titration process. All the samples were prepared in the glove box with oxygen concentration below 1 ppm and water concentration below 0.5 ppm, loaded in 1 mm quartz cuvettes, and sealed with hot glue and parafilm to prevent oxygen contamination.

3.2.4 Material characterization

Transmission Electron Microscope. The samples were prepared by drop casting a hexane dispersion of NPLs onto a carbon coated copper Transmission Electron Microscope (TEM) grid. The grid sat on filter paper during the drop casting to assist the solvent drying. TEM imaging was carried out using JEOL1400 TEM with an acceleration voltage of 120 kV. The TEM analysis estimated a NPLs surface area of $\sim$127 nm^2 (Fig. 3.2a).

Isothermal Titration Calorimetry. Isothermal Titration Calorimetry (ITC) experiments

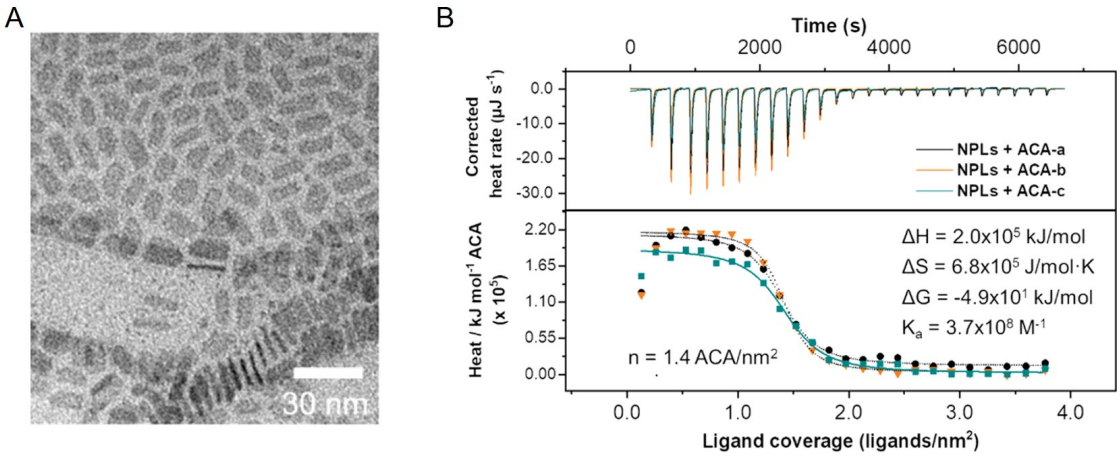

Figure 3.2: (a) TEM image of CdSe nanoplatelets (NPLs). The average lateral size is 15.5 nm x 8.2 nm (127.1 nm^2). b) ITC of NPLs decorated with 9-ACA ligands measured in three different runs. The average inflection point occurs at 1.4 ACA nm^{-2}. The calculated average binding constant (K_a) of 9-ACA to the NPLs surface is 3.7×10^8 M^{-1}.

were performed with a Nano ITC Low Volume from TA Instruments (Eschborn, Germany). The temperature was set to 25°C during all measurements. The effective cell volume was 300 μL, and a stirring rate of 350 rpm was chosen for all experiments. The data of heat vs. molar ratio were analyzed with an independent binding model using NanoAnalyze software, version 3.5.0 by TA Instruments. The ITC measurements were performed to estimate the amount of 9-ACA molecules per NPL and whether the native ligands removal and 9-ACA binding is favored. This technique provides information not only about the maximum ligand density achievable, but also about the binding constant of the ligands to the NPLs surfaces. Specifically, the concentrated 9-ACA solution was titrated into a dispersion of NPLs while stirring and the heat released from the ligand binding events was measured. Because the heat release stops when the NPL surface is saturated, this allows to estimate the maximum ligand density (Fig. 3.2b, top). Interestingly, 9-ACA exhibits a high binding constant to the NPLs surfaces (K_a = 3.7 $\times 10^8$ M^{-1}), which indicates that the equilibrium strongly favours the exchange of 9-ACA over the native ligands. Therefore, it is safe to assume that each 9-ACA introduced in the mixture binds to the NPLs until surface saturation. As shown in Fig. 3.2b, the maximum ligand density achievable by considering a homogeneous coverage of the NPL surfaces is 1.4 nm^{-2}.

Nanostructured systems

3.3 Nanophase-separated polymers

3.3.1 Synthesis of dye-free nanophase-separated polymers

The chemical structure of the components employed in the synthesis are reported in Fig. 3.3. The chemicals were purchased from Sigma-Aldrich, ABCR, Acros Organics, TCI (Tokyo Chemical Industry Co., Ltd.) or Inochem, Ltd. (Frontier Scientific, Inc) and were used as received. A 20 mL vial equipped with a stir bar was charged under ambient conditions with cetyltrimethylammonium chloride (**9**, CTAC, 250 mg), 2-hydroxyethyl methacrylate (**2**, HEMA, 2.66 g), methacrylic acid (665 mg), triethylene glycol dimethacrylate (**4**, TEG-diMA, 175 mg), butyl benzoate (**8**, BuBz, 500 mg) and triethylene glycol (750 mg). The mixture was heated in an

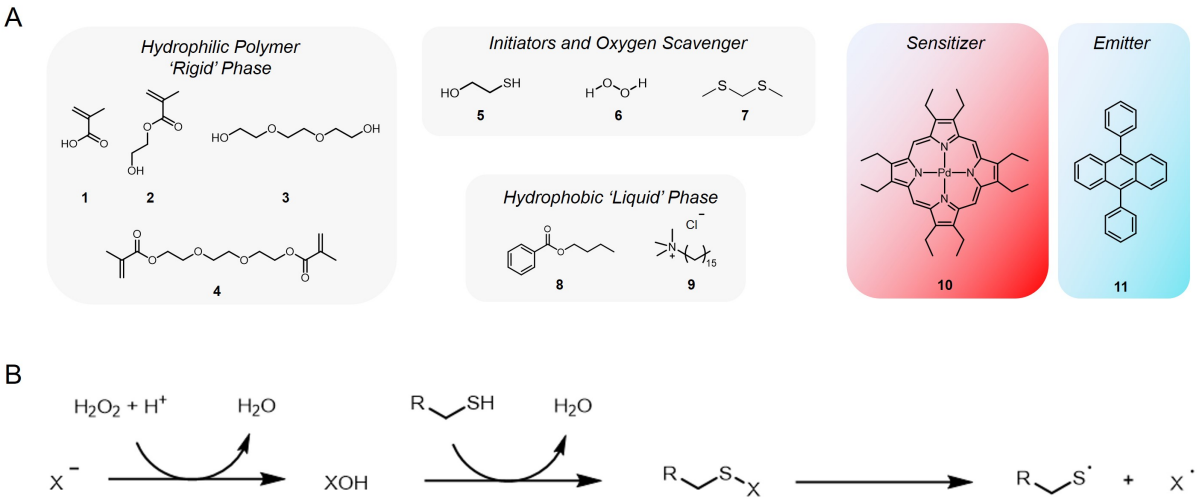

Figure 3.3: (a) Chemical structures of the green-to-blue upconverting polymer components: (**1**) methacrylic acid, (**2**) 2-hydroxyethyl methacrylate, (**3**) triethylene glycol, (**4**) triethylene glycol dimethacrylate, (**5**) 2-mercaptoethanol, (**6**) H_2O_2, (**7**) dimethylthiomethane, (**8**) butyl benzoate, (**9**) cetyltrimethylammonium chloride, (**10**) Pd(II) octaethylporphyrin, (**11**) 9,10-diphenylanthracene. (b) Proposed reaction scheme for the initiation process. A halide ion is first oxidized by reacting with H_2O_2, producing a hypohalous acid which is subsequently attacked by a thiol to give a sulfenyl halide. Finally, decomposition by homolytic cleavage of the sulfur/halogen (S-X) bond produces the radicals needed to initiate the polymerization. X=Cl, Br.

oil bath to 80 °C and stirred for 20 min to appear clear and homogeneous. The mixture was then removed from the oil bath and an aqueous solutions of H_2O_2 (**6**, 30%, 10 mg) and 2-

mercaptoethanol (**5**, 2-ME, 10 mg) were subsequently added. The mixture was briefly shaken and allowed to react for 1-2 min before dimethylthiomethane (**7**, DMTM, 27 mg) was added and the mixture was shaken again. The final mixture was filtered warm through a 0.2 μm PTFE-filter into either an optical glass cuvette or a 10 mL glass vial. The still clear mixture was left overnight at room temperature to obtain a transparent, hard material, which was kept in a sealed cuvette and used for quantitative optical measurements.

3.3.2 Synthesis of upconverting nanophase-separated polymers

Following the previous procedure, three upconverting systems were prepared, working in different spectral ranges. The green-to-blue upconverting material was prepared by substituting the butyl benzoate with a solution of palladium(II) octaethylporphyrin (**10** in Fig. 3.3, PdOEP, either 2×10^{-4} M or 8×10^{-4} M) in butyl benzoate (500 mg) and adding 9,10-diphenylanthracene (**11**, DPA, 25 mg). Assuming a final material density of 1 g cm^{-3}, the chromophore concentrations were 2×10^{-5} M or 8×10^{-5} M for PdOEP and 1.5×10^{-2} M for DPA. The dyes concentrations were also experimentally determined by means of absorption measurements and using the Lambert-Beer law and the sensitizer and emitter extinction coefficients to calculate the molar concentrations (Fig. 3.4a).

The red-to-blue upconverting material was prepared by substituting the butyl benzoate with a solution of palladium(II) tetraphenyltetrabenzoporphyrin (PdTPBP, 2×10^{-4} M) in butyl benzoate (500 mg) and adding 2,5,8,11-tetrakis(tert-butyl)perylene (TBPe, 4.8 mg). Assuming again a final density of 1 g cm^{-3}, the chromophore concentrations were 2×10^{-5} M for PdTPBP and 2×10^{-3} M for TBPe.

The near-infrared-to-yellow upconverting material was prepared by substituting the butyl benzoate with a solution of palladium(II) octabutoxyphthalocyanine (Pd(OBu)$_8$Pc, 10^{-5}) in butyl benzoate (500 mg) and adding rubrene (1 mg), corresponding to the final chromophore concentrations 10^{-5} M for Pd(OBu)$_8$Pc and 1.8×10^{-4} M for rubrene. The molecular structure of these two dye pairs are reported in Fig. 3.4b,c.

3.3.3 Material characterization

Differential scanning calorimetry. To get preliminary information about the polymers' composition, the materials' glass transition temperature T_g was determined through differential scanning calorimetry measurements (DSC) on dye-free samples employing a Mettler-

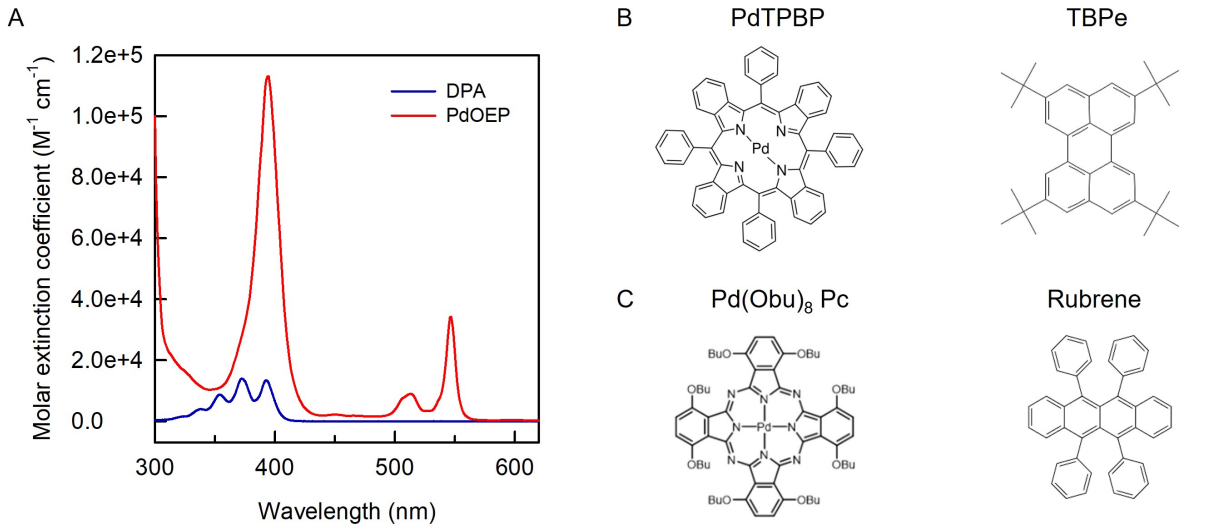

Figure 3.4: (a) Molar extinction coefficients of PdOEP (red line) and DPA (blue line) in BuBz. (b,c) Molecular structure of the sensitizer/emitter dye pairs for the red-to-blue upconverting material (panel b) and for the near-infrared-to-yellow upconverting material (panel c). The molecules are palladium(II) tetraphenyltetrabenzoporphyrin (PdTPBP) and 2,5,8,11-tetrakis(tert-butyl)perylene (TBPe) for the first composition, and palladium(II) octabutoxyphthalocyanine ($Pd(OBu)_8Pc$) and rubrene for the second composition.

Toledo DSC-1 equipped with a Huber TC100 cooling regulation system. To test the effects of butyl benzoate on the T_g itself, two samples were prepared, with and without butyl benzoate, following the procedure reported in Sec. 3.3.1 simply omitting the solvent in the second case. The measurements consisted of three heating cycles and were repeated three times for each sample. The first heating resulted in an endotherm assigned to water evaporation and was omitted for clarity, while the second and third heating cycles were equivalent, as reported in Fig. 3.5. The midpoint of the step change in the heat capacity is reported as the glass transition temperature. Importantly, the T_g recorded for the polymer containing the solvent lies between 50 and 52 °C, consistently with the results obtained with nanostructured materials with a similar composition.[262] Moreover, the polymer not containing the solvent has a T_g between 50 and 53 °C. This is an important result, because the T_g independence on the solvent suggests that the polymers are biphasic, with the rigid matrix well separated from a liquid phase, rather than having a mixed phase. The DSC measurements did not highlight other relevant transitions in the probed temperature range.

Oxygen transmission rate. Since oxygen is an effective quencher of triplet states, it is paramount for the polymeric matrix to afford efficient and long-lasting protection from it.

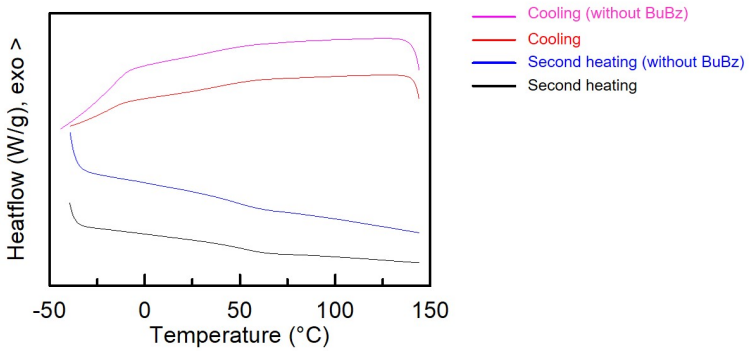

Figure 3.5: Differential scanning calorimetry (DSC) curves of dye-free poly(HEMA-co-MAA-co-TEG diMA)/CTAC polymers with (red and black curves) and without BuBz (pink and blue curves). All measurements consisted of three heating cycles and were repeated three times per sample. The first heating featured an endotherm attributed to water evaporation so the relative curves were omitted for clarity, while the second and third heating yielded equivalent curves. Both materials were prepared using the same procedure except for the addition of BuBz. The glass transition temperature (T_g) recorded for the BuBz-containing material falls between 50-52 °C, whereas it is between 50-53 °C without BuBz, consistent with a biphasic system. No other transitions were observed in the probed temperature range.

To probe this property, oxygen transmission rate (OTR) measurements were performed with a Mocon OX-TRAN MH 2/20 and SH 2/20 following the standard ASTM F1927-14. For these characterization, $\sim$ 0.2 mm thick polymer films, both dye-free and containing the green-to-blue upconverting dyes, were prepared, according to the procedure in Sec. 3.3.1 and filtering the final warm mixture into a petri dish acting as a mold with 0.2 mm stoppers and covered with a second petri dish to homogenize the film thickness. The resulting films were then extracted from the mold and cut into 4.5×4.5 cm^2 pieces. The OTR measurements were performed on triplicates of each film. Interestingly, the values found and reported in Tab. 3.1, expressed in cm^3 (m^2 day atm)$^{-1}$, are similar to those of poly(ethylene terephthalate) and polyamide 6, that are well-known polymers widely used for technological applications, as they afford a significant protection from atmospheric oxygen.[285,286]

Morphological studies

For the polymers morphological characterization different approaches were tested. In the first place, the polymers' structure was investigated through scanning electron microscopy, with a MIRA 3 LMH field-emission electron microscope (Tescan, Brno, Czech Republic), and to pre-

Sample	Dye-free material	Upconverting material
1	1.27	1.05
2	1.27	1.08
3	1.20	0.72
Average	**1.24 ± 0.04**	**0.95 ± 0.19**

Table 3.1: Oxygen transmission rate values obtained for triplicates of films of the dye-free nanophase-separated polymer and the green-to-blue upconverting nanophase-separated polymer, respectively. All values are given in cm^3 (m^2 day atm)$^{-1}$.

vent charging, the polymers were sputter-coated with a 2 nm thin layer of Pt/Pd (80:20) alloy prior to imaging. But this technique did not afford useful information about the coexistence of multiple phases, possibly because the small features collapse under imaging conditions, when the freshly fractured surfaces are exposed to ambient conditions.

Time-domain nuclear magnetic resonance. To circumvent this intrinsic limitation, a different approach was explored, and time-domain nuclear magnetic resonance (NMR) measurements were carried out on a 0.5 T Bruker Minispec mq20 instrument with proton Larmor frequency of 19.9 MHz, equipped with a static probe and a BVT3000 heater temperature control unit working with nitrogen gas. The temperature was calibrated using an external thermometer with an accuracy of 1 K. The precision is 0.1 K and the temperature is stable within that range during the measurement. The samples were left for ten minutes in the magnet to ensure thermal equilibration before starting the experiments.

Free-induction decay (FID) traces for rigid phase determination were acquired after a pulsed mixed magic sandwich echo (MSE) was performed on each sample with 128 scans. Domain size calculations were performed on FID traces collected after a MSE refocused Goldman-Shen sequence, using the Initial Rate Approximation for the sink (rigid) region. The receiver dead time was set to 12.7 μs, and phase switching time to 2.2 μs while the 90° pulse length was set to 2.10 μs.

Magic Sandwich Echo. The Magic Sandwich Echo sequence was employed to measure the rigid fraction f_R of the system. This method resolves different populations of protons within the sample by their mobility and is used to assess phase heterogeneity or to follow phase transitions such as crystallization. It was also used to provide evidence of the presence of interfaces, in terms of deviations between the amount of rigid and mobile fractions as compared

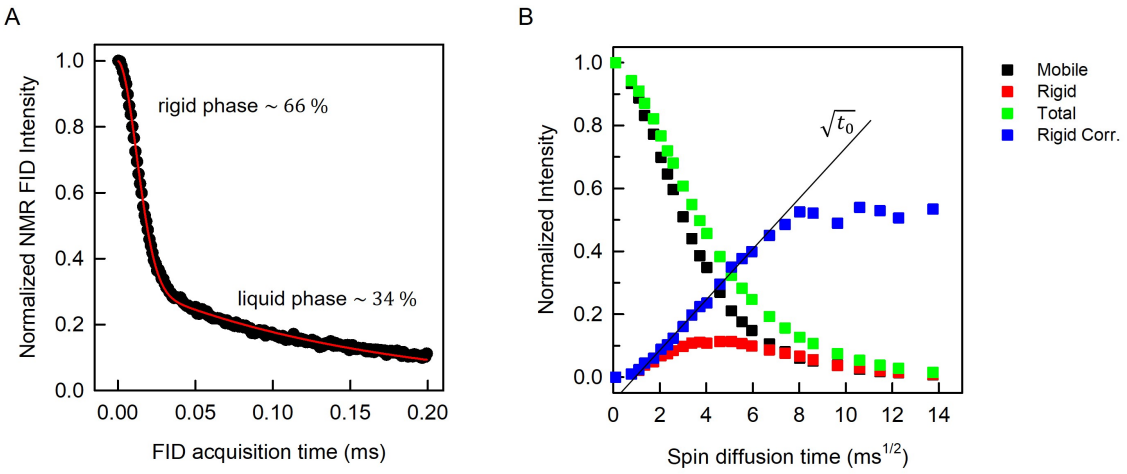

Figure 3.6: (a) Time-domain NMR free-induction decay (FID) trace (dotted curve) of the DPA:PdOEP upconverting nanophase-separated polymer, acquired with Magic Sandwich Echo (MSE) refocusing block at 303 K. The fitting curve (red solid line) points out a fast Gaussian relaxation that characterizes the rigid phase, accounting for $\sim 66\%$ of the intensity and a slower exponential relaxation associated with the mobile phase, accounting for the remaining $\sim 34\%$ of the intensity. (b) Spin diffusion experiment performed on the DPA:PdOEP upconverting nanophase-separated polymer. The raw total, rigid, and mobile fractions determined by fitting separate experiments with different diffusion times are presented. To offset τ_1 relaxation (τ_1 spin-lattice relaxation time), the rigid fraction data were corrected by pointwise normalization against the total signal intensity, and then fitted with Initial Rate Approximation to extract $\sqrt{t_0}$.

to the known proton amounts of the components associated to each phase. A 10 mm NMR tube containing a small cylinder cut from the upconverting material was prepared. To stabilize the sample, it was annealed at 353 K for several days directly in the tube before any measurement. The FID delay of the annealed sample at 303 K reported in Fig. 3.6a is well represented by a gaussian + exponential fitting, that assumes a system composed of two phases resolved by molecular mobility. Following the treatment of Maus et al.,[287] the FID traces were fitted with the following equation, yielding the rigid fraction f_R:

$$\frac{FID(t)}{FID(0)} = f_R e^{-(t/\tau_{2r})^2} + (1 - f_R) e^{-(t/\tau_{2m})} \tag{3.4}$$

The rigid fraction, associated to the gaussian component, is assessed at $\sim 66\%$.

Spin Diffusion data analysis. Following the treatment of Mauri et al.,[288] it is possible to measure the time associated to the spin diffusion process by performing Initial Rate Approximation of the sink phase buildup signal. In a mobile-phase selected experiment, with the dimension-

ality k (k = *1* for lamellar systems, 2 for cylinders, 3 for spheres or cubes), the mobile phase width d_{mob} directly follows from $\sqrt{t_0}$ according to the equation

$$d_{mob} = \frac{4k}{\pi} \frac{\rho_{rig}\sqrt{D_{mob}D_{rig}}}{\rho_{mob}\sqrt{D_{mob}} + \rho_{rig}\sqrt{D_{rig}}} \sqrt{t_0} \tag{3.5}$$

In the nanostructured polymer considered, the proton content of the weighted average of the mobile and rigid phases is 7.9% and 7.2%, respectively. Considering the mass density of BuBz, close to unity, and being the density of the rigid fraction close to 1.2 g cm^{-3}, typical of rigid acrylate polymers, the values of 1 g cm^{-3} and 1.3 g cm^{-3} were employed for ρ_{mob} and ρ_{rig} respectively. For the spin diffusion coefficient in the rigid phase, the established value D_{rig} = 0.8 nm^2 ms^{-1} was used, while a separate Hahn echo experiment performed on the material's mobile phase yielded a τ_2 (spin-spin relaxation time) of 0.27 ms, corresponding to a D_{mob} = 0.42 nm^2 ms^{-1}, according to the treatment of Spiess et al.[289] Spin diffusion data and analysis are presented in Fig. 3.6b. Following the treatment in Ref.[290] $\sqrt{t_0}$ was estimated to be 13.3 $s^{1/2}$, and was inserted in Eq. 3.5, therefore, with the approximations adopted, the average liquid domain diameter resulted 38 ± 6 nm.

3.4 Block copolymer stabilized nanostructured glassy polymers

All chemicals were purchased from Sigma-Aldrich, ABCR, Acros Organics, TCI (Tokyo Chemical Industry Co., Ltd.) or Inochem, Ltd. (Frontier Scientific, Inc) and were used as received.

3.4.1 Preparation of dye-free nanostructured polymers

A 20 mL vial equipped with a stir bar was charged under ambient conditions with poly(ethyleneglycol)-*block*-poly(propyleneglycol)-*block*-poly(ethyleneglycol) (PEG-PPG-PEG, 500 mg), 2-hydroxyethyl methacrylate (HEMA, 4.82 g, 4.5 mL), triethyleneglycol dimethacrylate (TEG-diMA163.8 mg, 0.15 mL) and hexyl benzoate (HexBz, 294 mg, 0.3 mL). The mixture was heated in an oil bath to 60 °C and stirred for 20 min until clear and homogeneous. The mixture was then removed from the oil bath and a saturated solution of NaBr in 0.1% aq. HCl (0.15 mL) was dropwise added under stirring. The stirrer was removed and 30% aq. H_2O_2 (10 mg) and 2-mercaptoethanol (2-ME, 10 mg) were added sequentially. The mixture was briefly shaken and allowed to react for 1-2 min before dimethylthiomethane (DMTM, 24 mg) was

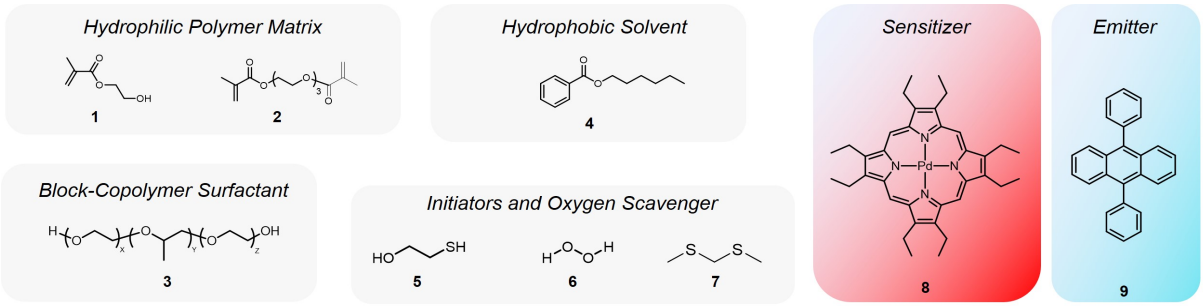

Figure 3.7: Chemical structures of the green-to-blue upconverting polymer components: (**1**) 2-hydroxyethyl methacrylate, (**2**) triethyleneglycol dimethacrylate, (**3**) poly(ethylene¬glycol)-*block*-poly(propyleneglycol)-*block*-poly(ethyleneglycol), (**4**) hexyl benzoate, (**5**) 2-mercaptoethanol, (**6**) H_2O_2, (**7**) dimethylthiomethane, (**8**) Pd(II) octaethylporphyrin, (**9**) 9,10-diphenylanthracene.

added and the mixture was shaken. The mixture was filtered warm through a 0.2 μm PTFE filter into either an optical glass cuvette or a 10 mL glass vial sealed with a polymer film. The clear mixture was left to cure for 24 h at room temperature to obtain a transparent, hard material, which was kept in the cuvette and used for quantitative optical measurements or in a glass vial.

For DSC characterization, also samples excluding either HexBz ("Dye-free w/o HexBz"), PEG-PPG-PEG ("Dye-free w/o PEG-PPG-PEG"), or both ("Cross-linked PHEMA"), were prepared. The quantities and stoichiometry of all remaining components were identical to that of the dye-free material. Also, a PEG-PPG-PEG/HexBz mixture was prepared mixing PEG-PPG-PEG (500 mg) and hexyl benzoate (294 mg, 0.3 mL) in a vial and subsequently heated with a heat gun to obtain a transparent, homogeneous mixture, which was then cooled to room temperature before performing DSC analysis.

3.4.2 Preparation of upconverting nanostructured polymers

Following the procedure for the dye-free polymers just presented, three different upconverting systems were developed. A green-to-blue upconverting material was prepared by substituting the hexyl benzoate with a solution of palladium(II) octaethylporphyrin (PdOEP) in hexyl benzoate (2×10^{-4} M, 294 mg, 0.3 mL). 9,10-diphenylanthracene (DPA, 25 mg, 7.6×10^{-5} mol) was added to the PdOEP solution, and the resulting mixture was heated to 60 °C until the dyes fully dissolved and it was added hot to the pre-polymerized mixture. Assuming a density of 1 g cm^{-3} for the final material, the chromophore concentrations were 1.9×10^{-5} M for PdOEP and 1.4×10^{-2} M for DPA.

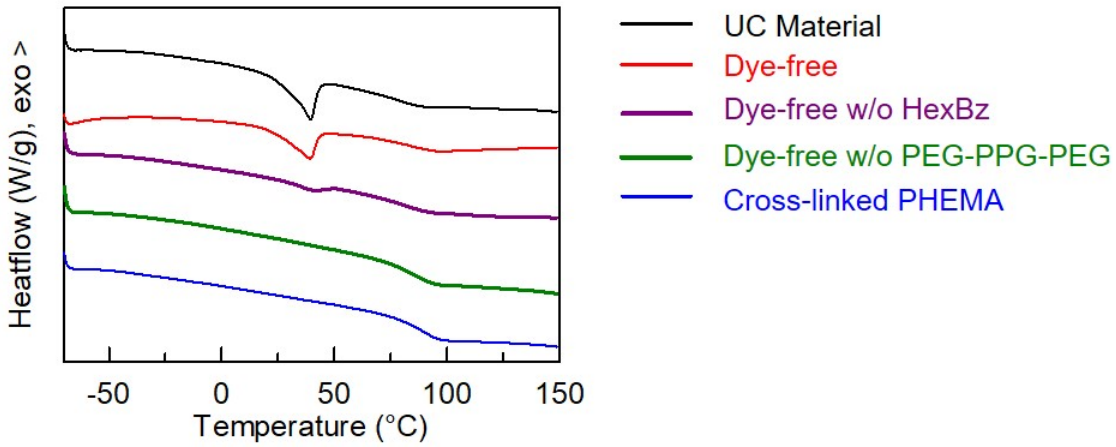

Figure 3.8: DSC traces of the cross-linked (CL) PHEMA (CL-PolyHEMA, blue curve), the cross-linked PHEMA containing only HexBz (CL-PolyHEMA + HexBz, green curve), the cross-linked PHEMA containing only the PEG-PPG-PEG (CL-PolyHEMA + PEG-PPG-PEG, purple curve), the dye-free nanophase-separated polymer (CL-PolyHEMA + PEG-PPG-PEG + HexBz, red curve), and the upconverting nanophase-separated polymer (UC Material, black curve) containing also the upconverting dyes.

Following this very same procedure, a red-to-blue upconverting system was obtained from palladium(II) tetraphenyltetrabenzoporphyrin (PdTPBP) in hexyl benzoate (2×10^{-4} M, 294 mg, 0.3 mL) and 2,5,8,11-tetrakis(tert-butyl)perylene (TBPe, 4.8 mg, 10^{-5} mol) with final chromophore concentrations of 1.9×10^{-5} M for PdTPBP and 1.9×10^{-3} M for TBPe, and a dark red-to-yellow upconverting system was produced from palladium(II) octabutoxyphthalocyanine ($Pd(OBu)_8Pc$) in hexyl benzoate (10^{-5} M, 294 mg, 0.3 mL) and rubrene (1 mg, 1.9×10^{-6} mol), resulting in the final chromophore concentrations of 9.5×10^{-6} M for $Pd(OBu)_8Pc$ and 1.7×10^{-4} M for rubrene. The molecular structure of the two upconverting dye pairs is reported in Fig. 3.4b.

3.4.3 Material characterization

The basic material characterization performed on this class of nanostructured polymers is the same of that carried out for the nanophase-separated polymers presented in the previous section, with the same instrumentation and techniques. The DSC characterization of the dye-free material and the upconverting system (Figure 3.8) reveals a T_g of 80-84 °C, attributed to the cross-linked poly(hydroxyethyl methacrylate) (PHEMA) matrix, which has a $T_g = 86$ °C. At

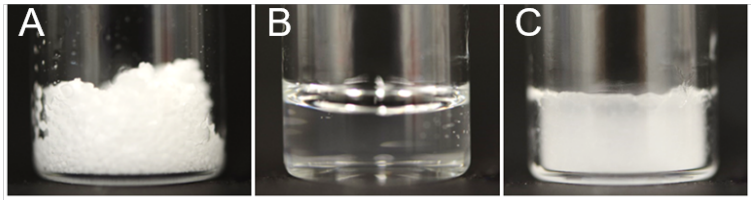

Figure 3.9: Images taken during the preparation of the PEG-PPG-PEG/HexBz mixture. (a) Combination of the two components at room temperature in a glass vial. No mixing is observed. (b) Heating the same vial as in (a) with a heat gun liquefied the PEG-PPG-PEG and produced a homogeneous, transparent mixture of the two components. (c) The mixture after being cooled to room temperature appeared opaque and with a semi-solid consistency.

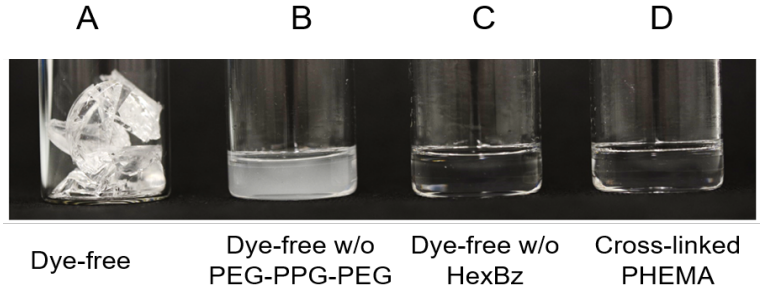

Figure 3.10: Bulk preparations of (a) the dye-free material, (b) the dye-free material without PEG-PPG-PEG (b), without hexyl benzoate (c), or without either hexyl benzoate or PEG-PPG-PEG, i.e., cross-linked PHEMA (d). The materials in (a), (c) and (d) are transparent, while the material in (b) is opaque. The dye-free material in (a) was shattered with a hammer, revealing its glassy nature.

room temperature, only the glass transition is visible when heating the upconverting and dye-free materials from 0 °C, and the exclusion of either PEG-PPG-PEG or hexyl benzoate from the dye-free material does not provoke a significant variation of this value.

However, cooling to -80 °C induces crystallization of what appears to be PEG domains of the block copolymer, and upon heating a melting event is observed at 40 °C, which is slightly lower than the melting temperature of neat PEG-PPG-PEG ($T_m = 60$ °C). The reduction in T_m appears to result from mixing the PEG-PPG-PEG and hexyl benzoate, given that a mixture of only these two components starts melting at 40 °C. As expected, no crystallization or melting events are observed when PEG-PPG-PEG is omitted from the dye-free material. However, if only the hexyl benzoate solvent is omitted, a weak endotherm remains at 40 °C, indicative of partial de-mixing of PEG-PPG-PEG and PHEMA.

The dye-free material without hexyl benzoate appears transparent, indicating good mixing

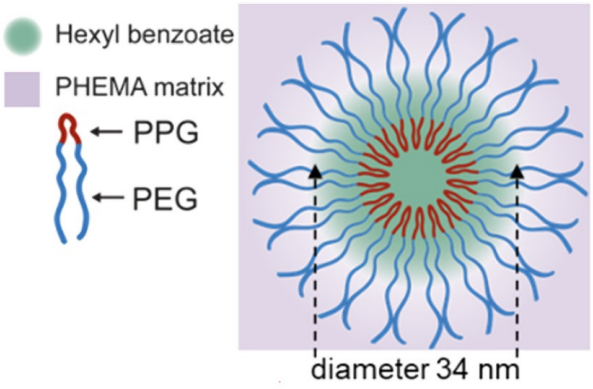

Figure 3.11: Idealized sketch of the nanodroplet structure achieved with the present synthesis protocol, drawn by combining the experimental results from DSC and time-domain NMR measurements.

between PEG-PPG-PEG and PHEMA at room temperature; on the other hand, the material without PEG-PPG-PEG appears opaque, indicating that the hexyl benzoate and PHEMA tend to phase-separate (Figures 3.9, 3.10).

Given the hydrophobicity of hexyl benzoate and the tendency of PEG-PPG-PEG to form micellar structures in hydrophilic environments,[261,291–294] it is reasonable to postulate that in the upconverting and dye-free materials hexyl benzoate forms hydrophobic droplets that promote the self-assembly of PEG-PPG-PEG into nanoscale structures. The resulting nanodroplets reasonably consist of a liquid core in which the PPG and a portion of the PEG blocks reside, with the remaining PEG blocks protruding out into the glassy PHEMA matrix to stabilize and limit the size of the droplets. An idealized sketch of the liquid nanodomains structure is reported in Fig. 3.11.

Furthermore, crystallization in the upconverting and dye-free materials occurs at -43 °C, i.e., at a much lower temperature than the PEG-PPG-PEG/HexBz mixture. Thus, while at least some of the PEG blocks reside in a sufficiently mobile environment to crystallize at low temperatures in the dye-free material, this process appears to be frustrated by structural constraints that stem from immobilization of a portion of the PEG-PPG-PEG chains in the surrounding matrix.

Morphological studies

To get morphological information about the samples, time-domain NMR measurements were carried out, similarly to the procedure in Sec. 3.3.3. The same general approach, techniques and data analysis were followed. The Magic Sandwich Echo sequence was employed to de-

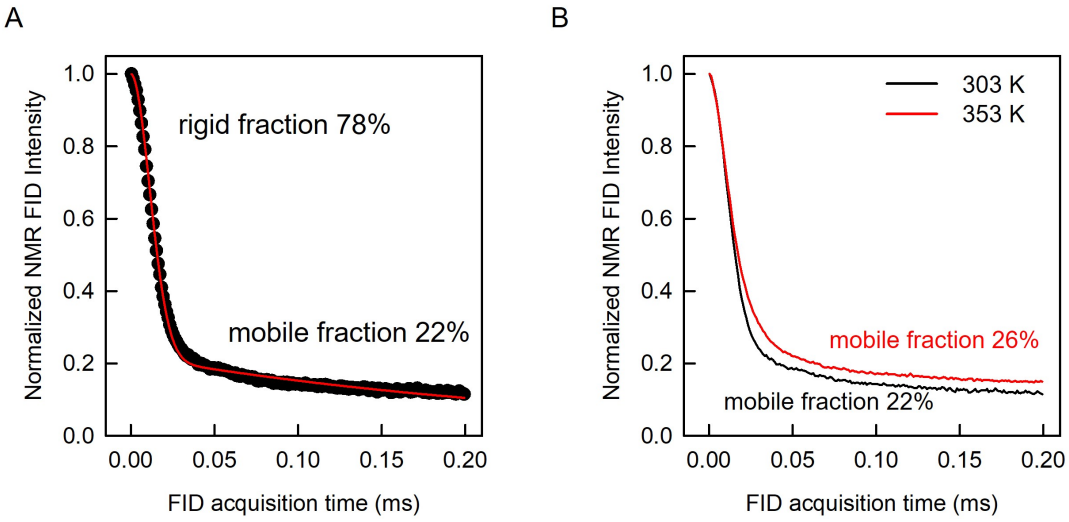

Figure 3.12: (a) Free-induction decay trace (dotted curve) acquired on the upconverting DPA:PdOEP glassy polymer after a MSE refocusing block at 303 K. The fitting curve with a gaussian + exponential function (solid curve) results in a rigid fraction of $\sim 78\%$, and a mobile fraction of $\sim 22\%$. (b) FID traces acquired on the upconverting DPA:PdOEP material after annealing at 303 K and 353 K, showing only a 4% increase of the mobile fraction over a 50 K temperature range.

termine the rigid fraction in the polymer.[287] The FID delay of the annealed sample at 303 K is relatively well represented by a gaussian + exponential fitting, as reported in Fig. 3.12a. The rigid fraction, associated to the Gaussian component, is assessed at 78%, but the fitting curve has also a small but non-negligible residual component in the region between 25 μs and 50 μs, possibly indicating the presence of significant amounts of interphase. As depicted in Fig. 3.12b, the same measurement was carried out also at 353 K, but in this temperature range the mobile fraction only changes from 22% to 26%, which is a small variation for such a temperature difference, indicating a clear separation between the rigid and mobile regions in the polymer.[295]

A more thorough analysis of the mobile region was performed using the Hahn Echo technique, often used to separate different components in heterogeneous systems.[296] As in MSE, different populations of protons and their carrier molecules give rise to different decays associated to different motional regimes, but the difference here lies in the timescale: different relaxations clumped together as "mobile fraction" can be distinguished and analyzed. The data, reported in Fig. 3.13a, were fitted with a biexponential decay, meaning that the mobile regions are actually composed of two components, one with $\tau_2 = 0.70$ ms, the other with $\tau_2 = 7.3$ ms. Combining the relative weights from the fitting procedure with the evaluation of the rigid fraction from

MSE and considering that a greater τ_2 is associated to faster molecules,[297] the overall material can be divided into three components, one rigid and two mobile. Table 3.2 reports the

	Expected protons	Associated protons	T_2 [ms]	Main Assignment
Comp. 1	84%	78%	< 0.05	Cross-linked PHEMA matrix
Comp. 2	10%	12%	0.72	Interface and PEG-PPG-PEG
Comp. 3	6%	10%	7.3	Hexyl benzoate

Table 3.2: Decomposition of the green-to-blue upconverting nanophase-separated glassy polymer into three components characterized by different TD-NMR relaxation parameters. The experimental relative weights of each component are also presented, together with the expected values calculated following a model that considers full phase separation of species that are chemically different.

three components, with the corresponding T_2 parameter and the expected and experimentally assigned relative weight of each component based on the proton amount associated to each component. The assignment is based on the typical relaxation behaviour of rigid matrices, and on the fact that a difference of one order of magnitude is a reasonable outcome when comparing the relaxation time of soft polymers and small molecules. The expected proton fractions associated with each phase were calculated considering the main chemical components reported in Fig. 3.7, but this model overestimates the rigid fraction, because it does not consider about 3% of mobile protons resulting from the minor components that, being small molecules, should be added to the mobile fractions. Also, the deviation of the assigned proton content from the expected values is more pronounced for the rigid phase, indicating the significant presence of interfaces, as suggested by the microscopic phase separation discussed in Fig. 3.10. Considering the chemical nature of the components, and knowing that the PEG and PPG blocks are hydrophilic and hydrophobic, respectively, the most likely structure that is consistent with this interphase is a dispersion of spherical nanodroplets in a rigid matrix. Within the droplets, the HexBz tends to concentrate in the core, while the amphiphilic block copolymer provides the interface between HexBz and the rigid matrix. It is reasonable to assume that HexBz is not fully segregated but it partially solvates the PEG-PPG-PEG, thus increasing the amount of mobile protons from 6% to 10%. The block copolymer shell, while contributing some protons to the inner mobile core, also mobilizes part of the glassy matrix, thus slightly decreasing the observed fraction of the rigid phase with respect to the theoretical expected value.

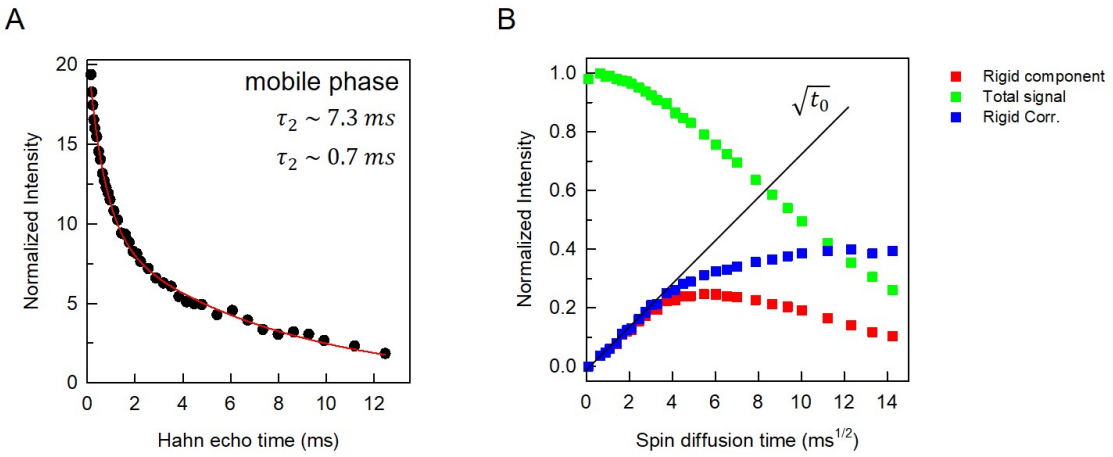

Figure 3.13: (a) Intensity of Hahn Echo (circles) relative to the mobile phase performed on the upconverting DPA:PdOEP material, fitted with a bi-exponential decay (red solid line). The resulting relaxation times τ_2 of the two mobile phases are $\tau_2 \sim 7.3$ ms and $\tau_2 \sim 0.7$ ms. (b) Spin diffusion experiment performed on the upconverting DPA:PdOEP material. The total normalized intensity (green curve) is reported together with the contribution from the rigid component (red curve) that was determined by fitting separate experiments with different diffusion times. To offset the τ_1 relaxation, the rigid fraction data were then corrected by pointwise normalization against the total signal intensity (blue curve), basically obtaining the rigid fraction extracted from each FID trace, and then fitted with Initial Rate Approximation to extract $\sqrt{t_0}$.

Spin diffusion analysis. Spin-diffusion experiments were carried out to assess the size of mobile nanodomains at 303 K, reported in Fig. 3.13b. The analysis of spin diffusion is based on fitting the MSE refocused FIDs, and thus does not consider the presence of two different relaxation regimes in the mobile phase. Since the analysis is based on the Initial Rate Approximation, which follows the onset of spin diffusion from the mobile to the rigid domain, and since the diffusion coefficient is inversely proportional to the τ_2 relaxation time, the value of 0.70 ms associated to the outer shell (block copolymer) was used to calculate the domain size. The estimation of the mobile domains diameter was carried out according to Eq. 3.5. Here, given the mobile and rigid fraction mass densities close to 1 g cm^{-3} and 1.2 g cm^{-3} respectively, and considering that the mobile phase is more proton rich, the values of $\rho_{mob} = 1.17$ g cm^{-3} and $\rho_{rig} = 1.2$ g cm^{-3} were employed. For the spin diffusion coefficient in the rigid phase, the established value $D_{rig} = 0.8$ nm^2 ms^{-1} was used, while $\tau_2 = 0.70$ ms yielded a $D_{mob} = 0.32$ nm^2 ms^{-1}.[289] The $\sqrt{t_0}$ was estimated to be 14.1 $s^{1/2}$.[290] As a result of the chosen approximations, 34 $\pm$ 6 nm is the average diameter of the liquid domains and this value de-

scribes a complex domain, where two mobile components form a single mobile droplet able to host the upconverting process.[239]

3.5 Bichromophoric emitters

All reagents and solvents were used as received, unless otherwise indicated. 4,12-dibromo[2.2]paracyclophane was purchased from Daicel Chiral Technologies (China) Co., Ltd. 4,4,5,5-tetramethyl-2-(3-perylenyl)-1,3,2-dioxaborolane was purchased from Inno-Chem Science and Technology Co., Ltd.

3.5.1 Synthesis of 4,12-diperylene[2.2]paracyclophane

The synthesis of 4,12-diperylene[2.2]paracyclophane (PCP), a derivative of perylene, was carried out following a method previously reported in literature.[298] The scheme of the synthetic route is illustrated in Fig. 3.14. The PCP was synthesized directly from the reaction of the corresponding 4,12-dibromo[2.2] paracyclophane and 4,4,5,5-tetramethyl-2-(3-perylenyl)-1,3,2-dioxaborolane by palladium-catalysed coupling reactions as follows.

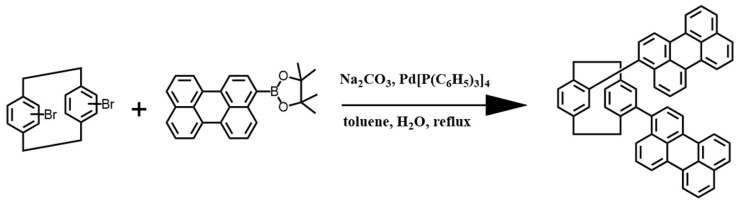

Figure 3.14: Synthetic route for the production of 4,12-diperylene[2.2]paracyclophane (PCP).

A mixture of 4,12-dibromo[2.2]paracyclophane (0.2 g, 0.54 mmol), 4,4,5,5-tetramethyl-2-(3-perylenyl)-1,3,2-dioxaborolane (0.45 g, 1.24 mmol), tetrakis (triphenylphosphine)-palladium(0) (0.05 g, 0.04 mmol) and toluene (10 mL) were put in a round-bottom flask equipped with a magnetic stirring bar. 4 mL sodium carbonate (0.14 g) aqueous solution was then added to the mixture. After degassing the reaction mixture several times by freezing and thawing cycles, the reaction was heated at 100 ℃ for 12 h. After cooling to room temperature, the mixture was dissolved in ethyl acetate. Then the reaction mixture was washed with water and the organic layer was separated and dried over Na_2SO_3. After solvent evaporation, the residue obtained was purified by column chromatography on SiO_2 (dichloromethane/*n*-hexane from 1/100 to 1/10 v/v as an eluent). The PCP yellow powder was collected.

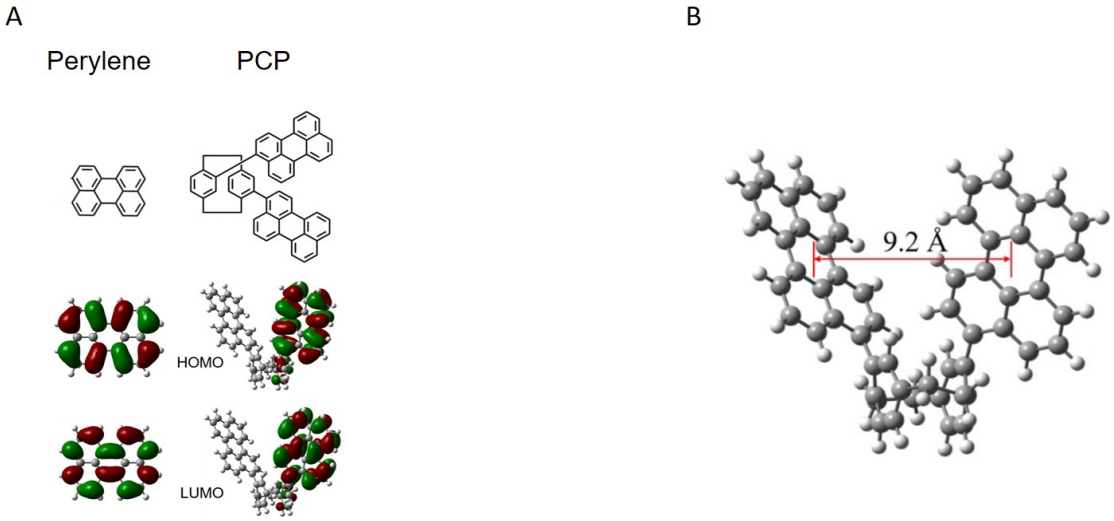

Figure 3.15: (a) Molecular structure of perylene (left) and PCP (right). Highest occupied molecular orbital (HOMO, the singlet S_0 ground state) and the lowest unoccupied molecular orbital (LUMO, the T_1 triplet state) of perylene and PCP obtained via DFT calculations. All geometries were optimized by Gaussian 09 using DFT with the PBE1PBE functional and the 6-311g* basis set. (b) Average distance between two perylene units in a PCP molecule calculated via DFT.

3.5.2 Material characterization

The chemical structure of PCP was identified by means of ^{1}H NMR, ^{13}C NMR and high-resolution mass spectrometry. The ^{1}H and ^{13}C NMR spectra recorded on a Bruker Fourier 400 (400 MHz) spectrometer. High-resolution mass spectral data were obtained using a SolariX maldi-P-100-3000 instrument.

^{1}H NMR (400 MHz, $CDCl_3$): δ 8.30 (d, $\mathcal{J}$ = 7.8 Hz, 2H), 8.28-8.17 (m, 6H), 7.96 (d, $\mathcal{J}$ = 7.8 Hz, 2H), 7.69 (d, $\mathcal{J}$ = 8.1 Hz, 4H), 7.51-7.46 (m, 4H), 7.37-7.28 (m, 4H), 6.93 (t, $\mathcal{J}$ = 6.6 Hz, 4H), 6.84 (d, $\mathcal{J}$ = 7.7 Hz, 2H), 3.18 (t, $\mathcal{J}$ = 20 Hz, 2H), 3.08 (t, $\mathcal{J}$ = 22.8 Hz, 2H), 2.95 (t, $\mathcal{J}$ = 8 Hz, 2H), 2.73 (t, $\mathcal{J}$ = 20 Hz, 2H).

^{13}C NMR (101 MHz, $CDCl_3$): δ 139.68, 139.33, 138.85, 136.47, 135.05, 134.70, 133.90, 132.98, 131.49, 131.24, 131.15, 131.02, 130.47, 127.73, 126.65, 126.41, 126.30, 125.95, 120.36, 120.28, 120.20, 119.79, 34.67, 34.51.

HR-MS (MALDI) for PCP ($C_{56}H_{36}$) m/z = 708.281153 (calculated), 708.28095 (observed).

Figure 3.15a reports the molecular structure of perylene and PCP. The comparison with perylene allows to highlight the structural differences introduced with the molecular design developed and the consequent variations in the triplet state energy. The figure shows the electronic

probability density of the highest occupied molecular orbital (HOMO, the S_0 ground state with singlet character) and the lowest unoccupied molecular orbital (LUMO, the T_1 state with triplet character) of PCP and perylene obtained via DFT calculations.[299] All geometries were optimized by Gaussian 09 using DFT with the PBE1PBE functional and the 6-311g* basis set. The modelling results show that both the HOMO and LUMO orbitals are mainly condensed on the perylene branch of the PCP, with a limited delocalization of the electronic cloud on the phenyl ring. With this technique also the energies of PCP and perylene T_1 and T_2 states were calculated: $T_1 = 0.7$ eV (PCP) and 0.72 eV (perylene), $T_2 = 1.42$ eV (PCP) and 2.65 eV (perylene), and using DFT calculations on the optimized geometries the average distance between two perylene units in a PCP molecule resulted 9.2 Å (Fig. 3.15b).

Hybrid sensitizers based on doped nanocrystals

Colloidal nanocrystals decorated with conjugated organic ligands have been recently proposed to extend the limited light-harvesting capability of molecular absorbers. Key to their functioning is efficient energy transfer from the nanocrystals to the triplet state of the ligands that sensitize the emitters triplets. The nanocrystal-to-ligand energy transfer efficiency is typically limited by parasitic processes, such as nonradiative hole-transfer to the ligand HOMO. A new exciton-manipulation approach is proposed that enables a loss-free energy transfer by electronically doping CdSe nanocrystals with gold cations that introduce hole-accepting intragap states above the HOMO energy of 9-anthracene carboxylic acid ligands. Upon photoexcitation, the nanocrystal hole is rapidly routed to the gold-level producing a long-lived bound exciton resonant with the ligand triplet, outcompeting hole-transfer leading to $\sim$100% efficient energy transfer that translates in upconversion quantum yield $\sim$12%, which is the highest performance for nanocrystal-based upconverters based on sTTA achieved so far and approaches the efficiencies of optimized organic systems.

4.1 Electronic doping as strategy for exciton manipulation

Over the past years, exceptional progress in the design of hybrid sensitizers has enabled a notable growth of the *s*TTA-UC performance since their first appearance in 2015 when cadmium selenide (CdSe) nanocrystals (NCs) decorated with 9-anthracene carboxylic acid (9-ACA) were

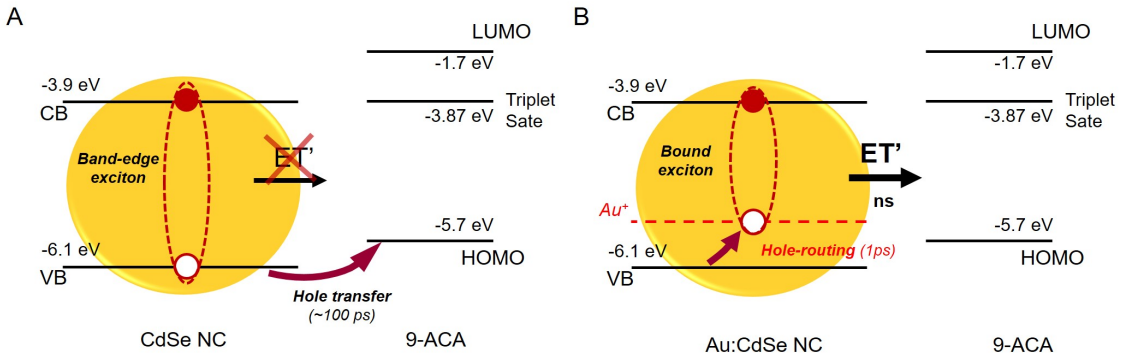

Figure 4.1: (a) Energy diagram and mechanistic picture of the hole-transfer process on the ligand HOMO that outcompetes ET′ in cadmium selenide (CdSe) nanocrystals (NCs) functionalized with 9-anthracene carboxylic acid (9-ACA).[300] (b) In CdSe NCs doped with gold impurities, hole-transfer is outpaced by the ultrafast localization of the photohole in the intragap states (1–2 ps vs $\sim$ 100 ps) associated with the *d*-levels of Au^{+}, leading to the formation of a bound exciton resonant with the 9-ACA triplet state. As a result, the ET′ step reaches 100% efficiency.

proposed as first example of hybrid sensitizers (Fig. 1.4). However, despite such advancements, the performances of hybrid *s*TTA-UC systems are still not as good as those of the best fully-organic systems,[191,199,208,211,212] because of deleterious processes that limit the efficiency of the energy transfer ET′. For example, trapping of band-edge (BE) carriers in defect states on the NCs surfaces might become particularly relevant when the native ligands used for the NCs synthesis are substituted with more bulky triplet acceptors, resulting in incomplete surface coverage.[301] Although this problem can be mitigated by shelling the NCs with wider energy gap semiconductors,[182,215,302] other loss phenomena are harder to circumvent, as they are intrinsically related to the NCs electronic structure and triplet acceptor molecules. For example, the highest occupied molecular orbital (HOMO) of common triplet acceptors lies above the valence band (VB) energy of most II-VI or IV-VI semiconductors, such as Zn, Cd or Pb chalcogenides[179,300] which, in NCs, is further shifted to lower energies with respect to vacuum by quantum confinement.[161] As a result, as shown in Figure 4.1a, in hybrid sensitizers composed of CdSe NCs functionalized with 9-ACA fast transfer ($\sim$ hundreds of ps)[301,303] of the photogenerated hole from the NC's VB to the 9-ACA HOMO, that lies at $\sim$ -5.7 eV with respect to vacuum,[300] can efficiently dissociate the excitons, outcompeting ET′ and precluding the upconversion process.[209,302] It is worth noting that the VB is less sensitive to quantum confinement than the conduction band (CB) since the hole effective mass is heavier than the electron effective mass in many chalcogenide semiconductors. Consequently, in these systems size control

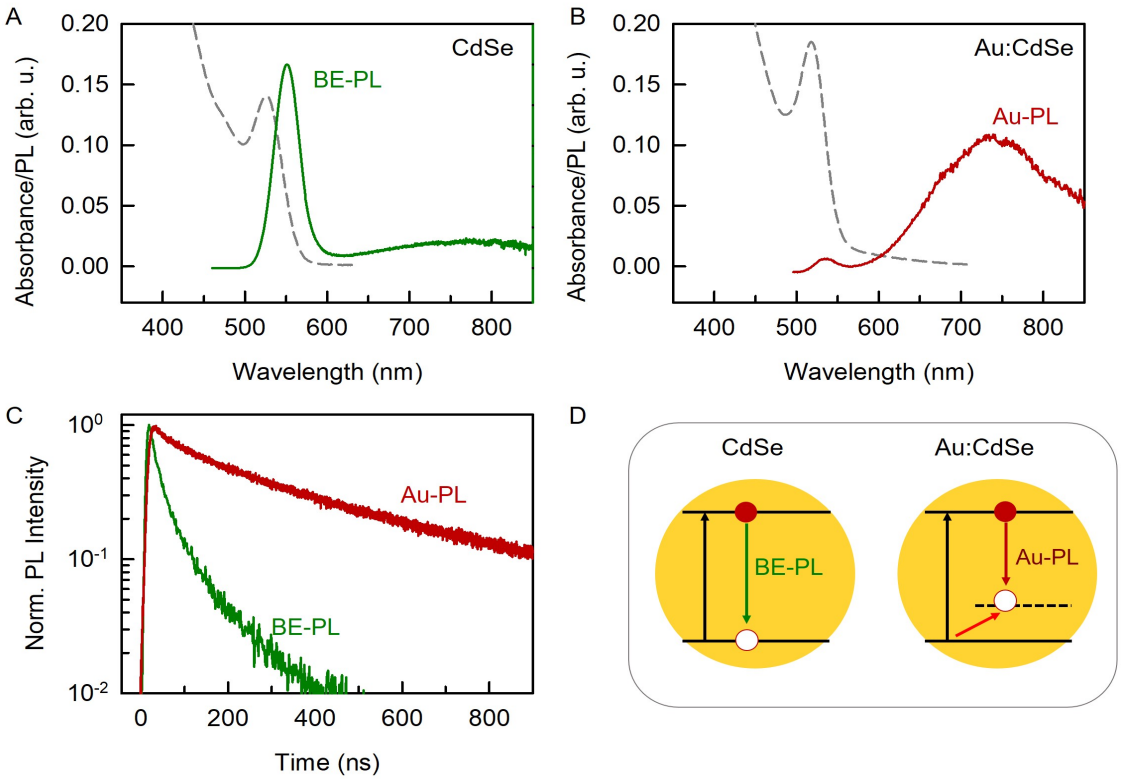

Figure 4.2: (a,b) The dashed lines represent the optical absorption spectra of native OA-capped undoped (a) and Au-doped (b) CdSe NCs in toluene. The solid lines are the photoluminescence (PL) spectra of OA-capped undoped (a) or Au-doped (b) CdSe NCs in toluene under a 460 nm cw excitation. The Au-doped NCs have a diameter of 2.5 nm. (c) PL intensity decay of the same OA-capped undoped (green line) and Au-doped (red line) CdSe NCs recorded at the respective PL maximum (530 and 730 nm, respectively) under pulsed laser excitation at 532 nm. (d) Emission mechanisms in undoped (left) and Au-doped (right) CdSe NCs.

is not sufficient to prevent hole-transfer, as by increasing the NC size the upward VB energy shift is too limited to rise its energy above the triplet acceptor HOMO. Moreover, increasing the size also lowers the CB energy, red-shifting the BE exciton emission and disrupting the spectral resonance with the ligands triplet state. Also, heterostructuring with wide energy gap shells would help to suppress the carrier transfer from NCs to surface ligands, but the increased donor-acceptor distance between the NCs core and the triplet acceptor would lower the ET′ rate in favour of radiative exciton recombination, as already reported for PbS/CdS and CdS/ZnS NCs functionalized with (5-carboxylic acid tetracene)[212,302] or 2,5-diphenyloxazole molecules.[182]

To solve these limitations, I propose a new strategy to suppress hole-transfer, by manipulation

of the NCs photophysical properties introducing an alternative and more favourable pathway available for the photogenerated hole. This scenario is realized employing NCs with an engineered intragap hole-accepting state lying above the HOMO energy of the triplet acceptor and characterized by a higher hole-capturing rate. As illustrated in Fig. 4.1b, the idea underpinning this approach is that ultrafast re-routing of the photogenerated BE hole into the intragap state should generate a bound exciton with a CB electron orbiting within the Coulomb potential of the localized hole, with energy matching the ligand triplet state. To do so, I employed CdSe

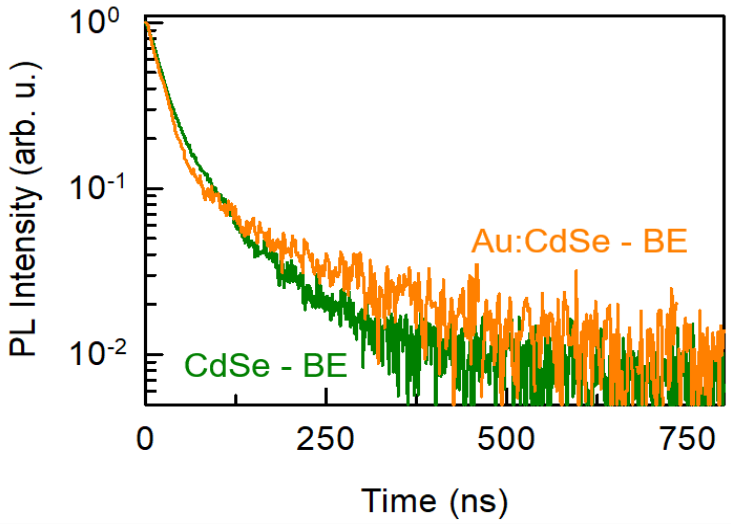

Figure 4.3: Band-edge PL intensity decay at 535 nm for CdSe and gold doped Au:CdSe NCs in toluene under a pulsed 405 nm laser excitation, acquired under the same experimental conditions.

NCs electronically doped with Au^+ cations, as in these systems, similarly to Cu^+- or Ag^+-doped NCs,[278,304,305] the *d*-electrons of Au^+ impurities in their $5d^{10}$ electronic configuration introduce intragap hole acceptor states pinned at ΔE_{VB-Au} ~0.6 eV above the VB maximum that capture the photohole in ~1-2 ps, following the transient oxidation of Au^+ to Au^{2+} according to $Au^+ + h_{VB} \rightarrow Au^{2+}$.[278] Being $\Delta E_{VB-Au} > \Delta E_{VB-HOMO}$ (~0.4 eV) and because the hole-localization in the Au^+ center is much faster than typical hole extraction processes, the use of doped NCs should lead to complete suppression of hole-transfer losses in advantage of the ET′.

4.2 Effectiveness of the hole-routing strategy

The sensitizer design proposed is meant to provide multiple benefits for the upconversion process: the intragap photohole would be unaffected by transfer to the triplet acceptor HOMO

(or trapping) maximizing the 9-ACA triplets sensitization and, owing to the reduced spatial overlap between the electron and hole wavefunctions, the exciton radiative recombination rate would be significantly lowered with respect to the BE exciton, thus favouring Dexter ET′ over radiative decay.[163] Also crucially, by operating on the energetics of the hole-related process, this scheme does not require heterostructuring with thick wide-bandgap shells, without imposing limitations to ET′ due to an increased donor-acceptor distance. To assess the effectiveness of this strategy, I performed side-by-side spectroscopic studies on toluene solutions of undoped CdSe NCs and Au-doped CdSe NCs (referred to as Au:CdSe) of comparable size before and after ligand exchange. To deal with results straightforwardly comparable, I prepared the dispersions with the same optical density of 0.13 at 532 nm. Figure 4.2 reports the optical absorption spectra, recorded following the method reported in Sec. 2.1, of CdSe and Au:CdSe capped with native oleic acid (OA). The absorption profiles are almost identical in shape, meaning that the doping strategy does not alter the electronic structure of the NC host.[278] They both show a well-defined 1S absorption peak at 520 nm, with a full width at half-maximum $\sim$ 32 nm consistent with good size homogeneity of the ensembles. Looking at the PL spectra and decay dynamics reported in Figure 4.2, some peculiar differences appear that inherently stem from the introduction of Au^+ impurities in the NC host. Upon cw excitation at 532 nm, the undoped NCs show the typical narrow bang-edge (BE) emission peaked at $\sim$530 nm, with a Stokes-shift of $\sim$ 80 meV from the 1S absorption peak (Fig. 4.2a). A weak and broad low energy emission is also detected and is typically attributed to emissive surface defects.[306] On the contrary, the Au:CdSe NCs show a different PL spectrum, where the BE emission is suppressed in favor of a broad, red-shifted emission peaked at $\sim$ 730 nm (1.70 eV), referred to as Au-PL. Consistently with previous works on NCs doped with metals from the 11 group,[278,304,305] this emission is ascribed to radiative recombination of the bound excitons formed between the photoexcited CB electrons and the holes localized on the intragap gold *d*-states. The notable Stokes-shift $\Delta E_{VB-Au} \sim 690$ meV between the Au-PL peak and the 1S absorption peak is the energy difference between the NCs VB and the *t*-states of gold impurities that result from the *d*-manifold splitting by the crystal field. To get an estimate of the excited states lifetime, I recorded the time decays of the BE and Au-PL emission peaks under a pulsed laser excitation at 532 nm. In this analysis, to reproduce the experimental data, I fitted the time decays with multiexponential functions and the effective lifetimes were calculated as

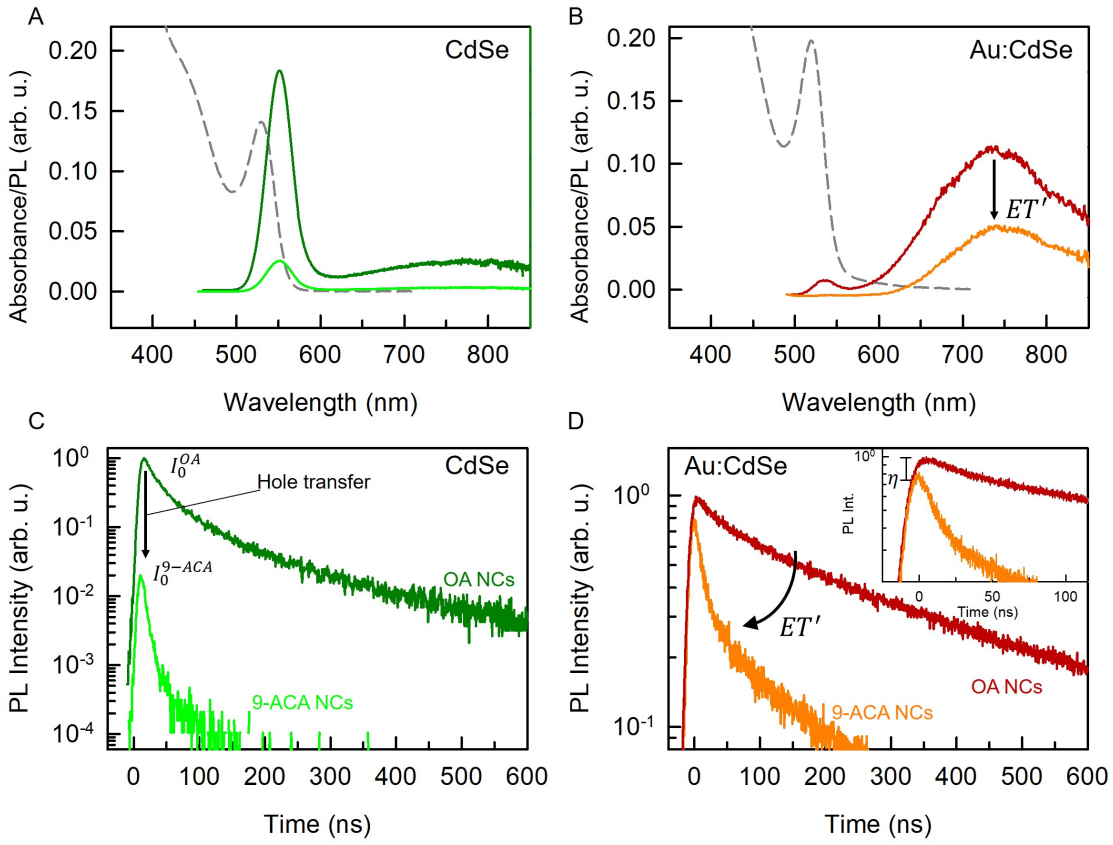

Figure 4.4: (a,b) The dashed lines show the absorption spectra of undoped (a) and Au-doped (b) NCs functionalized with 9-ACA, in toluene. The solid lines are the PL spectra of undoped (a) and Au-doped (b) CdSe NCs with either OA (dark green and red curves) or 9-ACA (light green and orange curves) ligands in toluene under a 460 nm cw excitation. The Au-doped NCs have a diameter of 2.5 nm. (c,d) Time-resolved PL intensity of the same undoped (c) or Au-doped (d) CdSe NCs with either OA or 9-ACA ligands recorded at the respective PL maximum (530 and 730 nm, respectively) under pulsed laser excitation at 532 nm. The inset in panel d is a magnification of the first $\sim$ 100 ns to highlight the η factor reduction. The excitation intensity was 0.5 mW cm^{-2}, the absorbance 0.13 OD at 532 nm for all samples. The measurement conditions were kept unchanged between pristine and 9-ACA functionalized samples to enable quantitative comparison between the respective PL intensities and dynamics.

weighted averages of the resulting components with weight A_i as

$$\tau = \frac{\sum_{i=1}^{n} A_i \tau_i}{\sum_{i=1}^{n} A_i}. \tag{4.1}$$

The undoped NCs BE emission decay at 530 nm has a multiexponential behavior as expected for unshelled CdSe NCs, with an effective lifetime $\tau_{BE}^{OA} \sim 40$ ns, while τ_{Au-PL}^{OA} is ~ 177 ns, much longer than the BE emission of the undoped counterpart. The long-lived nature of this intragap emission is consistent with the reduced spatial overlap between the wavefunctions of the electron delocalized in CB and of the hole localized on the Au impurities if compared to the BE exciton.[278] Interestingly, Figure 4.3 reports the comparison between the BE emission of undoped and doped NCs. Because the BE kinetics is unaffected by doping, the residual BE emission observed in Au:CdSe NCs arises from a small fraction of undoped NCs. According to the material characterization reported in Sec. 3.1.5 and Eq. 3.2, I estimated the NCs valence band and the dopant intragap states energies. From the NCs diameter equal to 2.5 nm, the approximated VB energy is $\sim$ -6.13 eV, thus the Au-level is at $\sim$ -5.44 eV, suggesting that hole-transfer on the ligand HOMO should be suppressed. Therefore, to determine whether the hole routing pathway is effective in suppressing the deleterious nonradiative losses affecting undoped NCs, and estimate the ET$'$ efficiency, I investigated the variations in PL intensity and dynamics upon substituting the native OA ligands with the triplet acceptor 9-ACA. As reported in Figure 4.4a,b, the main effect of ligand exchange is a cw PL intensity reduction, with no variations in the NCs 1S absorption profile. But the time decays highlight important differences about the origin of the PL quenching. In undoped NCs, after functionalization I noticed a relevant reduction of the zero-delay PL intensity (Fig. 4.4c). Defining the parameter η as the ratio between the zero-delay intensity after (I_0^{9-ACA}) and before (I_0^{OA}) functionalization

$$\eta = \frac{I_0^{9-ACA}}{I_0^{OA}}, \tag{4.2}$$

for the undoped NCs ensemble $\eta \sim 0.02$. Consistently with previous studies,[209] this dramatic loss that mirrors a massive reduction of the ability to transfer the excitons to the triplet acceptors is due to ultrafast exciton dissociation by hole transfer from the NCs VB to the ligands HOMO, with a minor contribution by hole trapping in surface defects introduced by ligand exchange. The exciton dissociation occurs on a timescale much faster than the experimental resolution and affects almost the entire NCs population ($>95\%$). The functionalization is also followed by a reduction of the PL lifetime ($\tau_{BE}^{9-ACA} \sim 5$ ns), which reflects the ET$'$ occurring in the subpopulation where the excitons are not affected by dissociation. I calculated the

efficiency of the ET$'$ channel from the lifetime reduction according to[28]

$$\Phi_{ET'} = 1 - \frac{\tau_{BE}^{9-ACA}}{\tau_{BE}^{OA}} \tag{4.3}$$

with $\Phi_{ET'} \sim 88\%$. Therefore, the ET$'$ channel itself is highly efficient, but the ultrafast hole transfer dominates the exciton decay, and the global triplet acceptor sensitization yield in the NCs ensemble is only $\Phi_{ET'}^{G} = \eta\Phi_{ET'} = 1.8\%$.

On the contrary, I observed a completely different scenario in the doped NCs ensemble. After

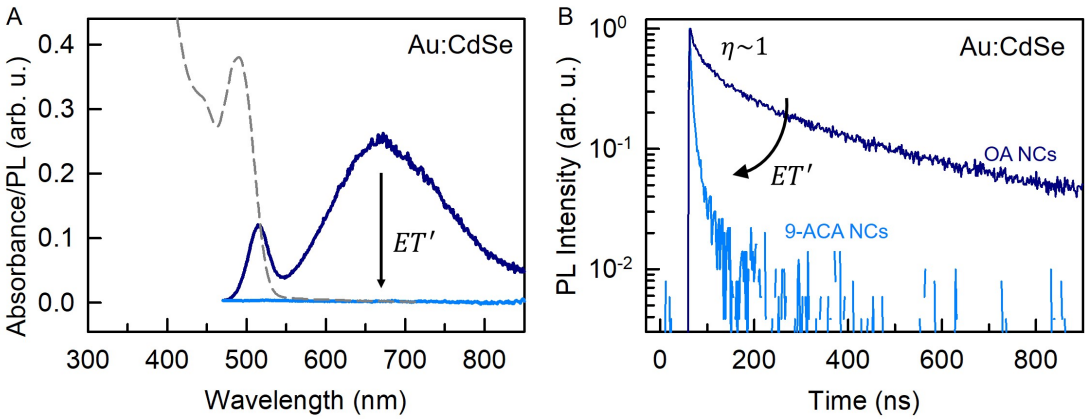

Figure 4.5: (a) Absorption spectrum (dashed line) of Au-doped NCs functionalized with 9-ACA, in toluene. The solid lines are the PL spectra of the OA-capped (dark blue) and 9-ACA-capped (light blue) Au-doped NCs, recorded under a cw 460 nm excitation. The doped NCs have a diameter of 2.3 nm. (b) PL intensity decay at 670 nm for the same NCs, recorded under a pulsed laser excitation at 532 nm. The excitation intensity was 0.5 mW cm^{-2}, the absorbance 0.13 OD at 532 nm for all samples. The measurement conditions were kept unchanged between pristine and 9-ACA functionalized samples so as to enable quantitative comparison between the respective PL intensities and dynamics.

functionalization, not only the PL lifetime shortened from $\tau_{Au-PL}^{OA} \sim 177$ ns to $\tau_{Au-PL}^{9-ACA} \sim 80$ ns with a $\Phi_{ET'} = 55\%$, but more importantly the zero-delay intensity drop was only $\eta \sim 0.82$, resulting in a global ET$'$ efficiency $\Phi_{ET'}^{G} = 45\%$. Since the intragap levels introduced by Au impurities are higher in energy than the 9-ACA HOMO level and being the hole localization on these levels more favorable than hole trapping, the probability to transfer the bound excitons and the fraction of NCs active for the sensitization process increase.

4.3 Optimization of energy resonance

Despite the notable enhancement of the global ET′ efficiency provided by the insertion of Au impurities in the NCs host with respect to undoped NCs, the performance of ET′ was still rather low. In fact, it is desirable to have an ET′ efficiency close to unity, especially for solar applications where it is crucial to transfer each exciton stored in the NCs. The low ET′ efficiency observed is the result of the unmatched energy resonance between the NCs bound excitons and the 9-ACA triplet excitons, that influences the Dexter energy transfer efficiency. The energy transfer is therefore efficient only for those NCs where the bound excitons are more energetic than the 9-ACA triplet state (1.83 eV),[141] so the process is exothermic. Conversely, for those NCs that do not have the right energetics the dopant-mediated emission dominates, resulting in the slow long-time tail in the decay in Figure 4.4d. Because the Au^+ states are pinned to the host VB, a straightforward strategy to tune the energy of the bound excitons to maximize the energy resonance consists in controlling the NCs size, taking care to fulfill the condition $\Delta E_{VB-Au} > \Delta E_{VB-HOMO}$. To probe this scenario, I considered smaller Au:CdSe NCs, with diameter of 2.3 nm, in toluene with optical density 0.13 at 532 nm. Since

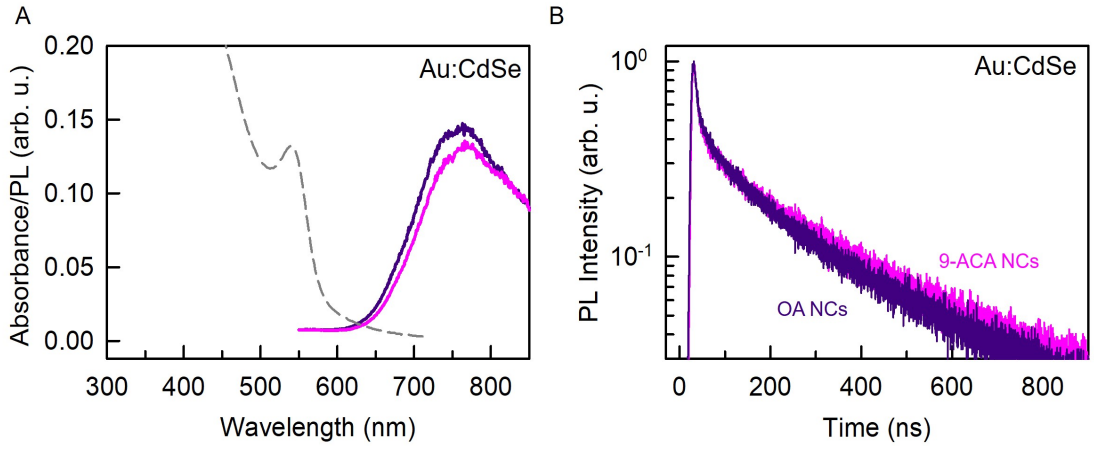

Figure 4.6: Absorption spectrum (dashed line) of Au-doped NCs functionalized with 9-ACA, in toluene. The solid lines are the PL spectra of the OA-capped (dark blue) and 9-ACA-capped (light blue) Au-doped NCs, recorded under a cw 460 nm excitation. The doped NCs have a diameter of 2.85 nm. (b) PL intensity decay at 770 nm for the same NCs, recorded under a pulsed laser excitation at 532 nm. The excitation intensity was 0.5 mW cm^{-2}, the absorbance 0.13 OD at 532 nm for all samples. The measurement conditions were kept unchanged between pristine and 9-ACA functionalized samples so as to enable quantitative comparison between the respective PL intensities and dynamics.

the energy bandgap is now wider, the 1S absorption peak is shifted at higher energies, peaked at $\sim$ 490 nm as shown in Fig. 4.5a, which also reports the PL spectrum of the NCs capped with the native OA ligands (dark blue curve), peaked at $\sim$ 670 nm ($\sim$ 1.91 eV). Looking at the change in cw PL intensity upon functionalization with 9-ACA ligands (light blue curve), the suppression of the residual Au-mediated PL is almost entirely complete. Consistently, because of ET$'$ the Au-mediated PL lifetime is reduced as illustrated in Fig. 4.5b, from $\tau_{Au-PL}^{OA} \sim$ 153 ns to $\tau_{Au-PL}^{9-ACA} \sim$ 4 ns with a $\Phi_{ET'} \sim 97\%$. Moreover, I did not observe any drop of the zero-delay PL intensity ($\eta \sim$1), meaning that the entire NCs population undergoes efficient ET$'$ instead of hole transfer and that the efficiency of the triplet sensitization is maximized. For this tailored system I obtained the notable global ET$'$ efficiency $\Phi_{ET'}^{G} \sim 100\%$, which is 50-fold greater than in the undoped counterpart and it is the highest value reached for hybrid sensitizers based on semiconductor NCs. It is worth stressing that these exceptional results stem from the advantages and versatility offered by the inherent properties of NCs -photophysical properties tunable through size control- in combination with the proposed doping strategy, that allows to manipulate the NCs photophysics.

I obtained a last instructive proof of the validity of the strategy proposed from the investigation of bigger NCs, with diameter $\sim$ 2.85 nm, to verify the effects of the minimization of the spectral resonance between the bound excitons and the 9-ACA triplet excitons. Figure 4.6 reports the cw spectra under cw 532 nm excitation (panel a) and the Au-PL time decays at 770 nm recorded under pulsed 532 nm laser excitation for doped NCs with native OA ligands and functionalized with 9-ACA. Importantly, the limited zero-delay intensity drop confirms that the condition $\Delta E_{VB-Au} > \Delta E_{VB-HOMO}$ is still properly satisfied, being VB = -6.1 eV from Eq. 3.2. But NCs with these features are not good sensitizers of the ligands triplet states. In fact, since both the cw spectra and kinetics remain almost unaffected by functionalization, only a minor fraction of NCs with the proper energetics can transfer the excitons to the ligands, with inefficient ET$'$ ($\Phi_{ET}^{'} = 12\%$).

4.4 *s*TTA-UC efficiency with optimized hybrid doped sensitizers

To probe more into detail the ability of hybrid sensitizers to sensitize the emitter triplets and the effects of the new hole-routing strategy on the upconversion efficiency, I investigated the

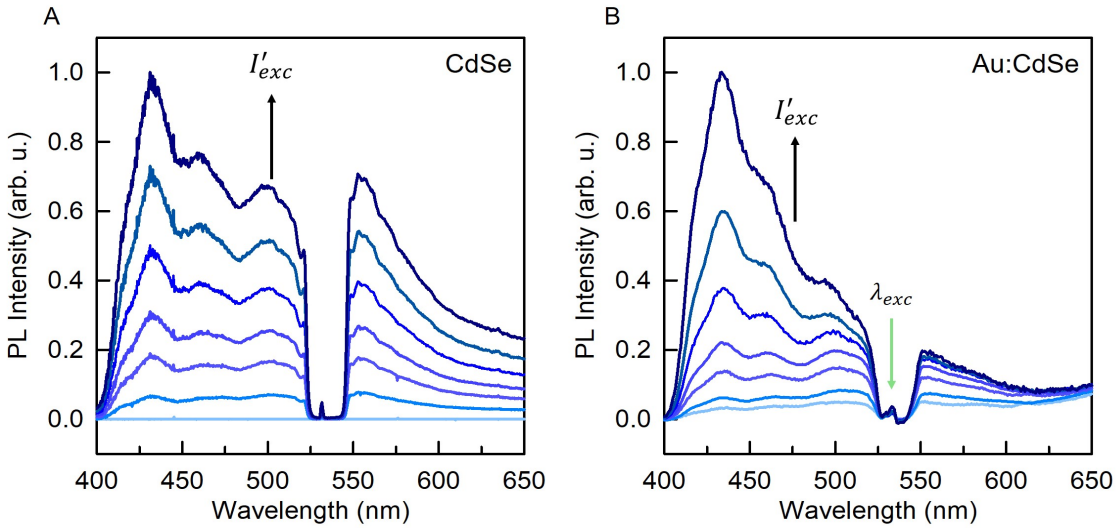

Figure 4.7: (a,b) PL spectra of the undoped CdSe (a) and Au:CdSe (b) NCs functionalized with 9-ACA in toluene with DPA (10^{-2} M) under a cw excitation at 532 nm as a function of the absorbed excitation intensity I'_{exc}. The laser stray light (λ_{exc}) was removed with a notch filter. The doped NCs employed have a diameter of 2.3 nm.

UC performances of a system composed of the optimized Au-doped NCs (i.e. with diameter 2.3 nm) decorated with 9-ACA, coupled with 9,10-diphenylanthracene (DPA, 10^{-2} M) in toluene. DPA was chosen as emitter as it is one of the best molecular annihilators/emitters for green-to-blue *s*TTA-UC,[32,33,35] with almost unity fluorescence efficiency. Moreover, the DPA triplet state is at 1.77 eV,[141] meaning that the ET$''$ process from 9-ACA to DPA is exothermic and favorable. To highlight the effects of the hole-routing strategy, I compared side-by-side the UC performances of an upconverting solution based on undoped NCs and of an upconverting solution based on doped NCs, with the same composition. In such a way, the difference in the global UC efficiency is only set by the efficiency of the sensitization process. To probe the upconverted PL (UC-PL), I selectively excited only the sensitizers at 532 nm, well below the DPA energy gap, therefore the DPA excited singlet states cannot be directly populated through photon absorption. Figure 4.7 illustrates the UC-PL intensity under increasing cw laser excitation intensity for the upconverting solutions with undoped (panel a) and doped (panel b) sensitizers. The spectra feature the emission profile of DPA peaked at 433 nm, and a residual emission from the NCs. The spectra were normalized to the residual intensity of the excitation laser, removed with a notch filter, to emphasize the incremental growth of the UC-PL over the residual NCs emission. A first important consideration directly arising from

the spectra is the different relative weight between the UC-PL and the residual NCs PL in the two samples. When I employed undoped NCs as harvesters, the NCs residual emission was extensive, almost comparable with the UC-PL even under high excitation intensities. This behavior is a direct consequence of inefficient triplet sensitization, caused by the hole trapping affecting undoped NCs as seen in Sec. 4.2, which lowers the UC efficiency. On the contrary, in the doped counterpart under the same excitation conditions the UC-PL is drastically dominant, as expected for the optimized sensitizers where almost the entire exciton population is transferred to the 9-ACA. Since the TTA is a bimolecular process, its efficiency depends on the competitiveness between the two emitter triplet decay channels, i.e. the spontaneous decay and annihilation, which is determined by the density of triplet states T_E available in the system. Therefore, the absorbed excitation intensity ($I'_{exc} = \alpha(\lambda_{exc})I_{exc}$) sets the ratio between the triplet spontaneous decay rate k_T and the TTA rate ($k_{TTA} = \gamma_{TT}T_E$) where I can express the triplet density as

$$T_E = I'_{exc}\Phi^G_{ET'}\Phi_{ET''} \tag{4.4}$$

defining two excitation regimes. In the low excitation regime ($k_T \gg k_{TTA)}$, the probability that two emitter triplet excitons collide within their lifetime is so low that they mainly decay via nonradiative spontaneous recombination and the TTA efficiency

$$\Phi_{TTA} = \frac{k_{TTA}}{k_{TTA} + k_T}$$

is proportional to the excitation intensity. Conversely, in the high excitation regime ($k_T \ll k_{TTA}$) the availability of triplet excitons is so large that their annihilation is highly probable before spontaneous recombination. This different behavior can be easily seen when measuring the time decay of the delayed UC emission in the two regimes. In this regard, Figure 4.8 shows the decay kinetics of the UC-PL (I_{uc}) under a modulated 532 nm laser excitation at high (dark blue, 10 W cm^{-2}) and low (light blue, 0.3 W cm^{-2}) excitation intensity. The kinetics are described by Eq. 1.16 and are orders of magnitude slower (on a μs timescale) than DPA prompt fluorescence with a lifetime of $\sim$ 8 ns in toluene,[307] and this behavior is a clear confirmation of the DPA excited singlets sensitization via TTA. Moreover, in the low power regime where $\Phi_{TTA} \ll 1$, Eq. 1.16 can be approximated with $I_{uc} \propto e^{-2k_T t}$, consistently with the single exponential decay observed under 0.3 W cm^{-2}, since the triplets populating the emissive DPA excited singlets preferentially decay via the spontaneous recombination channel. Fitting the experimental data with a single exponential function (red line in Fig. 4.8), I obtained $k_T = 6.8$

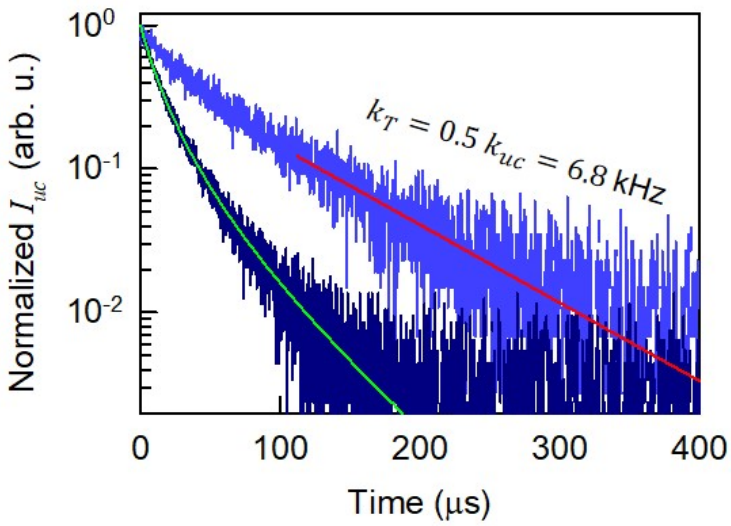

Figure 4.8: Upconverted PL intensity decay at 430 nm of the upconverting system based on doped NCs, recorded under a modulated 532 nm laser excitation at two different excitation intensities, 0.3 W cm^{-2} (light blue) and 10 W cm^{-2} (dark blue). The red line is the fit with a single exponential function of the long-time emission tail at low power, while the green line is the fit according to Eq. 1.16

kHz. By fitting the second decay with Eq. 1.16 (green curve) I obtained a TTA efficiency $\Phi_{TTA} = 90\%$ as expected for the high excitation intensity employed, that allows to pump efficiently the triplets population.

To have more accessible indications about the quality of the doped upconverting system I introduce the two *s*TTA-UC figures of merit, UC efficiency QY_{uc} and the threshold excitation intensity I_{th}. The QY_{uc} can be expressed as

$$\begin{aligned} QY_{uc}(I_{exc}) &= \frac{1}{2} f \beta \eta \Phi_{ET'} \Phi_{ET''} \Phi_{TTA}(I_{exc}) \\ &= \frac{1}{2} f \beta \Phi^{G}_{ET'} \Phi_{ET''} \Phi_{TTA}(I_{exc}) \end{aligned} \tag{4.5}$$

which differs from the definition given in Sec. 1.5.1 in the terms β and η, because the NCs considered here are not ideal. From the previous definition of the parameter η, $(1 - \eta)$ is the hole-transfer mechanism efficiency, while β is an empirical factor that gives the fraction of bright NCs in the ensemble. In fact, in unpassivated, core-only NCs, ultrafast quenching mechanisms can easily instantaneously switch off a fraction of NCs, most probably because of electron trapping in surface defects.[305] By using DPA as emitter the maximum QY_{uc} achievable is 50% as the statistical spin factor f is 0.5.[53] It is also useful to highlight the dependence of I_{th} on the parameters characteristic of the upconverting system. I adapted Eq. 1.13 to take into

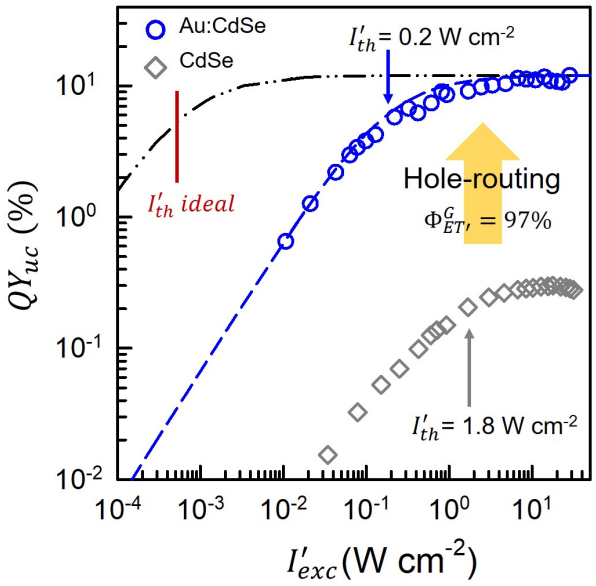

Figure 4.9: Upconversion quantum yield, QY_{uc}, as a function of the absorbed excitation intensity I'_{exc} at 532 nm. The dashed line is the theoretical value of QY_{uc} versus I'_{exc} calculated according to Eq. 4.5. The vertical arrows mark the excitation intensity threshold values using doped (blue arrow) or undoped (gray arrow) CdSe NCs as light harvesters. The dash-dotted line represents the theoretical QY_{uc} curve assuming the emitter triplet lifetime equal to 2 ms. The red vertical line highlights the corresponding theoretical threshold.

account the influence of the β and η factors in setting the triplets population, obtaining

$$I_{th} = \frac{(k_T)^2}{\alpha(\lambda_{exc})\beta\eta\gamma_{TT}\Phi_{ET'}\Phi_{ET''}} \tag{4.6a}$$

$$I_{th} \propto \frac{1}{\Phi^{G}_{ET'}} \tag{4.6b}$$

Importantly, since both figures of merit inherently depend on $\Phi^{G}_{ET'}$ -one linearly, the other inversely-, a quantification of the beneficial effects of the doping strategy can also be drawn from the comparison of the QY_{uc} dependency on the absorbed excitation intensity I'_{exc} for the doped and undoped systems. It is worth stressing that the comparison between different samples needs to be carried out considering the absorbed excitation intensity instead of the excitation intensity itself, to determine what are the differences in the UC performance given the same initial excited states density. For the same reason, when comparing the performance of different systems, the meaningful information comes from the absorbed threshold intensities $I'_{th} = \alpha(\lambda_{exc})I_{th}$.

The two trends are illustrated in Figure 4.9, and they both follow the typical behavior of a

bimolecular process: the QY_{uc} depends linearly on I'_{exc} through the Φ_{TTA} term under low excitation intensities, while it loses its dependence on I'_{exc} at high excitation intensities where it reaches its maximum value achievable, that I measured following a relative method (see Sec. 2.7), using a solution of rhodamine 6G (10^{-5} M, in ethanol) as standard with known emission efficiency (94%).[308] Notably, when employing the optimized doped sensitizers I measured the unprecedented value of $QY_{uc} = 12 \pm 1\%$, which is almost 40 times higher than the value measured with undoped sensitizers ($QY_{uc} = 0.3 \pm 1\%$). This exceptional result not only is the maximum upconversion efficiency reported so far for systems based on hybrid sensitizers, but also straightforwardly validates the proposed exciton manipulation strategy to drive the stored energy from NCs to triplet acceptor ligands, as the increment observed in the QY_{uc} aligns well with the enhancement of $\Phi^{G}_{ET'}$. Consistently, the effective suppression of the non-radiative hole transfer channel also reflects on the excitation threshold, which decreases from $I'_{th} = 1.8$ W cm^{-2} in the undoped system to $I'_{th} = 0.2$ W cm^{-2} when using the optimized doped sensitizers, thanks to the boosted triplet sensitization ability. Also, the experimental data acquired in the doped system (blue dots) are well reproduced by Eq. 4.5 (dashed blue curve) with the emitter fluorescence quantum yield of 90% in toluene,[309] Φ''_{ET} equal to unity in the rapid diffusion limit for the employed emitter concentration[227] and a β factor ~ 0.63. This result infers that about $\frac{2}{3}$ of the NCs in the ensemble are bright and active for the overall upconversion process, in agreement with previous results.[278]

Finally, to highlight the potential of the proposed hybrid sensitizers for future applications in solar devices, I applied the model presented in Eq. 4.5 considering an ideal system, where the sensitizers have the same properties of the optimized doped NCs discussed so far, but assuming to employ an emitter with an ideal triplet lifetime of 2 ms. In fact, given the I'_{th} dependence on the square of k_T (Eq. 4.6a), the emitter triplet lifetime strongly influences when the system enters the regime of maximum efficiency, therefore it is instructive to estimate which performances could be reached in an ideal system. Thereby, the theoretical behavior, reported in Fig. 4.9, is reproduced by the black dash-dotted curve. A triplet lifetime on this timescale could be achieved by choosing a better solvent or inserting the upconverting moieties in a proper polymer matrix able to protect the triplets from deleterious quenching channels. Interestingly, in this way the theoretical threshold, marked by the vertical red line, would be lowered below the AM1.5 solar irradiance.

4.5 Conclusions

In summary, I demonstrated a novel strategy to boost the efficiency of hybrid *s*TTA upconversion systems by using electronic-doped semiconductor NCs as light harvesters to populate the long-lived triplet states of surface-attached conjugated organic moieties. The key aspect of this design is the controlled introduction of a hole-accepting state associated with the electronic dopant within the NC forbidden gap that rapidly routes the photohole to an energy above the HOMO level of the organic ligand. This allows to completely suppress excitation losses by nonradiative hole-transfer that is a detrimental parasitic process strongly limiting the efficiency of conventional NC-based sensitizers for *s*TTA-UC. Owing to their nearly 100% nanocrystal-to-ligand ET yield, the functionalized doped-NCs enabled to obtain an upconversion yield of 12%, representing the record performance for hybrid upconverters based on *s*TTA. I highlight that the strategy proposed here is not limited to the discussed system, but it can be applied to any hybrid sensitizer which requires tuning the band alignment between its constituents. As such, this approach can be translated to engineer narrower bandgap NCs and obtain upconverters from the near-infrared region that can be directly coupled to existing devices to recover sub bandgap photons. Indeed, the nanocrystal size, composition, shape and dopant species, as well as the energy-receiving moiety can in principle be adapted to rationally design multicomponent systems for upwards as well as for down-conversion photonic applications that require efficient energy transport across any interface without incurring into losses due to ultrafast carrier transfer, including photochemical synthesis, photoredox catalysis, and singlet oxygen generation for photodynamic therapy. For instance, the observed overall effect could be obtained by using different dopants, such as copper, in the same CdSe host. The copper *d*-states are positioned only 350 meV above the VB maximum, which leads to a smaller Stokes shift, enabling to employ larger NCs with a lower bandgap energy as light harvesters.

CdSe nanoplatelets as light harvesters

Quasi 2D semiconductor nanoplatelets (NPLs) functionalized with polycyclic aromatic hydrocarbons acting as triplet bridges have been recently proposed as triplet sensitizers in hybrid sTTA-UC systems. Here, I investigate the behavior of 5-monolayer CdSe NPLs decorated with 9-anthracene carboxylic acid (9-ACA) ligands and their potential as sensitizers for sTTA-UC. Unlike nanocrystals, nanoplatelets feature a peculiar flat geometry yielding defined crystal facets with specific terminating atoms and an increased number of binding sites available for the triplet acceptor ligands. Therefore, thanks to the intrinsic surface properties, functionalized NPLs are extremely less sensitive than nanocrystals to the zero-delay fluorescence quenching that stems from the ligand exchange procedure which typically introduces surface defects. Moreover, I investigated the nanoplatelet-to-ligand energy transfer dependence on the surface coverage degree. As expected, the transfer efficiency increases upon increasing the number of triplet acceptor ligands. The second important information obtained from this investigation is that the 9-ACA molecules bound to the NPLs flat surface tend to form some sort of ordered structure that results in a significant redshift of the 9-ACA energy levels. According to the emitter employed, back energy transfer from excited emitters to sensitizers can be promoted, with consequent reduction of the sTTA-UC performance. This study ultimately highlights the importance of the optimization of the ligand binding on the surface of colloidal semiconductor nanoplatelets and can serve as a guideline to design more efficient hybrid upconversion systems.

5.1 The rationale behind semiconductor nanoplatelets as light harvesters

As discussed in the previous Chapters, the application of *s*TTA upconversion is still hindered by the narrow absorption bandwidth of common organic sensitizers, which limits their spectral-harvesting capability of solar light. Several strategies have been introduced to address this issue, such as the use of multicomponent or multilayer systems exploiting sensitizers with complementary absorption properties, whereas colloidal semiconductor nanocrystals have been proposed as broadband-absorbing component of hybrid *s*TTA-UC sensitizers to overcome the intrinsic limitations of molecular photosensitizers. A further development in this direction has been recently introduced by VanOrman and coworkers, who employed as light harvesters a different class of semiconductor nanostructures, the quasi 2D semiconductor nanoplatelets (NPLs).[203] Interestingly, NPLs share the fundamental properties of nanocrystals related to quantum confinement, but offer at the same time some critical advantages. In NPLs, the charge carriers motion is confined in just one dimension along the NPLs thickness, which results in the density of states changing from discrete levels, typical of nanocrystals, to a step-like quasi-continuum in NPLs, with each step at an energy corresponding to the *n-th* transition between the heavy hole and the electron.[310–313] Because the quantum confinement is along only one dimension, the NPLs spectral properties depend only on their thickness, with thinner NPLs affording higher energy emission.[314] This feature allows to inherently avoid inhomogeneous broadening because NPLs can be synthesized with excellent monodispersity, with exceptional monolayer thickness purity ($> 95\%$).[315] Moreover, in semiconductor nanostructures, the shape anisotropy is an important parameter that influences the nanostructure photophysical properties. In fact, as a consequence of the low dielectric constant of the surrounding media, the strength of electron-hole Coulomb coupling is a function of the surface-to-volume ratio of the nanostructure, resulting in an increased exciton binding energy in 2D NPLs compared to nanocrystals.[310] The increased exciton binding energy results in an enhanced exciton oscillator strength, which in NPLs gives rise to the so-called giant oscillator strength transitions (GOST).[316–318] The GOST effect is related to the exciton centre of mass coherent motion extended within the 2D NPLs, with their peculiar flat platelike geometry. Important consequences of the GOST effects are shorter radiative decay times and enhanced absorption cross sections.[310,314] As such, NPLs show inherent features that po-

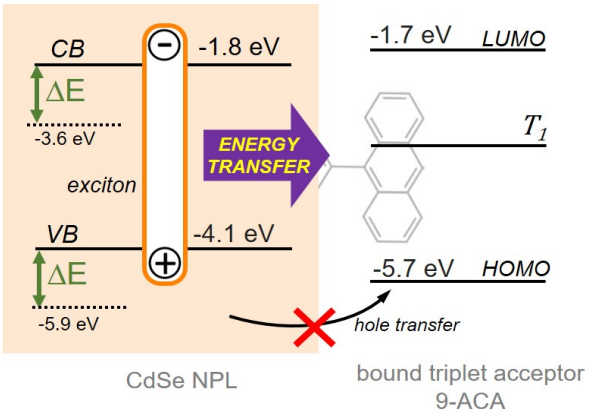

Figure 5.1: Sketch of the CdSe nanoplatelets (NPLs) electronic energies shift due to 9-ACA molecules attached to the surfaces, estimated from the results in Ref.[326]

tentially make them better light harvesters in comparison to the nanocrystals counterpart. They usually show exceptional fluorescence quantum yields, also $> 50\%$, in contrast with the value assessed around $\sim 10\%$ typical of the reference core-only nanocrystals used in hybrid *s*TTA upconversion studies.[211,310,319] Such high quantum yields help to circumvent energy loss pathways in interfacial triplet energy transfer caused by surface trap states.[165] Moreover, the stronger absorption oscillator strengths can help to boost the upconversion performance at low powers.[318,320]

Interestingly, Spittel et al. measured the absolute energy level positions with respect to vacuum for both 5 monolayers CdSe NPLs and 3.5 nm CdSe nanocrystals, detecting a great similarity between the two.[321] Therefore, by employing triplet acceptor ligands bound to the nanostructure surfaces, the ET efficiency from NPLs and nanocrystals to the triplet acceptors should be comparable. Still comparing CdSe NPLs and NCs, it is worth noting that while nanocrystals exhibit both (100) and (111) crystal facets on their surface, the NLPs surface raises mainly from their basal planes which only have (100) facets, that terminate with Cd atoms that can interact favourably with 9-ACA in the X-type fashion.[322–324] However, the (111) facets are neutral and are not able to bind directly to the 9-ACA COO- groups. These surfaces are typically passivated by an excess of metal ions, in the form of Z-type ligands ($M\text{-}X_2$),[325] but this layer was shown to be labile and can be easily displaced as a complex.[323] The removal of this layer can disrupt the passivation and reveal the midgap states associated to surface defects that act as fast recombination centers.[324] Thus the massive losses that limit the fluorescence efficiency of nanocrystals is also due to improper passivation of trap states, which can instead be inherently avoided with NPLs. Interestingly, Weiss et al. demonstrated that different ligands can induce a shift of the

NPLs absolute band energies without affecting the optical bandgap.[326] This effect can be therefore exploited as a tuning tool to keep the resonance with the ligand triplets while avoiding detrimental charge transfer processes due to improper alignment of the electronic levels. As shown in Fig. 5.1, according to literature, the common triplet acceptor 9-anthracene carboxylic acid (9-ACA) as ligands should induce a blue shift of the NPLs energies that should avoid hole transfer from the NPLs VB to the 9-ACA HOMO level, preventing the exciton disruption and maximizing the ET′ yield. The first example of hybrid sensitizers composed of CdSe NPLs

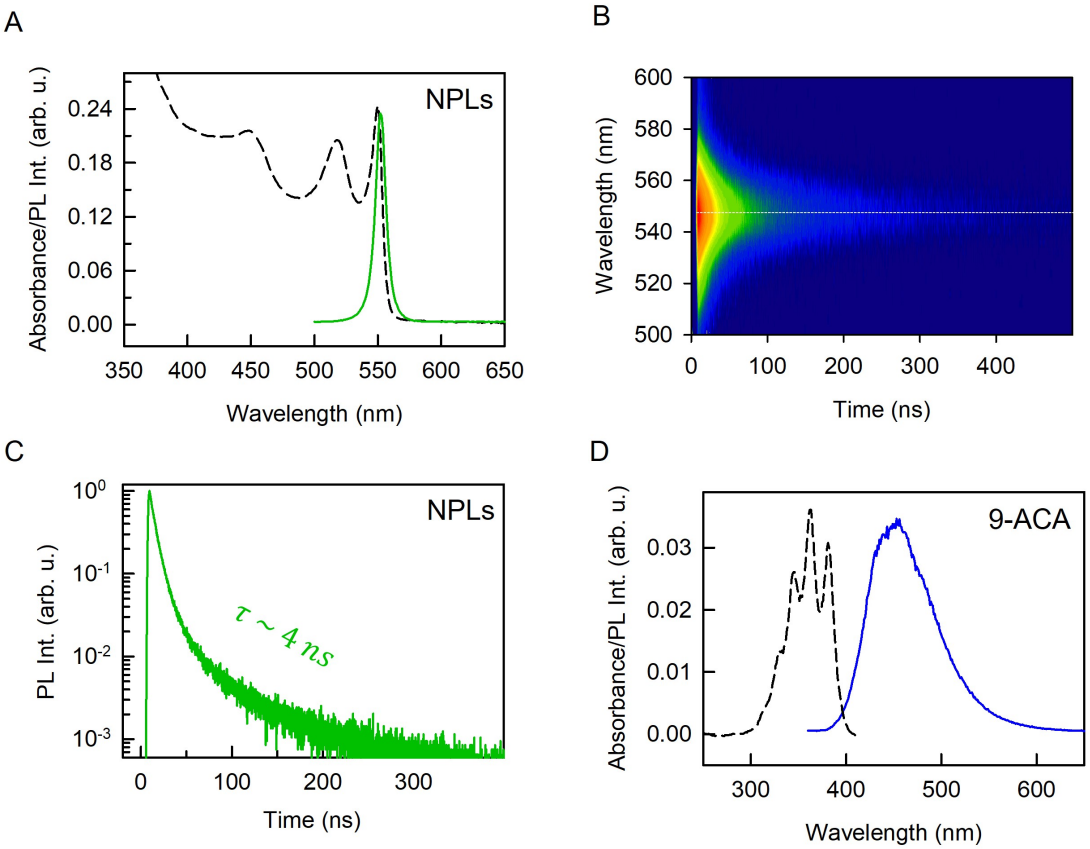

Figure 5.2: (a) Absorption (dashed line) and photoluminescence (PL, green line) spectra of pristine NPLs in hexane. The PL spectrum was acquired under a cw 510 nm excitation. (b) Contour plot of the spectrally resolved PL decay curves of NPLs in hexane recorded under pulsed 405 nm laser excitation (repetition rate 2 MHz). The dashed white line indicates the spectral position of the PL maximum at zero-delay time from the excitation pulse. (c) PL intensity decay at 555 nm of pristine NPLs in hexane under a pulsed 405 nm laser excitation (repetition rate 2 MHz). (d) Absorption (dashed line) and PL (blue line) spectra of 9-ACA in a solvent mixture of hexane, THF, toluene with ratio 80:15:70. The PL spectrum was acquired under a cw 350 nm excitation.

decorated by 9-ACA was reported by VanOrman et al.,[203] who demonstrated that their ability to perform *s*TTA upconversion when combined with 9,10-diphenylanthracene (DPA). The au-

thors obtained a good upconversion quantum yield QY_{uc} of 3%, comparable to typical values reported for nanocrystal-based sensitizers, but still far from the organic benchmark systems. Therefore, in this Chapter I investigate possible mechanisms and bottlenecks that limit the emitter triplet sensitization ability of hybrid sensitizers composed of CdSe nanoplatelets decorated with 9-ACA.

5.2 Photophysical properties of CdSe nanoplatelets

The 5-monolayer (5 ML) CdSe NPLs studied in this Chapter were synthesized as detailed in Sec. 3.2.2, with native myristic acid and oleic acid as stabilizing capping ligands. All the samples discussed in this Chapter were prepared in a glove box with oxygen concentration below 1 ppm and water concentration below 0.5 ppm, loaded in 1 mm quartz cuvettes, and sealed with hot glue and parafilm to prevent oxygen contamination. Figure 5.2a shows the absorption and photoluminescence spectra of a NPLs dispersion (1.4×10^{-7} M) in hexane, where the concentration was determined employing the well-established empirical relation between NPL size and absorption cross section.[327] The absorption profile, that I acquired according

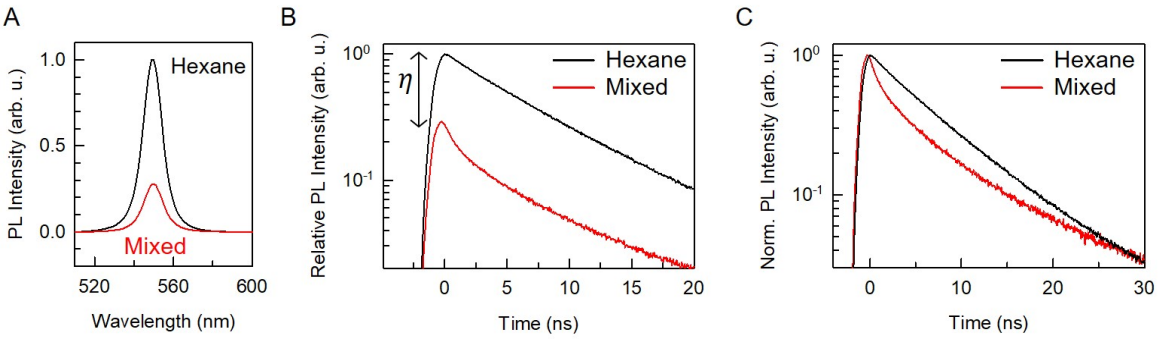

Figure 5.3: (a) PL spectrum of CdSe NPLs in hexane (black curve) and in the solvent mixture hexane, THF and toluene with ratio 80:15:70 (red curve), recorded under a cw 510 nm excitation. The two samples have the same optical density of 0.1 at the excitation wavelength. (b) PL intensity decay at 555 nm recorded under a pulsed 510 nm laser excitation (repetition rate 2 MHz) of the same samples. The parameter η highlights the zero-delay intensity loss appearing in the solvent mixture. Panel c reports the same kinetics but normalized to emphasize the exciton lifetime shortening in the solvent mixture.

to the method in Sec. 2.1, features the first excitonic peak at 550 nm due to the heavy hole-electron transition, in agreement with the NPLs thickness.[310,328] The PL spectrum, recorded under a cw 510 nm excitation, shows a bright peak at 552 nm, with two characteristics typical

of core-only NPLs.[310] The Stokes-shift between the first exciton peak in the absorption profile and the PL peak is almost null and the emission peak is extremely narrow, with a full width at half-maximum < 10 nm, associated to the sample's high monodispersity.[315] Panel b reports the contour plot of the spectrally resolved PL decay curves of NPLs recorded under pulsed 405 nm laser excitation, showing no spectral diffusion due to energy transfer or exciton migration, further validating the excellent NPLs monodispersity. The dashed white line indicates the spectral position of the PL maximum at zero-delay time from the excitation pulse. Panel c depicts the corresponding PL intensity decay at a single wavelength (555 nm), recorded under a pulsed 510 nm laser excitation, with an effective lifetime of 4 ns.[310] The native NPLs fluorescence quantum yield is $65\% \pm 10\%$ in hexane, that I measured following the relative method in Sec. 2.7, employing a solution of rhodamine B in ethanol as reference ($QY_{ref} = 70\%$).

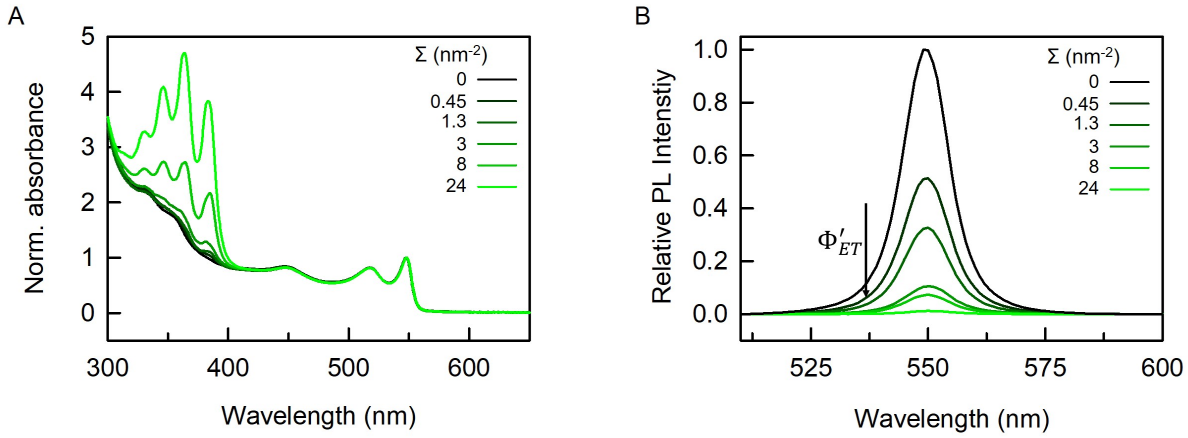

Figure 5.4: (a) Absorption profiles of pristine and decorated NPLs, normalized at the first excitonic peak, as a function of the nominal ligand density Σ. (b) Relative photoluminescence (PL) spectrum of CdSe nanoplatelets dispersions in the solvent mixture recorded under a cw 510 nm excitation as a function of Σ.

To decorate the NPLs with the triplet acceptor ligands 9-ACA, the native solvent was evaporated and the NPLs were re-dispersed in a solvent mixture of hexane, THF and toluene, with ratio 80:15:70, successively employed to dissolve 9-ACA for ligand exchange. The mixture composition was optimized to easily remove the native ligands and to favor the ligand exchange. To evaluate the solvent mixture effects on the NPLs photophysics, I performed cw and time-resolved photoluminescence measurements on pristine NPLs in hexane and in the solvent mixture. Figure 5.3 highlights the NPLs PL spectrum recorded under a cw 510 nm excitation (panel a) and PL intensity decay at 555 nm under a pulsed 510 nm laser excitation (panel

b and c), for pristine NPLs in hexane (black curves) and in the solvent mixture (red curves). Importantly, the pristine NPLs suffer from a strong reduction of the PL intensity, with an extensive drop (η) of the zero-delay intensity I_0 of about one order of magnitude (panel b), as well as an acceleration of the emission lifetime (panel c). This suggests the successful removal of the native capping ligands, because the surfaces are left unpassivated, resulting in the exciton quenching by ultrafast charge trapping.

The decoration of the NPLs surfaces was carried out following the procedure reported in Sec. 3.2.3, by varying the ratio between the NPLs and 9-ACA solutions to obtain the desired ligand density per NPL (Σ). Since Σ plays a key role in setting the ET$'$ rate and yield,[209] isothermal titration calorimetry (ITC) measurements were performed to estimate the amount of 9-ACA molecules per NPL, as previously discussed in Sec. 3.2.4. These measurements suggest that each 9-ACA introduced in the mixture binds to the NPLs until surface saturation, and the maximum ligand density achievable by considering a homogeneous surface coverage is $\Sigma = 1.4\ \mathrm{nm}^{-2}$.

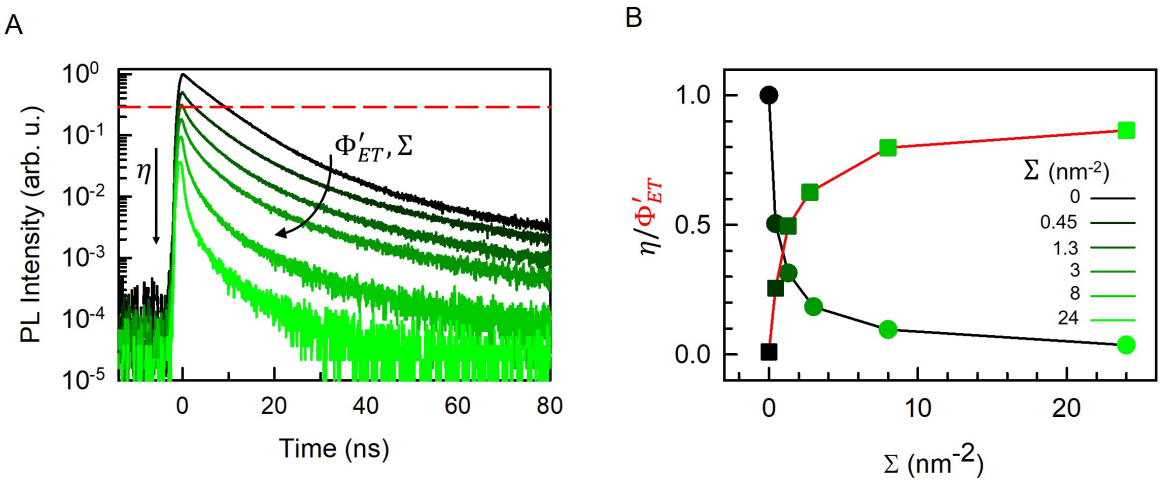

Figure 5.5: (a) Relative PL intensity decay at 555 nm recorded under pulsed excitation at 510 nm of the NPLs dispersions in the solvent mixture as a function of the nominal ligand density Σ (repetition rate 10 MHz). The red dashed line marks the zero-delay loss of PL intensity when pristine NPLs are moved in the solvent mixture employed for the ligands exchange. (b) Zero-delay intensity loss (η) and energy transfer efficiency (Φ'_{ET}) as a function of Σ derived from the experimental data in panel (a).

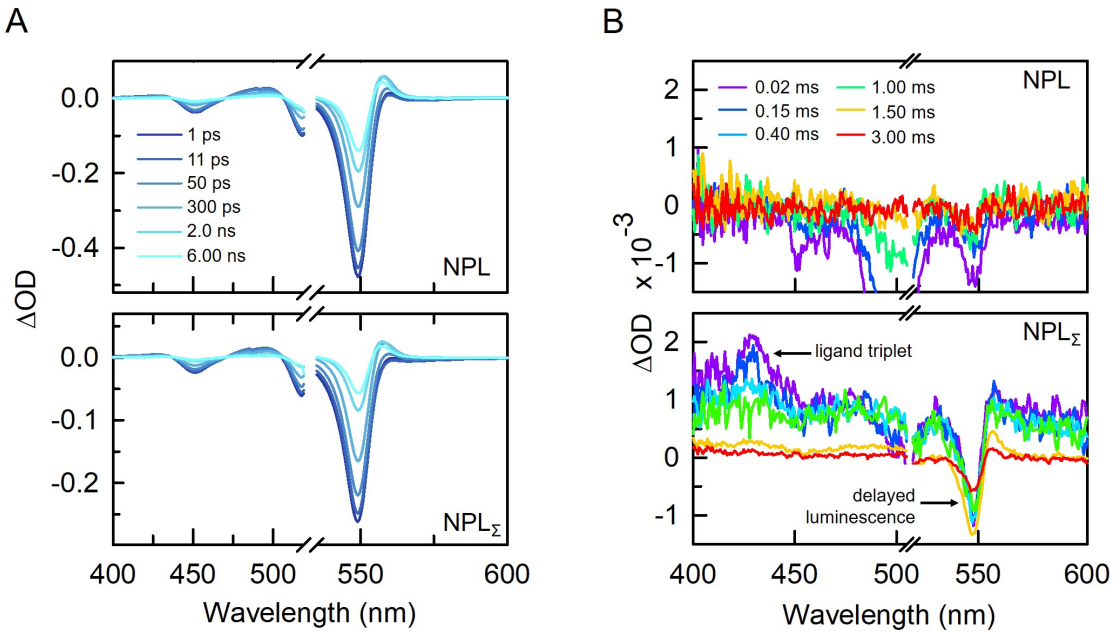

Figure 5.6: (a,b) Transient absorption (TA) spectrum on the nanosecond (a) and millisecond (b) timescale of pristine (top panel) and decorated (bottom panel) NPLs (NPL_{Σ}, $\Sigma = 24\,nm^{-2}$) under pulsed excitation at 510 nm (repetition rate 200 Hz).

5.3 Ligand density effects on the NPLs photophysics

To asses the effects of the ligand exchange procedure and of the ligand density Σ on the NPLs photophysics and ET$'$ dynamics I employed cw and time-resolved photoluminescence spectroscopy techniques on functionalized NPLs. To investigate the effects of ligand exchange, I prepared a series of NPLs samples with increasing 9-ACA density following the procedure in Sec. 3.2.3. Figure 5.4a depicts the absorption profiles of the sample series, normalized at the first exciton peak, to highlight the increasing 9-ACA contribution to the absorption spectrum. Panel b reports how the NPLs photoluminescence intensity is affected by Σ, under a cw 510 nm excitation. The reference PL spectrum of pristine NPLs refers to NPLs in hexane. For quantitative comparisons I performed the measurements under the same experimental conditions and I corrected the spectra for the different absorbance at the excitation wavelength. The PL intensity exhibits a progressive reduction upon increasing Σ, suggesting an increasing ET$'$ efficiency Φ'_{ET}, consistently with the increasing number of triplet acceptors.[329,330] Analogously, Fig. 5.5a shows the PL intensity decay at 555 nm recorded under a pulsed 510 nm laser excitation of the same sample series. The considerations about the measurements conditions and

spectra analysis apply here as well. Importantly, the time-resolved measurements allow to outline the processes involved in the emission quenching observed. With a nominal Σ = 0.45 nm^{-2}, which is insufficient to fully cover the NPL surfaces, I observed that the zero-delay intensity I_Σ is partially recovered with respect to the I_0 reduction observed for pristine NPLs in the solvent mixture (this I_0 reduction is represented as the horizontal dashed line in Fig. 5.5a). Also, the emission lifetime is slightly accelerated with respect to pristine NPLs suggesting the occurrence of ET$'$ towards the ligands.

By further increasing the amount of 9-ACA in the solution so to have Σ values beyond the nominal full coverage achievable, I observed a progressive acceleration of the exciton recombination dynamics, in agreement with an enhanced ET$'$ rate.[331] Defining the effective lifetime as when the PL intensity is reduced by a factor $^1/_e$, and employing the relation

$$\Phi'_{ET} = 1 - \frac{\tau_\Sigma}{\tau_0} \tag{5.1}$$

where τ_Σ and τ_0 are the effective lifetime of decorated NPLs with ligand coverage Σ and of pristine NPLs, respectively, the ET$'$ efficiency increases with Σ, and reaches the maximum value of 90% with $\Sigma = 24$ nm^{-2}, as highlighted by the red curve in Fig. 5.5b. Along with the

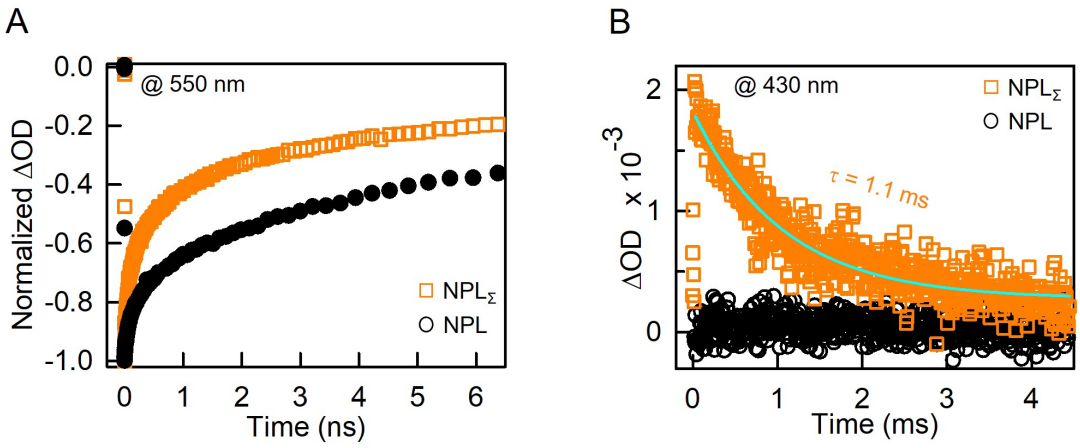

Figure 5.7: (a) Kinetics recorded at 550 nm from TA measurements on pristine NPLs (black dots) and on decorated NPLs with $\Sigma = 24$ nm^{-2} (NPL$_\Sigma$, orange squares) in the solvent mixture. (b) Kinetics recorded at 430 nm from TA measurements on the same samples. The solid line is the fit of experimental data with a single exponential decay function with characteristic lifetime $\tau = 1.1$ ms.

excitonic dynamics acceleration, the data also highlight a progressive reduction of I_Σ upon increasing Σ, which suggests the occurrence of ultrafast processes that reduce the fraction of NPLs able to sensitize the ligands triplets. As previously mentioned, a small amount of

9-ACA introduces a substantial recovery of the zero-delay loss affecting the pristine NPLs in the mixture solvent. This behavior suggests that the surface defects introduced by the native ligands removal promoted by the solvent mixture are partially passivated by 9-ACA. However, this recovery is not complete possibly because of the 9-ACA morphology. This ligand exhibits indeed a significantly larger steric hindrance in comparison to the native ligands, thereby, even if the native ligands removal is highly efficient, it is not possible to realize the same surface passivation with 9-ACA because of the larger size. Consequently, the surfaces are left partially unpassivated. The zero-delay loss arising with a given Σ can be quantified, similarly to Eq. 4.2, as

$$\eta = \frac{I_\Sigma}{I_0} \tag{5.2}$$

where I_Σ is the zero-delay intensity for the Σ considered and I_0 is the value in pristine NPLs. The η values for the Σ considered are reported in Fig. 5.5b (black curve).

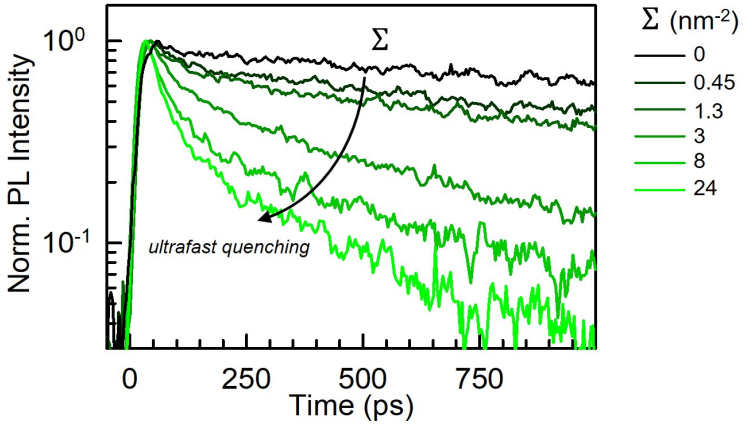

Figure 5.8: Time-resolved PL intensity of the NPLs dispersion series recorded at 555 nm under a pulsed laser excitation at 410 nm (repetition rate 76 MHz), as a function of Σ.

The effective occurrence of ET$'$ is further demonstrated by transient absorption (TA) experiments. Figure 5.6a shows the TA on a nanosecond timescale for a dispersion of pristine NPLs (top panel) and decorated NPLs with $\Sigma = 24$ nm^{-2} (NPL$_\Sigma$, bottom panel). No substantial differences are detectable in the wavelength-resolved spectrum, which is dominated by the NPL band-edge photoluminescence at 550 nm. Conversely, the NPL$_\Sigma$ kinetics at this wavelength reported in Fig. 5.7a shows an emission lifetime acceleration in agreement with the dynamics observed in the photoluminescence experiments previously discussed. On the other hand, in the milliseconds timescale the NPL$_\Sigma$ show an absorption feature peaked at 430 nm (Fig. 5.6b), absent in the pristine NPLs, which corresponds to the energy of the 9-ACA T_1-T_n transition.[141]

Moreover, the kinetics at 430 nm in Fig. 5.7b indicate an excited state lifetime of about 1 ms, in good agreement with the lifetime of the 9-ACA triplet state T_1.[141] These results demonstrate the occurrence of ET′ from the NPLs exciton to 9-ACA triplets essential for the *s*TTA upconversion process.

To assess if the zero-delay loss discussed in Fig. 5.5b can be ascribed to charge transfer processes from the NPLs to the ligands, I performed ultra-fast time-resolved measurements on the same sample series. The PL intensity decays at 555 nm recorded under a pulsed 410 nm ultrafast laser excitation are reported in Fig. 5.8. The hypothesis of charge transfer processes can be excluded because over a timescale of hundreds of picoseconds, characteristic of these processes in nanostructures, no significant quenching is observed.[301,303] This result is consistent with the predicted energy level shift induced by 9-ACA, that effectively prevents hole transfer from the NPLs VB to the 9-ACA HOMO level. However, because at the given Σ more than one

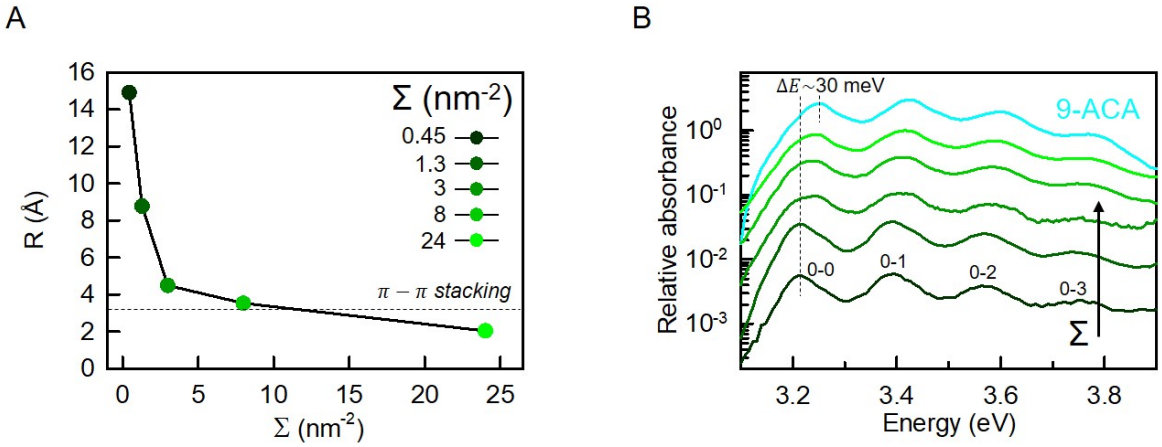

Figure 5.9: (a). Intermolecular distance R between ligands attached on the CdSe nanoplatelets as a function of the nominal surface ligands density Σ. The dotted horizontal line indicates the distance R = 3.5 Å at which the $\pi - \pi$ stacking interaction between two 9-ACA molecules is effective. (b) Absorption spectrum of the 9-ACA ligand in a diluted 10^{-6} M solution in the solvent mixture (light blue curve) and of the decorated NPLs dispersions as a function of Σ. The dotted vertical lines mark the energy of the 0-0 vibronic transition at the lowest coverage level ($\Sigma = 0.45$ nm^{-2}) and of the free molecule in solution.

ligand is attached to each NPL, ET′ should be complete. Moreover, by further increasing Σ, additional zero-delay losses appear, which lower η to 0.03 at $\Sigma = 24$ nm^{-2}, as demonstrated by the time-resolved data showed in Fig. 5.5b. These results suggest the appearance of additional exciton quenching processes with increasing efficiency at larger Σ occurring on a timescale

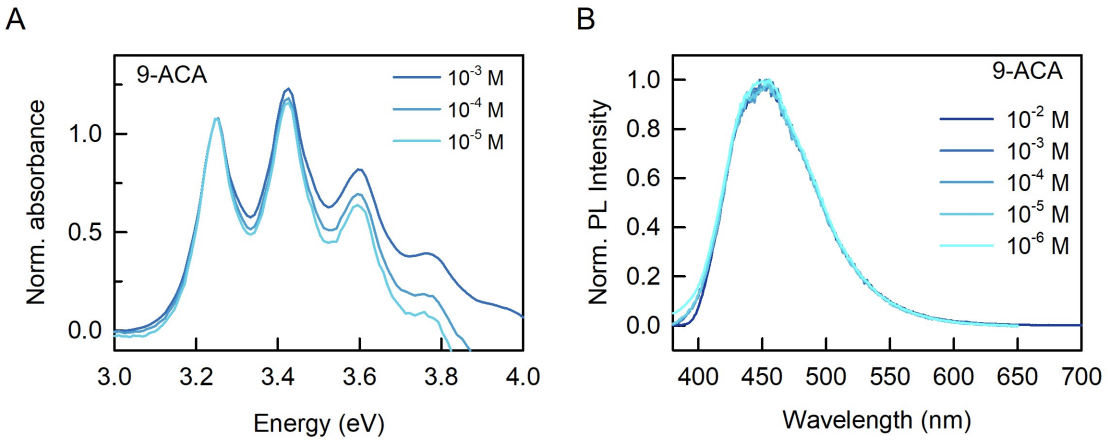

Figure 5.10: (a) Absorption spectra normalized to the low-energy replica of 9-ACA solutions in the solvent mixture at different concentrations, reported in the label. (b) Normalized PL spectra of a series of 9-ACA solutions in the solvent mixture at different concentrations, recorded under a cw 350 nm excitation.

too fast to be efficiently probed (tens of picoseconds).

5.4 Ligand stacking on the nanoplatelets surfaces

To shed light on the unexpected quenching observed at ultrashort times, I performed a series of absorption measurements on decorated NPLs. Figure 5.9a shows indeed the average intermolecular distance R between 9-ACA molecules bound to the NPLs surface estimated by considering the ligand exchange as a homogeneous process. The calculation shows that for $\Sigma < 3$ nm^{-2}, the R value is much larger than the $\pi - \pi$ stacking intermolecular distance ~ 35 $\mathring{A}$ typically observed between two anthracene moieties,[332] therefore the surface ligands should not interact for these Σ values. Conversely, for $\Sigma > 3$ nm^{-2}, the appearance of an interaction between the close packed anthracene units should be expected. Nevertheless, the absorption spectra of the decorated NPLs series reported in Fig. 5.9b suggest a different scenario. The absorption spectrum of a 9-ACA diluted solution in the solvent mixture is also reported as reference (light blue curve). Each spectrum features the vibronic replicas series typical of the anthracene core, due to the coupling of the electronic transition with C-H stretching modes. Importantly, the absorption peaks in decorated NPLs with $\Sigma \leq 1.4$ nm^{-2} are red shifted with respect to the free ligand of about 30 meV, which corresponds to the reorganization energy measured for anthracene molecules condensation by means of $\pi - \pi$ stacking.[27] At larger Σ

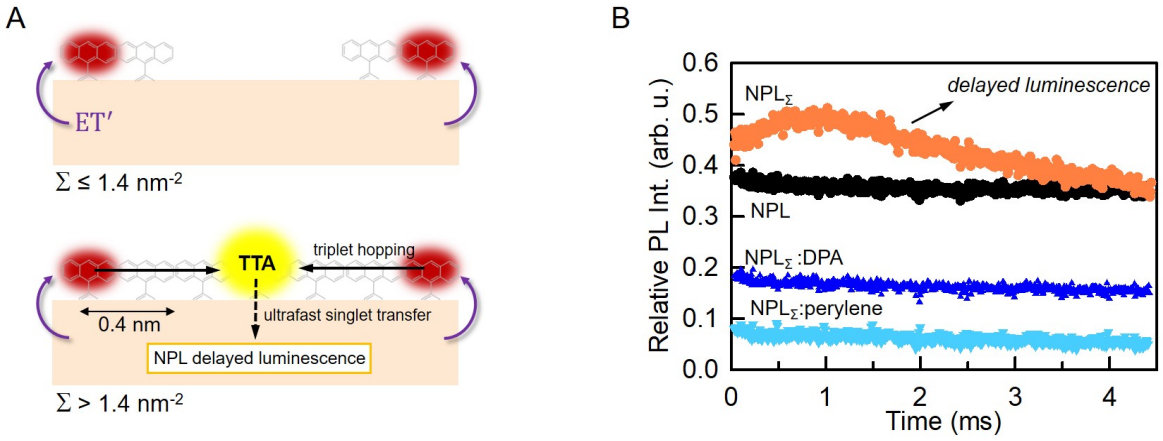

Figure 5.11: (a) Sketch of the decorated NPLs at low (top) and high (bottom) 9-ACA coverage level. In the high-coverage configuration, the close-packed ligands allow for diffusion of triplets generated by energy transfer (ET′), enabling TTA and the consequent delayed luminescence arising from back-energy transfer to the NPL of the upconverted singlets created by TTA among the close-packed ligands. (b) Kinetics at 550 nm of pristine NPLs, decorated NPL_{Σ} ($\Sigma = 1.3\ nm^{-2}$) and decorated NPLs in solution with emitters DPA (10^{-2} M) and perylene (2×10^{-3} M), respectively, under pulsed excitation at 532 nm (repetition rate 200 Hz) in the solvent mixture.

values, the absorption peaks become broader owing to the convolution of the spectra of both anchored and free ligands in solution, in agreement with the maximum coverage level achievable discussed previously. Therefore, these results suggest that the ligand exchange evolves in a island-like way, rather than being a homogeneous process. This leads to the formation of aggregates of 9-ACA molecules bound to the NPLs surfaces, as sketched in Fig. 5.11a. This finding allows to shed some light on the ET′ properties previously observed. At low Σ, the 9-ACA ligands are not uniformly distributed on the whole NPLs population, but rather bind preferentially on those NPLs with already a partial 9-ACA coverage. Thus a fraction of NPLs are not properly passivated and inefficiently sensitize the ligands triplets, as suggested by the low ET′ yield and the zero-delay loss shown in Fig. 5.5. At higher Σ, the average ET′ rate and yield on the decorated NPLs ensemble increase because more NPLs are effectively covered by more aggregated 9-ACA ligands that at some point form a layer of stacked molecules, as sketched in the bottom panel of Fig. 5.11a, while the ligands in excess remain in solution. To verify that the observed behavior is not related to 9-ACA aggregation in solution, I measured the absorption and PL spectra of a series of 9-ACA solutions in the solvent mixture at different concentrations. Since no difference is detected in the spectra over a wide concentration range,

it is safe to assume that the effects previously discussed are only due to the 9-ACA bound to the NPLs surfaces.

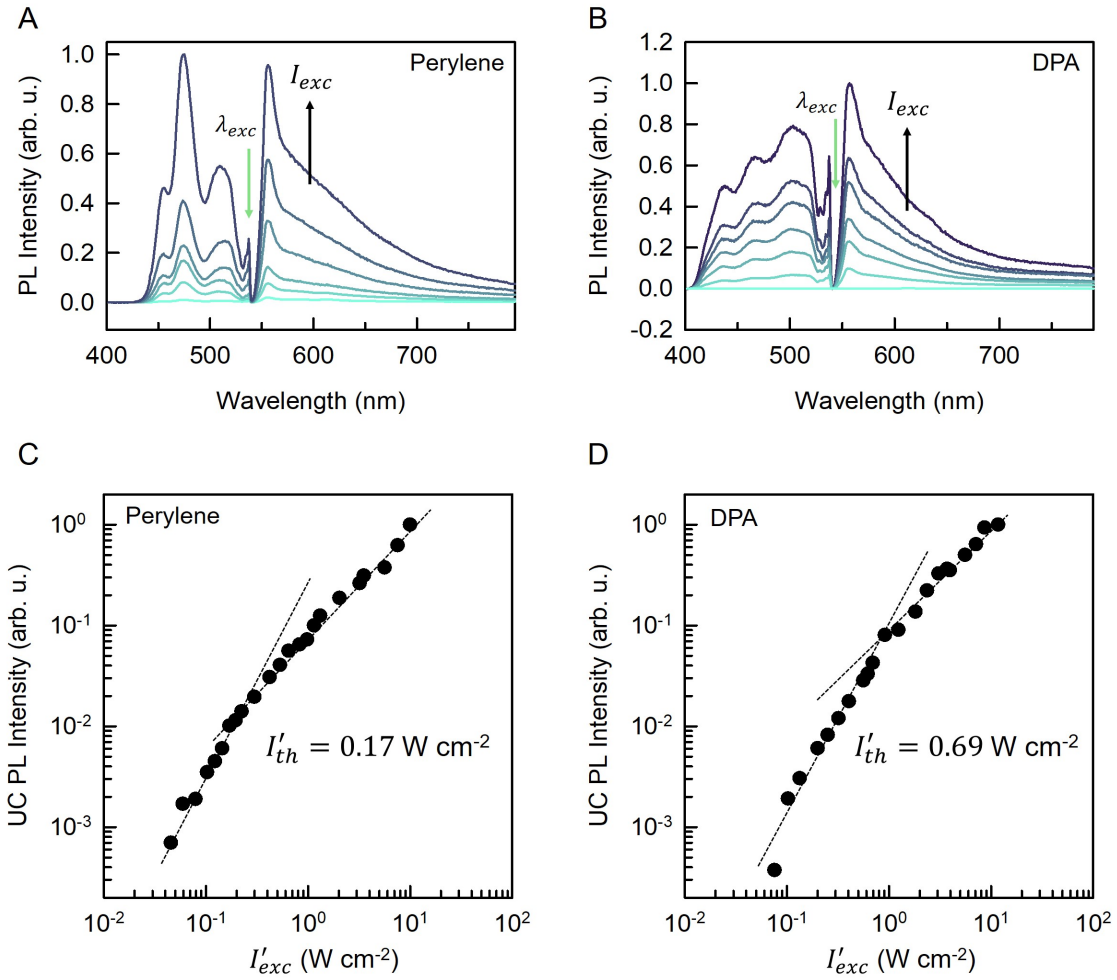

Figure 5.12: (a,b) PL spectra acquired as a function of the absorbed excitation intensity I'_{exc} of an upconverting system with CdSe NPLs with 9-ACA ($\Sigma = 24$ nm^{-2}) with optical density 0.1 at the excitation wavelength 532 nm and perylene (panel a) or DPA (panel b) as emitters, in the solvent mixture. The laser stray light was removed with a notch filter. Upconverted photoluminescence (UC PL) intensity as a function of I'_{exc} for the same systems (panel c for perylene, d for DPA). The dashed lines highlight the quadratic and linear trends (slope 2 and 1, respectively), crossing at the absorbed excitation threshold intensities I'_{th}.

The effects of this peculiar surface coverage are demonstrated by TA experiments reported in Fig. 5.11b, which shows the PL kinetics at 550 nm of decorated NPLs (orange curve) compared to the corresponding kinetics of pristine NPLs (black curve). Interestingly, upon decoration the NPLs exhibit a slow build-up of the emission followed by a slow and weak delayed fluorescence on the millisecond timescale. This delayed fluorescence suggests a slow diffusion of long

living triplets within the layer of stacked ligands allowing *in situ* TTA on single NPLs. In fact, the intermolecular distance between stacked anthracenes is small enough to allow the ligand triplet exciton diffusion within the 9-ACA ensemble on the NPLs surface. Therefore, if two triplet excitons are sensitized simultaneously on the same NPL, they can experience TTA and generate an upconverted high energy singlet state, which is promptly quenched by the NPLs through fast Förster ET given the ligand-to-NPL extreme vicinity and the complete energy resonance between the 9-ACA singlet and the NPL absorption. Conversely, no delayed emission is detected from pristine NPLs, and, remarkably, no delayed emission can be detected by coupling the decorated NPLs with two different emitters, DPA (dark blue curve) and perylene (light blue curve), able to deplete the ligand triplet population by ET$''$. Remarkably, this result demonstrates that the delayed fluorescence is directly related to the presence of unquenched ligand triplets on the NPLs surfaces. On the other hand, the presence of aggregates on the NPLs surface can also introduce quenching channels, which can be responsible of the additional ultrafast losses previously discussed. Further experiments are ongoing in this direction to assess further effects of the 9-ACA aggregates on the NPLs excitons properties.

5.5 Importance of the emitter selection

The performance of decorated NPLs as sensitizers for *s*TTA upconversion was tested in solution with two emitters, DPA and perylene. I employed two different emitters because the redshift of the ligand triplet energy observed can have crucial consequences on the choice of the emitter as it can affect the ET$''$ thermodynamic driving force. To avoid back-energy transfer and maximize the efficiency of the annihilating triplets sensitization, the ET$''$ should be exothermic, with the 9-ACA triplet slightly more energetic than the emitter.[139] To maximize the ET$'$ efficiency the upconverting solutions were prepared with the highest surface coverage ($\Sigma = 24$ nm^{-2}) and optical density 0.1 at the excitation wavelength of 532 nm. The emitter concentrations were chosen as high as possible compatibly with the molecular solubility in the solvent mixture, so 10^{-2} M for DPA and 2×10^{-3} M for perylene. Figure 5.12 shows the PL spectra (panel a and b) and the integrated upconverted PL intensity (panel c and d) that I recorded as a function of excitation intensity under a cw 532 nm laser excitation for the two systems (panels a-c are relative to perylene, panels b-d are relative to DPA as emitter respectively). The UC-PL vs absorbed excitation intensity I'_{th} trends exhibit the peculiar

quadratic-to-linear behavior expected for *s*TTA upconversion. But importantly, the absorbed excitation threshold intensity $I_{th}^{'}$ for the DPA-based system is 0.69 W cm^{-2}, four times higher than in the perylene-based system (0.16 W cm^{-2}). This implies that when employing DPA as emitter the system requires a greater amount of energy to efficiently start to upconvert. This different behavior can be ascribed to the triplet energy of DPA and perylene. In fact, at room temperature, the 9-ACA and DPA triplets are almost isoenergetic, considering the DPA triplet energy (1.77 eV)[141] and the energy difference of $\sim$ 30 meV that shifts the 9-ACA triplet energy from 1.83 eV to 1.80 eV,[141] and this has detrimental consequences on the net ET$^{''}$.[139] In fact, because back-energy transfer from excited DPA molecules towards the ordered ligands can easily occur, the number of emitter triplets that can annihilate decreases, resulting in an increased threshold intensity. Conversely, the perylene triplet energy is sufficiently low ($\sim$ 1.53 eV)[116,231] to prevent back energy transfer upon collision between excited perylene molecules and sensitizers.

5.6 Conclusions

In this Chapter, I demonstrated how CdSe NPLs decorated with proper conjugated hydrocarbons are promising candidates to work as hybrid sensitizers, offering many beneficial advantages over the more common semiconductor nanocrystals. These advantages are related to the inherent 1D confinement and to the NPLs peculiar surface properties. Since the NPLs expose the same crystal facets, high ligand coverage can be achieved, with beneficial effects for fast and efficient energy transfer. Isothermal titration calorimetry measurements allowed to study in detail the binding of 9-ACA to the NPLs surfaces and the maximum coverage achievable. Interestingly, I observed that NPLs surfaces are less sensitive to ligand exchange than nanocrystals, since the (100) crystal facet exposed by NPLs favors the ligand attachment without introducing surface defects that can act as deleterious nonradiative recombination centers. The thorough investigation of the energy transfer dependence on the surface coverage degree highlighted that, consistently with what already observed with nanocrystals, the transfer efficiency increases by increasing the number of ligands per NPL. But importantly, owing to the NPLs flat surface and the 9-ACA planar structure, the 9-ACA molecules attached to the NPLs surfaces can interact forming some ordered structure similar to anthracene crystals. The formation of these structures induces a redshift of the 9-ACA energy levels with respect to the

free ligands in solution, which can affect the energy resonance between ligand and emitter triplets and thereby the ligand-to-emitter energy transfer efficiency. As a result, according to the emitter employed, back-energy transfer from excited emitters to sensitizers can take place, reducing the *s*TTA-UC performance. This problem can be mitigated by using emitters with lower triplet energy, to preserve the thermodynamic driving force necessary for efficient forward energy transfer, or by introducing some bulkiness in the ligands structure to prevent their interaction. The results of this study highlight the importance of the optimization of the ligand binding on the nanoplatelets surface and can serve as a guideline to design more efficient hybrid upconversion systems based on semiconductor nanoplatelets.

Nanophase-separated glassy polymers

Upconversion sensitized by triplet–triplet annihilation proved to be remarkably efficient at low excitation intensities in solution, but becomes relatively ineffective in solid matrices since the typically limited molecular diffusion hinders the bimolecular interactions underpinning sTTA-UC. An open challenge for the translation of sTTA-UC to the solid-state, crucial for the development of real-world solar devices, is the realization of efficient solid-state upconverters that not only exhibit long-term stability but also are compatible with industrial fabrication processes. Here, I report nanophase-separated polymers that contain upconverting dyes in liquid nanodomains well-separated from the rigid phase, and that can be easily synthesized under ambient conditions. The nanostructured polymers fabricated show excellent optical quality, the notable upconversion efficiency of $\sim$ *23* $\%$*, and excellent stability in air, with only a limited performance reduction over a time span of three months. Moreover, the ability to confine the upconverting dyes in liquid domains of size* $<$ *50 nm translates in an increased effective local density of chromophores that enables hopping-assisted energy transfer and TTA and allows to activate the peculiar confined sTTA kinetics that enhances the material performance at low powers.*

6.1 Design and fabrication of nanophase-separated glassy polymers

It has been thoroughly demonstrated that *s*TTA-UC can be highly effective in environments like low viscosity solvents, because the large molecular diffusivities make energy transfer (ET) and triplet-triplet annihilation (TTA) extremely efficient, as discussed in Sec. 1.7. Nevertheless, solid materials are better suited for integration into technologically useful devices, but

the realization of solid-state upconverting materials that display high efficiency, low excitation threshold and good long-term stability, and which can be manufactured in a technologically exploitable manner, is still an open challenge. One of the main problems typically faced when the upconverting dyes are incorporated in solid matrices is that the bimolecular processes are typically hindered because of low molecular mobility.[236] To address this issue, several approaches have been explored to develop efficient solid-state upconverters, such as upconverting nanoparticles, macromolecular self-assemblies, dye doped polymers, organic glasses, and gels.[22,75,79,89,90,144,145,247,260,261,333–337] Each approach has its own advantages but also drawbacks, and it is still challenging to combine all the features requisite for a system to be technologically appealing, i.e., high chromophore density, oxygen protection, high upconversion efficiency, long-term stability, tunable mechanical properties, and easy and economical fabrication. Recently, nanophase-separated polymers composed of a glassy matrix and a liquid upconverting phase were proposed as an attractive platform to create solid-state *s*TTA-UC materials,[262] characterized by the *in-situ* formation of a phase-separated architecture featuring a liquid upconverting phase within a solid, cross-linked polymeric matrix. The liquid phase, stabilized by a surfactant, was based on a non-polar solvent in which the upconverting dyes were dissolved, while the polymer matrix was formed by polar monomers and optionally a cross-linker. This class of solid upconverters exhibited intriguing properties. The liquid nature of the upconverting phase yielded indeed a high upconversion efficiency, whereas the polymer matrix provided rather effective oxygen protection. However, they displayed a limited stability in both the idle condition and under irradiation.

To circumvent these limitations, rational modifications were developed upon the speculation that the upconversion efficiency decrease over time was at least partially related to dyes degradation owing to reactions with trapped residues (such as oxygen, unreacted monomers and initiators),[338,339] morphology instability, and/or slow evaporation of the somewhat volatile solvent (1-tert-butyl-3,5-dimethyl benzene) that was used to form the liquid phase.[262] Therefore, following a systematic investigation to determine how the various components influence the material properties, the initiator system, surfactant, solvent and plasticizer were replaced, and an oxygen scavenger was incorporated. Figure 3.3 illustrates the molecular structures of the moieties employed to fabricate the new upconverting nanophase-separated polymers, produced following the protocol in Sec. 3.3.1. The novel redox initiation system employed was inspired by microbiocidal mechanisms observed in immune cells, which pro-

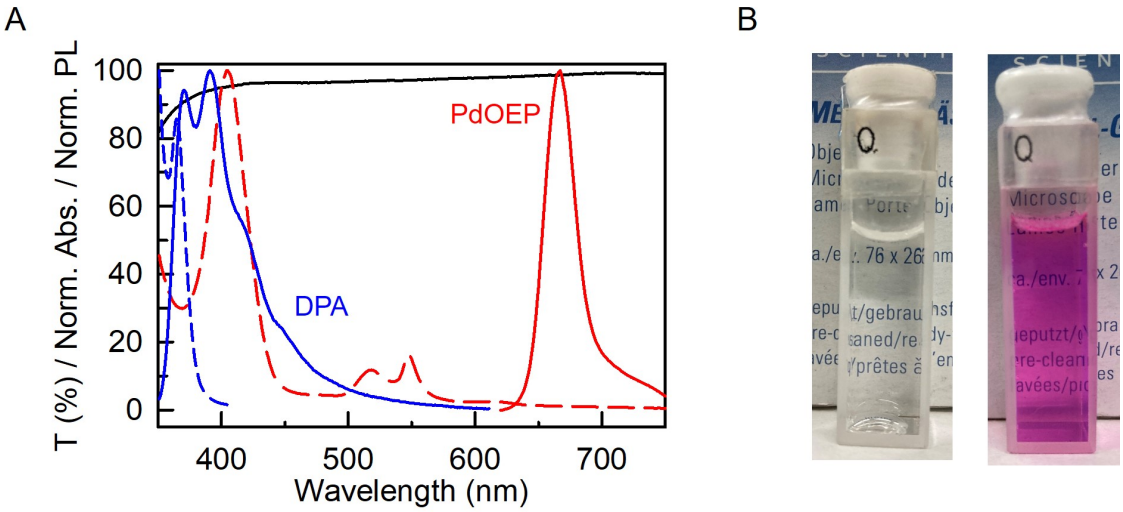

Figure 6.1: (a) Transmission spectrum of a dye-free nanophase-separated polymer sample (solid black line) superimposed to the absorption (dashed lines) and photoluminescence (PL, solid lines) spectra of the upconverting dyes employed, Pd(II) octaethylporphyrin (PdOEP, red) as sensitizer and 9,10-diphenylanthracene (DPA, blue) as annihilator/emitter in butyl benzoate. (b) Digital pictures of the dye-free nanophase-separated polymer (left) and of the upconverting DPA:PdOEP nanophase-separated polymer (right).

duce HOCl and HOBr by an enzyme-catalyzed reaction of the corresponding halides with biosynthetic H_2O_2. The hypohalous acids then react with heteroatomic species present in the biological medium, especially thiols, and generate unstable halogenated intermediates that dissociate into radicals at room temperature.[340,341] Under the assumption that this framework allows to carry out the polymerization under ambient conditions and that it affords relatively inert residues, halides (the counter-ion of the cetyltrimethylammonium surfactant) and methacrylic acid as proton source in the polymerization mixture were employed to generate radicals *in-situ* by sequentially adding H_2O_2 and a thiol to initiate the polymerization reaction. 2-mercaptoethanol was chosen as reducing agent, as it afforded transparent glasses when employing cetyltrimethylammonium bromide (CTAB) or chloride (CTAC) as surfactant/halogen source. A mixture of the hydrophilic monomers methacrylic acid (MAA, 13% w/w), 2-hydroxyethyl methacrylate (HEMA, 53% w/w) and triethylene glycol dimethacrylate (TEG-diMA, 3.5% w/w) was used to form the cross-linked, glassy polymer matrix upon free-radical polymerization. Butyl benzoate (BuBz) was selected as hydrophobic solvent, since solvents with higher boiling points occasionally provoked macrophase segregation. The system that yielded the highest upconversion photoluminescence (UC-PL) intensity was established

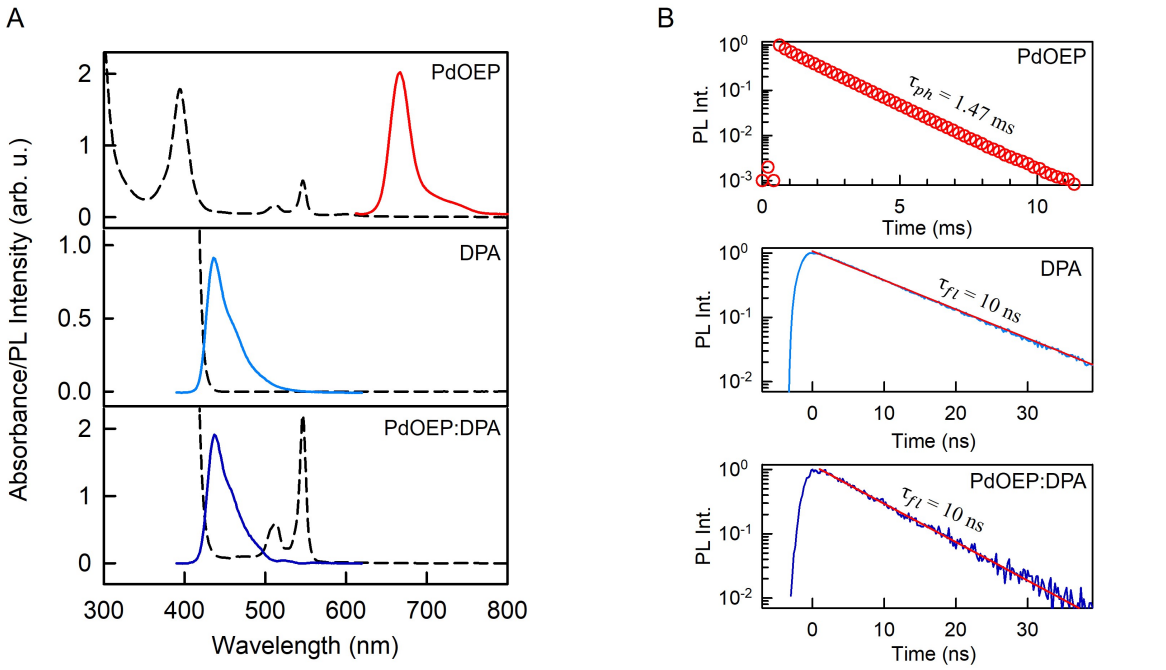

Figure 6.2: (a) Absorption (dashed lines) and photoluminescence spectra (solid lines) of the PdOEP (2×10^{-5} M, top), DPA (1.5×10^{-2} M, middle) and DPA:PdOEP (1.5×10^{-2} M : 8×10^{-5} M, bottom) nanophase-separated polymers. The PL spectra were recorded under cw excitation at 532 nm for the PdOEP sample and 380 nm for the samples containing DPA. (b) Top: time-resolved phosphorescence intensity at 670 nm of the reference PdOEP polymer under pulsed excitation at 532 nm, with characteristic lifetime τ_{ph}. Middle, bottom: fluorescence intensity decay at 435 nm under a pulsed 405 nm excitation, with characteristic lifetime τ_{fl} of the reference DPA sample (middle) and of the upconverting DPA:PdOEP sample (bottom). The solid lines are the fitting curves of the experimental data with single exponential decay functions.

empirically, using the well-known *s*TTA-UC sensitizer/emitter pair Pd(II) octaethylporphyrin (PdOEP) and 9,10-diphenylanthracene (DPA), and a combination containing triethylene glycol (15% w/w), BuBz (10% w/w) and CTAC (5% w/w). The nominal dye concentrations were 2×10^{-5} or 8×10^{-5} M for PdOEP and 1.5×10^{-2} M for DPA considering the total volume of the polymers composition and assuming a density of 1 g mL^{-1}. Dimethylthiomethane (DMTM, 0.5% w/w) was also incorporated in the mixture to act as a sacrificial oxygen scavenger,[342,343] yielding a notable improvement of the UC-PL stability. Figure 6.1a demonstrates the excellent optical quality of the proposed polymers by the transmission spectrum of a dye-free sample (black line), superimposed to the absorption (dashed lines) and photoluminescence (PL, solid lines) spectra of the upconverting dyes employed, PdOEP as sensitizer (red) and DPA as an-

nihilator/emitter (blue), in BuBz. In the visible spectral region between 400 and 700 nm, the dye-free sample with 1 cm optical path displays an average transmittance $> 90\%$, suggesting that the light scattering is negligible. The exceptional optical quality of the material is also demonstrated by the digital pictures (panel b) of the dye-free glassy polymer (left) and of the DPA:PdOEP upconverting glassy polymer (right).

As reported in Sec. 3.3.3 the polymers have a glass transition temperature (T_g) of 50-52 °C, regardless of the presence of BuBz in the sample. This T_g independence of the introduction of BuBz suggests the coexistence of a rigid matrix well-separated from the liquid phase containing the solvent, rather than being mixed together. A strong confirmation of the presence of multiple phases was obtained by means of time-domain NMR experiments. The proton magnetization relaxation measurements reported in Figure 3.6a show a bi-component relaxation dynamics indicative of the coexistence of a mobile and a rigid phase.[287,288,344] The analysis of spin diffusion experiments sets the average diameter of the mobile domains, assumed to be spherical for simplicity, at $\sim$ 38 nm.[345] Importantly, a rough estimation based on the liquid-to-rigid feed ratio sets the liquid volume to 10% of the total volume.

6.2 Photophysical properties at room temperature

In this section, I illustrate the photophysical properties of the newly developed nanophase-separated glassy polymers, that I investigated by means of cw and time-resolved spectroscopic measurements. For comparative studies, I considered green-to-blue DPA:PdOEP upconverting nanophase-separated polymer (1.5×10^{-2} M : 8×10^{-5} M), the corresponding reference polymers containing either DPA (1.5×10^{-2} M) or PdOEP (both 2×10^{-5} M and 8×10^{-5} M), as well as a reference solution of DPA:PdOEP (10^{-2} M : 8×10^{-5} M) in BuBz. All the samples considered were loaded in quartz Suprasil cuvettes with 1 cm optical path. Figure 6.2a reports the absorption spectra, performed following the method in Sec. 2.1, and photoluminescence spectra of the PdOEP, DPA and DPA:PdOEP nanophase-separated polymers. Panel b illustrates the intensity decay of the photoluminescence emission acquired at the PL peak for each sample. In the green spectral range, the samples containing the sensitizer feature the porphyrin characteristic absorption Q-band peaked at 540 nm (top and bottom panels). In the UV-blue region, the DPA molecules' absorption saturates over 3 OD at wavelengths shorter than 400 nm (middle and bottom panels). This confirms that in the DPA:PdOEP sample both

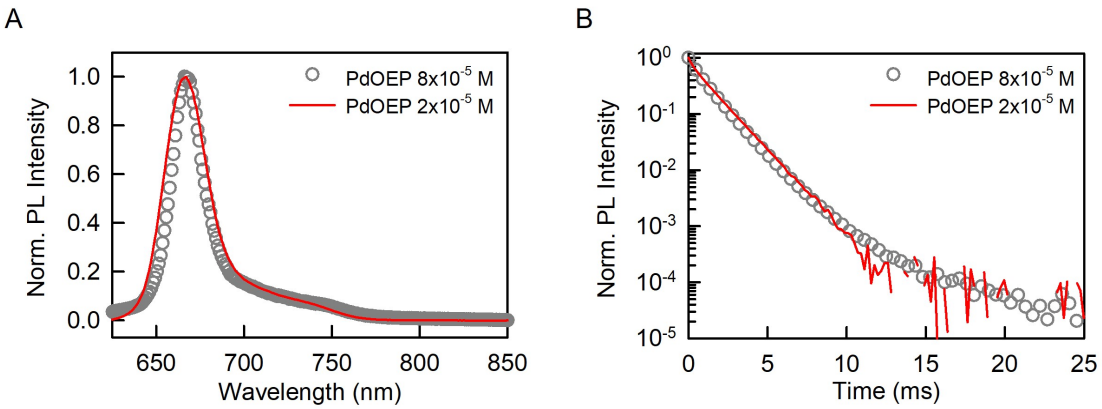

Figure 6.3: (a) PL spectrum of the reference PdOEP nanophase-separated polymers with porphyrin concentration 2×10^{-5} M (red curve) and 8×10^{-5} M (grey-dotted curve) PdOEP, acquired under cw 532 nm laser excitation. (b) Time-resolved PL intensity at 670 nm of the same two samples, acquired under pulsed 532 nm excitation.

dyes are effectively included in the host. Upon excitation at 532 nm, the PdOEP reference sample exhibits the typical red phosphorescence (red-PL) peaked at 670 nm, which decays as a single exponential with characteristic lifetime $\tau_{ph} = 1.47$ ms (panel b, top). The single exponential behavior suggests that these molecules experience a homogeneous environment meaning that there is only negligible partitioning between the segregated phases.[28] To assess these features I tested a PdOEP sample containing a small amount of sensitizer (2×10^{-5} M) to record the entire absorption spectrum without any saturation, whereas in the upconverting material the amount of PdOEP was increased for adequate absorbance at the excitation wavelength and to draw an accurate quantitative analysis of the upconversion performances. To investigate whether the analyses performed on the upconverting sample could be affected by possible contributions from sensitizer-sensitizer quenching or other concentration-dependent quenching mechanisms, I also probed a reference PdOEP sample with the same porphyrin concentration employed in the upconverting sample (8×10^{-5} M). As shown in Fig. 6.3, the porphyrin emission and lifetime remain unchanged in the high concentration sample, therefore the presence of quenching pathways competitive with energy transfer can be excluded. This is also confirmed by the average intermolecular distance between two porphyrins, that can be calculated as the diameter d of the sphere centered on a PdOEP molecule:

$$d = 2 \times \sqrt[3]{\frac{1[cm^3]3}{C_{local}4\pi}} \sim 16nm \tag{6.1}$$

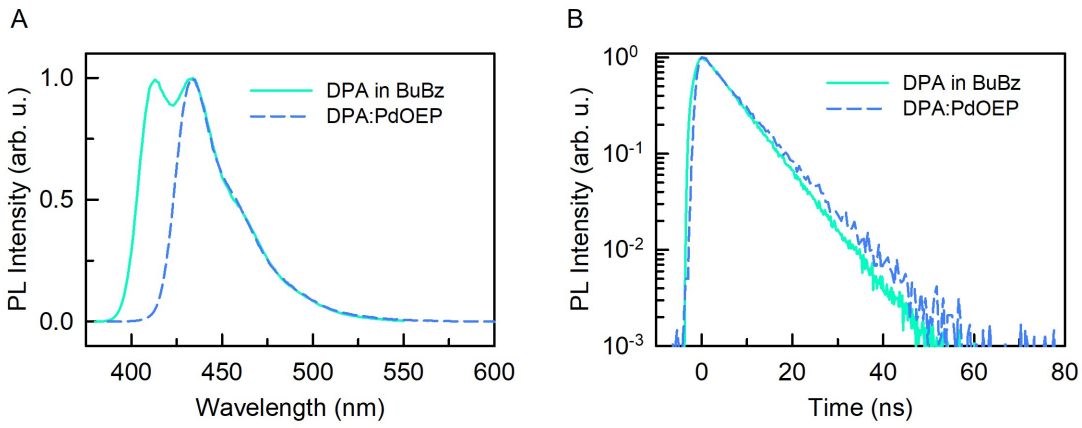

Figure 6.4: (a) Fluorescence emission spectrum of DPA in a reference dilute solution in BuBZ (DPA concentration 10^{-4} M, light blue curve) and UC-PL spectrum in the DPA:PdOEP polymer (blue curve), recorded under a cw 380 nm and 532 nm excitation, respectively. (b) DPA prompt fluorescence intensity decay at 433 nm, recorded under a pulsed 405 nm laser excitation, in the same two systems.

where C_{local} is the effective PdOEP concentration considering that the sensitizers accumulate preferentially in the liquid domains (*vide infra*), i.e. in 10% of the total volume according to the initial liquid-to-rigid feed ratio, thus $C_{local} = \frac{C_{PdOEP}}{0.1} = 8 \times 10^{-4}$ M. The intermolecular distance between two PdOEP molecules is so large to exclude deleterious interactions between excited sensitizers.

The DPA reference and the DPA:PdOEP upconverting polymer both exhibit a bright emission (blue-PL) peaked at 433 nm upon excitation at 380 nm matching the DPA fluorescence,[307] with characteristic decay time $\tau_{fl} = 10$ ns. Also this emission behaves as a single exponential function demonstrating the absence of partitioning for the emitter molecules as well. Figure 6.4a reports the comparison between the DPA fluorescence emission spectrum in a dilute solution in BuBZ (DPA concentration 10^{-4} M, light blue curve) and the UC-PL in the DPA:PdOEP polymer (blue curve), recorded under a cw 380 nm and 532 nm excitation, respectively. The UC-PL spectrum is identical to that of DPA in BuBz solution, except for the change in shape at high energies due to partial self-absorption. I also looked for possible variations in the DPA excited state lifetime. In this regard, Fig. 6.4b shows the DPA prompt fluorescence intensity decay at 433 nm, recorded under a pulsed 405 nm laser excitation, of the same two systems. The corresponding lifetimes are comparable, just slightly longer in the polymer consistently with self-absorption. Figure 6.5 illustrates the DPA prompt fluorescence decay in polymers with different DPA and PdOEP concentrations. Regardless of the system's composition, no

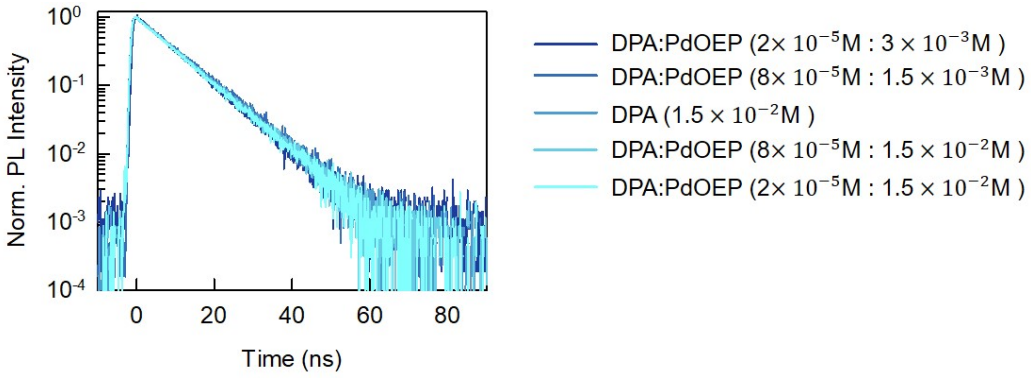

Figure 6.5: Time-resolved PL intensity at 433 nm of a series of nanophase-separated polymers with different sensitizer/emitter concentrations recorded under pulsed excitation at 405 nm (repetition rate 5 MHz). Independently of the sample composition, the DPA fluorescence intensity decays as a single exponential function with characteristic lifetime $\tau_{fl} \sim 10$ ns.

significant variation in τ_{fl} can be detected, therefore it is safe to exclude efficient parasitic deactivation channels due to the high amount of emitters employed or to the coexistence of PdOEP and DPA molecules, such as back-energy transfer from DPA singlets to sensitizers, despite the partial resonance between the DPA fluorescence and PdOEP absorption potentially can allow a Förster-type ET. In fact, the low sensitizer concentration sets the average intermolecular distance between DPA and PdOEP molecules to $\sim$ 16 nm (Eq. 6.1), about 5 times the Förster radius (3.1 nm) calculated on the basis of the PdOEP-DPA spectral overlap. Even considering the DPA singlet diffusion length of about 3.2 nm (calculated with Eqs. 1.28 and 1.33 from the BuBz viscosity of 2.7 cP at room temperature and from the DPA effective molecular radius of 0.45 nm)[41] back ET can be neglected. Importantly, as the PdOEP and DPA photophysical properties in the reference polymers do not significantly differ from those in BuBz, the synthetic procedure enables to localize the upconverting dyes primarily only in the liquid domains.

Figure 6.6a illustrates the behavior of the reference PdOEP sample and of the upconverting DPA:PdOEP sample upon cw laser excitation at 532 nm. The reference sample exhibits an intense red-PL (red curve), while the DPA:PdOEP upconverting polymer displays bright blue upconverted photoluminescence (UC-PL) peaked at 433 nm (blue curve). I compared the integrated red-PL intensity from the PdOEP sample (I_0) and the residual integrated red-PL (I) in the upconverting DPA:POEP sample in the presence of emitters, corrected for the sample absorbance at 532 nm (OD 0.25 and 0.08, respectively), obtaining an ET yield $\Phi_{ET} = 1 - \frac{I}{I_0} = 96\%$.[28] Also, Figure 6.6b reports the normalized kinetics of the red-PL emission at 670 nm in

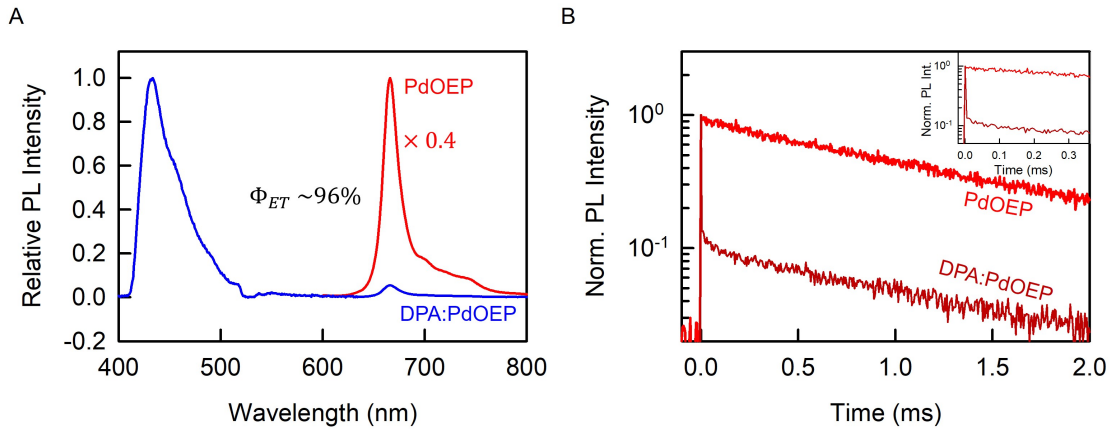

Figure 6.6: (a) Photoluminescence spectrum recorded under a cw 532 laser excitation of the DPA:PdOEP upconverting polymer (blue curve) and of the reference PdOEP polymer (red curve), rescaled for the different absorbance. The PdOEP curve was scaled for clarity. (b) Photoluminescence intensity decay recorded at 670 nm under a pulsed 532 laser excitation of the DPA:PdOEP upconverting polymer (dark red curve) and of the reference PdOEP polymer (red curve). The inset is a magnification of the first 300 μs to emphasize the recombination dynamics acceleration in the upconverting polymer owing to fast ET.

the two samples, acquired under pulsed 532 nm laser excitation. The time decay of the residual red-PL intensity in the upconverting polymer is bi-exponential, and about 95% of the emission is quenched promptly on a time scale faster than 10 μs, due to fast ET to DPA triplets, confirming the high ET efficiency obtained from steady-state measurements. But more interestingly, correlating the data acquired in cw experiments and the analysis of the time-resolved PL spectra provides information about the upconverting molecules location in the host. The residual red-PL kinetics shows indeed also a negligible secondary slow component with a lifetime of 1.55 ms, which suggests that a small fraction of sensitizers are incorporated in the rigid polymer, where ET is suppressed.[346] It is worth stressing that these results indicate that almost all the PdOEP molecules are included and mixed with the emitters in the liquid domains, where ET and TTA can take place.[225]

6.3 Temperature effects on bimolecular processes

I gained further interesting insights into the dyes arrangement within the polymer through temperature-dependent photoluminescence experiments. As already pointed out in Fig. 6.6b, at room temperature the cw PL spectrum of the DPA:PdOEP upconverting polymer recorded

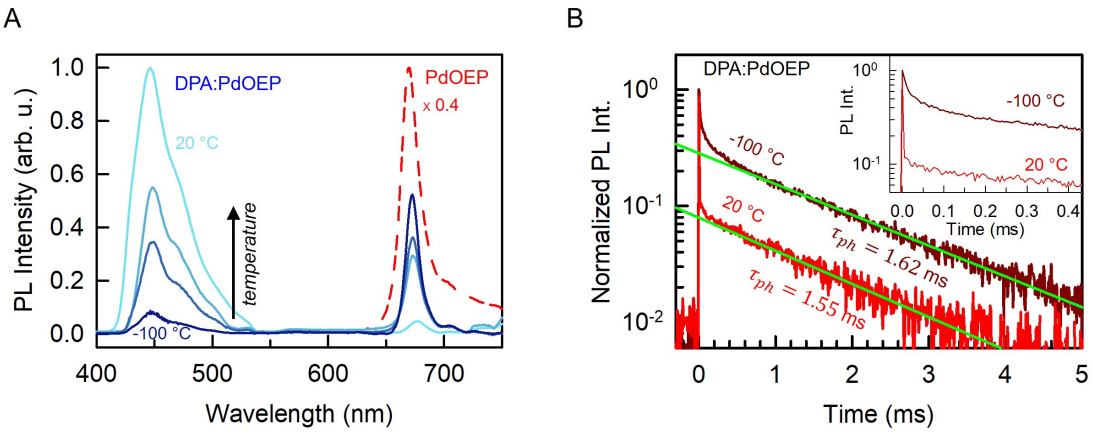

Figure 6.7: (a) PL spectra of the DPA:PdOEP upconverting polymer under cw laser excitation at 532 nm (3 W cm^{-2}) as a function of temperature (20 °C, 5 °C, -20 °C, -100 °C). The dashed line is the PL spectrum of the PdOEP reference polymer under the same excitation conditions at 20 °C. The spectra were corrected to account for the different sample absorbance. (b) Time-resolved PL intensity at 670 nm of the DPA:PdOEP upconverting polymer recorded under a pulsed laser excitation at 532 nm (repetition rate 10 Hz) at 20 °C (red curve) and -100 °C (dark red). The solid lines are the fitting curves of the long-time emission tails with a single exponential decay function. The inset highlights the first $\sim$ 400 μs of the temporal window explored.

upon excitation at 532 nm is dominated by UC-PL with negligible residual red-PL. Upon cooling the sample to -100 °C, well below the melting temperature of BuBz of -22 °C,[347] I observed a reduction of the UC-PL intensity by one order of magnitude, while the red-PL intensity experienced a 7-fold increase, indicating a reduction of the ET yield to $\sim 10\%$, as reported in Fig. 6.7a. On the contrary, in the upconverting BuBz reference solution, the UC-PL almost disappeared when cooled to -100 °C as reported in Fig. 6.8a, and the upconverted emission could only be detected at extremely high excitation intensities. Conversely, the sensitizer phosphorescence intensity grew of almost two orders of magnitude as a consequence of the complete ET inhibition upon solvent crystallization.

It is worth pointing out that the fact that the upconverting polymer is able to perform *s*TTA-UC even at low temperatures is ascribed to the effective dyes confinement in nanosized domains, because the intermolecular distance becomes as short as $\sim$ 2 nm at least for a fraction of molecules, enabling both ET and TTA without contributions from molecular translational diffusion. This description is in agreement with the estimated average intermolecular distance between DPA molecules of $\sim$ 2.6 nm calculated considering the increased DPA concentration $\sim 1.5 \times 10^{-1}$ M (Eq. 6.1) obtained through dyes confinement in liquid nanodomains.

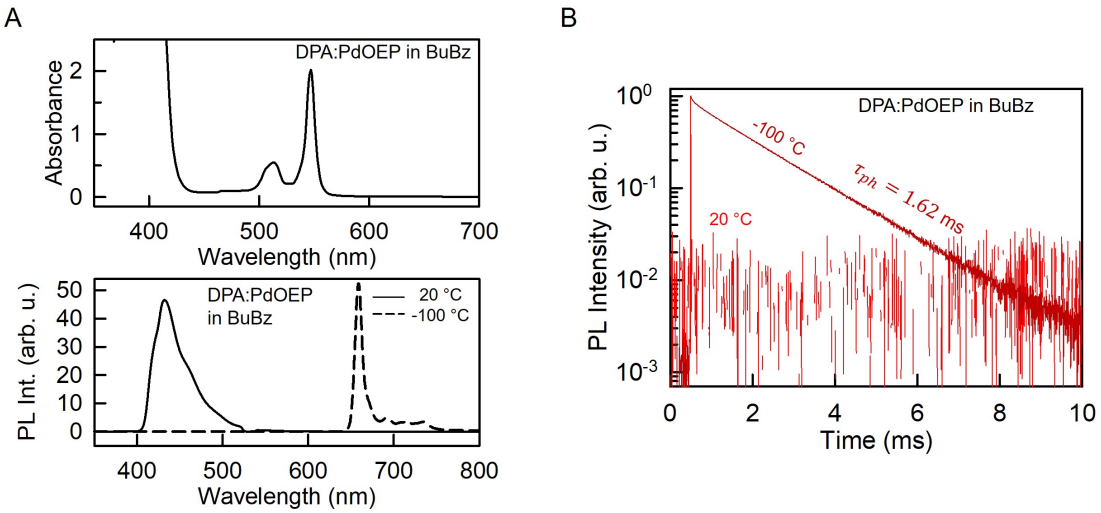

Figure 6.8: (a) Absorption (top) and PL (bottom) spectrum of the reference DPA:PdOEP solution in BuBz (1.5×10^{-2} M : 8×10^{-5} M) at room temperature (20 °C, solid line) and at -100 °C (dashed line), under cw laser excitation at 532 nm (150 W cm^{-2}). (b) Time-resolved PL intensity at 670 nm of the reference solution at 20 °C (red curve) and at -100 °C (dark red curve), under pulsed excitation at 532 nm (repetition rate 10 Hz). Upon freezing the sample, the emission intensity decays as a single exponential decay function with characteristic decay time $\tau_{ph} = 1.62$ ms.

Conversely, the strong phosphorescence enhancement and the UC-PL suppression seen in the frozen solution stem from blocking the dyes at a reciprocal distance of $\sim$ 6.0 nm at the given DPA concentration of 10^{-2} M, much larger than typical Dexter ET radii, with consequent suppression of both ET and TTA.[43,218,348]

I further confirmed this picture about the dyes arrangement within the nanostructured host by investigating the changes of UC-PL and red-PL kinetics upon freezing, especially in comparison with the BuBz reference solution behavior. In the frozen solution, the red-PL decay time lengthens consistently with suppressed ET, as reported in Fig. 6.8. Yet, the fast red-PL intensity drop that marks the efficient ET at room temperature is only partially slowed down in the frozen polymer, as shown in Fig. 6.7b, meaning that hopping-mediated ET is still viable. Moreover, for the upconverting polymer I observed the typical slow *s*TTA-UC recombination dynamics (Figure 6.9), that, at this temperature, can only occur through triplet exciton diffusion by hopping within the ensemble of close-packed DPAs without the assistance of translational molecular motions. Interestingly, the progressive deceleration of both UC-PL intensity decay (Fig. 6.9a) and rise time (Fig. 6.9b) upon lowering the temperature mirrors a decrease of the TTA rate. In fact, the UC-PL emission decay time reflects the anni-

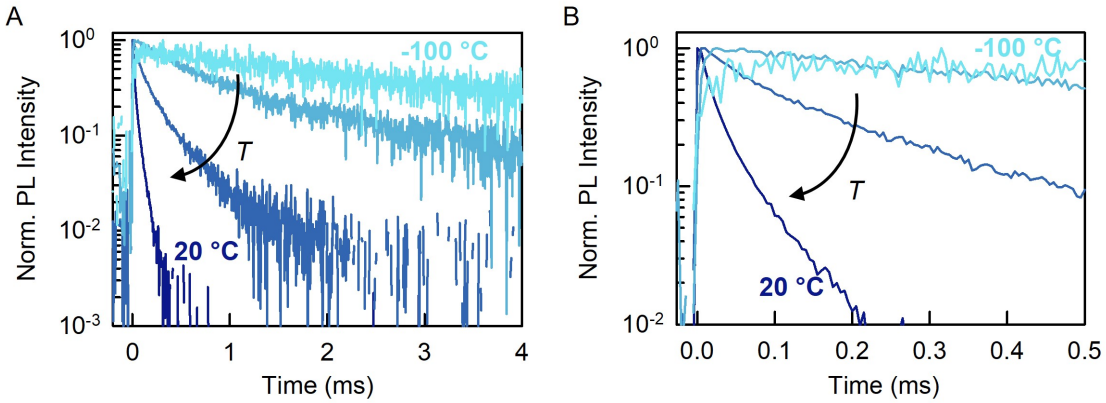

Figure 6.9: (a,b) Time-resolved UC-PL intensity decay (a) and rise (b) of the DPA:PdOEP upconverting polymer at 435 nm recorded as a function of temperature (20 °C, 5 °C, -20 °C, -100 °C), under pulsed laser excitation at 532 nm (repetition rate 10 Hz). The rise time deceleration to reach the emission intensity maximum after the excitation pulse observed upon lowering the temperature mirrors a TTA rate decrease due to hindered triplet diffusion.

hilating triplets lifetime, which are the energy reservoir to generate the upconverted singlets. In the first approximation, the emitter triplet lifetime is set by the spontaneous triplet decay rate k_T and by the TTA rate k_{TTA}. The $k_{TTA} = \gamma_{TTA}[T]$ is set by the emitter triplets density $[T]$ and by their diffusivity[46] which is strongly reduced by the low temperature effects on the hopping-mediated diffusion within the disordered dyes ensemble.[252] Accordingly, the UC-PL intensity decay at -100 °C features a single exponential behavior, because k_{TTA} is entirely governed by the hopping mechanism and thus is negligible if compared to k_T (k_T = 135 Hz at -100 °C, Fig. 6.10a).[47] Conversely, at room temperature the annihilation rate is large enough to dominate the DPA triplets recombination dynamics, thereby maximizing the conversion efficiency (*vide infra*). It is worth noting that the UC-PL in the frozen system decays in the millisecond timescale, as expected for unquenched DPA triplets (k_T = 844 Hz at 20 °C in BuBz, Figure 6.10b).[307] This demonstrates that the nanostructuring strategy mitigates the τ_T reduction commonly observed when translating from solution to the solid-state and that the nanodomains are a safe, defect-free environment for hopping triplets since the confined excitons do not reach nonradiative recombination centers during their diffusion.

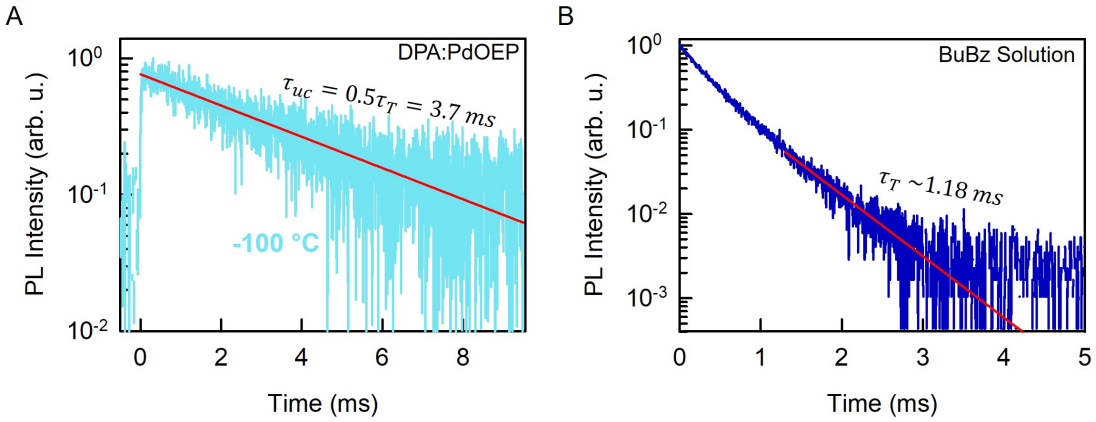

Figure 6.10: (a) UC-PL intensity decay of the DPA:PdOEP upconverting polymer recorded at 435 nm at -100 °C under pulsed 532 nm laser excitation (repetition rate 10 Hz). The solid line is the fit with a single exponential function with characteristic lifetime $\tau_{uc} = 0.5\tau_T = 3.7$ ms. The triplet spontaneous decay rate at -100 °C is given by $k_T = \frac{1}{\tau_T} = 135$ Hz. (b) UC-PL intensity decay of the reference upconverting solution in BuBz recorded at 435 nm under modulated excitation at 532 nm (repetition rate 70 Hz) at room temperature. The long-time tail of the curve is fitted (red line) with a single exponential decay function with characteristic decay time τ_{uc}, thereby the DPA triplet lifetime is $\tau_T = 2\tau_{uc} \sim 1.18$ ms ($k_T = 844$ Hz).

6.4 Confined *s*TTA regime

The peculiar behavior emerged from temperature-dependent measurements is a direct consequence of the controlled dye-accumulation without segregation and aggregation achieved in nanophase-separated polymers. This controlled dye-distribution has also crucial implications on the *s*TTA-UC mechanism, since it inherently influences the triplet exciton diffusion in a way profoundly different than in homogeneous materials. In this regard, Fig. 6.11 reports a sketch representing the different chromophore distributions[349] in an upconverting reference solution – which is representative of typical systems in solution as well as homogeneous solid materials – and in the nanophase-separated polymers. The hopping-assisted nature of triplet diffusion in the liquid nanodomains allows for a localized and efficient sensitization of the triplet excitons. Moreover, as already pointed out, the sensitizers confinement implies that in the liquid nanodomains the average mean distance at which two triplets are generated is much shorter than in materials that contain the same dyes concentration but homogeneously distributed. As a result, the TTA rate is intrinsically enhanced at lower excitation intensities

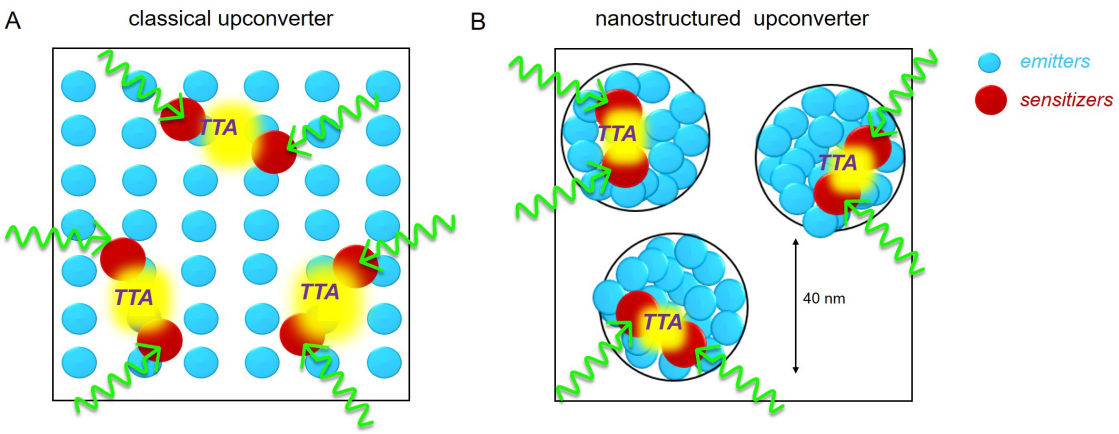

Figure 6.11: Sketch of the distribution of upconverting chromophores and triplet excitons upon absorption of green photons in a classical bulk upconverting material in which the dye molecules are homogeneously distributed (a), and a nanophase-separated polymer with the same volume and number of chromophores but accumulated in liquid nanodomains of mean size of $\sim$ 40 nm (b).

with respect to the homogenous counterpart. Therefore, the nanophase-separated polymers should be the ideal platform to observe the confined *s*TTA-UC regime discussed in Sec. 1.8.2 To provide evidence for this picture, I investigated the upconversion performance of the upconverting nanostructured polymer side-by-side with a BuBz solution containing the same global dyes amount. Figure 6.12a shows the upconversion quantum yield QY_{uc} measured as a function of the incident excitation intensity I_{exc} at 532 nm. In both cases, the QY_{uc} increases with I_{exc} and plateaus at the value of $23 \pm 3\%$, matching the limit imposed by the spin statistical probability of singlet generation with DPA as annihilator.[225] I measured the maximum QY_{uc} following the method reported in Sec. 2.7, employing as reference a solution of Pt(II) octaethylporphyrin (PtOEP 10^{-4} M) and DPA (10^{-2} M) in THF with known quantum yield (25%). Since the relative quantum yield measurement depends on the refractive index of the sample's medium (Eq. 2.4), for the nanostructured polymers I employed the value of 1.5 consistently with previous studies.[262] To verify that the absolute QY_{uc} value measured for the polymer was not sample dependent nor dependent on the laser spot position on the sample itself, I repeated the measurement on three different replicates and on three different spots for each sample, and the value that I report here is the corresponding average and the error is calculated as the standard deviation. The bright upconverted blue emission from the upconverting polymer under 532 nm excitation can be easily seen by naked eye as reported in the digital picture in Fig. 6.12c.

The QY_{uc} dependence on I_{exc} reported in Fig. 6.12a shows an important and peculiar difference of the *s*TTA-UC process between the bulk solution and the nanophase-separated polymer. In the reference solution the phenomenology typical of homogeneous upconverting system is clearly observed, with the QY_{uc} that increases linearly at low powers and then plateaus to its maximum value when TTA becomes the most efficient recombination channel for the emitter triplets. In this case, the excitation threshold intensity I_{th} is 2.1 W cm^{-2} (dashed vertical line in Fig. 6.12a).[41] However, for the nanophase-separated polymer the saturation to the maximum is super-linear, with the threshold set to 0.5 W cm^{-2} (solid vertical line), four times lower than in the reference solution. This peculiar dependence of the upconversion efficiency on I_{exc} is a fingerprint of the TTA process occurring in confined systems where the triplets are physically confined in discrete volumes smaller than the space potentially explored by the triplets random diffusion. Moreover, the dyes confinement reduces their average intermolecular distance, therefore when two emitter triplets are simultaneously created in the same confined space, they are so close that they decay by annihilation with unit TTA efficiency,[350] with a resulting QY_{uc} increased at low powers, reducing the excitation threshold with respect to the classical homogeneous bulk counterpart.[259]

A further demonstration of the occurrence of confined *s*TTA comes from the time-resolved PL data shown in Figure 6.12b. In the bulk-TTA regime the k_{TTA} and UC-PL kinetics are set by the excitation intensity,[47] thus the changes in the UC-PL kinetics induced by varying the excitation intensity mirror the relative weight variation between the triplet spontaneous recombination channel and the TTA channel. Conversely, for the upconverting polymer the UC-PL kinetics remain unchanged even varying the I_{exc} two orders of magnitude around I_{th}, as expected for the confined regime. In this case, the UC-PL time decay, which mirrors the triplet lifetime, shows an average lifetime $\tau_{uc} = 2 \times 10^{-2}$ ms, calculated as the time when the zero-delay intensity decreases by a factor $^1/_e$. The corresponding average decay rate is k_{uc} = (τ_{uc}^{-1}) $\sim$ 50 kHz, which is significantly larger than the triplet spontaneous decay rate $k_T = 844$ Hz. Therefore, $k_{uc} \sim k_{TTA}$ and, provided that at least two triplets are generated in the same confined volume, the TTA efficiency Φ_{TTA} = $\frac{k_{TTA}}{k_{TTA}+k_T} \sim 100\%$ is power independent.

This behavior is in line with the confined *s*TTA process, because an increase of I_{exc} leads to a growth of the nanodomains number that simultaneously contain at least one triplet pair. Also, the behavior observed with time-resolved measurements proves that the *bright* nanodomains are completely independent and isolated, with the triplet excitons that cannot interact with

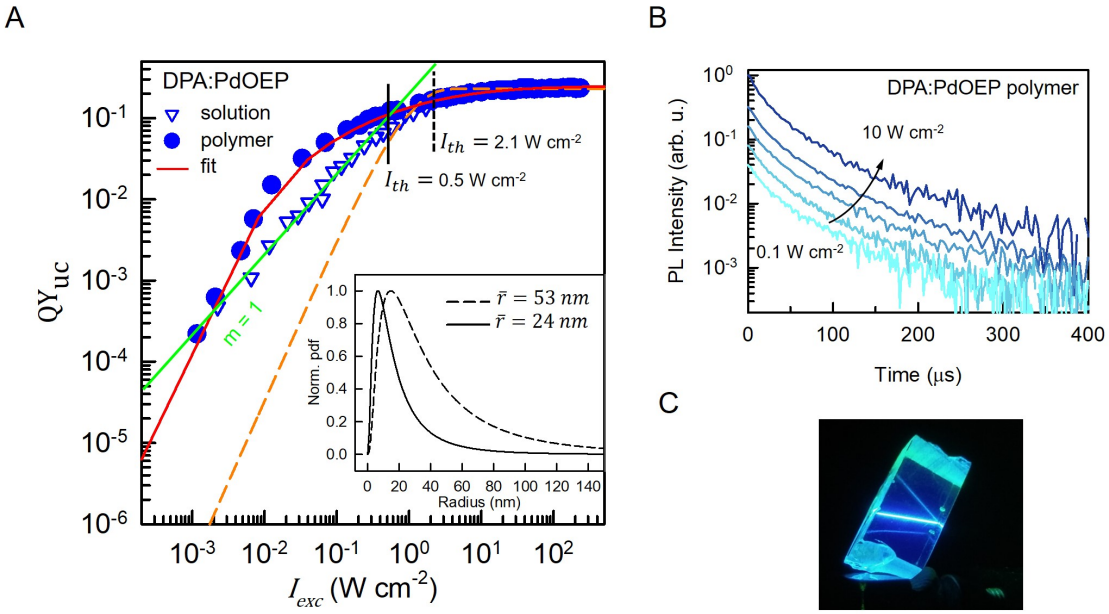

Figure 6.12: (a) *s*TTA upconversion quantum yield (QY_{uc}) of the DPA:PdOEP upconverting nanophase-separated polymer (1.5 $\times 10^{-2}$ M : 8 $\times 10^{-5}$ M, circles) and the reference DPA:PdOEP (1.5 $\times 10^{-2}$ M : 8 $\times 10^{-5}$ M) solution in BuBz (triangles) as a function of the incident excitation intensity I_{exc} at 532 nm. The short vertical lines mark the excitation intensity threshold I_{th} (solid line for the polymer, dashed line for the solution). The green curve is the fit of the solution low-power data with a straight line with slope $m = 1$, while the red curve is the fit of the polymer experimental data obtained by calculating QY_{uc} for an ensemble of nanodomains activated at different excitation intensities according to a size-dependent binomial excitation energy distribution with Eq. 1.43. The size distribution was assumed to be log-normal with a fitted mean diameter of 48 nm. The dashed orange curve reports the upconversion dependency on I_{exc} calculated assuming a binomial distribution of the excitation energy on a homogenous population of spherical UC nanodomains with a diameter of 40 nm. The inset depicts the "effective" log-normal size distribution that reproduces the experimental data (dashed curve) and the log-normal size distribution that describes the real size distribution in the polymer. (b) UC-PL intensity decay at 435 nm of the DPA:PdOEP upconverting nanophase-separated polymer recorded under a modulated 532 nm laser excitation at different excitation intensities. (c) Digital image of the DPA:PdOEP upconverting nanophase-separated polymer under laser excitation at 532 nm.

the triplets in other nanodomains. In agreement with the spin-diffusion experiments, the cw and time-resolved PL results confirm the presence of non-interacting upconverting nanostructures where confined *s*TTA occurs because their sizes are significantly smaller than the DPA triplet diffusion length. I estimated the lower-limit of the triplet diffusivity according to

$$D = \frac{k_{TTA}}{8\pi R_{TT}[T]} = 3 \times 10^{-7} cm^2 s^{-1} \tag{6.2}$$

where $k_{TTA} = 50$ kHz, $R_{TT} = 0.91$ nm is the effective triplet-triplet interaction distance for DPA triplets[41] and $[T]$ is the minimum density of annihilating triplets calculated considering two triplets in the same nanodomain of radius 20 nm (approximated value obtained from NMR measurements), resulting in the lower-limit diffusion length $L_T = \sqrt{\frac{6D}{k_T}} = 463$ nm, which is much greater than the nanodomain mean size.

This is the first observation of the confined *s*TTA in bulk materials. However, the QY_{uc} vs. I_{exc} behavior in the nanophase-separated polymers profoundly differs from that previously reported for monodispersed ensembles of nano-upconverters (e.g. MOFs). As already stated in Sec. 1.8.1, the QY_{uc} dependence on the I_{exc} in this kind of nano-upconverters strictly follows a binomial distribution of the excited states (Fig. 6.12a, orange dashed line).[259] This discrepancy is ascribed to the fact that the polymer nanostructuring results in a log-normal distribution of the liquid domains size.[266,267] To validate the proposed theoretical model introduced in Sec. 1.8.2, and to extrapolate an independent value of the mean liquid nanodomains size, I fitted the polymer power-dependent efficiency data with Eq. 1.43. As reported in Figure 6.12a, the experimental data are perfectly reproduced by the red solid line, calculated by assuming that the confined *s*TTA-UC occurs in an ensemble of spherical nanodomains characterized by an "effective" log-normal size distribution $L(r)'$ ($\mu = 3.57$ nm and $\sigma = 0.88$) corresponding to a mean domain radius of ~ 53 nm (Eq. 1.44), represented by the dashed curve in the inset of Fig. 6.12a. Thereby the log-normal distribution $L(r)$ ($\mu = 2.78$ nm, $\sigma = 0.88$) that describes the real size distribution (represented by the solid curve in the inset) has a mean radius of ~ 24 nm (Eq. 1.42). This result is in excellent agreement with the data obtained from time-resolved NMR measurements, further confirming the intrinsic nanostructured architecture of the material and highlighting the crucial role of nanostructuring in setting the material macroscopic upconversion properties. Moreover, this analysis validates the theoretical model proposed to describe the overall *s*TTA-UC behavior in the confined regime.

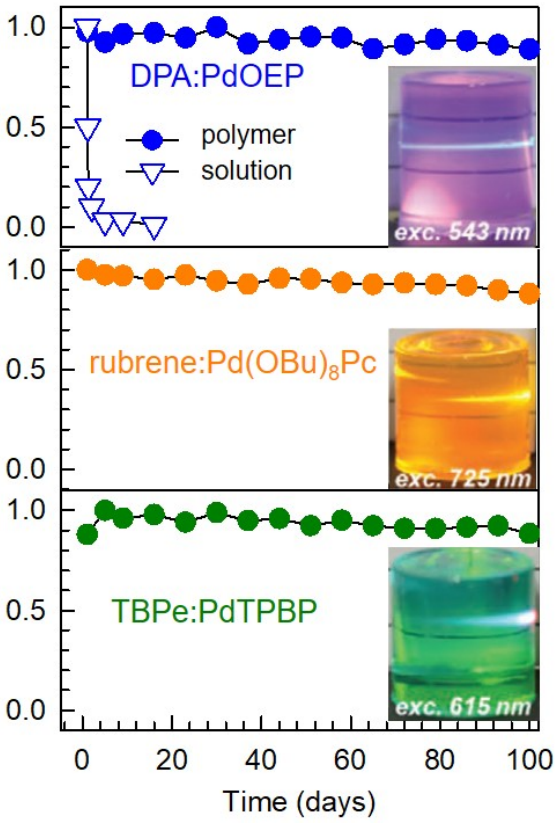

Figure 6.13: UC-PL integrated intensity measured under excitation with a Xe lamp over a prolonged period for nanostructured polymers containing DPA:PdOEP (top, 1.5 $\times 10^{-2}$ M : 8 $\times 10^{-5}$ M, λ_{exc} = 543 nm), rubrene:Pd(OBu)$_8$Pc (middle, λ_{exc} = 725 nm), and TBPe:PdTPBP (bottom, λ_{exc} = 615 nm) as upconverting dye pairs, respectively. All measurements were performed on samples prepared under ambient conditions and kept in glass cuvettes sealed with a polymer film. The insets show pictures of the respective materials exhibiting upconversion. For comparison, the top panel reports the same measurement for the DPA:PdOEP solution in BuBz (triangles).

6.5 Material stability and synthesis versatility

One of the crucial properties an upconverter must possess for real-world devices is long-term stability afforded by efficient oxygen protection. As previously pointed out, one of the remarkable innovations introduced in the nanophase-separated polymers is the oxygen scavenger moiety that not only allows to perform the synthesis under ambient conditions (greatly simplifying the process since working in a glove box is no more necessary) but also should provide excellent long-term protection from air. The oxygen transmission rate measurements reported in Sec. 3.3.3 are a first confirmation of the oxygen shielding afforded by the polymer matrix.[285,286] To further assess this property also on long timescales, stability check measure-

ments were performed. Remarkably, the data reported in Figure 6.13 show that the nanophase-separated polymer does not suffer from significant efficiency losses ($<10\%$) after storing the sample for more than 3 months, a striking result if compared to the previously observed loss of $\sim 50\%$ during half of this time span.[262] Conversely, the reference solution loses its upconversion ability completely within ten days, thereby demonstrating the excellent oxygen shielding effect of the polymer host.

To probe whether the developed synthetic route allows also to employ different upconverting dyes so that to work in different spectral regions, upconverting polymers containing two different upconverting dye pairs were fabricated (see Sec. 3.3.2). Palladium(II) tetraphenyltetrabenzoporphyrin (PdTPBP) and 2,5,8,11-tetrakis(tert-butyl)perylene (TBPe) were employed as sensitizer and emitter for the red-to-blue upconverting system (middle panel), while palladium(II) octabutoxyphthalocyanine ($Pd(OBu)_8Pc$) and rubrene were the sensitizer and emitter of the upconverting system from the near-infrared to the yellow spectral range (bottom panel). Remarkably, not only the optical quality of these materials is optimal, but they also shown a shelf-life similar to the DPA:PdOEP system. These results corroborate the designed synthetic strategy versatility to fabricate in air industrially processable upconverters, that in principle can be loaded with a given dye pair necessary to work in a specific spectral region according to the application of interest.

6.6 Conclusions

In this Chapter I reported the successful development of upconverting nanostructured rigid polymers. The modifications introduced changed the nanostructuring outcome with respect to previously reported glassy polymers giving rise to important enhancement of the system performances. The materials exhibit the excellent upconversion yield of $\sim 23\%$, which is comparable to that of the best solution-based systems. The optimized synthetic route allows to carry out the synthesis in a simple one-pot procedure in air and the materials show excellent operational stability, with long-term oxygen protection. Efficient electronic interaction between upconverting moieties is achieved by embedding the chromophores in isolated, nanosized liquid domains within the rigid host polymer. The co-localization of sensitizers and emitters increases their local density to extremely high values without partitioning or aggregation effects that could affect the material optical quality. It also enables ET and TTA to occur by molecular

diffusion supported by hopping-mediated energy migration. Moreover, the confinement of triplet exciton pairs in non-communicating domains allows the upconversion process to work in a protected defect-free environment, avoiding trivial energy losses, and to reach the confined *s*TTA regime where the annihilation yield is maximized independently of the excitation intensity. The effective local increase of the triplet exciton density leads to an enhanced upconversion performance at lower incident powers with respect to the corresponding liquid solution. Therefore, controlled nanostructuring is a powerful design concept to manipulate safely the local dyes density in solid systems and, at the same time, to tune the *s*TTA-UC dynamics to reach ultralow upconversion thresholds. The best trade-off between nanostructure size and energy distribution probability, together with an enhanced absorption by including larger sensitizers amounts, can enable indeed to achieve high-efficiency upconverting polymers at excitation intensities well below the solar irradiance. Importantly, it is worth emphasizing that the controlled confinement is not only useful to achieve chromophores concentrations that cannot be managed by standard synthetic routes, but also as a general approach to enhance the upconversion yield independently of the composition. This can be of particular interest in applications where the excitation intensities are intrinsically limited, as in the case of solar technologies. Considering their striking stability and mechanical properties, the compatibility of the fabrication route with straightforward and readily scalable processes, and the possibility to incorporate potentially any dye pair, these materials are appealing not only in the upconversion framework, but also for those technological applications, such as molecular photonics, photon management or optoelectronics, that require high quality transparent solid-state materials.

Block copolymer stabilized nanostructured glassy polymers

The typically limited molecular mobility in solid-state upconverters implies that particular architectures must be developed to facilitate the short-range interactions underpinning the sTTA-UC. A viable option towards efficient short-range bimolecular processes is to incorporate liquid upconverting domains into solid polymeric matrices. Another possibility consists in reducing the intermolecular distance between the dyes on a nanometer scale, allowing exciton migration to be assisted by triplet-hopping. I report herein the effective development of nanostructured polymers that combine both these features. The glassy nanostructured polymers proposed contain liquid upconverting nanodroplets that are stabilized with a block copolymer surfactant and are fabricated under ambient conditions in a one-step synthetic route thanks to the incorporation of an oxygen scavenger. The dyes concentrate in nanoscale domains that offer high translational mobility and are formed by block copolymer/solvent assemblies enabling hopping-mediated energy transfer and triplet-triplet annihilation between the dyes which impart the polymer with a threshold excitation intensity that is half of that of the corresponding bulk upconverting solutions containing the same dyes. The materials feature exceptional optical quality and stability, as well as the excellent maximum upconversion efficiency of $\sim$*20* $\%$*.*

7.1 Development of the nanostructured glassy polymers

In the previous Chapters, I pointed out that the typically high molecular mobility in low viscosity solvents make bimolecular interactions extremely effective in these environments, while

peculiar architectures and morphologies must be developed to reach comparable performances in solid-state materials.[75,79,89,90,144,145,247,259–262,333,334,337,351] I demonstrated how nanostructured glassy materials, consisting of a continuous, rigid polymer matrix and a discontinuous liquid phase, are an appealing platform towards solar technologies.[262] In fact, the upconverting dyes preferentially accumulate in the liquid phase, composed of independent domains of size $<$ 50 nm making the upconversion process highly efficient. But if the upconverting domains liquid nature affords overall performances comparable to those obtained in common upconverting solutions, the ability to confine the upconverting dyes in these nanodomains results in an essential surplus value. By reducing the intermolecular distance r down to the typical values necessary for triplet-triplet interactions ($r \sim$ 1-2 nm),[218,348] the triplet propagation becomes partially independent of molecular translational motions by enabling hopping-assisted exciton diffusion and relieving the strict necessity of high molecular mobility, which is not so straightforward to achieve in the solid-state. Moreover, the effective confinement diffusing triplets activates the confined *s*TTA regime, which, together with the corresponding localized increment of the excitation energy density, enhances the upconversion efficiency at low excitation intensities compared to the homogeneous upconverting counterparts.

In this Chapter, I introduce glassy nanostructured polymer systems conceptually similar to those discussed in Chapter 6, but where the liquid upconverting nanodomains are stabilized with a block copolymer surfactant. The optimal upconversion performances exhibited are preserved, but the number of components employed is reduced, making the synthetic procedure simpler, and superior optical quality is achieved.

The idea to use amphiphilic poly(ethyleneglycol)-*block*-poly(propyleneglycol)-*block*-poly(ethyleneglycol) (PEG-PPG-PEG) block copolymers stems from the fact that they are well-known, commercial non-ionic surfactants able to form stable micelles in water[352] and have been notably used for nanoparticle size control,[353,354] templating of porous materials[291,292] and upconversion in aqueous medium,[261] therefore they are good candidates to stabilize nanodroplets of a hydrophobic solvent containing upconverting dyes in a polar monomer mixture, allowing the formation of nanostructured polymer glasses containing these micelles upon monomer polymerization. This process is somewhat reminiscent of templating approaches used to create porous polymeric materials,[355,356] although in the latter case the micelles merely served to create the pores. Figure 3.7 in Sec. 3.4 reports the chemical structure of all the components used for the materials fabrication, carried out under ambient conditions following

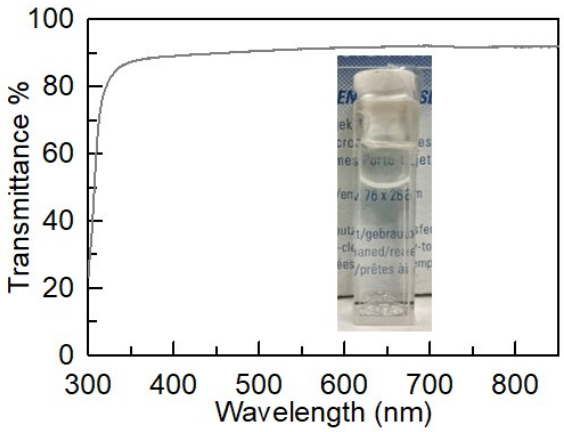

Figure 7.1: Transmittance spectrum (path length 1 cm) and a digital picture of the nanostructured polymer without dyes.

a simple one-step procedure that can be easily scaled up, and this represents an important benefit for technological applications. A mixture containing 2-hydroxyethyl methacrylate (HEMA, 80.9% w/w), triethylene glycol dimethacrylate (TEG-diMA, 2.7% w/w), the triblock copolymer having a number-average molecular weight of 14,600 g mol^{-1} and a PEG content of 82.5% w/w (PEG-PPG-PEG, 8.4% w/w), and hexyl benzoate (HexBz, 5% w/w) as a hydrophobic solvent was polymerized by free-radical polymerization, initiated by a modified version of a bio-mimetic initiation system known to produce relatively inert residues, as discussed in the previous Chapter. A saturated solution of aqueous NaBr (2.5% w/w) in 0.1% HCl and H_2O_2 (30% in water, 0.16% w/w) was used to generate the hypohalous acids needed as electrophilic halogen source, and 2-mercaptoethanol (2-ME, 0.16% w/w) was used as the reducing agent to generate the radicals initiating the polymerization. Dimethylthiomethane (DMTM, 0.4% w/w) was also incorporated in the reaction mixture as a sacrificial oxygen scavenger, to improve the shelf-life and stability of the upconverting system through free-oxygen depletion.[342]

The transmittance spectrum of the dye-free nanostructured material is shown in Figure 7.1, which I recorded employing the same method in Sec. 2.1, which shows a transmittance $\geq 90\%$ over the entire range between 450 nm and 850 nm, with 1 cm optical path. Given that $\sim 8\%$ of the transmittance is due to reflection at the quartz/air interfaces, the material exhibits the remarkable transmittance $\geq 98\%$ in this spectral range. This is a striking result since it suggests that, despite the presence of nanosized liquid domains, the fraction of scattered light is negligible, with an absorption coefficient of $\sim 1 - 2 \times 10^{-2}$ cm^{-1}, making the nanostructured

material an ideal medium for light transport given the limited losses for scattering. The excellent material quality is also emphasized by the digital picture reported in the same Figure.
A first upconverting material was fabricated by adding Pd(II) octaethylporphyrin (PdOEP) as sensitizer and 9,10-diphenylanthracene (DPA) as emitter in HexBz to the reaction mixture, for green-to-blue upconversion, as reported in Sec. 3.4.2. The nominal dye concentrations were 1.9×10^{-5} M for PdOEP and 1.4×10^{-2} M for DPA, according to the composition total volume and assuming the material's density to be 1 g mL^{-1}. Differential scanning calorimetry (DSC, Fig. 3.8) characterization of the dye-free material and upconverting system reveals a glass transition temperature (T_g) of 80-84 °C, attributed to the cross-linked poly(hydroxyethyl methacrylate) (PHEMA) matrix, which has a $T_g = 86$ °C. At room temperature, only the glass transition is visible when heating the upconverting and dye-free materials from 0 °C, and importantly the exclusion of either PEG-PPG-PEG or hexyl benzoate from the dye-free material does not significantly alter this value. As reported in Sec. 3.4, the material characterization suggests that the resulting nanodroplets consist of a liquid core in which the PPG and a portion of the PEG blocks reside, with the remaining PEG blocks protruding out into the glassy PHEMA matrix to stabilize and limit the droplets size. Time-domain NMR experiments were performed to confirm the presence of multiple phases and to obtain an estimate of the liquid nanodomain size. The proton magnetization relaxation measurements reported in Figure 3.12a depict a bi-component relaxation dynamics compatible with the coexistence of a rigid (PHEMA) and a presumably liquid phase in which the dye molecules are able to experience high translational mobility.[287] The relaxation dynamics of the high-mobility fraction can be fitted with a bi-exponential decay function (Fig. 3.13a), meaning that the corresponding domains have two components with different relaxation times of 0.7 and 7.3 ms. All these data strongly suggest that the hydrophobic HexBz forms nanometer-sized liquid droplets that are stabilized by the amphiphilic block copolymer as sketched in Figure 3.11. The spin diffusion experiments provided an average diameter of the high-mobility domains, assumed to be spherical, of 34 $\pm$ 6 nm.[345]

7.2 Nanostructured polymers photophysics

To assess the photophysical properties of this new upconverting material and to find a further validation of the material's morphology, I investigated an upconverting sample containing

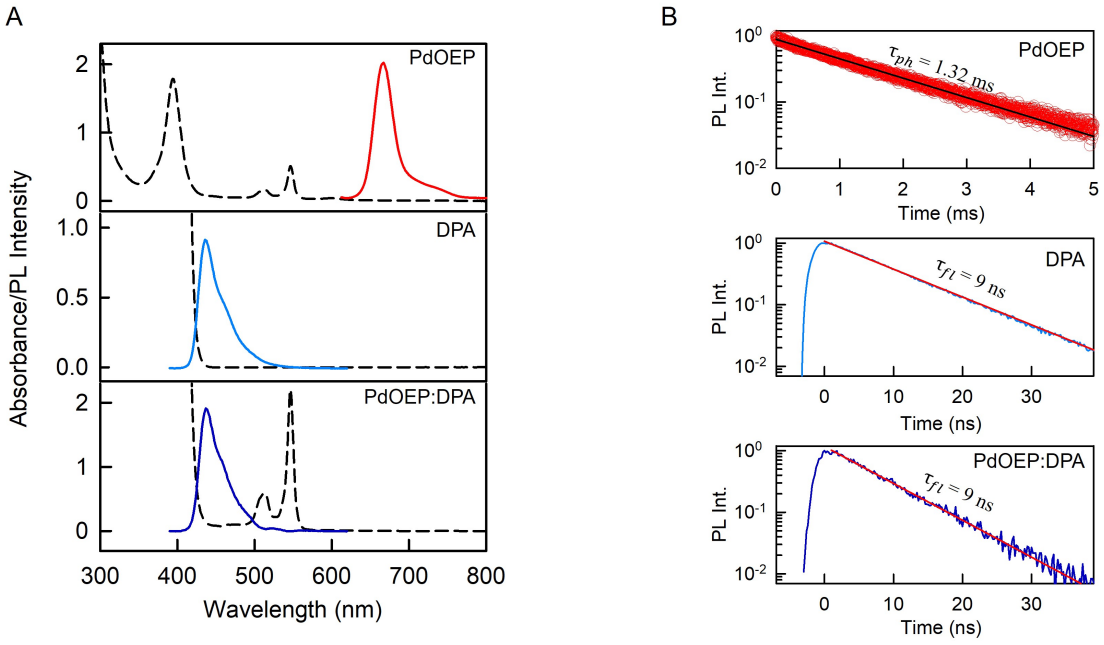

Figure 7.2: (a) Absorption spectrum (dashed lines) of the reference polymers containing PdOEP (1.9×10^{-5} M, top panel) or DPA (1.4×10^{-2} M, middle panel), and of the upconverting DPA:PdOEP (1.4×10^{-2} M : 1.9×10^{-5} M) polymer. The solid lines are the photoluminescence spectra of the same samples recorded under a cw 532 nm for the PdOEP sample and under a cw 380 nm excitation for the samples containing DPA. All the samples were prepared in quartz cuvettes with 1 cm optical path. (b) Time-resolved phosphorescence intensity at 670 nm with characteristic lifetime τ_{ph} recorded under a pulsed 532 nm excitation (top panel). Fluorescence intensity decay at 435 nm recorded under a pulsed 405 nm excitation, with characteristic lifetimes τ_{fl}, for the reference DPA polymer (middle panel) and for the upconverting DPA:PdOEP polymer (bottom panel). The red solid lines are the fit of the experimental data with single exponential decay functions.

PdOEP and DPA (1.9×10^{-5} M and 1.4×10^{-2} M, respectively), the corresponding reference samples containing either PdOEP (1.9×10^{-5} M) or DPA (1.4×10^{-2} M), and a reference solution of DPA:PdOEP with the same dye concentration in HexBz, by means of continuous wave (cw) and time-resolved photoluminescence spectroscopy techniques. All samples were prepared in quartz Suprasil cuvettes with 1 cm optical path.

Figure 7.2a displays the absorption spectra of the above-mentioned polymers, acquired following the method reported in Sec. 2.1. In the visible range, the spectra of the samples that contain PdOEP (top and bottom panels) exhibit the characteristic Q-band peaked at 540 nm. The spectrum of the reference polymer containing only the porphyrin also shows the PdOEP's Soret band at 394 nm, while the absorbance of the samples containing DPA (middle and bottom

panels) saturates below 400 nm given the high DPA concentration. Upon excitation at 532 nm, the PdOEP sample exhibits red phosphorescence (red-PL) peaked at 670 nm, whose intensity decays as a single exponential function with a characteristic lifetime $\tau_{ph} = 1.32$ ms (top panel of Fig. 7.2b), suggesting that these molecules are all embedded in the same environment.[28] The samples containing DPA and DPA:PdOEP exhibit a bright blue luminescence peaked at 435 nm when excited at 380 nm, with decay time $\tau_{fl} = 9$ ns, assigned to prompt DPA fluorescence.[307] In both cases, it decays as a single exponential function, which indicates that also the emitter molecules sense one environment only. Importantly, the red-PL emission shows

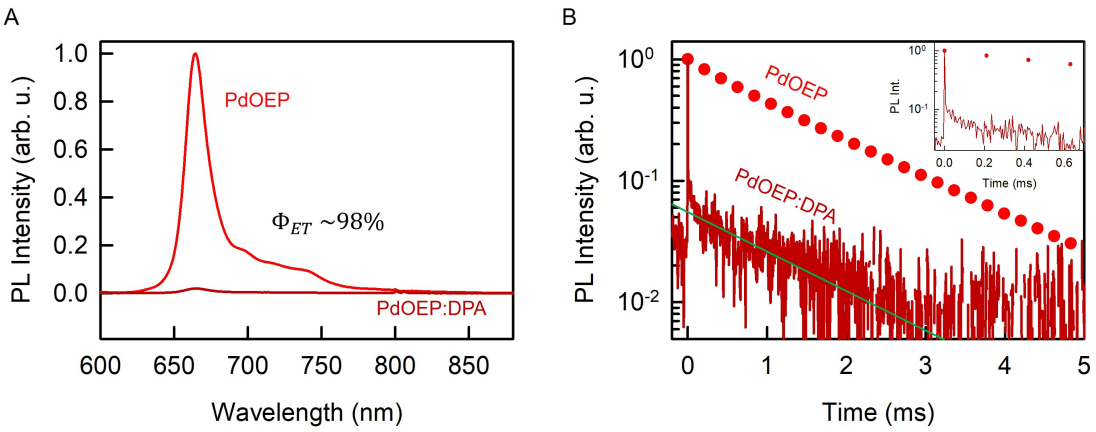

Figure 7.3: (a) Photoluminescence spectrum recorded under a cw 532 nm laser excitation for the reference PdOEP polymer (1.9×10^{-5} M, red curve) and for the upconverting DPA:PdOEP (1.4×10^{-2} M : 1.9×10^{-5} M, dark red curve) polymer. For quantitative comparisons the spectra were recorded under the same excitation conditions. Since the optical density at 532 nm of the two samples is the same, it was not necessary to correct the spectra for the different samples absorbance. (b) Phosphorescence intensity decay at 670 nm recorded under pulsed 532 nm excitation for the same two samples. The green line highlights the long-lived tail in the DPA:PdOEP emission with the same lifetime as the reference PdOEP polymer. The inset is a magnification of the decays over the first 600 μs to emphasize the change in the recombination dynamics due to efficient energy transfer that translates into the accelerated dynamics.

a dramatic intensity reduction in the upconverting DPA:PdOEP polymer, as depicted in Fig. 7.3a, which illustrates the comparison between the PL spectrum of the PdOEP (red curve) and the DPA:PdOEP (brown curve) samples upon cw excitation at 532 nm, that I recorded under the same experimental and acquisition conditions. From the ratio between the integrated red-PL intensity with (I) and without (I_0) emitters I calculated the ET yield $\Phi_{ET} = 1 - \frac{I}{I_0} = 98\%$.

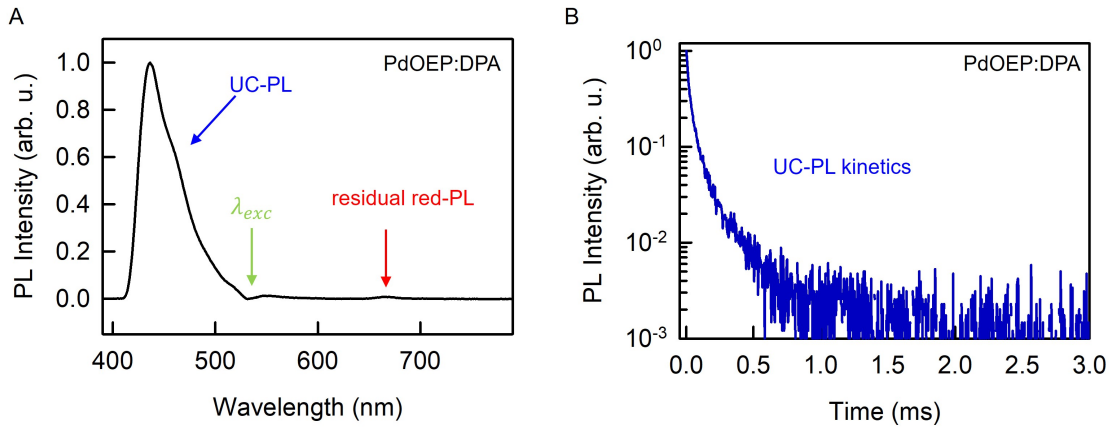

Figure 7.4: (a) Emission spectra of the DPA:PdOEP upconverting polymer recorded under cw laser excitation at 532 nm (3 W cm^{-2}). (b) UC-PL intensity decay of the DPA:PdOEP upconverting polymer recorded at 433 nm under 532 nm modulated laser excitation at 10 W cm^{-2} (repetition rate 70 Hz).

The analysis of the corresponding PL intensity decays (Fig. 7.3b) gives further information about the environment that the chromophores sense within the host polymer. If the porphyrin emission in the reference sample shows a single exponential decay with $\tau_{ph} = 1.32$ ms, in the upconverting sample it shows a bi-exponential behavior, with a fast component with $\tau_{fast} \sim 3$ μs and a long component $\tau_{long} = 1.32$ ms, compatible with τ_{ph}. The figure inset highlights how the red-PL is quenched in the first hundreds of μs in the upconverting sample as a result of efficient energy transfer. It is worth noting that the fast component has a relative weight A = 96 $\pm$ 1% of the total decay intensity and mirrors the efficient emission quenching provided by fast ET from PdOEP triplets to DPA triplets, because of dyes incorporation in the high-mobility environment afforded by the HexBz-rich nanodroplets. I therefore calculated the transfer efficiency as $\Phi_{ET} = 1 - \frac{\tau_{fast}}{\tau_{ph}} \sim 96 \pm 1\%$, which validates the steady-state result. To exclude that this analysis could be dependent on the laser spot position on the sample, the kinetics reported is an average from six different measurements each taken in a different spot. Also, the negligible secondary slow component with characteristic lifetime τ_{long} suggests that ca. 4 % of sensitizers are incorporated in the rigid polymer phase, with no emitters close enough to undergo ET. This finding supports the conclusion that almost all PdOEP molecules are successfully mixed with DPA in the liquid phase, where collisional bimolecular interactions can effectively take place.[41] Figure 7.4a reports the entire PL spectrum recorded under cw laser excitation at 532 nm of the DPA:PdOEP polymer. Besides a negligible red-PL due to the small fraction of sensitizers that do not transfer the excitation to the emitters, the spectrum

is characterized by an intense blue upconverted emission UC-PL. Panel b reports the UC-PL intensity decay at 433 nm recorded under a modulated 532 nm laser excitation at 10 W cm^{-2} to highlight the slow dynamics on the millisecond timescale typical of *s*TTA-UC.

7.3 Temperature effects on the polymers photophysics

I gained more insights into the dyes incorporation in the materials investigating the photophysical properties as a function of temperature. I first cooled the upconverting sample down

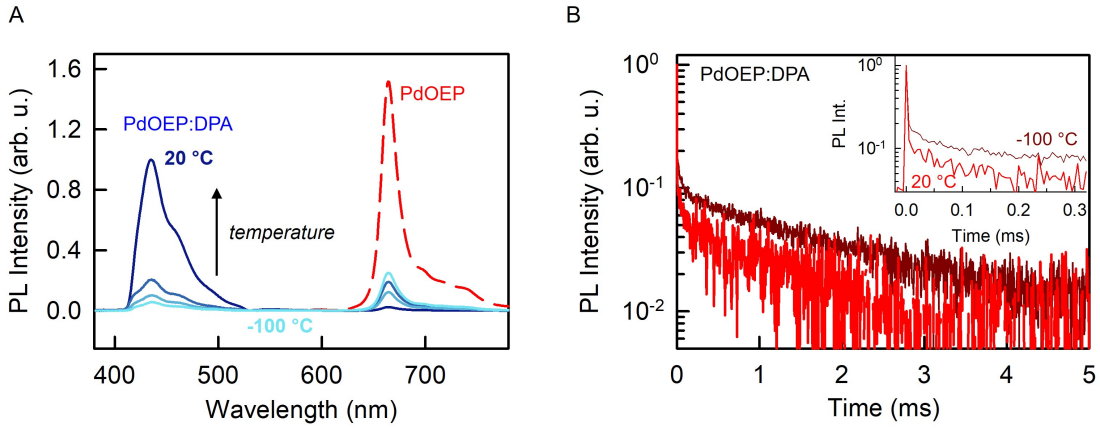

Figure 7.5: (a) Emission spectra of the DPA:PdOEP upconverting polymer recorded as a function of temperature (20 °C, 5 °C, -20 °C, and -100 °C), under cw laser excitation at 532 nm (3 W cm^{-2}). The red dashed curve is the phosphorescence spectrum of the PdOEP reference polymer recorded under the same excitation conditions at 20 °C. (b) Phosphorescence intensity decay of the DPA:PdOEP upconverting polymer, recorded at 670 nm under 532 nm pulsed laser excitation (repetition rate 10 Hz), at 20 °C (red curve) and -100 °C (dark red curve). The inset shows a magnification of the decays in the first 300 μs.

to -100 °C, so well below the melting temperature of HexBz (-20 °C), the crystallization temperature (-43°C) of the PEG blocks and all thermal transitions seen in the DSC experiments. As reported in Fig. 7.5a, the UC-PL intensity recorded under cw 532 nm excitation, decreases upon freezing the sample, but without being completely suppressed. Interestingly, since in this temperature range all translational motions are completely suppressed, the UC process must take place through hopping-mediated bimolecular interactions, and the sensitizers and emitters must be both localized in nanodomains to have intermolecular distances so short to allow the triplet hopping. Because the upconverting dyes employed are hydrophobic they are preferably or even exclusively incorporated in the hydrophobic nanodomains made of HexBz

and the block copolymer, which constitute ca. 5% of the total volume according to the initial feed ratio. Therefore, the local DPA concentration may be as high as 2.8×10^{-1} M, calculated as $\frac{1.4\times10^{-2}}{0.05}$ M and corresponding to a $C_{local} = 1.69 \times 10^{20}$ molecules cm^{-3}. From this local, effective concentration I calculated the average intermolecular distance between DPA molecules as the diameter of the sphere centered on a DPA molecule: $d = 2 \times \sqrt[3]{\frac{1[cm^3]3}{C_{local}4\pi}} =$ 2.25 nm. Thus, the distance d is sufficiently small to enable TTA to some extent also without molecular translational diffusion when the nanodomains are frozen.[41] Similarly, the PdOEP concentration may be as high as 3.8×10^{-4} M, which gives an average intermolecular distance between the PdOEP molecules $d' \sim 20$ nm, suggesting that deleterious interactions between the sensitizer molecules in the nanodomains should be avoided. It should also be noted that

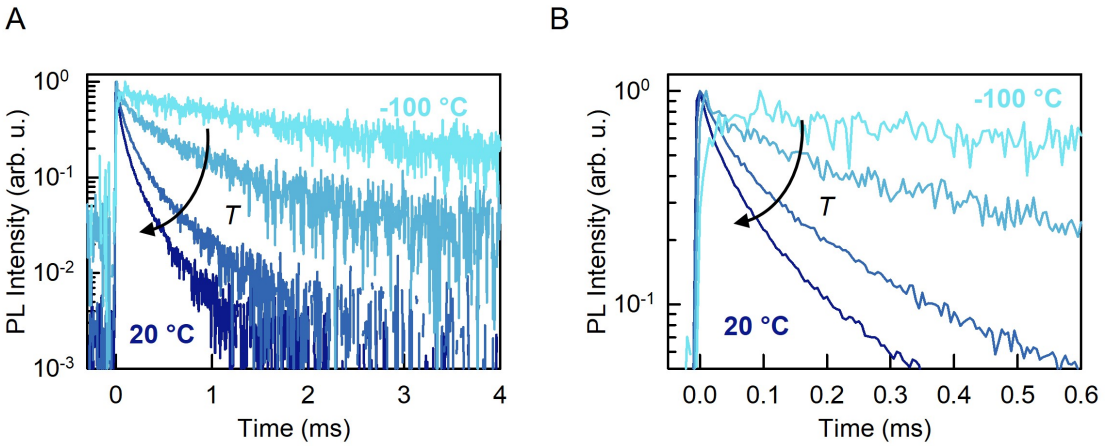

Figure 7.6: (a,b) UC-PL intensity decay (a) and rise (b) of the DPA:PdOEP upconverting polymer recorded at 435 nm as a function of temperature (20 °C, 5 °C, -20 °C, -100 °C) under pulsed laser excitation at 532 nm (repetition rate 10 Hz).

the high DPA concentration implies that also the average PdOEP-DPA distance equals the d value, with a single sensitizer molecule being surrounded by several annihilators. This means that even upon freezing the system, the ET is efficient, as pointed out from the analysis of the residual red-PL in the upconverting polymer (Fig. 7.5a). Despite a mild increase of the red-PL intensity at -100 °C, which mirrors the reduction of the ET efficiency contribution associated to the translational diffusion, the ratio between the integrated residual red-PL with and without DPA still yields a $\Phi_{ET} \sim 85\%$. This result corroborates that the average PdOEP-DPA intermolecular distance is of the order of one nanometer for most sensitizer/emitter pairs in the nanodomains, and thereby the ET is mainly governed by intermolecular hopping, that accounts for at least $^{0.85}/_{0.97} = 87\%$ of the total ET yield at 20 °C. I further confirmed the dyes

confinement in nanodomains through time-resolved photoluminescence investigations. As reported in Fig. 7.5b, the efficient red-PL quenching that marks the fast ET at 20 °C is almost unaffected upon cooling the upconverting polymer to -100 °C (highlighted in the inset), corroborating the cw ET yield data at low temperature. Moreover, the data show that the relative weight of the fast emission component decreases to $A^{'} = 90\ \%$, but its characteristic decay time is unchanged. Consequently, the Φ_{ET} is still $\sim 90\%$ and only a minor fraction of sensitizers ($\frac{A-A^{'}}{A} = 6\%$) does not participate in the ET process in the frozen sample. Specifically, the fraction of the PdOEP population de-activated upon freezing is $6\% - 4\% = 2\%$ of the total amount, considering the inactive 4% of sensitizers embedded in the matrix rigid phase as discussed above. On the same line, it is still possible to observe the *s*TTA-UC recombination dynamics even at -100 °C (Fig. 7.6). The correlated deceleration of both UC-PL intensity decay

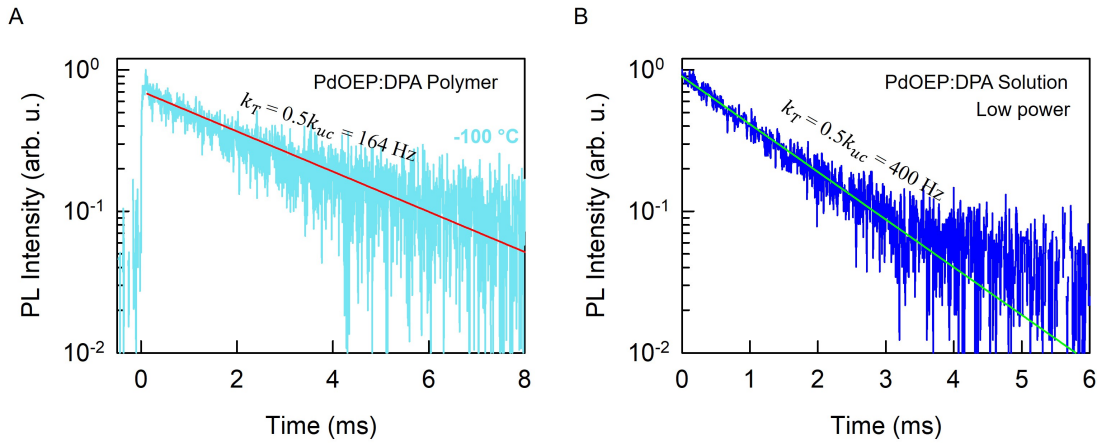

Figure 7.7: (a) Time-resolved UC-PL emission of the DPA:PdOEP polymer at 435 nm recorded at -100 °C under pulsed laser excitation at 532 nm (repetition rate 10 Hz). The solid line is the fit of the signal with a single exponential function (red line) with characteristic lifetime $\tau_{uc} = 0.5 \times \tau_T = 3.05$ ms. Therefore, the triplet spontaneous decay rate at -100 °C is $k_T = \frac{1}{\tau_T} = 164$ Hz. (b) Time-resolved UC-PL emission of the reference DPA:PdOEP (1.5×10^{-2} M : 1.9×10^{-5} M) solution in hexyl benzoate recorded at 435 nm under low power (200 mW cm^{-2}) modulated laser excitation at 532 nm (repetition rate 70 Hz) at room temperature. The experimental data are fitted with a single exponential decay function (green line) with characteristic decay time τ_{uc}, from which the DPA triplet lifetime results $\tau_T = 2 \times \tau_{uc} \sim 2.5$ ms (corresponding to a decay rate of 400 Hz).

(Fig. 7.6a) and rise time (Fig. 7.6b) upon lowering the temperature translates in the reduction of the TTA rate k_{TTA}, owing to the suppression of fast translational molecular motions in the frozen matrix, resulting in a slower, hopping-mediated TTA process within the ensemble of

close-packed DPAs.[46,252] Consistently, at -100 °C the UC-PL intensity decay exhibits a single exponential behavior in the millisecond time range, as expected for unquenched DPA triplets when the k_{TTA} is negligible with respect to the spontaneous triplet decay rate $k_T = 164$ Hz ($\tau_T = 6$ ms, Figure 7.7a).[47] Despite the ET yield is almost preserved, the UC-PL intensity at low temperature is reduced, because of the reduced TTA efficiency. Conversely, at room temperature the UC-PL intensity globally decays in a time $\tau_{uc} = 55$ μs that is much shorter than the intrinsic triplet lifetime, meaning that the TTA ($k_{TTA} \sim k_{uc} = \frac{1}{\tau_{uc}} = 18$ kHz) outcompetes the DPA triplets' spontaneous recombination rate ($k_T = 400$ Hz at 20°C as reported in Figure 7.7b).[47]

It is not trivial to carry out an accurate estimation of the pure hopping contribution to the TTA at room temperature, because it is not feasible to decouple the temperature effect on the hopping and translational mechanisms. Nevertheless, the steady-state measurements in Fig. 7.5a show that when the TTA is exclusively driven by triplet hopping at -100 °C, the UC-PL corresponds to 7% of the emission intensity at room temperature. Therefore, this value can be considered as the minimum contribution of pure hopping to the upconversion process, estimated under the most unfavorable conditions for TTA.

7.4 Upconversion performances in nanostructured polymers

To determine if the polymer morphology achieved in the proposed class of solid-state materials can influence also the upconversion performances in terms of figures of merit and dependence on the excitation intensity, I investigated these properties in the upconverting polymer as well as in a reference solution in HexBz with the same dyes concentration, so the samples optical density at 532 nm is the same (OD = 0.08). Figure 7.8 reports the *s*TTA-UC emission intensity decay of the nanostructured upconverting material (panel a) and of the DPA:PdOEP reference solution in HexBz (panel b), which I recorded as a function of the excitation intensity I_{exc} under a modulated 532 nm laser excitation. By varying the excitation intensity, I did not observe any variation in the UC-PL kinetics from the nanostructured polymer, consistently with the occurrence of the confined TTA-regime, where the k_{TTA} relies only on the excitation energy distribution within the upconverting nanodomains ensemble. This result is also corroborated by the comparison between the DPA triplet diffusion length and the mobile nan-

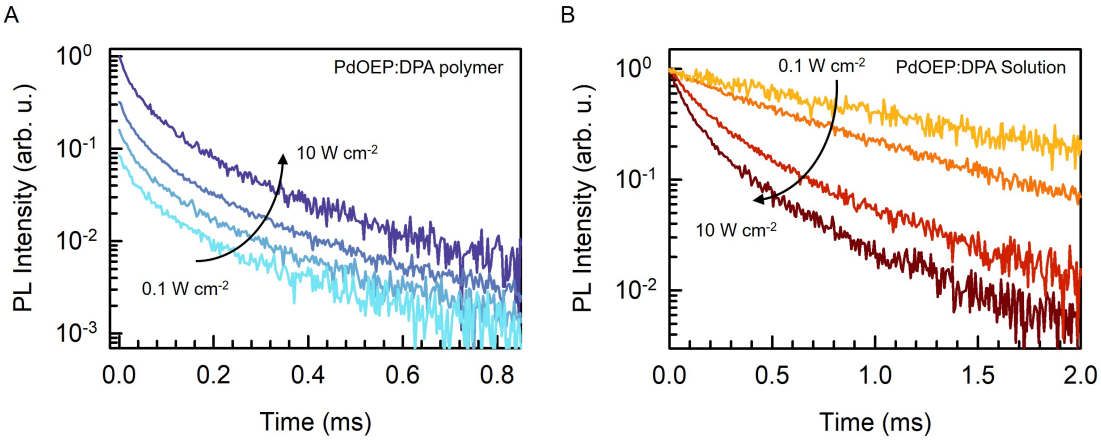

Figure 7.8: (a) UC-PL intensity decay at 435 nm of the DPA:PdOEP (1.4×10^{-2} M : 1.9×10^{-5} M) upconverting nanostructured polymer and (b) of the reference solution of DPA:PdOEP (1.5×10^{-2} M : 1.9×10^{-5} M) in hexyl benzoate as a function of the incident excitation intensity I_{exc} under a modulated 532 nm laser excitation (repetition rate 70 Hz).

odomain mean size obtained experimentally through time-domain NMR measurements. In fact, following the same approach illustrated in Sec. 6.4, applying Eq. 6.2, and considering the average nanodomain radius of 20 nm, the triplet diffusivity lower-limit is $D_T = 1.33 \times 10^{-7}$ cm^2 s^{-1}, therefore the lower-limit triplet diffusion length L_T is 447 nm, much greater than the average nanodomain diameter. Therefore, two triplets created in the same domain within their lifetime always annihilate before recombination. Conversely, the DPA:PdOEP reference solution exhibits the typical dependence on the I_{exc} which sets the k_{TTA}, consistently with a bulk homogeneous system.[138] The occurrence of the confined TTA kinetics also reflects on the trend of the upconversion quantum yield QY_{uc} as a function of I_{exc} in steady-state conditions, as shown in Figure 7.9a. For the upconverting polymer (blue circles) and the reference solution (orange triangles) the upconversion yield increases with increasing I_{exc} until the maximum QY_{uc} is reached. I measured the maximum QY_{uc} following the relative method reported in Sec. 2.7, using a solution composed of Pt(II) octaethylporphyrin (10^{-4} M) and DPA (10^{-2} M) in THF with $QY_{uc} = 25$ % as reference, and the polymer refractive index was assumed to be 1.5, similarly to previous works.[262] Importantly, I calculated the QY_{uc} as an average of nine measurements, performed on three independent samples, with three measurements per each sample choosing different excitation spots, and I obtained $QY_{uc} = 20 \pm 1$ % (circles), which matches the value of the reference solution (22 ± 1%, triangles). The power density was $I_{exc} =$ 20 W cm^{-2}, so in the regime of maximum efficiency.

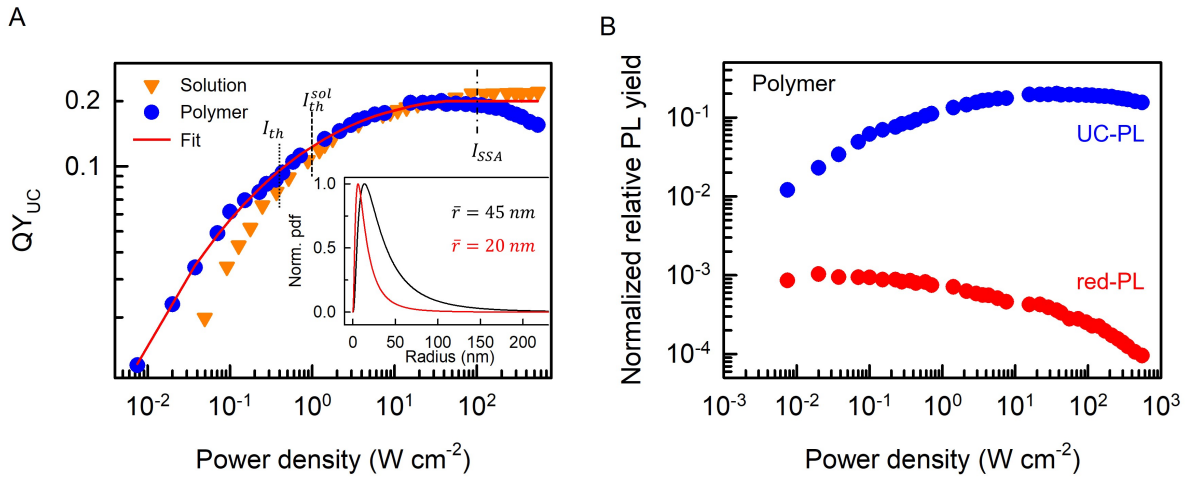

Figure 7.9: (a) *s*TTA upconversion quantum yield QY_{uc} of the upconverting polymer (blue dots) and the reference solution (orange triangles) under cw laser excitation at 532 nm as a function of I_{exc}. The short vertical lines mark the threshold excitation intensities: dotted line for the polymer, I_{th}, dashed line for the solution, I_{th}^{sol}. The dash-dotted vertical line marks the threshold intensity for the singlet-singlet annihilation activation (I_{SSA}) between DPA singlets populated by TTA. The solid line is the fit of the polymer experimental low-power data with the theoretical efficiency calculated considering an ensemble of upconverting nanodomains activated at different excitation intensities according to a size-dependent binomial statistics of excitation energy distribution, according to Eq. 1.43. The size distribution was assumed to be log-normal with an average diameter of 40 nm. The inset depicts the log-normal size distribution that reproduces the experimental data (black curve) and the log-normal size distribution that describes the real size distribution in the ensemble (red curve). (b) Normalized relative photoluminescence yield of the upconverted (blue circles) and of the residual sensitizer (red circles) emission in the DPA:PdOEP upconverting polymer.

Importantly, the QY_{uc} vs. I_{exc} plots highlight that the UC properties in the polymer differ from those observed in the corresponding solution at both low and high excitation intensities. At low power, the upconverting polymer exhibits a larger UC efficiency than the solution, because the excitation energy localization in the liquid domains enhances the TTA probability with respect to the homogeneous solution. Accordingly, the nanostructured polymer shows an excitation intensity threshold I_{th} of 0.4 W cm^{-2}, less than half the I_{th} of the reference solution (1.0 W cm^{-2}). It is worth noting that due to the considerable viscosity of HexBz (4.06 cP) and the low absorption at the excitation wavelength, the threshold value is higher than what typically observed for the same chromophores in low viscosity solvents (e.g. the THF viscosity is 0.48 cP at room temperature).[333]

To obtain an estimation of the nanodomains mean size, I applied the theoretical model proposed in Sec. 1.8.2, by fitting the experimental QY_{uc} vs. I_{exc} data with Eq. 1.43. The red solid line in Figure 7.9a is the fit of the QY_{uc} experimental data according to an excitation energy distribution in an ensemble of nanodomains characterized by a log-normal size distribution with average radius of 40 nm.[266] The inset of Fig. 7.9a shows the log-normal size distribution involved: the black curve takes into account the greater absorbing ability of the bigger nanodomains and therefore was used to fit the experimental data ($\mu = 3.42$ nm and $\sigma = 0.89$), corresponding to a mean nanodomain radius of 45 nm, while the red curve is the log-normal distribution that describes the real nanodomain size distribution in the system ($\mu = 2.62$ nm, $\sigma = 0.89$), resulting in a mean nanodomain radius of 20 nm, in excellent agreement with the structural data obtained by spin diffusion experiments.

It is worth noting that the red curve perfectly reproduces the experimental data until the I_{exc} of 100 W cm^{-2} is reached, where the discrepancy between expected and observed conversion yield is significant. A further increase of I_{exc} induces an efficiency loss that is not observed in the reference solution and that can be ascribed to the occurrence of singlet-singlet annihilation (SSA) in the nanodomains. Due to the high number of upconverted singlets on one side and the small size of the high-mobility domains on the other, the density of singlets created under large I_{exc} is sufficiently high to promote SSA with a rate k_{SSA} that is comparable to the singlet radiative decay rate $k_S = \frac{1}{\tau_{fl}} \sim 0.1$ GHz. Therefore, a second threshold intensity I_{SSA} can be identified, which marks the beginning of an excitation regime where SSA quenches the emitter fluorescence, reducing as a consequence the QY_{uc}.[33] To verify this hypothesis, I calculated the k_{SSA} between two DPA singlet excitons as $k_{SSA} = \gamma_{SS}[S]$, where γ_{SS} is the SSA second order rate constant and $[S]$ is the singlet exciton density, depending on the triplet exciton density $[T]$ through $[S] = \frac{1}{2} f[T]$, where the factor $\frac{1}{2}$ accounts for the fact that two triplets are requisite to obtain one singlet and f is the usual spin-statistical factor. The second order rate constant γ_{SS} can be calculated with the relation valid in the rapid diffusion limit $\gamma_{SS} = 8\pi D_S R_{SS}$, where $D_S = 1.2 \times 10^6$ cm^2 s^{-1} is the DPA diffusivity in HexBz at room temperature and $R_{SS} = 2.4$ nm is the Förster radius, taken as effective interaction distance between two DPA singlets. According to the modeling proposed, given the sample optical density of 0.08 at 532 nm, at the excitation intensity of 100 W cm^{-2} the k_{SSA} is ~ 0.3 GHz, thereby competitive with the DPA spontaneous singlet decay rate k_S.

An important observation can be drawn from Fig. 7.9b, which depicts the relative PL yield of

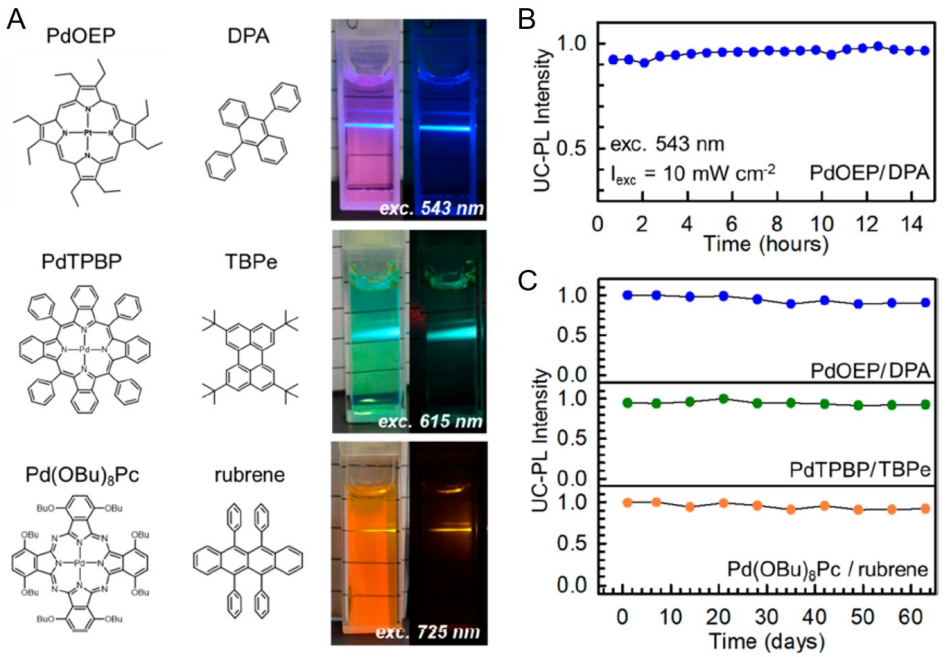

Figure 7.10: (a) Molecular structures of the different dye pairs incorporated in the glassy nanostructured polymer matrix. The pictures show the corresponding upconverting polymers in quartz cuvettes with 1 cm path length under irradiation at 543, 615, or 725 nm respectively. The samples are shown under ambient light and in the dark. (b) Evolution of the upconverted PL integrated intensity (UC-PL) of the upconverting polymer containing PdOEP:DPA (1.9×10^{-5} M:1.4×10^{-2} M) upon continuous irradiation at 543 nm (10 mW cm^{-2}) over 15 hours. (c) Integrated intensity of the UC-PL measured under excitation with a Xe lamp over 70 days for nanostructured polymers containing PdOEP:DPA, PdTPBP:TBPe (2×10^{-5} M:2×10^{-3} M) and Pd(OBu)8Pc:rubrene (10^{-5} M:1.8×10^{-4} M) as upconverting dye pairs, respectively.

the UC-PL compared to the residual PdOEP emission (red-PL) as a function of the excitation intensity. The red-PL intensity starts to decrease under a relatively low I_{exc} suggesting the occurrence of interactions between the excited sensitizers. Nevertheless, this loss in the PdOEP emission yield does not reflect on the corresponding UC-PL yield, which on the contrary follows the predicted model and it starts to decrease only above the I_{SSA}. This means that the residual PdOEP emission comes entirely from the negligible fraction of sensitizers in the rigid polymer matrix, while deleterious interactions do not affect the sensitizers in the mobile nanodomains, otherwise a concomitant reduction of the UC-PL yield should have been observed as well. This result is a further confirmation of the picture for the dye incorporation proposed.

7.5 Material versatility and stability

To test the stability of the upconverting materials under continuous irradiation, a DPA:PdOEP polymer, freshly prepared in-air, was exposed to continuous irradiation from a HeNe laser ($\lambda_{exc} = 543$ nm) at a power density of 10 mW cm^{-2} without any further protection from ambient conditions. The data collected over 15 hours reflect an excellent stability, as no loss of intensity was observed (Figure 7.10b).

To investigate the versatility of this new approach in the development of upconverting nanostructured materials able to work in different spectral ranges, polymers containing two other sensitizer/emitter pairs were fabricated, namely PtTPBP:TBPe and Pd(OBu)8Pc:Rubrene (see Sec. 3.4.2).[124,357] The molecular structures of the upconverting dyes employed are reported in Fig. 7.10a, along with digital pictures of the corresponding upconverting polymers in quartz cuvettes under irradiation at 543, 615, or 725 nm, respectively, both under ambient light and in the dark. All the systems display bright upconverted emission in different spectral ranges. Importantly, all three samples exhibit a remarkable shelf-life, with only negligible losses of the upconverted emission intensity over the time span of more than 2 months, as illustrated in panel c of Fig. 7.10.

7.6 Conclusions

To summarize, I reported a new strategy to fabricate *s*TTA-based upconverting nanostructured phase-segregated materials in which liquid nanodroplets that contain the upconverting dyes are stabilized with a block copolymer surfactant. This approach allows to reduce the number of components employed during fabrication with respect to other approaches, it affords final materials with superior optical quality, while an excellent conversion efficiency, comparable to that of the best solution-based systems, is achieved. The co-localization of sensitizers and emitters in liquid nanosized domains increases their local density to extremely high values $\geq 10^{-1}$ M without partitioning or aggregation effects that could affect the material's optical quality. This artificial confinement of triplet excitons in independent domains enables the *s*TTA-UC upconversion process to take place under conditions that minimize the influence of defects and to reach the confined *s*TTA regime, where the annihilation yield is maximized independently of the excitation intensity. Overall, this leads to a better *s*TTA-UC performance at

lower excitation intensities with respect to the corresponding liquid reference solution. These solid-state upconverters also show excellent stability and mechanical properties. These findings, considering the simplified fabrication route developed, its compatibility with scalable processes and the possibility to incorporate *a priori* any chromophore or luminescent nanomaterial according to the application demands, make these materials appealing for optical and photonic technological applications.

Bichromophoric annihilators to optimize the singlet generation efficiency

The still limited availability of emitters suitable to maximize the efficiency of singlet generation through triplet-triplet annihilation hinders the enhancement of the upconversion quantum efficiency beyond the values commonly achieved with standard sensitizer/emitter pairs. To address this issue, I report here the design and development of a fluorescent bichromophoric perylene derivative as annihilator that, when paired with a metallic porphyrin as sensitizer in a low viscosity solution, allows to achieve a record red-to-green external upconversion yield of 42%. This achievement directly stems from the annihilator's optimized photophysical properties that allow to reach a unit triplets-to-singlets conversion efficiency and from the annihilator structural features that guarantee high fluorescence yield even at high dye concentrations.

8.1 Molecular design rationale

Since the rapid development of *s*TTA-UC systems commenced a few decades ago, many upconverting systems have been proposed where optimized sensitizer/annihilator pairs afford upconversion quantum yields QY_{uc} greater than 20% also at excitation intensities comparable to the solar irradiance.[17–19] These encouraging results have been achieved mainly because of the huge efforts spent to develop efficient light harvesters/sensitizers, covering moieties from transition-metal complexes and metallic porphyrins to surface engineered semiconductor nanocrystals.[130,195,358] Nevertheless, the application of *s*TTA-UC is still deficient because of the typically challenging synthesis of efficient annihilators. Recently, Kimizuka and Yanai et al.

developed an excellent UV emitter, 1,4-bis((triisopropylsilyl) ethynyl)naphthalene (TIPS-Nph), reporting the highest visible-to-UV *s*TTA-UC efficiency of 10%, with the theoretical maximum set to 50%.[359] Also, some researchers designed a series of tetracene dimers, oligomers and dendrimers based on 9,10-diphenylanthracene (DPA) as annihilators, suggesting the promotion of the conversion efficiency through intramolecular TTA.[360–362] However, due to the structural planarity and rigidity of these annihilators, the process yield is still too limited.

Great attention has been dedicated to perylene, considered the ideal annihilator emitter for *s*TTA-UC for it satisfies important requisites towards the optimization of the upconversion performances. In fact, it shows almost unit fluorescence efficiency in diluted solutions and the $T_1 \rightarrow S_0$ transition is strictly forbidden yielding a T_1 lifetime on the milliseconds timescale, which favors the TTA over the triplet spontaneous recombination. Moreover, the substantial T_2 - T_1 energy difference satisfies the condition $E(T_2) \gg 2E(T_1) + k_BT$ (Sec. 1.3), and prevents the formation of both a quintet and high-energy triplets, resulting in a statistical factor $f \sim 1$, with the excited singlet generation as the only possible TTA outcome.[363–367] All these factors allow to maximize the external upconversion quantum yield (QY_{out}), defined as the ratio between the number of the upconverted photons that are effectively emitted and collected and the number of absorbed photons. The highest external upconversion yield reported so far is 38%, achieved with perylene coupled to palladium(II) tetraphenyltetrabenzoporphyrin (PdTPBP) in THF.[34] However, due to its structural planarity, perylene suffers from fluorescence quenching and excimer formation at high concentrations.[368] Excimers are formed as evanescent collisional complexes between an excited and a ground state molecule, thus their formation probability is usually enhanced by increasing the dye density.[369] To overcome this intrinsic issue, some perylene-derivative annihilators have been proposed, based on the addition of specific groups like alkyl, carbonitrile, or acetenyl groups meant to preclude aggregation.[370–372] But among these systems, the highest upconversion efficiency achieved is 17%, so still lower than with perylene and PdTPBP.

In this Chapter, I report the design of a new fluorescent bichromophoric perylene derivative, 4,12-diperylene[2.2]paracyclophane (PCP) working as triplet annihilator/emitter, with two twisted perylene chromophores in spatial orientation (Fig. 3.15). The molecular design includes a flexible spacer between two perylene units that should limit the $\pi - \pi$ stacking of perylene owing to the twisted structure, especially at high concentrations. By DFT calculation the average distance between the perylene chromophores was estimated to be 9.2 Å (see

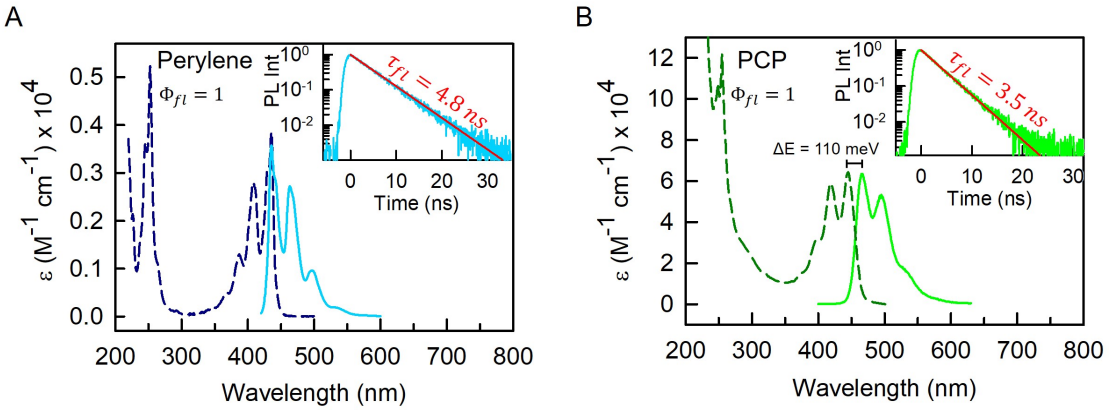

Figure 8.1: Molar extinction coefficient (dashed lines) and photoluminescence spectra of perylene (panel a) and PCP (panel b) in THF diluted solution (10^{-7} M). The PL spectra were recorded under a cw 370 nm excitation. The insets show the photoluminescence intensity decay recorded at the respective emission maximum under pulsed laser excitation at 405 nm (repetition rate 10 MHz). The solid lines are the fit of the experimental data with a single exponential decay function with characteristic lifetime τ_{fl}.

Sec. 3.5.2), large enough to avoid detrimental intermolecular interactions that could affect the perylene electronic properties, but sufficiently short to promote future application in solid-state upconverters, where the excitation energy can diffuse by intermolecular hopping.[360]

8.2 Photophysical properties of PCP

To assess if and how the structural modifications introduced by the PCP design can affect the photophysical properties with respect to perylene, I investigated side-by-side diluted solutions of PCP and perylene in THF by means of cw and time-resolved spectroscopy measurements, and I also tested how these properties are affected by the chromophore concentration. All the samples discussed in this Chapter were prepared in a glove box with oxygen concentration below 1 ppm and water concentration below 0.5 ppm, loaded in 1 mm quartz cuvettes, and sealed with hot glue and parafilm to prevent oxygen contamination. Figure 8.1 shows the main photophysical properties of a diluted (10^{-7} M) solution of perylene (panel a) and of PCP (panel b) in THF. The absorption and fluorescence profiles of the two molecules are quite similar. The PL spectra were recorded under a cw 370 nm excitation. The PCP first allowed electronic transition $S_0 \rightarrow S_1$ lies in the visible spectral range, with a maximum absorption peak at 445 nm, where the molar extinction coefficient ϵ is 6×10^4 M^{-1} cm^{-1}, i.e. about 20 times larger than for perylene. The absorption profile shows a series of vibronic replicas at 418 nm and 395

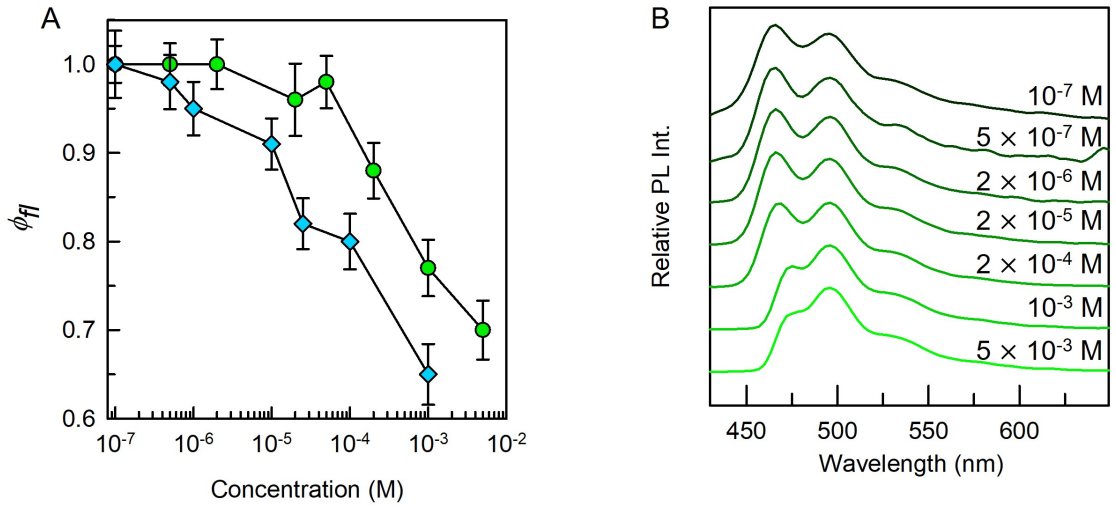

Figure 8.2: (a) PCP (dots) and perylene (diamonds) photoluminescence quantum yield Φ_{fl} as a function of the dye concentration in THF. (b) Photoluminescence spectra of the same PCP solution series as in (a) recorded under cw excitation at 380 nm.

nm, due to the coupling with the C-H vibrational modes ($\sim$ 160-180 meV) that are mirrored in the photoluminescence spectrum peaked at 465 nm.[373] The emission Stokes shift from the absorption is 110 meV, much greater than in perylene where it is negligible, which suggests a quite rigid structure with a limited molecular rearrangement in the excited state. The PCP fluorescence quantum yield Φ_{fl} in this diluted solution is $\sim$1, measured following the method in Sec. 2.7 with a diluted DPA solution in THF as reference. For this measurement I prepared the two solutions with optical density of 0.1 at the excitation wavelength of 370 nm in quartz cuvettes with 1 cm optical path. The insets of Fig. 8.1 report the fluorescence kinetics of the two molecules recorded at the respective PL maximum upon pulsed laser excitation at 405 nm. Both the decays are well fitted by a single exponential function, with a lifetime $\tau_{fl} = 4.8$ ns (corresponding to a decay rate $k_{fl} = 208$ MHz) for perylene, and $\tau_{fl} = 3.5$ ns ($k_{fl} = 285$ MHz) for PCP. The slight redshift of the PCP electronic energies and its excellent emission properties suggest that, despite the different molecular structure, PCP and perylene share similar fundamental photophysical properties and therefore PCP likely shows the attractive properties of perylene as annihilator. The computational analysis of the molecular system reported in the material characterization section (Sec. 3.5.2) supports this picture. The fact that PCP shows energies and emission properties very similar to those of perylene hints indeed that also the triplet states energies should be comparable, and the DFT calculations result in an estimated

$T_2 > 2\times T_1$ for both perylene and PCP. Despite this is a strictly qualitative comparison, since the calculated triplet energies can vary significantly according to the constraints imposed, this finding suggests that also PCP should be an excellent annihilator.[142]

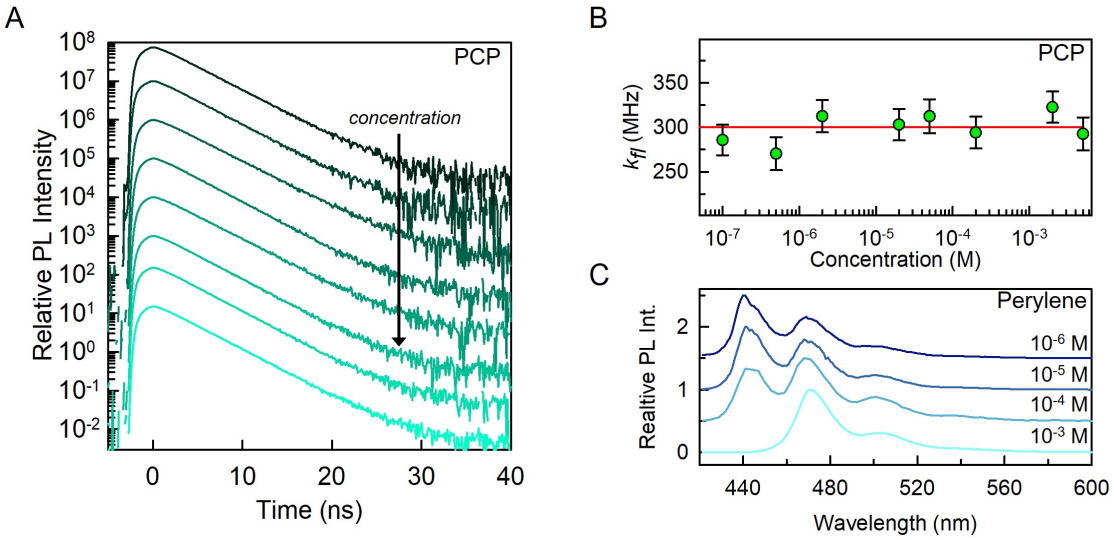

Figure 8.3: (a) Photoluminescence intensity decay recorded at 460 nm under a pulsed laser excitation at 405 nm (repetition rate 10 MHz) of PCP solutions in THF as a function of the concentration (10^{-7} M, 5×10^{-7} M, 2×10^{-6} M, 2×10^{-5} M, 5×10^{-5} M, 2×10^{-4} M, 2×10^{-3} M, 5×10^{-3} M). (b) Fluorescence decay rate k_{fl} recorded at 460 nm under pulsed laser excitation at 340 nm (repetition rate 10 MHz) for the same PCP solution series as in Fig. 8.2. (c) Photoluminescence spectra of a series of perylene solutions under cw excitation at 380 nm recorded as a function of perylene concentration, reported in the label.

To verify whether the PCP design strategy is effective in preventing aggregation that ultimately sets the molecular Φ_{fl}, I monitored the PCP emission yield as a function of concentration, compared to the perylene counterpart. This analysis is crucial since a quite large annihilator concentration is requisite to maximize the sensitizer-to-annihilator energy transfer efficiency. The external upconversion quantum yield QY_{out} can be limited because of partial self-absorption of the upconverted light generated from emitters with a fluorescence yield $QY_{fl} < 1$.[374] Moreover, in the specific case of perylene additional efficiency losses must be considered because of the appearance of aggregated species at high concentrations that introduce competitive energy dissipation channels.[375] In this perspective, Fig. 8.2a reports the experimental Φ_{fl} as a function of the PCP (circles) and perylene (diamonds) concentration, ranging from 10^{-7} M to 5×10^{-3} M in THF solution. Interestingly, for PCP the Φ_{fl} remains almost unaltered until above 10^{-4} M, then starts to decrease, reaching the value of 70% at the

maximum concentration employed (5×10^{-3} M). Remarkably, the Φ_{fl} reduction observed at high concentrations is less pronounced if compared to perylene over the same concentration range. I investigated these samples series by cw and time-resolved PL experiments to identify the origin of this efficiency loss. As shown in Fig. 8.2b, for PCP no variations in the emission profile can be detected until 10^{-3} M, while for perylene the emission spectrum starts to be affected at the concentration of 10^{-4} M (Fig. 8.3c). This effect can be ascribed to a less efficient emission self-absorption because of the larger Stokes shift in PCP. No substantial changes are

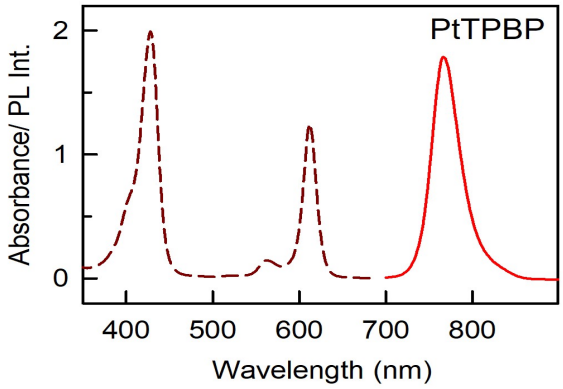

Figure 8.4: Absorption (dashed line) and phosphorescence (solid line) spectrum of PtTPBP in THF solution (10^{-4} M). The phosphorescence spectrum was recorded under a cw 635 nm laser excitation.

observed in the recombination rate of excited PCP molecules k_{fl}, which remains well assessed at around 300 MHz, as illustrated in Fig. 8.3a,b. This result suggests that the formation of excimeric species,[372] able to quench the dye photoluminescence,[376,377] is less effective in the PCP samples. The excimer formation is well known for perylene, which tends to form dark excimers, that cannot be directly probed with photoluminescence spectroscopy techniques.[376,377] Nevertheless, it is not possible to exclude *a priori* the spontaneous or photoinduced formation of stable PCP aggregates,[369] which can partially reabsorb the fluorescence, lowering the global yield without affecting the emission recombination kinetics. Despite the existence of excimers and stable aggregates should be still verified, the absence of fluorescence quenching strongly supports the conclusion that the peculiar PCP structure helps to reduce the excimer formation with respect to monomeric perylene,[368] allowing to employ higher dye concentrations without introducing critical energy losses.

8.3 *s*TTA-UC performances with PCP as annihilator

According to Eq. 1.11 and 1.12, it is well established that in *s*TTA-UC the external upconversion quantum yield depends on two annihilator's properties, the fluorescence efficiency and the statistical spin factor *f*. Because the thermodynamic limit of 50%[143] can only be reached

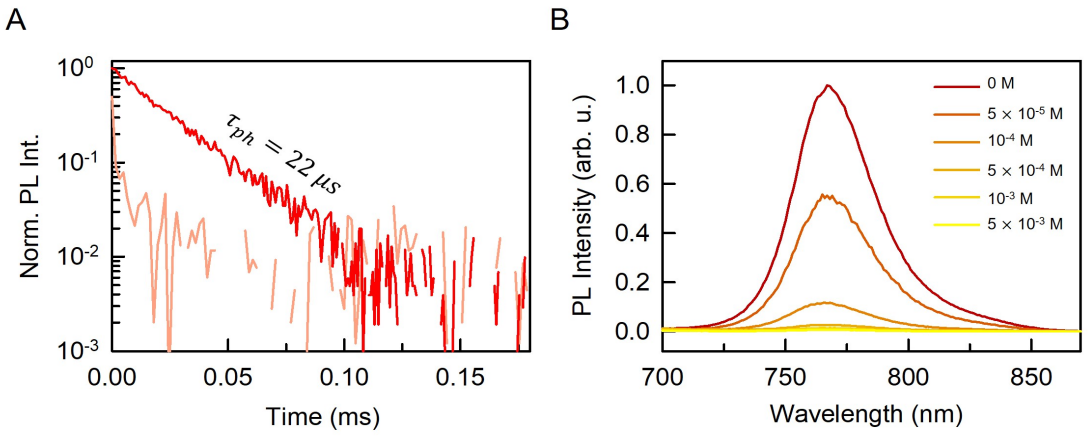

Figure 8.5: (a) Phosphorescence intensity decay recorded at 795 nm in a THF solution of PtTPBP (5 $\times 10^{-4}$ M) with (orange) and without (red) PCP (10^{-5} M) under modulated laser excitation at 635 nm (repetition rate 500 Hz). (b) Phosphorescence spectrum in a THF solution of PtTPBP (10^{-5} M), recorded under a cw 635 nm laser excitation, as a function of the PCP concentration (reported in the label), from which the Φ_{ET} values were calculated, reported in Table 8.1 (*vide infra*).

if each TTA event has one emissive singlet as outcome, its achievement depends on the annihilator electronic properties. After the investigation about the PCP fluorescence yield and its dependence on the chromophore concentration, I tested its ability as annihilator/emitter for the *s*TTA-UC in combination with the metalated porphyrin platinum(II) tetraphenyltetrabenzoporphyrin (PtTPBP) employed as triplet sensitizer in THF. The choice of PtTPBP as sensitizer of PCP triplets was dictated by the beneficial features afforded.[116] First, the central metal ion in the molecular structure yields a unit Φ_{ISC} followed by phosphorescence emission. In Fig. 8.4 the absorption and PL spectrum of a reference PtTPBP solution (10^{-4} M in THF) are reported. Upon cw 635 nm laser excitation a bright phosphorescence peaked at 785 nm can be observed (red curve), resonant with the perylene triplet at 820 nm,[16] with a phosphorescence yield of 22%, that I measured following the method in Sec. 2.7 using as reference Alexafluor^{TM} 647 in a PBS aqueous solution with known fluorescence quantum yield (33%),[378] and characteristic lifetime of 22 μs (Fig. 8.5a, red curve), long enough to grant efficient energy transfer towards

the PCP triplets. Moreover, the PCP photoluminescence ranging from 450 nm to 600 nm falls in the transparency window of PtTPBP delimited by the Soret and the Q-absorption bands[29–31] peaked at 430 nm and 613 nm respectively, thereby limiting the reabsorption of upconverted photons and back-energy transfer from the PCP upconverted singlets. In this regard, Fig.8.6b reports the PCP emission intensity decay at 475 nm recorded under a pulsed 405 nm laser excitation in the PCP:PtTPBP solution. Since the PCP fluorescence lifetime does not change in the presence of sensitizers, it is safe to exclude the presence of back-energy transfer from the PCP excited singlets to PtTPBP.

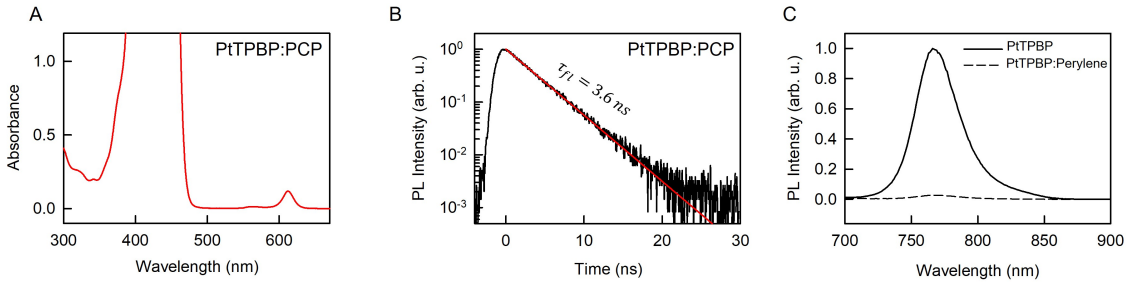

Figure 8.6: (a) Absorption spectrum of a solution of PCP:PtTPBP (5×10^{-4} M : 10^{-5} M) in THF. The sample optical density at 635 nm is 0.006, corresponding to the absorption coefficient of 0.14 cm^{-1}. (b) Photoluminescence intensity decay recorded at 475 nm under a pulsed laser excitation at 405 nm (repetition rate 10 MHz) of a PCP:PtTPBP (5×10^{-4} M : 10^{-5} M) solution. The PCP fluorescence lifetime does not change with and without sensitizer, suggesting the absence of efficient back-energy transfer from the PCP excited singlets to PtTPBP at this PCP concentration. (c) Phosphorescence spectrum of PtTPBP (10^{-5} M) in THF solution without (solid line) and with perylene (10^{-4} M, dashed line), recorded under a cw 635 nm laser excitation.

I then investigated the upconversion properties of a PtTPBP (10^{-5} M) and PCP (5×10^{-4} M) solution in THF. The absorption spectrum of the upconverting solution is reported in Fig. 8.6a. The sample optical density at 635 nm is 0.006, corresponding to the absorption coefficient of 0.14 cm^{-1}. As depicted in Fig. 8.7a, under cw laser excitation at 635 nm the solution exhibits a bright green upconverted emission, matching the PCP fluorescence spectrum. A digital picture of the bright upconverted emission upon 635 nm laser excitation is reported in Fig. 8.9a. Fig. 8.5b highlights the efficient phosphorescence quenching in the presence of emitters, and from the comparison between the integrated phosphorescence intensity without (I_0) and with (I) PCP, I calculated the energy transfer yield $\Phi_{ET} = 1 - \frac{I}{I_0} = 98\%$, an excellent result also confirmed by time-resolved experiments that show the effective quenching of the sensitizer

emission because of energy transfer (Fig. 8.5a). A similar ET efficiency is also observed for perylene at the same concentration (Fig. 8.6c), therefore it is reasonable to speculate that the PCP and perylene triplet energies do not significantly differ. Importantly, Fig. 8.5b also highlights the increasing ET efficiency upon increasing the PCP concentration. From the reduction of the PL intensity I calculated the ET efficiency for each PCP concentration and the results are reported in Tab. 8.1.

The occurrence of *s*TTA-UC is further demonstrated by cw and time-resolved experiments carried out as a function of the excitation intensity I_{exc}. As expected, the upconverted emission intensity increases upon increasing I_{exc} as reported in Fig. 8.7a. Fig. 8.7b shows the upcon-

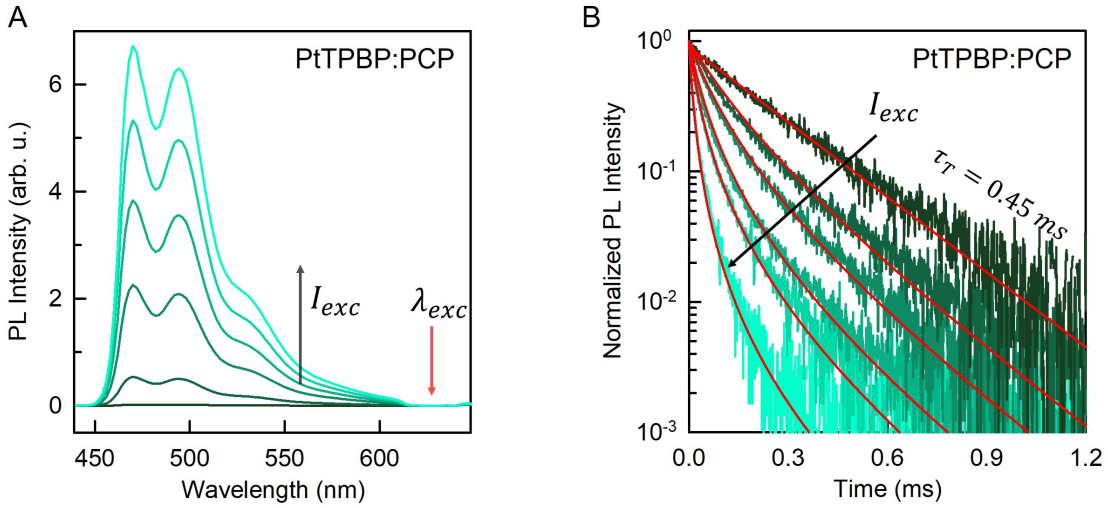

Figure 8.7: (a) Photoluminescence spectrum of a PCP:PtTPBP (5×10^{-4} M : 10^{-5} M) in THF as a function of the excitation intensity (I_{exc}) at 635 nm (λ_{exc}). (b) Upconverted fluorescence intensity decay at 460 nm under modulated excitation at 635 nm (repetition rate 200 Hz) recorded as a function of I_{exc}. The red lines are the fitting curves of the experimental data with Eq. 1.16. At the lowest excitation intensity employed, the TTA yield $\Phi_{TTA} = 0$ and the upconverted fluorescence decays as a single exponential function with characteristic lifetime $\tau_{uc} = 0.5 \times \tau_T = 0.225$ ms. By increasing the I_{exc}, the fitting procedure resulted in Φ_{TTA} equal to 0, 0.55, 0.72, 0.80, 0.90 and 0.96, respectively.

verted emission intensity (I_{uc}) decay at 460 nm as a function of I_{exc} upon a modulated 635 nm laser excitation. At any employed excitation intensity, the kinetics are significantly slower that the prompt PCP fluorescence, confirming the involvement of long living triplet states in the generation of the emissive singlet states. Moreover, consistently with the expected power-dependent TTA kinetics behaviour, the kinetics accelerate upon increasing the I_{exc}. At the lowest I_{exc} employed, 0.1 W cm^{-2}, the signal decays as a single exponential function with

characteristic lifetime $\tau_{uc} = 0.225$ ms, equal to twice the PCP triplet lifetime $\tau_T = 2\tau_{uc} = 0.45$ ms ($k_T = \frac{1}{\tau_T} = 2.2$ kHz). Eq. 1.16, knowing τ_T, allows to carefully analyze the upconverted emission kinetics under increasing excitation intensities. The solid lines in Fig. 8.7b are the fitting curves of the experimental data where the only free parameter is the TTA yield Φ_{TTA}, which grows from 0 at $I_{exc} = 0.1$ W cm^{-2} to 96% at $I_{exc} = 50$ W cm^{-2}. This behavior mirrors the intrinsic bimolecular nature of the TTA process, owing to the k_{TTA} and Φ_{TTA} dependence on I_{exc}, that sets the triplet density available for annihilation.

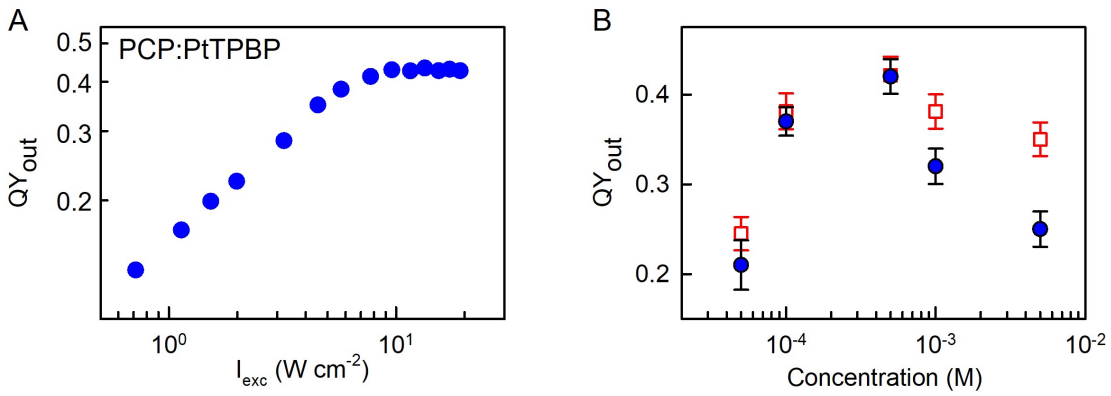

Figure 8.8: (a) *s*TTA-UC upconversion external quantum yield QY_{out} for a PCP:PtTPBP (5×10^{-4} M : 10^{-5} M) solution in THF as a function of the incident excitation intensity I_{exc} under cw laser excitation at 635 nm. (b) Comparison between the theoretical QY_{out} values (squares, also reported in Tab. 8.1) calculated using Eq. 1.11 from independently determined parameters and the experimental values (dots) measured as a function of the PCP concentration under an $I_{exc} = 20$ W cm^{-2}.

This strong dependence on I_{exc} also shows up in the behavior of QY_{out}. Under cw 635 nm laser excitation, as predicted by the model of TTA in homogeneous upconversion systems, at low powers the TTA is negligible and QY_{out} depends linearly on I_{exc}, while QY_{out} plateaus to a constant value at high excitation powers, where Φ_{TTA} is equal to unity, consistently with the time-resolved results. The threshold excitation intensity is I_{th} 1.3 W cm^{-2}, which is larger than the typical values observed in solution-based upconverters, because of the system's low absorption at the excitation wavelength and the relatively short lifetime of the annihilating triplets. Importantly, I measured the QY_{out} under an excitation intensity of 20 W cm^{-2}, well above the threshold intensity, and it resulted 42 $\pm$ 3%, which is the highest performance observed for *s*TTA-UC to date. I performed this measurement following the method in Sec. 2.7, using as reference the same solution employed for the determination of the PtTPBP phospho-

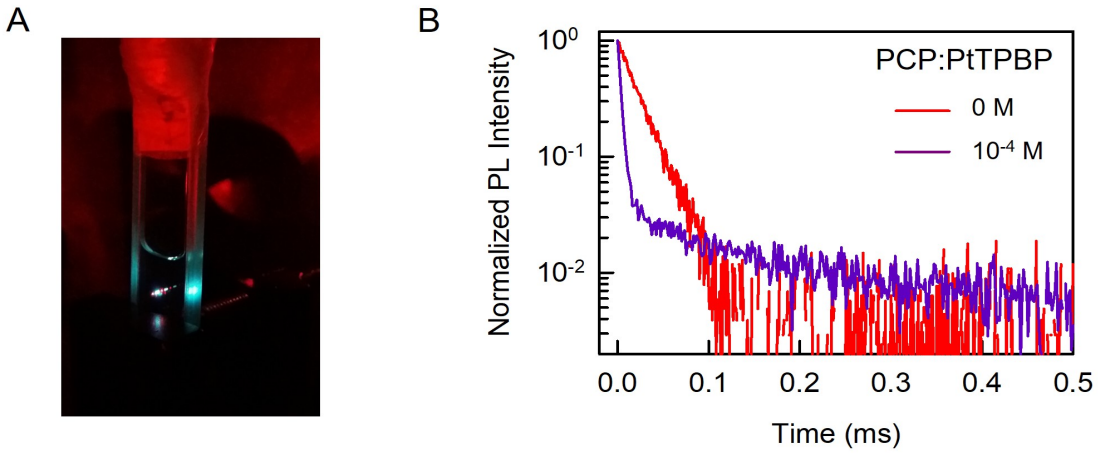

Figure 8.9: (a) Digital picture of the upconverting solution (PCP:PtTPBP in THF, 5×10^{-4} M : 10^{-5} M) upon cw 635 nm laser excitation. (b) Phosphorescence intensity decay recorded under a 635 nm modulated laser excitation (repetition rate 500 Hz) at 795 nm in a THF solution of PtTPBP (10^{-5} M, red curve), and in an upconverting PCP:PtTPBP solution (10^{-4} M : 10^{-5} M, purple curve) in THF.

rescence quantum yield. The same result was also obtained in an independent measurement employing methylene blue ($QY_{ref} = 3\%$)[379] as reference. As further confirmation, the maximum QY_{out} was measured also using the solution with TTBP:PtTPBP in THF reported in Ref.[269] as reference ($QY_{ref} = 27\%$), obtaining $QY_{out} = 41 \pm 2\%$. Moreover, the measured QY_{out} value is in agreement with the expected value reported in Tab. 8.1, calculated according to Eq. 1.11. Notably, these results infer that the statistical factor $f = 1$, which means that the TTA cannot populate either the quintet states or the T_2, and confirm that PCP preserves the perylene electronic properties, which are an essential requisite to enhance the QY_{out} owing to the maximization of the singlet generation yield. Table 8.1 reports the QY_{out} values calculated using Eq. 1.11, with f and $\Phi_{ISC} = 1$, and with the ET and fluorescence efficiencies measured experimentally considering different PCP concentrations obtained from the measurements in Figures 8.2a and 8.5b, compared with the corresponding QY_{out} values measured experimentally (QY^*_{out}) for each PCP concentration. This comparison is also highlighted in Fig. 8.8b. Interestingly, by decreasing the PCP concentration to 10^{-4} M, the gain in Φ_{fl} is balanced by a reduction of Φ_{ET} resulting in a measured QY_{out} of $37 \pm 3\%$. If the PCP concentration is further decreased below 10^{-4} M or increased above 10^{-3} M, the QY_{out} undergoes a severe reduction, even worse than what predicted. The discrepancy at low concentrations can be ascribed to the involvement of back-energy transfer from PCP triplets to the sensitizers. In fact, as reported in

PCP Concentration [M]	Φ^*_{ET}	Φ^*_{fl}	QY_{out}	QY^*_{out}
5×10^{-3}	1	0.7	0.35	0.25
10^{-3}	0.99	0.77	0.38	0.32
5×10^{-4}	0.98	0.86	0.42	0.42
10^{-4}	0.82	0.93	0.39	0.37
5×10^{-5}	0.53	0.98	0.26	0.21

Table 8.1: External upconversion quantum yield values calculated (QY_{out}) using Eq. 1.11, with f and $\Phi_{ISC} = 1$, and with the ET and fluorescence efficiencies measured experimentally with different PCP concentrations (Φ^*_{ET}, Φ^*_{fl}), compared to the corresponding external upconversion quantum yield values measured experimentally QY^*_{out} for each PCP concentration.

Fig. 8.9b I recorded the phosphorescence intensity decay at 795 nm, under a modulated 635 nm laser excitation, of the reference PtTPBP solution (red curve) and of an upconverting solution with PCP concentration 10^{-4} M (purple curve). The slow component observed in the upconverting solution has a lifetime longer than the spontaneous phosphorescence lifetime of 22 μs and it indicates the occurrence of back-energy transfer from the long-living PCP triplets to the sensitizer triplets, which results in a delayed PtTPBP phosphorescence.[138] On the contrary, further studies are still required to assess the behavior at very high PCP concentrations.

8.4 Conclusions

The newly designed annihilator/emitter chromophore enabled to reach the exceptional external quantum efficiency of 42% for photon upconversion based on *s*TTA, close to the theoretical upper limit of 50%. The experimental results indicate that for the newly designed PCP dye the energetic condition $E(S_1) \ll 2E(T_1) + k_BT \ll E(T_2)$ is satisfied, therefore the generation of emissive singlets by TTA is maximized and the output light intensity is only limited by the emitter fluorescence efficiency, and/or by the sensitizer-to-emitter energy transfer yield. These findings suggest that a derivation from known molecular systems with excellent upconversion properties is a viable and promising strategy to develop new chromophores suitable to realize efficient annihilators, especially for visible-to-UV or near-infrared-to-visible upconverters. Achieving efficient TTA in these spectral ranges would significantly boost the application of the *s*TTA-UC mechanism, allowing to enhance the efficiency of *s*TTA-UC devices, such as so-

lar cells and OLEDs which already show technological appealing performances. Importantly, the peculiar molecular bichromophoric structure designed is helpful in limiting aggregation phenomena that usually affect conjugates systems at high dyes concentrations, and it can be relevant especially in future development of solid-state upconverters.

Perspective

In this last Chapter, I apply the theoretical models for the classical and confined *s*TTA-UC regimes described in Secs. 1.8.1-1.8.2 to highlight the great potential of nanostructured materials, such as nanophase-separated glassy polymers, in solar applications. I compare the *s*TTA-UC performances of an ideal homogeneous bulk UC system, of a confined single-sized UC system and of a confined UC system with log-normal size distribution. The models allow to identify how the *s*TTA-UC performances change by changing structural parameters (e.g. the nanostructures mean radius or the size distribution),[259,262] or composition parameters (such as the system optical density or the emitter triplet lifetime). The aim of these comparisons is to point out the advantages introduced by the excitation energy confinement, which influence the *s*TTA-UC performances, but also to emphasize the structural and composition properties needed to optimize the conversion performances in each system considered. The important information gained through the theoretical calculations sheds light on the design requisites of solid-state upconverters to make future implementation of solid-state upconverters in solar technologies possible. Importantly, to give a general perspective of the potential future achievements employing this class of materials, I report the theoretical *s*TTA-UC performances that can be achieved in an ideal situation, i.e. by incorporating broadband sensitizers in nanostructured polymers. Importantly, this composition represents the meeting point of the two main topics discussed in this PhD thesis, since I investigated on one side hybrid systems with the goal to increase the upconverter storage ability, while on the other I demonstrated the numerous advantages introduced by the upconverting dye confinement in nanosized domains. Therefore, as a whole this combined composition represents an ideal solid-state upconverter that can potentially pave the way towards real-life solar devices. Importantly, I performed the

theoretical calculations reported using the solar irradiance at 1.5AM as reference, in order to visually point out the potential advantages afforded by the ideal upconverter.

Results

In applying the previously discussed classical and confined *s*TTA-UC models, I consider ideal green-to-blue upconverting organic systems, where the theoretical results can be straightforwardly compared to experimental data. I assume a unity optical density at the excitation

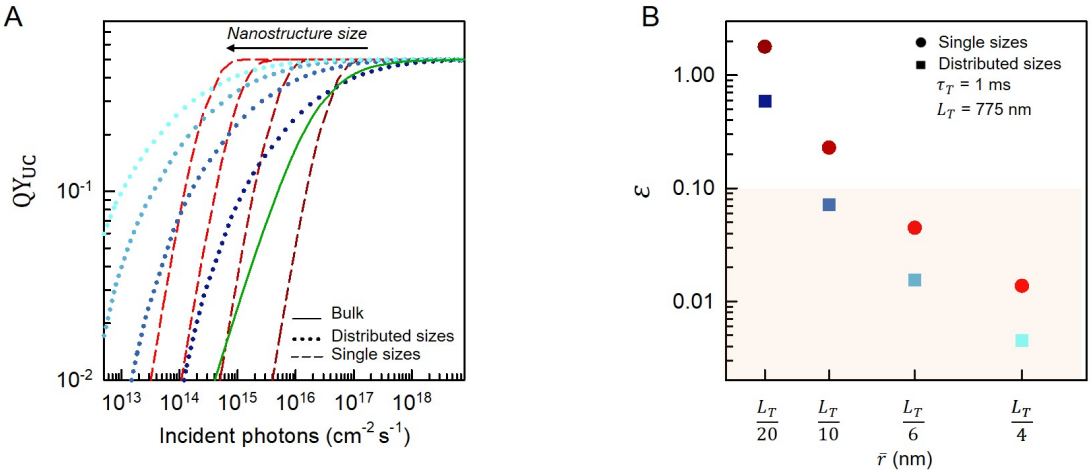

Figure 9.1: (a) *s*TTA-upconversion quantum yield QY_{uc} dependency on the excitation intensity I_{exc} for a classical bulk system (solid curve, calculated with Eq. 1.11), for an identical single-sized UC-centers ensemble (dashed curves, calculated with Eq. 1.38) and for a log-normally size-distributed UC-centers ensemble (dotted curves, calculated with Eq. 1.43). I assumed optical density 1 at the excitation wavelength of 532 nm, $D_T = 10^{-6}$ cm^2 s^{-1} and $\tau_T = 1$ ms, yielding $L_T = 775$ nm. The parameter ρ is set equal to 0.1, f, Φ_{ET} and Φ_{fl} equal to unity. Moreover, for both confined systems I considered a set of four values of the UC-centers mean radius $\overline{r} = \frac{L_T}{4}, \frac{L_T}{6}, \frac{L_T}{10}$ and $\frac{L_T}{20}$ (from right to left, according to the arrow direction). (b) Dependency of $\epsilon = \frac{I'_{th}}{I_{th}}$ on $\overline{r}$ for a single-sized UC-centers ensemble (dots) and for a log-normally distributed UC-centers ensemble (squares). The shaded area denotes the region of effective gain in the threshold reduction, where $\epsilon < 0.1$.

wavelength of 532 nm for all the systems discussed. I set the annihilating triplets diffusivity to $D_T = 10^{-6}$ cm^2 s^{-1} and their lifetime $\tau_T = 1$ ms, which are typical values observed in the most studied upconverters in solution,[41] where the annihilator concentration can be as large as 10^{-2} M, and according to Eq. 1.33, the diffusion length is $L_T = 775$ nm, thus the rapid diffusion condition is satisfied. When considering confined systems, the parameter ρ (i.e. the ratio

between the total volume of the excited liquid nanodomains containing the absorbing dyes and the total excitation volume,) is set equal to 0.1. This value allows to treat the system as a model case where the dye confinement affords a significant increase of the excitation energy density by one order of magnitude, therefore the confinement effects on the *s*TTA-UC kinetics are expected to be relevant. For simplicity, the parameters f, Φ_{ET} and Φ_{fl} are considered equal to unity, thus the maximum yield achievable is 0.5, according to energy conservation. Figure 9.1 illustrates the results of the calculation for the upconversion yield dependence on the excitation intensity for a bulk solution (solid curve, calculated with Eq. 1.11), an ensemble of identical single-sized UC-centers (dashed curves, calculated with Eq. 1.38) and a log-normally size-distributed UC-centers ensemble (dotted curves, calculated with Eq. 1.43). To identify

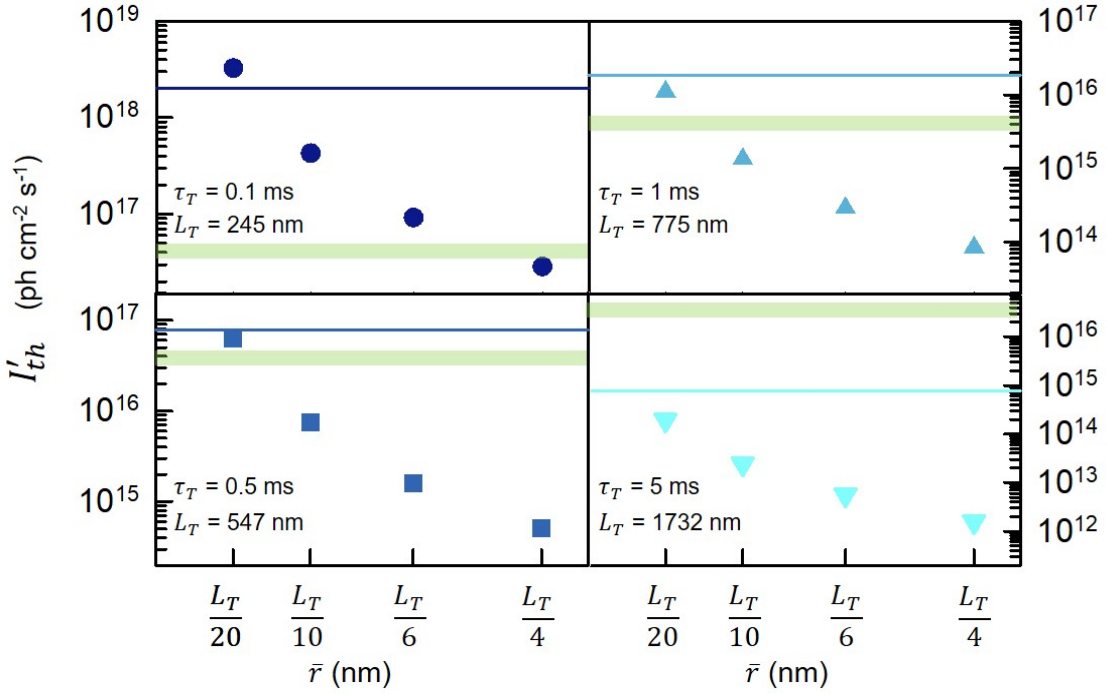

Figure 9.2: Dependency of I'_{th} on $\bar{r}$ for an ensemble of UC-centers log-normally distributed considering four different emitter triplet lifetimes, $\tau_T = 0.1$ ms (dots), $\tau_T = 0.5$ ms (squares), $\tau_T = 1$ ms (up-triangles), and $\tau_T = 5$ ms (down-triangles). The solid lines represent the I_{th} in the corresponding reference bulk solutions. The shaded stripes show the photon density absorbed by a model *s*TTA-UC system under solar irradiance in the AM1.5 condition assuming a 100 nm wide absorption band around the 532 nm excitation wavelength.

the correlation between UC-center size and upconversion yield, I accounted for four different values of the UC-centers mean radius $\bar{r}$, ranging from $\frac{L_T}{4}$ down to $\frac{L_T}{20}$, and I generated the

four log-normal distributions considering each mean radius $\overline{r}$ and $\sigma = 0.88$. I employed this σ value since it is the one I obtained experimentally in the model system discussed in Chapter 6, therefore it is a reasonable value that can be obtained experimentally and describes a real system.

The advantage introduced by the confinement strategy is paramount. Except for $\overline{r} = \frac{L_T}{20}$, in both confined systems the threshold excitation intensity (denoted I'_{th}) decreases significantly with respect to the solution (denoted I_{th}). Moreover, the reduction of the threshold intensity is clearly more extensive when considering UC-centers with larger $\overline{r}$ values, in agreement with Eq. 1.43, because it is more probable for larger UC-centers to contain two excitons simultaneously. This effect is particularly evident in the log-normally distributed ensemble, because, as discussed in the earlier text, in this configuration the larger UC-centers in the distribution contain an increased number of light harvesters. Therefore, their excitation probability is fur-

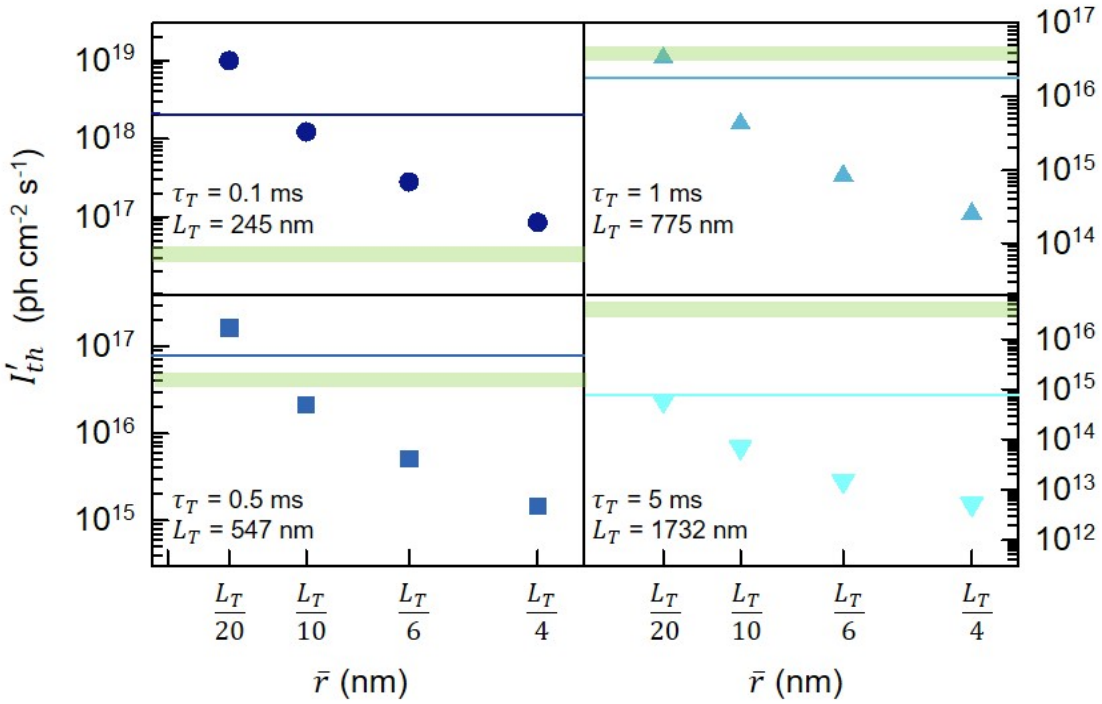

Figure 9.3: Dependency of I'_{th} on $\overline{r}$ for an ensemble of single-sized UC-centers considering four different emitter triplet lifetimes, $\tau_T = 0.1$ ms (dots), $\tau_T = 0.5$ ms (squares), $\tau_T = 1$ ms (up-triangles), and $\tau_T = 5$ ms (down-triangles). The solid lines represent the I_{th} in the corresponding reference bulk solutions. The shaded stripes show the photon density absorbed by a model *s*TTA-UC system under solar irradiance in the AM1.5 condition assuming a 100 nm wide absorption band around the 532 nm excitation wavelength.

ther enhanced by their higher absorption ability. This feature is easy to see in Fig. 9.1a, which shows that, once fixed the $\overline{r}$, the log-normally distributed ensemble is more efficient at low excitation powers than the corresponding single-sized ensemble. This finding is confirmed by the data in Fig. 9.1b, which reports the ratio

$$\epsilon = \frac{I_{th}^{'}}{I_{th}} \tag{9.1}$$

which provides an estimation of the effective gain in the low power *s*TTA-UC performance afforded by nanostructuring, as a function of the UC-centers average size. Regardless of the $\overline{r}$ value, a broad size distribution is always more beneficial than having monodispersed UC-centers. This is a key result from the material fabrication perspective, because it means that high control over the UC-centers size is not only unnecessary, but also disadvantageous, thus allowing to relax some constraints in the material synthesis. The shaded area denotes the region where the threshold reduction becomes interesting for applications, i.e. when $\epsilon < 0.1$. Importantly, a strong confinement down to $\overline{r} = \frac{L_T}{20}$ is not so beneficial in the log-normal distribution ensemble ($\epsilon = 0.6$) and, notably, it is deleterious in the single-size ensemble ($\epsilon = 1.8$), with a threshold higher than in the reference solution because the UC-centers are so small that only at extremely high powers the $P_{n\geq 2}$ value becomes relevant. On the other hand, larger $\overline{r}$ values allow to reduce extensively the system threshold, with expected ϵ values lower than 0.01 for $\overline{r} = \frac{L_T}{4}$. This means that the global upconversion threshold can be reduced by more than two orders of magnitude with respect to a bulk homogeneous system, without operating on the chromophores properties or concentrations, but only by acting on their spatial arrangement. This finding further demonstrates the validity of the nanostructured polymers design strategy and, most importantly, that there is no need of a highly controlled dye confinement to boost the upconversion performances at low powers. The optimal UC-center average size must be properly tuned to find a trade-off between the achievement of the confined *s*TTA kinetics, to lose the dependency on the triplets diffusivity, and the maximization of the UC-center multiple excitation probability, with consequent further simplifications in the material synthesis.

Relying on Eqs. 1.13 and 1.39, I investigated the role of the emitter triplet lifetime τ_T to probe further advantages of the confinement concept, since it is a crucial parameter that affects the *s*TTA-UC process. The τ_T role in determining the threshold and its extremely high sensitivity to the environment make it often the most critical point to deal with when developing new upconverters in the solid-state. Figure 9.2 reports the $I_{th}^{'}$ calculated for a log-normally dis-

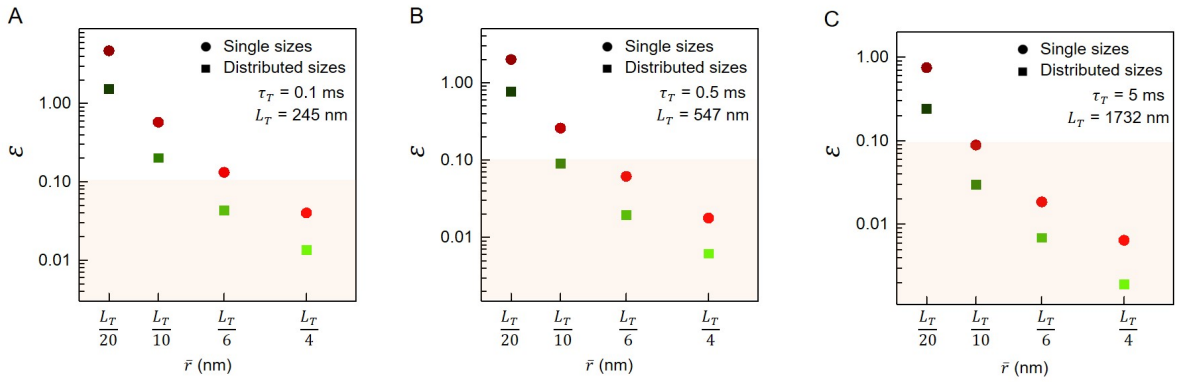

Figure 9.4: Dependency of ϵ on $\overline{r}$ for a single-sized UC-centers ensemble (dots) and for a log-normally distributed UC-centers ensemble (squares), when $\tau_T = 0.1$ ms (a), $\tau_T = 0.5$ ms (b) and $\tau_T = 5$ ms (c). The shaded areas denote the regions of effective gain in the threshold reduction, where $\epsilon < 0.1$.

tributed UC-centers ensemble as a function of τ_T, in a range between 5 ms down to 0.1 ms, and keeping fixed the triplet diffusivity coefficient D_T. These results confirm that the optimal UC-center mean size is $\overline{r} = \frac{L_T}{4}$, which allows the nanostructured system (dots) to have a threshold more than two orders of magnitude lower than the corresponding homogeneous solution (solid lines), independently of the triplet diffusion length set by each τ_T value. I obtained analogous results for a single-sized UC-centers ensemble, depicted in Figure 9.3.

Using the results in Fig. 9.2 I calculated and reported in Fig. 9.4, the ϵ values also for $\tau_T = 0.1$ ms, $\tau_T = 0.5$ ms and $\tau_T = 5$ ms to highlight the effectiveness of the nanostructuring strategy in boosting the UC performances.

The analysis performed so far allows to draw some important considerations regarding the potential implementation of solid-state upconverters in solar technologies. The shaded green stripes show the photon density absorbed by a typical *s*TTA-UC system under solar irradiance in the AM1.5 condition (I_{sun}). Specifically, it indicates the harvested photon flux considering a 100 nm wide absorption band around the 532 nm excitation wavelength, which can be obtained in broadband absorption systems based on a multi-sensitizers composition[74,155,156] or that exploit semiconductor nanostructures (e.g. nanocrystals)[141,193] as light harvesters. With τ_T as large as 5 ms, even a classical upconverting solution system works below the solar irradiance, thereby in this case the nanostructuring process is not strictly necessary from a performance point of view, unless exceptionally low excitation intensities are involved. Nonetheless, the confinement can be of course useful since illumination conditions are not always optimal during daytime, and it would afford an effective irradiance lower than I_{sun}. However, it is hard

to achieve so large τ_T values even with the best annihilators that usually feature lifetimes ~ 1 ms in organic solvents.[380] As reported in Fig. 9.2b, in this condition the nanostructuring can

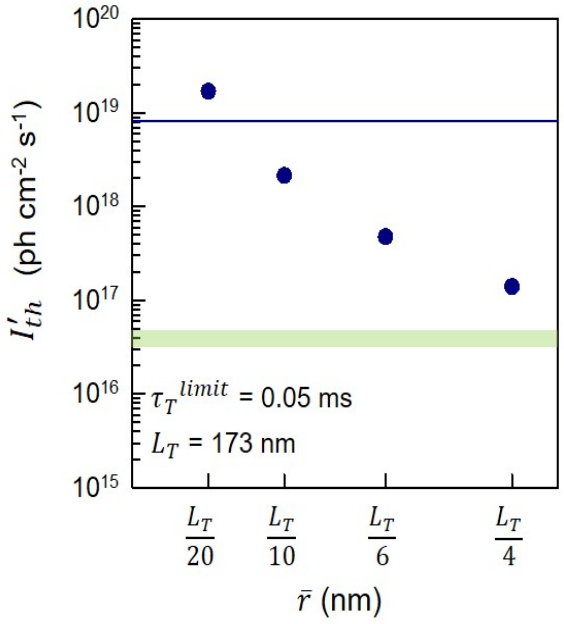

Figure 9.5: Dependency of I'_{th} on $\overline{r}$ for an ensemble of UC-centers log-normally distributed, for the τ_T lower-limit value $\tau_T^{\text{limit}} = 0.05$ ms (dots). The solid line refers to the I_{th} in the corresponding reference bulk solution. The shaded stripe shows the photon density absorbed by a model *s*TTA-UC system under solar irradiance in the AM1.5 condition considering a 100 nm wide absorption band around the 532 nm excitation wavelength.

be really useful to develop technologically appealing upconverters that work at the extremely low excitation intensity of $\sim 0.01 I_{sun}$. Most importantly, the confinement enables the *s*TTA-UC to work under solar illumination also in systems with $\tau_T \ll 1$ ms. The case of $\tau_T = 0.5$ ms is rather instructive as it is clear that just by changing the nanostructures mean radius the outcome is severely different. While the solution threshold is above the solar irradiance, by realizing an UC-center ensemble with average size $\overline{r} = \frac{L_T}{10}$ the I'_{th} shifts below I_{sun}. Even using emitters with $\tau_T = 0.1$ ms an optimized confinement enables to have efficient upconversion at subsolar excitation intensities.

I also identified $\tau_T^{\text{limit}} = 0.05$ ms as the lower-limit value for the emitter triplet lifetime, because, as reported in Fig. 9.5, for $\tau_T < \tau_T^{\text{limit}}$ the confinement strategy results ineffective in reducing significantly the I'_{th}, unless an extremely fast diffusion environment is employed to compensate the short lifetime of the annihilating excitons and keep the L_T reasonably large.

As last consideration, I discuss the rationale employed in the selection of the UC-centers mean

radii $\overline{r}$, from $\frac{L_T}{20}$ to $\frac{L_T}{4}$, and the range of radii r chosen to generate the log-normal distributions to perform the theoretical calculations reported so far. The results reported in Fig. 9.1 point out that the relative weight of larger UC-centers in setting the excitation threshold is higher than the smaller ones because of their enhanced absorption ability. Thereby dealing with UC-centers with sizes distributed log-normally with mean size $\overline{r}$ is to be preferred to monodispersed UC-centers with size $\overline{r}$, because it allows to reduce the excitation threshold. Nevertheless, considering a too large size distribution would result in losing the confinement condition, retrieving the standard bulk *s*TTA-UC regime in larger UC-centers with a potential reduction of the efficiency at low powers. Therefore it is essential to verify that the confined

D_T [cm^2 s^{-1}]	τ_T [s]	L_T [nm]	$\overline{r}$	$\overline{r}/L_T$
10^{-6}	10^{-4}	245	$L_T/20$	0.1
10^{-6}	5×10^{-4}	548	$L_T/10$	0.2
10^{-6}	10^{-3}	775	$L_T/6$	0.34
10^{-6}	5×10^{-3}	1732	$L_T/4$	0.51

Table 9.1: Parameters employed for the calculation of triplet diffusion lengths and upconversion quantum yields in the confined *s*TTA-UC condition.

condition is satisfied for any configuration analyzed. In this regard, for each triplet lifetime and triplet diffusion length L_T considered, I chose the mean radius $\overline{r}$ of the UC-center distributions as $\frac{L_T}{20}$, $\frac{L_T}{10}$, $\frac{L_T}{6}$ and $\frac{L_T}{4}$. Since the diffusion length L_T is the mean displacement that a randomly diffusing exciton reaches from its generation point, for isotropic diffusion L_T is the diameter of the sphere explored by the exciton during its lifetime, therefore the volume accessible to the triplet excitons is, respectively, $\frac{1}{1000}$, $\frac{1}{125}$, $\frac{1}{27}$ and $\frac{1}{8}$ of the volume that can be potentially explored by the triplets. This means that for each $\overline{r}$ considered, the condition to have confined *s*TTA-UC is satisfied, even in the limit case of $\overline{r} = \frac{L_T}{4}$.

Moreover, I generated the log-normal distributions with mean radius $\overline{r}$ and with $\sigma = 0.88$ as parameters, and I adopted the rationale to employ distributions calculated over a range of r values up to a reference value $r' > \overline{r}$, which is the size that marks the 90% of the integrated log-normal distribution area, thus accounting for 90% of the UC-centers in the ensemble. As reported in Table 9.1, $r' < L_T$ for all the distributions employed, thus demonstrating that the confinement condition is always satisfied in the ranges of sizes considered for the calculations.

Radius $\overline{r}$	$\tau_T = 0.1$ ms	$\tau_T = 0.5$ ms	$\tau_T = 1$ ms	$\tau_T = 5$ ms
$L_T/_{20}$	1.00	1.00	1.00	1.00
$L_T/_{10}$	1.00	1.00	0.97	0.93
$L_T/_{6}$	0.97	0.90	0.86	0.74
$L_T/_{4}$	0.89	0.73	0.66	0.55
$L_T/_{3}$	0.72	0.53	0.45	0.26
$L_T/_{2}$	0.43	0.25	0.20	0.10

Table 9.2: TTA yield Φ_{TTA} as a function of the single-size nanostructure radius $\overline{r}$ and triplet lifetime calculated with $\overline{T}_E = 13$. The Φ_{TTA} is calculated as the ratio between the annihilation rate (k_{TTA}) and the total triplet decay rate ($k_{TTA} + k_T$).

Table 9.2 reports the annihilation yield Φ_{TTA} values calculated for a single-sized UC-centers ensemble when the excitation intensity is the minimum required to have two triplet excitons per UC-center, so that to have an annihilation event. With a binomial energy distribution this happens when the average number of triplet excitons per UC-center $\overline{T}_E$ is about 13. I calculated the Φ_{TTA} according to $\Phi_{TTA} = \frac{k_{TTA}}{k_{TTA}+k_T}$, treating the UC-centers ensemble as a bulk system in solution to have a direct comparison between the annihilation rate and the triplet spontaneous decay rate. Specifically, I assumed the ensemble as monodispersed, because it can be seen as a limit case of the log-normally distributed ensemble. As reported in Tab. 9.2, I selected as upper limit of $\overline{r}$ the value $\frac{L_T}{4}$, because it is the largest $\overline{r}$ value that guarantees a $\Phi_{TTA} \geq 0.5$. For larger sizes, the density of annihilating triplets for each nanostructure is too low to have an annihilation rate competitive with the spontaneous decay rate. Therefore, according to these considerations, the confined-TTA regime is fulfilled in good approximation.
To conclude this last Chapter, I would like to stress that the findings obtained with the proposed model to describe nanostructured materials, along with the observations derived from the studies of the two solid-state polymeric upconverters presented in Chapters 6 and 7, are of utmost importance for future real-life technologies. By emphasizing the role of structural and composition parameters in setting the *s*TTA-UC performances, these results can be used as valuable guidelines for the development and implementation of solid-state upconverters in solar technologies. If the best trade-off between nanostructure size and energy distribution is found the maximum upconversion efficiency can be achieved at excitation intensities orders of magnitude lower that the solar irradiance. Notably, I shown that the beneficial dyes

confinement effects are relevant especially when molecular species featuring relatively short triplet lifetimes are involved, that are usually discarded since excessively high excitation intensities would be necessary to work properly in bulk solutions, and that can be now exploited if incorporated in a proper nanostructured system. This finding significantly broadens the family of emitters that can be now considered for future developments and, most importantly, it suggests a potential way to fully exploit the *s*TTA upconversion to recover near-infrared photons with energies below the silicon bandgap, as recently proposed.[381] Indeed, in this energy range the triplet excitons recombination rates are usually intrinsically faster, resulting in short lifetimes that hinder their use under solar irradiance. The *s*TTA confinement concept can be therefore a straightforward method to realize efficient upconverters from the near-infrared to the visible spectral range working at subsolar irradiance and therefore fabricate photonic devices suitable to be implemented in current photovoltaic technologies.

Conclusions

During the three years of my PhD studies I had the opportunity to understand in detail the fascinating photophysical process of photon upconversion assisted by triplet-triplet annihilation, unveiling its features and properties thanks to the spectroscopy facilities in the laboratory of Advanced photophysics of molecular semiconductors led by Prof. Francesco Meinardi, Prof. Sergio Brovelli, and Prof. Angelo Monguzzi. By keeping this central topic as leading route of my PhD project, I investigated photon upconversion in a variety of systems, profoundly different on many levels, revealing its captivating versatility. Thanks to paramount international collaborations, my PhD studies focused on addressing two important issues that currently limit the application of upconverters in solar technologies, i.e. the limited storage ability of common organic sensitizers and the poor upconversion performances typically observed in solid-state upconverters, which are intrinsically better suited for technological applications than liquid upconverting solutions.

After an overview of photon upconversion assisted by triplet-triplet annihilation, a brief description of the experimental methods employed in my studies and the materials characterization (Chapter 1, 2 and 3), in Chapter 4, I investigated CdSe nanocrystals doped with gold impurities and decorated with 9-anthracene carboxylic acid as innovative broadband hybrid sensitizers. The development of such sensitizers was fostered by the necessity to overcome the deleterious hole transfer from the nanocrystal valence band to the ligand HOMO level affecting undoped nanocrystals, that ultimately hinders the emitter triplet sensitization. The electronic doping strategy allows to insert into the nanocrystals energy gap localized hole-accepting states, characterized by a higher hole-capturing rate with respect to the ligand HOMO level. Thereby, right after excitation the photogenerated hole localizes in 1-2 ps on the dopant state

forming a bound exciton with the electron in conduction band that is effectively transferred to the ligand triplet states. Crucially, by changing the host size one can optimize the energy resonance between the bound exciton and the ligand triplet state, in order to maximize the energy transfer efficiency. Owing to the accomplished optimization of the energy transfer step, I achieved the upconversion efficiency of 12%, which is the record performance obtained so far for hybrid sensitizers. The results of this work were published in the journal *Advanced Materials* (DOI 10.1002/adma.202002953).

In Chapter 5, I discussed how CdSe nanoplatelets are desirable light harvesters moieties in hybrid sensitizers. Their peculiar surface and photophysical properties make semiconductor nanoplatelets decorated with proper conjugated organic molecules hybrid sensitizers with potentially optimal sensitization performances. The analysis of the sensitizer-to-ligand energy transfer efficiency assessed that the transfer step is not affected by detrimental hole transfer to the ligands thanks to favorable energy level alignment induced by 9-anthracene carboxylic acid bound to the nanoplatelets surfaces. Moreover, the study of the sensitizer-to-ligand energy transfer dependence on the surface ligand density revealed that the surface coverage via ligand exchange is not homogeneous but proceeds in an island-like way promoted by $\pi - \pi$ stacking, resulting in the formation of aggregates of ligand molecules on the surface, which causes a redshift of the ligand triplet energy. This phenomenon has important repercussions on the emitter choice, since the thermodynamic driving force of the ligand-to-emitter energy transfer can be deeply affected.

I then examined how the photophysics of *s*TTA-UC changes when moving from a bulk homogeneous system like a solution to a confined system, where the triplet excitons are localized in nanosized centers much smaller than the volume that they can potentially explore by diffusion, limiting the dependence of the *s*TTA-UC efficiency on molecular diffusion. In Chapters 6 and 7 I studied two different nanostructured polymers that show similar macroscopic properties and upconversion performances but fabricated through different approaches. They both feature liquid droplets of mean size less than 50 nm, where the upconverting dyes accumulate, embedded in a rigid polymer matrix. In the material discussed in Chapter 6 the liquid nanodomains are composed almost entirely of hexyl benzoate, while in the material discussed in Chapter 7 they consist of a liquid core containing the PPG and part of the PEG blocks, with the remaining PEG blocks protruding out into the glassy matrix stabilizing the droplets themselves. I shown how this class of materials offers many advantages; for instance,

they can be easily fabricated in a one-step synthesis under air conditions and the synthetic procedures developed enable to localize the upconverting dyes only in the liquid domains, therefore the intermolecular distances allow the short-range interactions between triplet excitons to occur mainly by hopping within the disordered close-packed dyes ensemble, with only a secondary contribution from molecular translational diffusion. Moreover, I shown that because the nanodomains volume is a small fraction of the host volume (5-10%), the effective local triplet excitons density is enhanced with respect to the corresponding solution with equal global dyes concentration, resulting in an enhanced upconversion efficiency at low excitation intensities. More generally, I highlighted that the controlled dyes confinement is not only useful to achieve chromophores concentrations that cannot be managed by standard synthetic routes, but also as a general approach to enhance the upconversion yield independently of the composition, especially when the excitation intensities are intrinsically limited.
I then pointed out how the peculiar structure underlies several beneficial advantages towards technological applications. The polymeric matrix provides rigid bulk materials that can be employed in real-world applications and it proved to confer striking long-term stability and efficient oxygen protection. The synthetic routes allow to avoid molecular aggregation and segregation even when employing extremely high dyes concentrations, yielding transparent, high optical quality materials that can be easily employed in all those technological fields such as molecular photonics, photon management or optoelectronics that require transparent materials. The results of the study in Chapter 6 were published in the journal *Advanced Functional Materials* (DOI 10.1002/adfm.202004495), while those in Chapter 7 were published in *ACS Applied Materials & Interfaces* (DOI 10.1021/acsami.1c09813).

In Chapter 8, I discussed how the achievement of excellent upconversion external quantum yields is usually hindered by the lack of annihilators with optimized photophysical properties. I introduced a perylene derivative as new annihilator/emitter, which was designed with the goal to prevent molecular aggregation especially at high dye concentrations to ultimately maximize its fluorescence efficiency. Importantly, by employing PCP as annihilator/emitter, I measured an external upconversion efficiency of 42%, which is the highest value recorded so far and it is not far from the thermodynamic limit of 50%. This exceptional result directly stems from the PCP molecular structure, as it allows to limit the fluorescence efficiency losses observed in perylene arising from aggregation and excimer formation along with partial self-absorption of the emitted upconverted light, while keeping the optimal photophysical

properties of monomeric perylene that guarantee a maximized singlet generation upon TTA. The results of this study were published in the journal *Journal of Materials Chemistry C* (DOI 10.1039/D1TC01569A).

In the final Chapter, I applied the theoretical model that I developed to describe the *s*TTA-UC process in confined systems, reported in Chapter 1 and validated by the studies in Chapters 6 and 7, to draw a perspective of the performances that can be achieved in the future by developing proper solid-state upconverters. I compared the *s*TTA-UC performances of an ideal homogeneous bulk UC system, of a confined single-sized UC system and of a confined UC system with log-normal size distribution, to point out how these performances are affected by structural and composition parameters. If the best trade-off between nanostructure size and energy distribution is met the maximum upconversion efficiency can be achieved at excitation intensities orders of magnitude lower that the solar irradiance. Therefore, with this approach I emphasized the paramount strengths afforded by the nanostructuring strategy and the important information gained through the theoretical calculations can work as guidelines for the design of solid-state upconverters to make their future implementation in solar technologies feasible. This work was published in the journal *Journal of Applied Physics* (DOI 10.1063/5.0034943).

As final consideration, I would like to emphasize that since *s*TTA-UC is extensively studied not only in the solar field, but also in diverse fields such as cellular bio-imaging, photodynamic therapy, optoelectronics, or anti-counterfeit, the results emerged from my PhD work can be implemented in a variety of technological fields and devices, even not strictly related to solar technologies.

Collaborations

The results of my PhD project have been enriched by several collaborations with researchers from international institutions and companies. Thanks to these collaborations, I had the chance to not only work on interesting novel materials, but also to learn about new experimental techniques along with broadening my background knowledge.

The results presented in Chapter 4 were fostered by the collaboration with Glass to Power Spa. Dr. Chiara Capitani synthesized the undoped and Au-doped CdSe nanocrystals and performed the ligand exchange procedure. The structural and elemental analysis of gold clusters and nanocrystals was performed by Dr. Rosaria Brescia, Dr. Mirko Prato at Istituto Italiano di Tecnologia in Genoa (Italy), and by Prof. Marcello Campione and Dr. Carlo Santambrogio from the University of Milano-Bicocca.

The synthesis of CdSe nanoplatelets discussed in Chapter 5, along with the ligand exchang protocol, was performed and optimized by Dr. Henry Halim from the research group led by Prof. Andreas Reidinger from the Max-Planck Institute for Polymer Research in Mainz, Germany. The group of Prof. Reidinger also performed the ITC and TEM characterization, along with transient absorption measurements.

The nanostructured polymers discussed in Chapters 6 and 7 were developed, optimized and synthesized by Dr. Felipe Saenz from the research group led by Prof. Christoph Weder from Adolphe Merkle Institute at the University of Fribourg, Switzerland. Dr. Saenz also performed the material characterization with TEM and DSC measurements. I also collaborated with Dr. Michele Mauri from the University of Milano-Bicocca, who performed the TD-NMR characterization of the materials and gave precious insights on the polymers properties and morphology.

Finally, the results from Chapter 8 stem from a collaboration with Prof. Pengfei Duan from the National Center for Nanoscience and Technology in Beijing, China. Dr. Wenjing Sun and Dr. Tonghan Zhao designed and synthesized the bichromophoric annihilator PCP. Prof. Duan's group also performed the material characterization with NMR and HR-MS measurements along with DFT calculations. They also performed independent upconversion quantum yield measurements.

Bibliography

[1] Shockley, W.; Queisser, H. J., *Journal of Applied Physics*, **1961**, 32, 510-519.

[2] Pedrini, J.; Monguzzi, A., *Journal of Photonics for Energy*, **2017**, 8, (16), 022005.

[3] Armaroli, N.; Balzani, V., *Chemistry - A European Journal*, **2016**, 22 (1), 32-57.

[4] De Vos, A., *Journal of Physics D: Applied Physics*, **1980**, 13 (5), 839.

[5] Zheng, T.; Runowski, M.; Martín, I. R.; Lis, S.; Vega, M.; Llanos, J., *Advanced Optical Materials*, **2021**, 9 (12), 2100386.

[6] Pawlicki, M.; Collins, H. A.; Denning, R. G.; Anderson, H. L., *Angewandte Chemie International Edition*, **2009**, 48 (18), 3244-3266.

[7] Zhou, J.; Liu, Z.; Li, F., *Chemical Society Reviews*, **2012**, 41 (3), 1323-1349.

[8] Chen, C.; Zheng, S.; Song, H., *Chemical Society Reviews*, **2021**, 50 (12), 7250-7329.

[9] Trupke, T.; Green, M. A.; Wurfel, P., *Journal of Applied Physics*, **2002**, 92, 4117-4122.

[10] Parker, C. A.; Hatchard, C. G., *Proceedings of the Royal Society of London. Series A, Mathematical and Physical Sciences*, **1962**, 269 (1339), 574-584.

[11] Parker, C. A.; Hatchard, C. G., *Transactions of the Faraday Society*, **1963**, 59, 284-295.

[12] Parker, C. A., Hatchard, C. G.; Joyce, T. A., *Nature*, **1965**, 205, 1282–1284.

[13] Parker, C. A. Joyce, T. A., *Chemical Communications*, 4, 108b-109.

[14] Parker, C. A.; Hatchard, C. G., *Proceedings of the Chemical Society*, **1962**, 386–387.

[15] Parker, C. A., *Advances in Photochemistry*, **1964**, 2, 305–383.

[16] Kozlov, D. V.; Castellano, F. N., *Chemical Communications*, **2004**, (24), 2860-2861.

[17] Keivanidis, P. E.; Baluschev, S.; Miteva, T.; Nelles, G.; Scherf, U.; Yasuda, A.; Wegner, G., *Advanced Materials*, **2003**, 15 (24), 2095-2098.

[18] Yanai, N.; Kimizuka, N., *Accounts of Chemical Research*, **2017**, 50 (10), 2487-2495.

[19] Duan, P. F.; Yanai, N.; Kimizuka, N., *Chemical Communications*, **2014**, 50 (86), 13111-13113.

[20] Christoph, G. J.; Stefan, F., *Advanced Optical Materials*, **2015**, 3 (4), 510-535.

[21] Trupke, T.; Shalav, A.; Richards, B. S.; Würfel, P.; Green, M. A., *Solar Energy Materials & Solar Cells*, **2006**, 90 (18), 3327-3338.

[22] Monguzzi, A.; Oertel, A.; Braga, D.; Riedinger, A.; Kim, D. K.; Knüsel, P. N.; Bianchi, A.; Mauri, M.; Simonutti, R.; Norris, D. J.; Meinardi, F., *ACS Applied Materials & Interfaces*, **2017**, 9 (46), 40180-40186.

[23] Khnayzer, R. S.; Blumhoff, J.; Harrington, J. A.; Haefele, A.; Deng, F.; Castellano, F. N., *Chemical Communications*, **2012**, 48 (2), 209-211.

[24] Ferreira, R. A. S.; Correia, S. F. H.; Monguzzi, A.; Liu, X.; Meinardi, F., *Materials Today*, **2020**, 33, 105-121.

[25] Cheng, Y. Y.; Fückel, B.; MacQueen, R. W.; Khoury, T.; Clady, R. G. C. R.; Schulze, T. F.; Ekins-Daukes, N. J.; Crossley, M. J.; Stannowski, B.; Lips, K.; Schmidt, T. W., *Energy & Environmental Science*, **2012**, 5 (5), 6953-6959.

[26] Klessinger, M.; Michl, J., *Excited States and Photochemistry of Organic Molecules.*, Vch Pub, **1995**.

[27] Pope, M.; Swenberg, C. E.; Pope, M., *Electronic processes in organic crystals and polymers.* Oxford University Press: New York, **1999**.

[28] Lakowicz, J. R., *Principles of Fluorescence Spectroscopy.*, Springer Science: New York, **2013**.

[29] Borisova, S. M.; Papkovskyb, D. B.; Ponomarevc, G. V.; DeTomad, A. S.; Safe, R.; Klimanta, I., *Journal of Photochemistry and Photobiology A: Chemistry*, **2009**, 206, 87-92.

[30] Bansal, A. K.; Holzer, W.; Penzkofer, A.; Tsuboi, T., *Chemical Physics*, 330, 118-129.

[31] Papkovsky, D. B.; O'Riordan, T. C., *Journal of Fluorescence*, **2005**, 15 (4), 569-584.

[32] Baluschev, S.; Miteva, T.; Yakutkin, V.; Nelles, G.; Yasuda, A.; Wegner, G., *Physical Review Letters*, **2006**, 97 (14), 143903.

[33] Monguzzi, A.; Tubino, R.; Hoseinkhani, S.; Campione, M.; Meinardi, F., *Physical Chemistry Chemical Physics*, **2012**, 14 (13), 4322-4332.

[34] Hoseinkhani, S.; Tubino, R.; Meinardi, F.; Monguzzi, *Physical Chemistry Chemical Physics*, **2015**, 17 (6), 4020–4024.

[35] Gray, V.; Moth-Poulsen, K.; Albinsson, B.; Abrahamsson, M., *Coordination Chemistry Reviews*, **2018**, 362, 54-71.

[36] Schulze, T. F.; Schmidt, T. W., *Energy & Environmental Science*, **2015**, 8 (1), 103-125.

[37] Kitazawa, M.; Yabe, T.; Hirata, Y.; Okada, T., *Journal of Molecular Liquids*, **1995**, 65 (6), 321-324.

[38] Yang, P.; Wu, W.; Zhao, J.; Huang, D.; Yi, X., *Journal of Materials Chemistry*, **2012**, 22 (38), 20273-20283.

[39] Wang, Z.; Zhao, J.; Barbon, A.; Toffoletti, A.; Liu, Y.; An, Y.; Xu, L.; Karatay, A.; Yaglioglu, H. G.; Yildiz, E. A.; Hayvali, M., *Journal of the American Chemical Society*, **2017**, 139 (23), 7831-7842.

[40] Turro, N. J., *Journal of Chemical Education*, **1969**, 46 (1), 2-6.

[41] Monguzzi, A.; Mezyk, J.; Scotognella, F.; Tubino, R.; Meinardi, F., *Physical Review B*, **2008**, 78 (19), 195112.

[42] Schmidt, T. W.; Castellano, F.N, *The Journal of Physical Chemistry Letters*, **2014**, 5, 4062-4072.

[43] Dexter, D. L., *The Journal of Chemical Physics*, **1953**, 21 (5), 836-850.

[44] Albinsson, B.; Mårtensson, J., *Journal of Photochemistry and Photobiology C: Photochemistry Reviews*, **2008**, 9 (3), 138-155.

[45] Albinsson, B.; Eng, M. P.; Pettersson, K.; Winters, M. U., *Physical Chemistry Chemical Physics*, **2007**, 9, 5847-5864.

[46] Jortner, J.; Choi, S.-I.; Katz, J. L.; Rice, S. A., *Physical Review Letters*, **1963**, 11 (7), 323-326.

[47] Cheng, Y. Y.; Fückel, B.; Khoury, T.; Clady, R. G. C. R.; Tayebjee, M. J. Y.; Ekins-Daukes, N. J.; Crossley, M. J.; Schmidt, T. W., *The Journal of Physical Chemistry Letters*, **2010**, 1 (12), 1795-1799.

[48] Charlton, J. L.; Dabestani, R.; Saltiel, J., *Journal of the American Chemical Society*, **1983**, 105, 3473–3476.

[49] Saltiel, J.; Atwater, B., *Advances in Photochemistry.*:, Wiley: New York, **1988**.

[50] Bachilo, S. M.; Weisman, R. B., *The Journal of Physical Chemistry A*, **2000**, 104 (33), 7711-7714.

[51] Bossanyi, D. G.; Sasaki, Y.; Wang, S.; Chekulaev, D.; Kimizuka, N.; Yanai, N.; Clark, J., *The Journal of American Chemical Society Au*, **2021**, 1 (12), 2188–2201.

[52] McLean, A. J.; Truscott, T. G., *Journal of Chemical Society, Faraday Transactions*, **1990**, 86, 2671–2672.

[53] Groff, R. P.; Merrifield, R. E.; Avakian, P., *Chemical Physics Letters*, **1970**, 5 (3), 168-170.

[54] Kobayashi, S.; Kikuchi, K.; Kokubun, H., *Chemical Physics Letters*, **1976**, 42 (3), 494-497.

[55] Cheng, Y. Y.; Khoury, T.; Clady, R.; Tayebjee, M. J. Y.; Ekins-Daukes, N. J.; Crossley, M. J.; Schmidt, T. W., *Physical Chemistry Chemical Physics*, **2010**, 12, 66–71.

[56] Baluschev, S.; Yakutkin, V.; Miteva, T.; Avlasevich, Y.; Chernov, S.; Aleshchenkov, S.; Nelles, G.; Cheprakov, A.; Yasuda, A.; Müllen, K.; Wegner, G., *Angewandte Chemie International Edition*, **2007**, 46 (40), 7693-7696.

[57] Oldenburg, M.; Turshatov, A.; Busko, D.; Wollgarten, S.; Adams, M.; Baroni, N.; Welle, A.; Redel, E.; Wöll, C.; Richards, B. S.; Howard, I. A., *Advanced Materials*, **2016**, 28 (38), 8477-8482.

[58] Santbergen, R.; Goud, J. M.; Zeman, M.; van Roosmalen, J. A. M.; van Zolingen, R. J. C., *Solar Energy Materials & Solar Cells*, **2010**, 94 (5), 715-723.

[59] Dilbeck, T.; Hanson, K., *The Journal of Physical Chemistry Letters*, **2018**, 9 (19), 5810–5821.

[60] Monguzzi, A.; Borisov, S. M.; Pedrini, J.; Klimant, I.; Salvalaggio, M.; Biagini, P.; Melchiorre, F.; Lelii, C.; Meinardi, F., *Advanced Functional Materials*, **2015**, 25 (35), 5617-5624.

[61] Monguzzi, A.; Braga, D.; Gandini, M.; Holmberg, V. C.; Kim, D. K.; Sahu, A.; Norris, D. J.; Meinardi, F., *Nano Letters*, **2014**, 14 (11), 6644–6650.

[62] Zou, W.; Visser, C.; Maduro, J. A.; Pshenichnikov, M. S.; Hummelen, J. C., *Nature Photonics*, **2012**, 6, 560.

[63] Fischer, S.; Mehlenbacher, R. D.; Lay, A.; Siefe, C.; Alivisatos, A. P.; Dionne, J. A., *Nano Letters*, **2019**, 19 (6), 3878-3885.

[64] Mao, C.; Min, K.; Bae, K.; Cho, S.; Xu, T.; Jeon, H.; Park, W., *ACS Photonics*, **2019**, 6 (8), 1882-1888.

[65] de la Moraa, M. B.; Amelines-Sarriab, O.; Monroyd, B. M.; Hernández-Péreze, C. D.; Lugo, J. E., *Solar Energy Materials and Solar Cells*, **2017**, 165, 59-71.

[66] Smith, M. B.; Michl, J., *Chemical Reviews*, **2010**, 110 (11), 6891–6936.

[67] Congreve, D. N..; Lee, J.; Thompson, N. J.; Hontz, E.; Yost, S. R.; Reusswig, P. D.; Bahlke, M. E.; Reineke, S.; Van Voorhis, T.; Baldo, M. A., *Science*, **2013**, 340 (6130), 334–337.

[68] Ehrler, B.; Musselman, K. P.; Bohm, M. L.; Friend, R. H.; Greenham, N. C., *Applied Physics Letters*, **2012**, 101 (15), 153507.

[69] Nattestad, A.; Cheng, Y. Y.; MacQueen, R. W.; Schulze, T. F.; Thompson, F. W.; Mozer, A. J.; Fückel, B.; Khoury, T.; Crossley, M. J.; Lips, K.; Wallace, G. G.; Schmidt, T. W., *The Journal of Physical Chemistry Letters*, **2013**, 4 (12), 2073-2078.

[70] Chandrasekaran, S.; Ngo, Y. L. T.; Sui, L.; Kim, E. J.; Dang, D. K.; Chung, J. S.; Hur, S. H., *Dalton Transactions*, **2017**, 46 (40), 13912-13919.

[71] Kim, H. I.; Kwon, O. S.; Kim, S.; Choi, W.; Kim, J. H., *Energy and Environmental Science*, **2016**, 9 (3), 1063-1073.

[72] Kim, J.-H.; Kim, J.-H., *Journal of the American Chemical Society*, **2012**, 134 (42), 17478-17481.

[73] Zhou, Y.; Ruchlin, C.; Robb, A. J.; Hanson, K., *ACS Energy Letters*, **2019**, 4 (6), 1458-1463.

[74] Dilbeck, T.; Hill, S. P.; Hanson, K., *Journal of Materials Chemistry A*, **2017**, 5 (23), 11652-11660.

[75] Kwon, O. S.; Kim, J.-H.; Cho, J. K.; Kim, J.-H., *ACS Applied Materials & Interfaces*, **2015**, 7 (1), 318-325.

[76] Singh-Rachford, T. N.; Castellano, F. N., *Coordination Chemistry Reviews*, **2010**, 254 (21), 2560-2573.

[77] Gray, V.; Dzebo, D.; Abrahamsson, M.; Albinsson, B.; Moth-Poulsen, K., *Physical Chemistry Chemical Physics*, **2014**, 16 (22), 10345-10352.

[78] Goldschmidt, J. C.; Fischer, S., *Advanced Optical Materials*, **2015**, 3 (4), 510-535.

[79] Li, C.; Koenigsmann, C.; Deng, F.; Hagstrom, A.; Schmuttenmaer, C. A.; Kim, J.-H., *ACS Photonics*, **2016**, 3 (5), 784-790.

[80] Sheng, W.; Yang, J.; Li, J.; Liu, G.; Lin, Z.; Long, J.; Xiao, S.; Tan, L., Chen, Y., *Energy & Environmental Science*, **2021**, 14 (6), 3532-3541.

[81] Dilbeck, T.; Wang, J. C.; Zhou, Y.; Olsson, A.; Sykora, M.; Hanson, K., *The Journal of Physical Chemistry C*, **2017**, 121 (36), 19690-19698.

[82] Hill, S. P.; Banerjee, T.; Dilbeck, T.; Hanson, K., *The Journal of Physical Chemistry Letters*, **2015**, 6 (22), 4510-4517.

[83] Hill, S. P.; Dilbeck, T.; Baduell, E.; Hanson, K., *ACS Energy Letters*, **2016**, 1 (1), 3-8.

[84] Mattiello, S.; Monguzzi, A.; Pedrini, J.; Sassi, M.; Villa, C.; Torrente, Y.; Marotta, R.; Meinardi, F.; Beverina, L., *Advanced Functional Materials*, **2016**, 26 (46), 8446-8446.

[85] Askes, S. H. C.; Bonnet, S., *Nature Reviews Chemistry*, **2018**, 2, pages 437–452.

[86] Nagai, A.; Miller, J. B.; Kos, P.; Elkassih, S.; Xiong, H.; Siegwart, D. J., *ACS Biomaterials Science & Engineering*, **2015**, 1 (12), 1206–1210.

[87] Liu, Q.; Yang, T.; Feng, W.; Li, F., *Journal of the American Chemical Society*, **2012**, 134 (11), 5390–5397.

[88] Liu, Q.; Xu, M.; Yang, T. S.; Tian, B.; Zhang, X. L.; Li, F. Y., *ACS Applied Materials & Interfaces*, **2018**, 10 (12), 9883-9888.

[89] Park, J.; Xu, M.; Li, F.; Zhou, H.-C., *Journal of the American Chemical Society*, **2018**, 140 (16), 5493-5499.

[90] Askes, S. H. C.; Leeuwenburgh, V. C.; Pomp, W.; Arjmandi-Tash, H.; Tanase, S.; Schmidt, T.; Bonnet, S., *ACS Biomaterials Science & Engineering*, **2017**, 3 (3), 322-334.

[91] Zhang, R.; Guan, Y.; Zhu, Z.; Lv, H.; Li, F.; Sun, S.; Li, J., *ACS Applied Materials & Interfaces*, **2019**, 11 (41), 37479–37490.

[92] Zhang, J.; Zhang, R.; Liu, K.; Li, Y.; Wang, X.; Xie, X.; Jiao, X.; Tang, B., *Chemical Communications*, **2021**, 57 (67), 8320-8323.

[93] Chen, S.; Weitemier, A. Z.; Zeng, X.; He, L.; Wang, X.; Tao, Y.; Huang, A. J. Y.; Hashimotodani, Y.; Kano, M.; Iwasaki, H.; Parajuli, L. K.; Okabe, S.; Teh, D. B. L.; All, A. H.; Tsutsui-Kimura, I.; Tanaka, K. F.; Liu, X.; McHugh, T. J., *Science*, **2018**, 359 (6376), 679-683.

[94] Sasaki, Y.; Oshikawa, M.; Bharmoria, P.; Kouno, H.; Hayashi-Takagi, Moritoshi Sato, M.; Ajioka, I.; Yanai, N.; Kimizuka, N., *Angewandte Chemie*, **2019**, 131 (49), 17991-17997.

[95] You, M.; Zhong, J.; Hong, Y.; Duan, Z.; Lin, M.; Xu, F., *Nanoscale*, **2015**, 7 (10), 4423-4431.

[96] Han, Y.; Li, H.; Wang, Y.; Pan, Y.; Huang, L.; Song, F.; Huang, W., *Scientific Reports*, **2017**, 7 (1), 1-8.

[97] Hagstrom, A. L.; Lee, H.-L.; Lee, M.-S.; Choe, H.-S.; Jung, J.; Park, B.-G.; Han, W.-S.; Ko, J.-S.; Kim, J.-H.; Kim, J.-H., *ACS Applied Materials & Interfaces*, **2018**, 10 (10), 8985-8992.

[98] Yin, W.; Yu, T.; Chen, J.; Hu, R.; Yang, G.; Zeng, Y.; Li, Y., *ACS Applied Materials & Interfaces*, **2021**, 13 (48), 57481–57488.

[99] Liu, H.; Xu, J.; Wang, H.; Liu, Y.; Ruan, Q.; Wu, Y.; Liu, X.; Yang, J. K. W., *Advanced Materials*, **2019**, 31 (15), 1807900.

[100] Scheucher, E.; Wilhelm, S.; Wolfbeis, O. S.; Hirsch, T.; Mayr, T., *Microsystems & Nanoengineering*, **2015**, 1 (1), 15026.

[101] Zach, P. W.; Maierhofer, M.; Püschmann, S. D.; Klimant, I.; Borisov, S. M., *Dyes and Pigments*, **2018**, 159, 610-618.

[102] Borisov, S. M.; Larndorfer, C.; Klimant, I., *Advanced Functional Materials*, **2012**, 22, 4360–4368.

[103] Kwon, O. S.; Song, H. S.; Conde, J.; Kim, H. I.; N. Artzi, N.; Kim, J. H., *ACS Nano*, **2016**, 10, 1512−1521.

[104] Qiu, X.; Zhou, Q.; Zhu, X.; Wu, Z.; Feng, W.; Li, F., *Nature Communications*, **2020**, 11 (1), 4.

[105] Thévenaz, D. C.; Monguzzi, A.; Vanhecke, D.; Vadrucci, R.; Meinardi, F.; Simon, Y. C.; Weder, C., *Materials Horizons*, **2016**, 3, 602-607.

[106] Jewell, M. P.; Greer, M. D.; Dailey, A. L.; Cash, K. J., *ACS Sensors*, **2020**, 5 (2), 474−480.

[107] Heinrich, E.; Avlasevich, Y.; Landfester, K.; Baluschev, S., *ACS Omega*, **2021**, 6 (29), 18860-18867.

[108] Iyisan, B.; Thiramanas, R.; Nazarova, N.; Avlasevich, Y.; Mailänder, V.; Baluschev, S.; Landfester, K., *Biomacromolecules*, **2020**, 21 (11), 4469-4478.

[109] Gao, C.; Wong, W. W. H.; Qin, Z.; Lo, S.-C.; Namdas, E. B.; Dong, H.; Hu, W., *Advanced Materials*, **2021**, 33 (45), 2100704.

[110] Deng, R.; Qin, F.; Chen, R.; Huang, W.; Hong, M.; Liu, X., *Nature Nanotechnology*, **2015**, 10 (3), 237-242.

[111] Di, D.; Yang, L.; Richter, J. M.; Meraldi, L.; Altamimi, R. M.; Alyamani, A. Y.; Credgington, D.; Musselman, K. P.; MacManus-Driscoll, J. L.; Friend, R. H., *Advanced Materials*, **2017**, 29 (13), 1605987.

[112] Kondakov, D. Y. *Philosophical Transactions of the Royal Society A*, **2015**, 373 (2044), 20140321.

[113] Yang, Z.; Mao, Z.; Xie, Z.; Zhang, Y.; Liu, S.; Zhao, J.; Xu, J.; Chi, Z., Aldredb, M. P., *Chemical Society Reviews*, **2017**, 46 (3), 915-1016.

[114] Ogawa, T.; Hosoyamada, M.; Yurash, B.; Nguyen, T. Q.; Yanai, N.; Kimizuka, N., *Journal of the American Chemical Society*, **2018**, 140, 8788.

[115] Fan, C.; Wei, L.; Niu, T.; Rao, M.; Cheng, G.; Chruma, J. J.; Wu, W.; Yang, C., *The Journal of the American Chemical Society*, **2019**, 141, 15070-15077.

[116] Singh-Rachford, T. N.; Castellano, F. N., *The Journal of Physical Chemistry Letters*, **2010**, 1 (1), 195-200.

[117] Zhao, J.; Ji, S.; Guo, H., *RSC Advances*, **2011**, 1, 937-950.

[118] McCusker, C. E.; F. N. Castellano, *Chemical Communications*, **2013**, 49 (34), 3537-3539.

[119] Börjesson, K.; Rudquist, P.; Gray, V.; Moth-Poulsen, K., *Nature Communications*, 7, 12689.

[120] Fayad, R.; Bui, A. T.; Shepard, S. G.; Castellano, F. N., *ACS Applied Energy Materials*, **2020**, 3 (12), 12557−12564.

[121] Boyde, S.; Strouse, G. F.; Jones, W. E.; Meyer, T. J., *Journal of the American Chemical Society*, **1989**, 111, 7448.

[122] Islangulov, R. R.; Kozlov, D. V.; Castellano, F. N., *Chemical Communications*, **2005**, 30, 3776-3778.

[123] Radiunas, E.; Raišys, S.; Juršėnas, S.; Jozeliūnaitė, A.; Javorskis, T.; Šinkevičiūtė, U.; Orentas, E.; Kazlauskas, K., *Journal of Materials Chemistry C*, **2020**, 8 (16), 5525-5534.

[124] Singh-Rachford, T. N.; Castellano, F. N., *Journal of Physical Chemistry A*, **2008**, 112 (16), 3550−3556.

[125] Han, J.; Zhang, J.; Shi, Y.; Duan, P., *The Journal of Physical Chemistry Letters*, **2021**, 12 (12), 3135−3141.

[126] Han, J. L.; You, J.; Yonemura, H.; Yamada, S.; Wangab, S. R.; Liab, X. G., *Photochemical & Photobiological Sciences*, **2016**, 15 (8), 1039-1045.

[127] Islangulov, R. R.; Lott, J.; Weder, C.; Castellano, F. N., *Journal of the American Chemical Society*, **2007**, 129 (42), 12652−12653.

[128] Gray, V.; Börjesson, K.; Dzebo, D.; Abrahamsson, M.; Albinsson, B.; Moth-Poulsen, K., *The Journal of Physical Chemistry C*, **2016**, 120 (34), 19018−19026.

[129] Aulin, Y. V.; van Sebille, M.; Moes, M.; Grozema, F. C.; *RCS Advances*, **2015**, 5, 107896-107903.

[130] Wu, W.; Wu, X.; Zhao, J.; Wu, M., *Journal of Materials Chemistry C*, **2015**, 3 (10), 2291-2301.

[131] Bharmoria, P.; Bildirir, H.; Moth-Poulsen, K., *Chemical Society Reviews*, **2020**, 49, 6529-6554.

[132] Gallaher, J. K.; Wright, K. M.; Frazer, L.; MacQueen, R. W.; Crossley, M. J.; Castellano, F. N.; Schmidt, T. W., *Energy & Environmental Science*, **2021**, 14 (10), 5541-5551.

[133] Amemori, S.; Sasaki, Y.; Yanai, N.; Kimizuka, N., *Journal of the American Chemical Society*, **2016**, 138 (28), 8702–8705.

[134] Sasaki, Y.; Amemori, S.; Kouno, H.; Yanai, N.; Kimizuka, N., *Journal of Materials Chemistry C*, **2017**, 21 (5), 5063-5067.

[135] Wei, Y.; Zheng, M.; Chen, L.; Zhou, X.; Liu, S., *Dalton Transactions*, **2019**, 48 (31), 11763-11771.

[136] Sasaki, Y.; Amemori, S.; Yanai, N.; Kimizuka, N., *Bulletin of the Chemical Society of Japan*, **2021**, 94 (6), 1760-1768.

[137] Nienhaus, L.; Wu, M.; Bulovic, V.; Baldo, M. A.; Bawendi, M. G., *Dalton Transactions*, **2018**, 47, 8509-8516.

[138] Meroni, D.; Monguzzi, A.; Meinardi, F., *Journal of Chemical Physics*, **2020**, 153 (11), 114302.

[139] Cheng, Y. Y.; Burkhard, F.; Tony, K.; Clady, R. G. C. R.; Ekins-Daukes, N. J.; Crossley, M. J.; Schmidt, T. W.; *The Journal of Physical Chemistry A*, **2011**, 115 (6), 1047-1053.

[140] Lei, Y.; Chen, K.; Tang, G.; Zhao, J.; Gurzadyan, G. G.; *Journal of Photochemistry and Photobiology A: Chemistry*, **2020**, 398, 112573.

[141] Mongin, C.; Garakyaraghi, S.; Razgoniaeva, N.; Zamkov, M.; Castellano, F. N., *Science*, **2016**, 351 (6271), 369.

[142] Nishimura, N.; Gray, V.; Allardice, J. R.; Zhang, Z.; Pershin, A.; Beljonne, D.; Rao, A., *ACS Materials Letters*, **2019**, 1 (6), 660-664.

[143] Zhou, Y.; Castellano, F. N.; Schmidt, T. W.; Hanson, K., *ACS Energy Letters*, **2020**, 5 (7), 2322-2326.

[144] Ogawa, T.; Yanai, N.; Monguzzi, A.; Kimizuka, N., *Scientific Reports*, **2015**, 5, 10882.

[145] Perego, J.; Pedrini, J.; Bezuidenhout, C. X.; Sozzani, P. E.; Meinardi, F.; Bracco, S.; Comotti, A.; Monguzzi, A., *Advanced Materials*, **2019**, 31 (40), 1903309.

[146] Yakutkin, V.; Aleshchenkov, S.; Chernov, S.; Miteva, T.; Nelles, G.; Cheprakov, A.; Baluschev, S., *Chemistry – A European Journal*, **2008**, 14, 9846-9850.

[147] Duncan, T. V.; Rubtsov, I. V.; Uyeda, H. T.; Therien, M. J., *Journal of the American Chemical Society*, **2004**, 126, 9474-9475.

[148] Singh-Rachford, T. N.; Nayak, A.; Muro-Small, M. L.; Goeb, S.; Therien, M. J.; Castellano, F. N., *Journal of the American Chemical Society*, **2010**, 132, 14203-14211.

[149] Turro, N. J.; Ramamurthy, V.; Scaiano, J,. *Modern Molecular Photochemistry of Organic Molecules.*, University Science Books, 2010.

[150] Henry, B. R.; Siebrand, W.,: *Organic Molecular Photophysics.*, Wiley, New York, NY, **1973**.

[151] Shi, J.; Izquierdo, M. A.; Oh, S.; Park, S. Y.; Milián-Medina, B.; Roca-Sanjuán, D.; Gierschner, J., *Organic Chemistry Frontiers*,**2019**, 6, 1948.

[152] Andrade, S. M.; Teixeira, R.; Costa, S. M. B.; Sobral, A. J. F. N., *Biophysical Chemistry*, **2008**, 133 (1-3), 1-10.

[153] Izawa, S.; Hiramoto, M., *Nature Photonics*, **2021**, 15, 895–900 —.

[154] Hagstrom, A. L.; Fan Deng, F.; Kim, J.-H., *ACS Photonics*, **2017**, 4 (1), 127–137.

[155] Baluschev, S.; Yakutkin, V.; Wegner, G.; Miteva, T.; Nelles, G.; Yasuda, A.; Chernov, S.; Aleshchenkov, S.; Cheprakov, A., *Applied Physics Letters*, **2007**, 90 (18), 181103.

[156] Pedrini, J.; Monguzzi, A.; Meinardi, F., *Physical Chemistry Chemical Physics*, **2018**, 20 (15), 9745-9750.

[157] Hagstrom, A. L.; Weon, S.; Choi, W.; Kim, J.-H., *ACS Applied Materials & Interfaces*, **2019**, 11 (14), 13304-13318.

[158] Garakyaraghi, S.; Castellano, F. N., *Inorganic Chemistry*, **2018**, 57, 2351-2359.

[159] He, S.; Luo, X.; Liu, X.; Li, Y.; Wu, K., *The Journal of Physical Chemistry Letters*, **2019**, 10 (7), 5036–5040.

[160] Kovalenko, M. V.; Manna, L.; Cabot, A.; Hens, Z.; Talapin, D. V.; Kagan, C. R.; Klimov, V. I.; Rogach, A. L.; Reiss, P.; Milliron, D. J.; Guyot-Sionnnest, P.; Konstantatos, G.; Parak, W. J.; Hyeon, T.; Korgel, B. A.; Murray, C. B.; Heiss, W., *ACS Nano*, **2015**, 9 (2), 1012-1057.

[161] Pietryga, J. M.; Park, Y.-S.; Lim, J.; Fidler, A. F.; Bae, W. K.; Brovelli, S.; Klimov, V. I., *Chemical Reviews*, **2016**, 116 (18), 10513-10622.

[162] Mongin, C.; Moroz, P.; Zamkov, M.; Castellano, F. N., *Nature Chemistry*, **2017**, 10, 225.

[163] Han, Y.; He, S.; Luo, X.; Li, Y.; Chen, Z.; Kang, W.; Wang, X.; Wu, K., *Journal of the American Chemical Society*, **2019**, 141 (33), 13033-13037.

[164] Wen, S.; Zhou, J.; Schuck, P. J.; Suh, Y. D.; Schmidt, T. W.; Jin, D., *Nature Photonics*, **2019**, 13 (12), 828-838.

[165] Luo, X.; Han, Y.; Chen, Z.; Li, Y.; Liang, G.; Liu, X.; Ding, T.; Nie, C.; Wang, M.; Castellano, F. N.; Wu, K., *Nature Communications*, **2020**, 11 (1), 28.

[166] Yoffe, A. D., *Advances in Physics*, **1993**, 42 (2), 173-262.

[167] Klimov, V. I., *Nanocrystal quantum dots*, Second Edition, CRC Press, **2002**.

[168] Brus, L., *The Journal of Chemical Physics*, **1983**, 79, (11), 5566-5571.

[169] Efros A. L.; Efros, Al. L., *Soviet Physics - Semiconductors*, **1982**, 16 (7), 772–78.

[170] Kim, S.; Fisher, B.; Eisler, H. J.; Bawendi, M., *Journal of the American Chemical Society*, **2003**, 125 (38), 11466-11467.

[171] Balet, L.; Ivanov, S.; Piryatinski, A.; Achermann, M.; Klimov, V. I., *Nano Letters*, **2004**, 4 (8), 1485-1488.

[172] Ivanov, S. A.; Nanda, J.; Piryatinski, A.; Achermann, M.; Balet, L. P.; Bezel, I. V.; Anikeeva, P. O.; Tretiak, S.; Klimov, V., *The Journal of Physical Chemistry B*, **2004**, 108 (30), 10625-10630.

[173] Reiss, P.; Protière, M.; Li, L., *Small*, **2009**, 5 (2), 154-168.

[174] García-Santamaría, F.; Chen, Y.; Vela, J.; Schaller, R. D.; Hollingsworth, J. A.; Klimov, V. I., *Nano Letters*, **2009**, 9 (10), 3482-3488.

[175] Balet, L. P.; Ivanov, S. A.; Piryatinski, A.; Achermann, M.; Klimov, V. I., *Nano Letters*, **2004**, 4 (8), 1485–1488.

[176] Milleville, C. C.; Chen, E. Y.; Lennon, K. R.; Cleveland, J. M.; Kumar, A.; Zhang, J.; Bork, J. A.; Tessier, A.; LeBeau, J. M.; Chase, D. B.; Zide, J. M. O.; Doty, M. F., *ACS Nano*, **2019**, 13 (1), 489–497.

[177] Boles, M. A.; Ling, D.; Hyeon, T.; Talapin, D. V., *Nature Materials*, **2016**, 15 (2), 141-153.

[178] Alivisatos, A. P., *Journal of Physical Chemistry*, **1996**, 100 (31), 13226-13239.

[179] Donegá, C. d. M., *Chemical Society Reviews*, **2011**, 40 (3), 1512-1546.

[180] Alivisatos, A. P., *Science*, **1996**, 271, 933-937.

[181] Rigsby, E. M.; Lee, K.; Sun, J.; Fishman, D. A.; Tang, M. L., *The Journal of Chemical Physics*, **2019**, 151 (17), 174701.

[182] Gray, V.; Xia, P.; Huang, Z.; Moses, E.; Fast, A.; Fishman, D. A.; Vullev, V. I.; Abrahamsson, M.; Moth-Poulsen, K.; Tang, M. L., *Chemical Science*, **2017**, 8 (8), 5488-5496.

[183] Lai, R.; Wu, K., *The Journal of Chemical Physics*, **2020**, 153, 114701.

[184] Davis, N. J. L. K.; Allardice, J. R.; Xiao, J.; Petty, A. J.; Greenham, N. C.; Anthony, J. E.; Rao, A., *The Journal of Physical Chemistry Letters*, **2018**, 9 (6), 1454-1460.

[185] Tabachnyk, M.; Ehrler, B.; Gélinas, S.; Bohm, M. L.; Walker, B. J.; Musselman, K. P.; Greenham, N. C.; Friend, R. H.; Rao, A., *Nature Materials*, **2014**, 13, 1033-1038.

[186] He, S.; Lai, R.; Jiang, Q.; Han, Y.; Luo, X.; Tian, Y.; Liu, X.; Wu, K., *Angewandte Chemie International Edition*, **2020**, 59 (40), 17726-17731.

[187] Nienhaus, L.; Wu, M.; Geva, N.; Shepherd, J. J.; Wilson, M. W. B.; Bulović, V.; Van Voorhis, T.; Baldo, M. A.; Bawendi, M. G., *ACS Nano*, **2017**, 11 (8), 7848-7857.

[188] Einzinger, M.; Wu, T.; Kompalla, J. F.; Smith, H. L.; Perkinson, C. F.; Nienhaus, L.; Wieghold, S.; Congreve, D. N.; Kahn, A.; Bawendi, M. G.; Baldo, M. A., *Nature*, **2019**, 571 (7763), 90-94.

[189] Zhang, Q.; Li, B.; Huang, S.; Nomura, H.; Tanaka, H.; Adachi, C., *Nature Photonics*, **2014**, 8, 326.

[190] Kim, D. H.; D'Aléo, A.; Chen, X. K.; Sandanayaka, A. D. S.; Yao, D.; Zhao, L.; Komino, T.; Zaborova, E.; Canard, G.; Tsuchiya, Y.; Choi, E.; Wu, J. W.; Fages, F.; Brédas, J. L.; Ribierre, J. C.; Adachi, C., *Nature Photonics*, **2018**, 12 (2), 98-104.

[191] Huang, Z.; Li, X.; Mahboub, M.; Hanson, K. M.; Nichols, V. M.; Le, H.; Tang, M. L.; Bardeen, C. J., *Nano Letters*, **2015**, 15 (8), 5552-5557.

[192] Thompson, N. J.; Wilson, M. W. B.; Congreve, D. N.; Brown, P. R.; Scherer, J. M.; Bischof, T. S.; Wu, M.; Geva, N.; Welborn, M.; Voorhis, T. V.; Bulovic, V.; Bawendi, M. G.; Baldo, M. A., *Nature Materials*, **2014**, 13, 1039-1043.

[193] Wu, M.; Congreve, D. N.; Wilson, M. W. B.; Jean, J.; Geva, N.; Welborn, M.; Van Voorhis, T.; Bulović, V.; Bawendi, M. G.; Baldo, M. A., *Nature Photonics*, **2015**, 10, 31.

[194] VanOrman, Z. A.;Bieber, A. S.; Wieghold, S.; Nienhaus, L., *MRS Communications*, **2019**, 9 (3), 924-935.

[195] Xia, P.; Raulerson, E. K.; Coleman, D.; Gerke, C. S.; Mangolini, L.; Tang, M. L.; Roberts, S. T., *Nature Chemistry*, **2020**, 12 (2), 137-144.

[196] Huang, Z.; Simpson, D. E.; Mahboub, M.; Li, X.; Tang, M. L., *Chemical Science*, **2016**, 7 (7), 4101-4104.

[197] Izakura, S.; Gu, W.; Nishikubo, R.; Saeki, A., *The Journal of Physical Chemistry C*, **2018**, 122 (26), 14425-14433.

[198] Huang, Z.; Xu, Z.; Mahboub, M.; Liang, Z.; Jaimes, P.; Xia, P.; Graham, K. R.; Tang, M. L.; Lian, T., *Journal of the American Chemical Society*, **2019**, 141 (25), 9769-9772.

[199] Mahboub, M.; Maghsoudiganjeh, H.; Pham, A. M.; Huang, Z.; Tang, M. L., *Advanced Functional Materials*, **2016**, 26 (33), 6091-6097.

[200] Kortan, A.; Hull, R.; Opila, R.; Bawendi, M.; Steigerwald, M.; Carroll, P.; Brus, L. E., *Journal of the American Chemical Society*, **1990**, 112 (4), 1327-1332.

[201] LaMer, V. K.; Dinegar, R. H., *Journal of the American Chemical Society*, **1950**, 72 (11), 4847-4854.

[202] VanOrman, Z. A.; Conti, C. R.; Strouse, G. F.; Nienhaus, L., *Chemistry of Materials*, **2021**, 33 (1), 452–458.

[203] VanOrman, Z. A.;Bieber, A. S.; Wieghold, S.; Nienhaus, L., *Chemistry of Materials*, **2020**, 32 (11), 4734–4742.

[204] Lai, R.; Sang, Y.; Zhao, Y.; Wu, K.; *Journal of the American Chemical Society*, **2020**, 142 (47), 19825–19829.

[205] Meinardi, F.; McDaniel, H.; Carulli, F.; Colombo, A.; Makarov, N., A.; Velizhanin, K., S.; Simonutti, R.; Klimov, V., I.; Brovelli, S., *Nature Nanotechnology*, **2015**, 10, 878–885.

[206] Huang, Z.; Tang, M. L., *Journal of the American Chemical Society*, **2017**, 139 (28), 9412-9418.

[207] Han, Y.; He, S.; Wu, K., *ACS Energy Letters*, **2021**, 6 (9), 3151–3166.

[208] Li, X.; Huang, Z.; Zavala, R.; Tang, M. L., *The Journal of Physical Chemistry Letters*, **2016**, 7 (11), 1955-1959.

[209] Ronchi, A.; Brazzo, P.; Sassi, M.; Beverina, L.; Pedrini, J.; Meinardi, F.; Monguzzi, A., *Physical Chemistry Chemical Physics*, **2019**, 21 (23), 12353-12359.

[210] De Roo, J.; Huang, Z.; Schuster, N. J.; Hamachi, L. S.; Congreve, D. N.; Xu, Z.; Xia, P.; Fishman, D. A.; Lian, T.; Owen, J. S.; Tang, M. L., *Chemistry of Materials*, **2020**, 32 (4), 1461-1466.

[211] Huang, Z.; Li, X.; Yip, B. D.; Rubalcava, J. M.; Bardeen, C. J.; Tang, M. L., *Chemistry of Materials*, **2015**, 27 (21), 7503-7507.

[212] Mahboub, M.; Huang, Z.; Tang, M. L., *Nano Letters*, **2016**, 16 (11), 7169-7175.

[213] Okumura, K.; Mase, K.; Yanai, N.; Kimizuka, N., *Chemistry – A European Journal*, **2016**, 22 (23), 7721-7726.

[214] Mase, K.; Okumura, K.; Yanai, N.; Kimizuka, N., *Chemical Communications*, **2017**, 53 (59), 8261-8264.

[215] Huang, Z.; Xia, P.; Megerdich, N.; Fishman, D. A.; Vullev, V. I.; Tang, M. L., *ACS Photonics*, **2018**, 5 (8), 3089-3096.

[216] Hou, L.; Olesund, A.; Thurakkal, S.; Zhang, X.; Albinsson, B., *Advanced Functional Materials*, **2021**, 31, 2106198-2106198.

[217] Beery, D.; Wheeler, J. P.; Arcidiacono, A.; Hanson, K., *ACS Applied Energy Materials*, **2020**, 3 (1), 29-37.

[218] Inokuti, M.; Hirayama, F., *The Journal of Chemical Physics*, **1965**, 43 (6), 1978-1989.

[219] Stryer, L.; Thomas, D. D.; Meares, C. F., *Annual Review of Biophysics and Bioengineering*, **1982**, 11 (1), 203-222.

[220] Monguzzi, A.; Tubino, R.; Meinardi, F., *International Journal of Photoenergy*, **2008**, 2008, 5.

[221] Kobashi, H.; Morita, T.; Mataga, N., *Chemical Physics Letters*, **1973**, 20 (4), 376-378.

[222] Hassoon, S.; Lustig, H.; Rubin, M. B.; Speiser, S., *The Journal of Physical Chemistry*, **1984**, 88 (25), 6367-6374.

[223] Köhler, A.; Bässler, H., *Materials Science and Engineering: R: Reports*, **2009**, 66 (4), 71-109.

[224] Perrin, F., *Comptes Rendus*, **1924**, 178, 1978-1980.

[225] Monguzzi, A.; Tubino, R.; Meinardi, F., *Physical Review B*, **2008**, 77 (15), 155122.

[226] Mikhnenko, O. V.; Blom, P, W. M.; Nguyen, T. Q., *Energy & Environmental Science*, **2015**, 8, 1867-1888.

[227] Thomas, D. D.; Carlsen, W. F.; Stryer, L., *Proceedings of the National Academy of Sciences of the United States of America*, **1978**, 75 (12), 5746-5750.

[228] Gösele, U.; Hauser, M.; Klein, U. K. A.; Frey, R., *Chemical Physics Letters*, **1975**, 34 (3), 519-522.

[229] Keizer, J., *Chemical Reviews* **1987**, 87(1), 167-180.

[230] Islam, M. A., *Physica Scripta*, **2004**, 70 (2-3), 120-125.

[231] Zhou, Q.; Zhou, M.; Wei, Y.; Zhou, X.; Liu, S.; Zhang, S.; Zhang, B., *Physical Chemistry Chemical Physics*, **2017**, 19, 1516-1525.

[232] Smallwood, I., *Handbook of Organic Solvent Properties.*, Elsevier Science, 2012.

[233] Porter, G.; Windsor, M. W., *Discussions of the Faraday Society*, **1954**, 17 (0), 178-186.

[234] Baluschev, S.; Yakutkin, V.; Miteva, T.; Wegner, G.; Roberts, T.; Nelles, G.; Yasuda, A.; Chernov, S.; Aleshchenkov, S.; Cheprakov, A., *New Journal of Physics*, **2008**, 10 (1), 013007.

[235] Singh-Rachford, T. N.; Castellano, F. N., *The Journal of Physical Chemistry A*, **2009**, 113 (20), 5912-5917.

[236] Simon, Y. C.; Weder, C., *Journal of Materials Chemistry*, **2012**, 22 (39), 20817-20830.

[237] Bennison, M. J.; Collins, A. R.; Zhang, B.; Evans, R. C., *Macromolecules*, **2021**, 54 (12), 5287–5303.

[238] Jiang, X.; Guo, X.; Peng, J.; Zhao, D.; Ma, Y., *ACS Applied Materials & Interfaces*, **2016**, 8 (18), 11441-11449.

[239] Monguzzi, A.; Mauri, M.; Bianchi, A.; Dibbanti, M. K.; Simonutti, R.; Meinardi, F., *Journal of Physical Chemistry C*, **2016**, 120 (5), 2609–2614.

[240] Monguzzi, A.; Bianchi, F.; Bianchi, A.; Mauri, M.; Simonutti, R.; Ruffo, R.; Tubino, R.; Meinardi, F., *Advanced Energy Materials*, **2013**, 3 (5), 680-686.

[241] Sakamoto, Y.; Tamai, Y.; Ohkita, H., *The Journal of Chemical Physics*, **2020**, 153 (16), 161102.

[242] Lin, T. A.; Perkinson, C. F.; Baldo, M. A., *Advanced Materials*, **2020**, 32 (26), 1908175.

[243] Felter, K. M.; Fravventura, M. C.; Koster, E.; Abellon, R. D.; Savenije, T. J.; Grozema, F. C., *ACS Energy Letters*, **2020**, 5 (1), 124-129.

[244] Sittig, M.; Schmidt, B.; Görls, H.; Bocklitz, T.; Wächtler, M.; Zechel, S.; Hager, M. D.; Dietzek, B., *Physical Chemistry Chemical Physics*, **2020**, 22 (7), 4072-4079.

[245] Kouno, H.; Sasaki, Y.; Yanai, N.; Kimizuka, N., *Chemistry – A European Journal*, **2019**, 25 (24), 6124-6130.

[246] Kimizuka, N.; Yanai, N.; Morikawa, M., *Langmuir*, **2016**, 32 (47), 12304–12322

[247] Duan, P.; Yanai, N.; Nagatomi, H.; Kimizuka, N., *Journal of the American Chemical Society*, **2015**, 137 (5), 1887-1894.

[248] Bharmoria, P.; Yanai, N.; Kimizuka, N., *Gels*, **2019**, 1 (5), 18.

[249] van Son, M. H. C.; Berghuis, A. M.; Eisenreich, F.; de Waal, B.; Vantomme, G.; Gómez Rivas, J.; Meijer, E. W., *Advanced Materials*, **2020**, 32 (48), 2004775.

[250] Munn, R. W.; Silbey, R., *The Journal of Chemical Physics*, **1985**, 83 (4), 1854-1864.

[251] Scholes, G. D., *Annual Review of Physical Chemistry*, **2003**, 54 (1), 57-87.

[252] Grisanti, L.; Olivier, Y.; Wang, L.; Athanasopoulos, S.; Cornil, J.; Beljonne, D., *Physical Review B*, **2013**, 88 (3), 035450.

[253] Ern, V.; Avakian, P.; Merrifield, R. E., *Physical Review*, **1966**, 148 (2), 862-867.

[254] Ern, V., *Physical Review Letters*, **1969**, 22 (8), 343-345.

[255] Monguzzi, A.; Ballabio, M.; Yanai, N.; Kimizuka, N.; Fazzi, D.; Campione, M.; Meinardi, F., *Nano Letters*, **2018**, 18 (1), 528-534.

[256] Rowe, J. M.; Zhu, J.; Soderstrom, E. M.; Xu, W.; Yakovenko, A.; Morris, A. J., *Chemical Communications*, **2018**, 54 (56), 7798-7801.

[257] Ogawa, T.; Yanai, N.; Kouno, H.; Kimizuka, N., *Journal of Photonics for Energy*, **2017**, 8 (2), 022003.

[258] Hosoyamada, M.; Yanai, N.; Ogawa, T.; Kimizuka, N., *Chemistry – A European Journal*, **2016**, 22 (6), 2060-2067.

[259] Meinardi, F.; Ballabio, M.; Yanai, N.; Kimizuka, N.; Bianchi, A.; Mauri, M.; Simonutti, R.; Ronchi, A.; Campione, M.; Monguzzi, A., *Nano Letters*, **2019**, 19 (3), 2169-2177.

[260] Wohnhaas, C.; Friedemann, K.; Busko, D.; Landfester, K.; Baluschev, S.; Crespy, D.; Turshatov, A., *ACS Macro Letters*, **2013**, 2 (5), 446-450.

[261] Sanders, S. N.; Gangishetty, M. K.; Sfeir, M. Y.; Congreve, D. N., *Journal of the American Chemical Society*, **2019**, 141 (23), 9180-9184.

[262] Vadrucci, R.; Monguzzi, A.; Saenz, F.; Wilts, B. D.; Simon, Y. C.; Weder, C., *Advanced Materials*, **2017**, 29 (41), 1702992.

[263] Najafov, H.; Lee, B.; Zhou, Q.; Feldman, L. C.; Podzorov, V., *Nature Materials*, **2010** ,9, 938–943.

[264] Wang, F.; Deng, R.; Wang, J.; Wang, Q.; Han, Y.; Zhu, H.; Chen, X.; Liu, X., *Nature Materials*, **2011**, 10 (12), 968–973.

[265] Amemori, S.; Gupta, R. K.; Böhm, M. L.; Xiao, J.; Huynh, U.; Oyama, T.; Kaneko, K.; Rao, A.; Yanai, N.; Kimizuka, N., *Dalton Transactions*, **2018**, 47 (26), 8590-8594.

[266] Söderlund, J.; Kiss, L. B.; Niklasson, G. A.; Granqvist, C. G., *Physical Review Letters*, **1998**, 80 (11), 2386-2388.

[267] Limpert, E.; Stahel, W.; Abbt, M., *BioScience*, **2001**, 51 (5), 341–352.

[268] Shimizu, K.; Crow, E. L., *Lognormal distributions: theory and applications*, New York, NY: Dekker, **1988**.

[269] Yanai, N.; Suzuki, K.; Ogawa, T.; Sasaki, Y.; Harada, N.; Kimizuka, N., *The Journal of Physical Chemistry A*, **2019**, 123 (46), 10197-10203.

[270] Yang, Y. A.; Wu, H.; Williams, K. R.; Cao, Y. C., *Angewandte Chemie International Edition*, **2005**, 44 (41), 6712-6715.

[271] Pradhan, N.; Goorskey, D.; Thessing, J.; Peng, X., *Journal of the American Chemical Society*, **2005**, 127 (50), 17586-17587.

[272] Chen, D.; Viswanatha, R.; Ong, G. L.; Xie, R.; Balasubramaninan, M.; Peng, X., *Journal of the American Chemical Society*, **2009**, 131 (26), 9333-9339.

[273] Eilers, J.; Groeneveld, E.; Donegá, C. d. M.; Meijerink, A., *The Journal of Physical Chemistry Letters*, **2012**, 3 (12), 1663-1667.

[274] Kang, M. S.; Sahu, A.; Frisbie, C. D.; Norris, D. J., *Advanced Materials*, **2013**, 25 (5), 725-731.

[275] Sahu, A.; Kang, M. S.; Kompc, A.; Notthoff, C.; Wills, A. W.; Deng, D.; Winterer, M.; Frisbie, C. D.; Norris, D. J., *Nano Letters*, **2012**, 12 (5), 2587–2594.

[276] Muhammed, M. A. H.; Aldeek, F.; Palui, G.; Trapiella-Alfonso, L.; Mattoussi, H., *ACS Nano*, **2012**, 6 (10), 8950-8961.

[277] Beatriz Santiago-González, B.; Monguzzi, A.; Pinchetti, V.; Casu, A.; Prato, M.; Lorenzi, R.; Campione, M.; Chiodini, N.; Santambrogio, C.; Meinardi, F.; Manna, L.; Brovelli, S., *ACS Nano*, **2017**, 11 (6), 6233–6242.

[278] Capitani, C.; Pinchetti, V.; Gariano, G.; Santiago-González, B.; Santambrogio, C.; Campione, M.; Prato, M.; Brescia, R.; Camellini, A.; Bellato, F.; Carulli, F.; Anand, A.; Zavelani-Rossi, M.; Meinardi, F.; Crooker, S. A.; Brovelli, S., *Nano Letters*, **2019**, 19 (2), 1307–1317.

[279] Luo, Z.; Yuan, X.; Yu, Y.; Zhang, Q.; Leong, D. T.; Lee, J. Y.; Xie, J., *Journal of the American Chemical Society*, **2012**, 134 (40), 16662-16670.

[280] Gijzeman, O. L. J.; Kaufman, F.; Porter, G., *Journal of Chemical Society, Faraday Transactions*, **1973**, 69, 708-720.

[281] Yu, W. W.; Qu, L.; Guo, W.; Peng, X., *Chemistry of Materials*, **2003**, 15 (14), 2854-2860.

[282] Chun-Yen, C.; Chiu-Ting, C.; Chih-Wei, L.; Ya-Hui, H.; Pi-Tai, C.; Yi-Hsuan, C.; Hsin-Tien, C., *Small*, **2005**, 1 (12), 1215-1220.

[283] Hendricks, M. P.; Campos, M. P.; Cleveland, G. T.; Jen-La Plante, I.; Owen, J. S., *Science*, **2015**, 348 (6240), 1226-1230.

[284] Tessier, M. D.; Biadala, L.; Bouet, C.; Ithurria, S.; Abecassis, B.; Dubertret, B., *ACS Nano*, **2013**, 7 (4), 3332-3340.

[285] Siracusa, V.; Genovese, L.; Ingrao, C.; Munari, A.; Lotti, N., *Polymers*, **2018**, 10 (5), 502.

[286] Lange, J.; Wyser, Y., *Packaging Technol. Sci*, **2003**, 16 (4), 149-158.

[287] Maus, A.; Hertlein, C.; Saalwächter, K., *Macromolecular Chemistry and Physics*, **2006**, 207 (13), 1150-1158.

[288] Mauri, M.; Mauri, L.; Causin, V.; Simonutti, R., *Analytical methods*, **2011**, 3 (8), 1802-1809.

[289] Mellinger, F.; Wilhelm, M.; Spiess, H. W. *Macromolecules*, **1999**, 32 (14), 4686-4691.

[290] Mauri, M.; Thomann, Y.; Schneider, H.; Saalwächter, K., *Solid State Nuclear Magnetic Resonance*, *2008*, 34 (1-2), 125–141.

[291] Li, Y.; Kruk, M., *RSC Advances*, **2015**, 5 (85), 69870–69877.

[292] Zhao, T.; Elzatahry, A.; Li, X.; Zhao, D., *Nature Reviews Materials*, **2019**, 4 (12), 775–791.

[293] Park, H. J.; Treich, G. M.; Helming, Z. D.; Morgan, J. E.; Ryu, C. Y.; Hwang, H. S.; Jung, G. Y., *Macromolecular Research*, **2015**, 23 (1), 13–20.

[294] Li, Y.; Yi, J.; Kruk, M., *Chemistry European Journal*, **2015**, 21 (36), 12747–12754.

[295] Mauri, M.; Floudas, G.; Simonutti, R., *Polymers*, **2018**, 10 (6), 665.

[296] Jepsen, S. M.; Pedersen, H. T.; Engelsen, S. B., *Journal of the Science of Food and Agriculture*, **1999**, 79 (13), 1793–1802.

[297] Besghini, D.; Mauri, M.; Simonutti, R., *Applied Sciences*, **2019**, 9 (9), 1801.

[298] Zhao, T. H.; Han, J. L.; Qin, X. J.; Zhou, M. H.; Duan, P. F., *Journal of Physical Chemistry Letters*, **2020**, 11 (1), 311-317.

[299] M. J. Frisch; G. W. Trucks; H. B. Schlegel; G. E. Scuseria; M. A. Robb; J. R. Cheeseman; G. Scalmani; V. Barone; B. Mennucci; G. A. Petersson; H. Nakatsuji; M. Caricato; X. Li; H. P. Hratchian; A. F. Izmaylov; J. Bloino; G. Zheng; J. L. Sonnenberg; M. Hada; M. Ehara; K. Toyota; R. Fukuda; J. Hasegawa; M. Ishida; T. Nakajima; Y. Honda; O. Kitao; H. Nakai; T. Vreven; J. A. Montgomery; Jr.; J. E. Peralta; F. Ogliaro; M. Bearpark; J. J. Heyd; E. Brothers; K. N. Kudin; V. N. Staroverov; T. Keith; R. Kobayashi; J. Normand; K. Raghavachari; A. Rendell; J. C. Burant; S. S. Iyengar; J. Tomasi; M. Cossi; N. Rega; J. M. Millam; M. Klene; J. E. Knox; J. B. Cross; V. Bakken; C. Adamo; J. Jaramillo; R. Gomperts; R. E. Stratmann; O. Yazyev; A. J. Austin; R. Cammi; C. Pomelli; J. W. Ochterski; R. L. Martin; K. Morokuma; V. G. Zakrzewski; G. A. Voth; P. Salvador; J. J. Dannenberg; S. Dapprich; A. D. Daniels; O. Farkas; J. B. Foresman; J. V. Ortiz; J. Cioslowski; Fox, D. J., *Gaussian 09, Revision E.01, Gaussian, Inc., Wallingford CT* **2013**.

[300] Djurovich, P. I.; Mayo, E. I.; Forrest, S. R.; Thompson, M. E., *Organic Electronics*, **2009**, 10 (3), 515–520.

[301] Califano, M.; Gómez-Campos, F. M., *Nano Letters*, **2013**, 13 (5), 2047-2052.

[302] Huang, Z.; Xu, Z.; Mahboub, M.; Li, X.; Taylor, J. W.; Harman, W. H.; Lian, T.; Tang, M. L., *Angewandte Chemie International Edition*, **2017**, 56 (52), 16583-16587.

[303] Ding, T. X.; Olshansky, J. H.; Leone, S. R.; Alivisatos, A. P., *Journal of the American Chemical Society*, **2015**, 137 (5), 2021-2029.

[304] Pinchetti, V.; Di, Q.; Lorenzon, M.; Camellini, A.; Fasoli, M.; Zavelani-Rossi, M.; Meinardi, F.; Zhang, J.; Crooker, S. A.; Brovelli, S., *Nature Nanotechnology*, **2018**, 13 (2), 145-151.

[305] Brovelli, S.; Galland, C.; Viswanatha, R.; Klimov, V. I., *Nano Letters*, **2012**, 12 (8), 4372-4379.

[306] Baker, D. R.; Kamat, P. V., *Langmuir*, **2010**, 26 (13), 11272-11276.

[307] Montalti, M.; Credi, A.; Prodi, L.; Gandolfi, M. T.; Michl, J.; Balzani, V., *Handbook of photochemistry*. CRC Press: Boca Raton, Fla.; London; New York, N.Y., *2006*

[308] Brouwer, A. M., *Standards for photoluminescence quantum yield measurements in solution (IUPAC Technical Report)*, **2011**, 83 (12), 2213.

[309] Darmanyan, A. P., *Chemical Physics Letters*, **1982** 91 (5), 396-400.

[310] Ithurria, S.; Tessier, M. D.; Mahler, B.; Lobo, R. P. S. M.; Dubertret, B; Efros, Al. L., *Nature Materials*, **2011**, 10, 936-941.

[311] Gippius, N.; Yablonskii, A.; Dzyubenko, A.; Tikhodeev, S.; Kulik, L.; Kulakovskii, V.; Forchel, A., *Journal of Applied Physics*, **1998**, 83 (10), 5410-5417.

[312] Kulik, L.; Kulakovskii, V.; Bayer, M.; Forchel, A.; Gippius, N.; Tikhodeev, S., *Physical Review B*, **1996**, 54 (4), R2335.

[313] Tikhodeev, S.; Gippius, N.; Yablonskii, A.; Dzyubenko, A.; Kulik, L.; Kulakovskii, V.; Forchel, A., *Physica Status Solidi A*, **1997**, 164 (1), 179-182.

[314] Li, Q.; Lian, T., *Accounts of Chemical Research*, **2019**, 52 (9), 2684–2693.

[315] Ithurria, S.; Dubertret, B., *Journal of the American Chemical Society*, **2008**, 130 (49), 16504-16505.

[316] Achtstein, A. W.; Schliwa, A.; Prudnikau, A.; Hardzei, M.; Artemyev, M. V.; Thomsen, C.; Woggon, U., *Nano Letters*, **2012**, 12 (6), 3151-3157.

[317] Benchamekh, R.; Gippius, N. A.; Even, J.; Nestoklon, M.; Jancu, J. M.; Ithurria, S.; Dubertret, B.; Efros, A. L.; Voisin, P., *Physical Review B*, **2014**, 89 (3), 035307.

[318] Tessier, M. D.; Javaux, C.; Maksimovic, I.; Loriette, V.; Dubertret, B., *ACS Nano*, **2012**, 6 (8), 6751–6758.

[319] Naeem, A.; Masia, F.; Christodoulou, S.; Moreels, I.; Borri, P.; Langbein, W., *Physical Review B*, **2015**, 91 (12), 121302(R).

[320] Yu, J.; Chen, R., *InfoMat*, **2020**, 2 (5), 905-927.

[321] Spittel, D.; Poppe, J.; Meerbach, C.; Ziegler, C.; Hickey, S. G.; Eychmüller, A., *ACS Nano*, **2017**, 11 (12), 12174-12184.

[322] Knauf, R. R.; Lennox, J. C.; Dempsey, J. L., *Chemistry of Materials*, **2016**, 28 (13), 4762-4770.

[323] Anderson, N. C.; Hendricks, M. P.; Choi, J. J.; Owen, J. S., *Journal of the American Chemical Society*, **2013**, 135 (49), 18536-18548.

[324] Owen, J., *Science*, **2015**, 347 (6222), 615-616.

[325] Moreels, I.; Lambert, K.; De Muynck, D.; Vanhaecke, F.; Poelman, D.; Martins, J. C.; Allan, G.; Hens, Z., *Chemistry of Materials*, **2007**, 19 (25), 6101-6106.

[326] Zhou, Q.; Cho, Y.; Yang, S.; Weiss, E. A.; Berkelbach, T. C.; Darancet, P.,*Nano Letters*, **2019**, 19 (10), 7124–7129.

[327] Yeltik, A.; Delikanli, S.; Olutas, M.; Kelestemur, Y.; Guzelturk, B.; Demir, H. V., *The Journal of Physical Chemistry C*, **2015**, 119 (47), 26768–26775.

[328] She, C.; Fedin, I.; Dolzhnikov, D. S.; Dahlberg, P. D.; Engel, G. S.; Schaller, R. D.; Talapin, D. V., *ACS Nano*, **2015**, 9 (10), 9475–9485.

[329] Piland, G. B.; Huang, Z.; Tang, M. L.; Bardeen, C. J., *The Journal of Physical Chemistry C*, **2016**, 120 (11), 5883-5889.

[330] Xia, P.; Huang, Z.; Li, X.; Romero, J. J.; Vullev, V. I.; Pau, G. S. H.; Tang, M. L., *Chemical Communications*, **2017**, 53 (7), 1241-1244.

[331] Zhang, J.; Kouno, H.; Yanai, N.; Eguchi, D.; Nakagawa, T.; Kimizuka, N.; Teranishi, T.; Sakamoto, M., *ACS Photonics*, **2020**, 7 (7), 1876–1884.

[332] Janiak, C., *Journal of the Chemical Society, Dalton Transactions*, **2000**, (21), 3885-3896.

[333] Duan, P.; Asthana, D.; Nakashima, T.; Kawai, T.; Yanai, N.; Kimizuka, N., *Faraday Discussions*, **2017**, 196 (0), 305-316.

[334] Kim, J.-H.; Deng, F.; Castellano, F. N.; Kim, J.-H., *Chemistry of Materials*, **2012**, 24 (12), 2250-2252.

[335] Vadrucci, R.; Weder, C.; Simon, Y. C., *Journal of Materials Chemistry C*, **2014**, 2 (16), 2837-2841.

[336] Vadrucci, R.; Weder, C.; Simon, Y. C., *Materials Horizons*, **2015**, 2 (1), 120-124.

[337] Kamada, K.; Sakagami, Y.; Mizokuro, T.; Fujiwara, Y.; Kobayashi, K.; Narushima, K.; Hirata, S.; Vacha, M., *Materials Horizons*, **2017**, 4 (1), 83-87.

[338] Lal, J.; Green, R., *Journal of Polymer Science*, **1955**, 17 (85), 403-409.

[339] Bowen, R.; Argentar, H., *The Journal of the American Dental Association*, **1967**, 75 (4), 918-923.

[340] Davies, M. J.; Hawkins, C. L., *Free radical research*, **2000**, 33 (6), 719-729.

[341] Hawkins, C. L.; Brown, B. E.; Davies, M. J., *Archives of Biochemistry and Biophysics*, **2001**, 395 (2), 137-145.

[342] Dzebo, D.; Moth-Poulsen, K.; Albinsson, B., *Photochemical & Photobiological Sciences*, **2017**, 16 (8), 1327-1334.

[343] Monguzzi, A.; Tubino, R.; Salamone, M.; Meinardi, F., *Physical Review B*, **2010**, 82 (12), 125113.

[344] Bonetti, S.; Farina, M.; Mauri, M.; Koynov, K.; Butt, H. J.; Kappl, M.; Simonutti, R., *Macromolecular rapid communications*, **2016**, 37 (7), 584-589.

[345] Mauri, M.; Thomann, Y.; Schneider, H.; Saalwächter, K., *Solid state nuclear magnetic resonance*, **2008**, 34 (1-2), 125-141.

[346] Kadish, K.; Guilard, R.; Smith, K. M., *Porphyrin Handbook: Multporphyrins, Multiphthalocyanines and Arrays.*, Saint Louis: Elsevier Science, **2012**.

[347] O'Neil, M. J.; Heckelman, P. E.; Dobbelaar, P. H.; Roman, K. J.; Kenny, C. M.; Karaffa, L. S.; Royal Society of, C., *The Merck index: an encyclopedia of chemicals, drugs, and biologicals*. Royal Society of Chemistry: Cambridge, UK, **2013**.

[348] Köhler, A.; Bässler, H., *Journal of Materials Chemistry*, **2011**, 21 (12), 4003-4011.

[349] Zimmermann, J.; Mulet, R.; Scholes, G. D.; Wellens, T.; Buchleitner, A., *The Journal of Chemical Physics*, **2014**, 141 (18), 184104.

[350] Monguzzi, A.; Mauri, M.; Frigoli, M.; Pedrini, J.; Simonutti, R.; Larpent, C.; Vaccaro, G.; Sassi, M.; Meinardi, F., *The Journal of Physical Chemistry Letters*, **2016**, 7 (14), 2779-2785.

[351] Bharmoria, P.; Hisamitsu, S.; Sasaki, Y.; Kang, T. S.; Morikawa, M.; Joarder, B.; Moth-Poulsen, K.; Bildirir, H.; Mårtensson, A.; Yanai, N.; Kimizuka, N., *Journal of Materials Chemistry C*, **2021**, 9 (35), 11655-11661.

[352] Alexandridis, P.; Holzwarth, J. F.; Hatton, T. A., *Macromolecules*, **1994**, 27 (9), 2414–2425.

[353] Lin, Y.; Smith, T. W.; Alexridis, P., *Journal of Dispersion Science and Technology*, **2002**, 23 (4), 539–553.

[354] Liu, H. Y.; Prévost, S.; Gradzielski, M., *Zeitschrift für Physikalische Chemie*, **2012**, 226 (7-8), 675–694.

[355] Zou, Y.; Zhou, X.; Ma, J.; Yang, X.; Deng, Y., *Chemical Society Reviews*, **2020**, 49 (4), 1173–1208.

[356] Cummins, C.; Lundy, R.; Walsh, J. J.; Ponsinet, V.; Fleury, G.; Morris, M. A., *Nano Today*, **2020**, 35, 100936.

[357] Askes, S. H. C.; Pomp, W.; Hopkins, S. L.; Kros, A.; Wu, S.; Schmidt, T.; Bonnet, S., *Small*, **2016**, 12 (40), 5579–5590.

[358] Lu, Y.; Wang, J.; McGoldrick, N.; Cui, X.; Zhao, J.; Caverly, C.; Twamley, B.; Máille, O.; Gearoid, M.; Irwin, B.; *Angewandte Chemie International Edition*, **2016**, 55, 14688-14692.

[359] Harada, N.; Sasaki, Y.; Hosoyamada, M.; Kimizuka, N.; Yanai, N., *Angewandte Chemie International Edition*, **2021**, 60 (1), 142-147.

[360] Dzebo, D.; Borjesson, K.; Gray, V.; Moth-Poulsen, K.; Albinsson, B., *Journal of Physical Chemistry C*, **2016**, 120 (41), 23397-23406.

[361] Yu, S.; Zeng, Y.; Chen, J.; Yu, T.; Zhang, X.; Yang, G.; Li, Y., *RSC Advances*, **2015**, 5 (86), 70640-70648.

[362] Olesund, A.; Gray, V.; Mårtensson, J.; Albinsson, B., *Journal of the American Chemical Society*, **2021**, 143 (15), 5745–5754.

[363] Giri, G.; Prodhan, S.; Pati, Y. A.; Ramasesha, S., *The Journal of Physical Chemistry A*, **2018**, 122 (43), 8650–8658.

[364] Isukapalli, S. V. K., Lekshmi, R. S.; Samanta, P. K.; Vennapusa, S. R., *The Journal of Chemical Physics*, **2020**, 153 (12), 124301.

[365] Cravcenco, A.; Hertzog, M.; Ye, C.; Iqbal, M. N.; Mueller, U.; Eriksson, L.;Borjesson, K., *Science Advances*, **2019**, 5 (9), eaaw5978.

[366] Aldongarov, A.; Barashkov, N. N.; Irgibaeva, I., *International Journal of Quantum Chemistry*, **2007**, 107 (13), 2331–2342.

[367] Clarke, R. H.; Hochstrasser,R. M., *Journal of Molecular Spectroscopy*, **1969**, 32, 309–319.

[368] Ye, C.; Gray, V.; Martensson, J.; Borjesson, K., *Journal of the American Chemical Society*, **2019**, 141 (24), 9578-9584.

[369] Santiago-Gonzalez, B.; Monguzzi, A.; Mikel Azpiroz, J.; Prato, M.; Erratico, S.; Campione, M.; Lorenzi, R.; Pedrini, J.; Santambrogio, C.; Torrente, Y.; De Angelis, F.; Meinardi, F.; Brovelli, S., *Science*, **2016**, 353 (6299), 571-575.

[370] Fallon, K. J.; Churchill, E. M.; Sanders, S. N.; Shee, J.; Weber, J. L.; Meir, R.; Jockusch, S.; Reichman, D. R.; Sfeir, M. Y.; Congreve, D. N.; Campos, L. M., *Journal of the American Chemical Society*, **2020**, 142 (47), 19917-19925.

[371] Huang, L.; Wu, W. T.; Li, Y.; Huang, K.; Zeng, L.; Lin, W. H.; Han, G., *Journal of the American Chemical Society*, **2020**, 142 (43), 18460-18470.

[372] Ye, C.; Gray, V.; Kushwaha, K.; Kumar Singh, S.; Erhart, P.; Borjesson, K., *Physical Chemistry Chemical Physics*, **2020**, 22 (3), 1715-1720.

[373] Birks, J. B., *Photophysics of aromatic molecules. Photophysics of aromatic molecules*, **1970**.

[374] Guo, X.; Liu, Y.; Chen, Q.; Zhao, D.; Ma. Y., *Advanced Optical Materials*, **2018**, 6 (4), 1700981.

[375] Ilharco, L. M.; Santos, A. M.; Silva, M. J.; Martinho, J. M. G., *Langmuir*, **1995**, 11, 2419—2422.

[376] Mataga, N.; Torihashi, Y.; Ota, Y., *Chemical Physics Letters*, **1967**, 1 (9), 385-387.

[377] Katoh, R.; Sinha, S.; Murata, S.; Tachiya, M., *Journal of Photochemistry & Photobiology, A: Chemistry*, **2001**, 145 (1-2), 23-34.

[378] Johnson I., *Molecular probes handbook: a guide to fluorescent probes and labeling technologies.* Life Technologies Corporation: Carlsbad, Cal., **2010**.

[379] Han, J. L.; Zhang, J.; Zhao, T. H.; Liu, M. H.; Duan, P. F., *CCS Chemistry*, **2020**, 2, 665–674.

[380] Turro, N. J., *Journal of Chemical Education*, **1969**, 46 (1), 2.

[381] Gholizadeh, E. M.; Prasad, S. K. K.; Teh, Z. L.; Ishwara, T.; Norman, S.; Petty, A. J.; Cole, J. H.; Cheong, S.; Tilley, R. D.; Anthony, J. E.; Huang, S.; Schmidt, T. W., *Nature Photonics*, **2020**, 14 (9), 585-590.

Acknowledgments

Il lavoro raccolto in questa tesi è il frutto di tre anni intensi fatti non solo di giorni passati in laboratorio, ma anche, e forse soprattutto, di esperienze e relazioni umane che hanno reso tutto il percorso ricco di ricordi e persone che porterò sempre con me. Uso quindi queste ultime pagine per ringraziare tutti coloro che mi hanno accompagnato in questa avventura, chi più chi meno, chi direttamente chi indirettamente, ma ugualmente lasciando il segno.

In primo luogo, ringrazio i miei professori, Prof. Meinardi, Prof. Monguzzi e Prof. Brovelli, per avermi guidato in tutti questi anni nell'affascinante mondo dell'infinitamente piccolo. Grazie per avermi sempre spronato, incuriosito e guidato nell'attività di ricerca.

Ringrazio Valerio Whaley, per avermi inondato di sapere scientifico, ma soprattutto di ogni tipo di cultura dal dubbio gusto. Grazie per il tuo costante supporto, per la tua amicizia, per le ore passate in laboratorio con musica di altissimo livello, per il cibo di altissimo livello. Grazie per essere stato una colonna portante in questo percorso.

Ringrazio Chiara CC, Fabiana Fabietti e Valeria Vale, avete sempre portato sorrisi infiniti, risate a non finire, affetto e unione anche nei momenti più difficili. Non sarebbe stata la stessa cosa senza di voi e l'unico neurone condiviso.

Grazie a Jack per tutte le volte che sei entrato in ufficio a staccarmi il mouse e farmi i dispetti, a FraBruni per la solarità che porti sempre, a Frappa e i tuoi sondaggi croccantini, a Sara per averci sempre creduto fino in fondo nonostante le catastrofi naturali e per portare sempre un dolcetto con te da condividere, a Dario TP per avermi fatto giocare con i colori al cadmio, ad Andrea e le tue inconfutabili verità sull'oroscopo, a Metiu per esserti sempre sincerato che stessi bene, a Grace per avere sempre risposto alle mie domande sulla chimica e per il tuo affetto, a Zaffa e la tua stampante 3D, a Erbio e i tuoi mandarini pre-sbucciati, a Cristina per le avventure insieme in America, ad Abhi per le informazioni sull'India e a tutti i tesisti che, anche se per poco tempo, hanno fatto da sfondo, caotico, ma sempre rinvigorente.

Ringrazio il Prof. Musser per avermi accolto nel suo gruppo di ricerca per sei mesi alla Cornell

University nonostante le numerose peripezie da affrontare in questo tormentato 2021. Quindi ringrazio il gruppo di ricerca *Light-Matters* con Woojae, Scott, David, Soham, Thomas, Alison e ovviamente Basil per questa esperienza a Ithaca.
Grazie agli amici di sempre, Sara, Paola, Chiara, Sara, Laura, Luca, Marco, Dario, (e a quelli che stanno per arrivare) che siete sempre presenti, anche se sparsi per il mondo tra New York, Oxford e Borgarello.
Ringrazio tutta la mia numerosa famiglia, per essere sempre unita, in ogni momento. Mamma, Papi, La, grazie.
E grazie a Te, la mia meravigliosa colonna sonora.